



# UNIVERSITÀ DI PARMA

UNIVERSITA' DEGLI STUDI DI PARMA

DOTTORATO DI RICERCA IN  
INGEGNERIA CIVILE E ARCHITETTURA

CICLO XXXI°

**PARC\_CL 2.1 Crack Model  
for the Capacity Assessment of New and  
Existing Reinforced Concrete Structures  
using Non-linear Finite Element Analysis**

Coordinatore:  
Chiar.mo Prof. Andrea Carpinteri

Tutore:  
Chiar.ma Prof.ssa Beatrice Belletti

Dottoranda: Francesca Vecchi

Anni 2015-2018



# Summary

---

In Italy, non-ductile reinforced concrete structures, designed and built in areas declared seismic by the current regulations, are an important part of the building heritage. These structures have been designed to resist only gravitational loads, without considering the actions induced by earthquakes; consequently, the structural elements of these buildings are often undersized and lack structural details. The lack of structural details generates unexpected collapses, typically not present in new buildings, and linked to brittle failure on the concrete side or to the instability of the longitudinal rebars. Moreover, most of these buildings date back to the post-war period and therefore reached and surpassed their service life; therefore, scenarios of degradation and decay are configured for the mechanical properties of the structural elements.

Recent and past seismic events (L'Aquila, April 6th 2009; Finale Emilia, May 20th 2012; Medolla, May 29th 2012; Rieti, August 24th 2016; Norcia, October 30th 2016) have highlighted the seismic vulnerability of old reinforced concrete buildings, making the theme of the existing buildings modeling of great interest. For these reasons, a crack model for the prediction of the structural response of new and existing reinforced concrete buildings subjected to static and dynamic loadings, called PARC\_CL 2.1 (abbreviation of Physical Approach for Reinforced Concrete under Cyclic Loading condition) is proposed.

The PARC\_CL 2.1 crack model allows to take into account plastic and irreversible deformations in the unloading-reloading phases, considering the hysteretic cycles of concrete and steel. These phenomena are of great relevance for cyclic and dynamic analyses because they always provided a plastic and irreversible component of the deformation.

The PARC\_CL 2.1 crack model has been implemented as a user subroutine within a finite element program (ABAQUS) in order to combine the need for an accurate modeling of the material behavior with the potential of a valid commercial solver.

The PARC\_CL 2.1 model also allows evaluating the effects induced by shrinkage, which can strongly influence the serviceability state of RC structures, as well as the interaction between steel and cracked concrete (tension-stiffening).

Finally, the PARC\_CL 2.1 model has been extended to the evaluation of existing structures behaviour, implementing, in first analysis, two constitutive laws able to consider the damage of the longitudinal reinforcement in compression. The buckling of longitudinal reinforcements can strongly influence the response of reinforced concrete structural elements, especially when it is associated with existing buildings characterized by poor quality of execution and absence of adequate stirrups. In fact, reinforced concrete structures, built before the modern seismic codes, were designed only for gravitational loads, without considering the horizontal actions induced by earthquakes. The structural elements of these structures generally have a sub-dimensioned cross-section which, when subjected to large transverse and/or cyclic deformations, fail for spalling of concrete cover with consequent buckling of the longitudinal reinforcement. Indeed, during loading inversions, the concrete prevents the development of high compressive deformations in steel bars, but, when the concrete fails, the compressive steel strains increase with buckling of longitudinal rebars. The buckling of longitudinal reinforcement is avoided or limited by the stabilising effect provided by stirrups if they are not too distant.

Buckling of longitudinal reinforcement can be obtained by different modelling approaches, as for example adopting discrete reinforcement, using non-linear steel-concrete interface elements and considering the geometric non-linearity. In the case of cracking models, as the PARC\_CL 2.1 model, it is instead necessary to adopt a constitutive law for the steel able to consider the effects induced by buckling.

The comparison of the experimental evidence with the results obtained from the non-linear finite elements analyses, by means the PARC\_CL 2.1 crack model, demonstrated the efficiency and potentiality of the proposed model. Future developments will be necessary for the application of the model to the evaluation of the seismic behaviour of degraded structures.

# Sommario

---

In Italia le strutture in calcestruzzo armato non duttili, progettate e costruite in zone dichiarate sismiche dalla attuale normativa, costituiscono una importante porzione del patrimonio edilizio. Tali strutture sono state progettate per resistere ai soli carichi gravitazionali, senza considerare le azioni indotte dal sisma; di conseguenza gli elementi strutturali di questi edifici sono spesso sottodimensionati e privi degli opportuni dettagli costruttivi. Queste carenze generano meccanismi di collasso tipicamente legati a rotture fragili lato calcestruzzo o all'instabilità delle barre verticali, non individuabili in edifici di nuova costruzione. Inoltre, la maggior parte di tali edifici risale al trentennio post-bellico e ha quindi raggiunto e superato la propria vita utile; si configurano pertanto scenari di degrado e decadimento anche delle proprietà meccaniche degli elementi strutturali.

I recenti e passati eventi sismici (l'Aquila, 6 Aprile 2009; Finale Emilia; 20 Maggio 2012; Medolla, 29 Maggio 2012; Rieti, 24 Agosto 2016; Norcia, 30 Ottobre 2016) hanno mostrato l'elevata vulnerabilità del patrimonio edilizio italiano, rendendo il tema della modellazione di edifici esistenti di grande attualità e interesse. Questi sono stati i presupposti che hanno indotto alla realizzazione di un modello fessurativo per la previsione della risposta strutturale di edifici in cemento armato sia nuovi che esistenti denominato PARC\_CL 2.1 (abbreviazione di Physical Approach for Reinforced Concrete under Cyclic Loading condition).

Il modello PARC\_CL 2.1 consente di valutare le deformazioni plastiche e irreversibili in fase di scarico-ricarico sia del calcestruzzo sia dell'acciaio. Tali fenomeni sono di rilevante importanza nelle analisi cicliche statiche e dinamiche in quanto in tali tipi di sollecitazione è sempre prevista una componente plastica ed irreversibile della deformazione.

Il modello fessurativo PARC\_CL 2.1 è stato implementato come user subroutine all'interno di un programma ad elementi finiti (ABAQUS) al fine di conciliare la necessità di

un'accurata modellazione del comportamento del materiale con le potenzialità di un valido solutore commerciale.

Il modello consente inoltre di valutare gli effetti indotti dal ritiro oltre che l'interazione tra acciaio e calcestruzzo fessurato (tension-stiffening).

Il modello PARC\_CL 2.1 è stato infine esteso alla valutazione del comportamento di strutture esistenti, implementando, in prima analisi, due legami costitutivi per l'acciaio capaci di simulare il danno delle armature longitudinali a compressione. L'instabilità (buckling) delle armature longitudinali può influenzare in modo consistente la risposta degli elementi strutturali in cemento armato specialmente quando si parla di edifici esistenti realizzati con scarsa qualità esecutiva e caratterizzati da staffature inadeguate o talvolta assenti. Infatti, le strutture in cemento armato, costruite prima dell'entrata in vigore dei codici sismici moderni, erano progettate per resistere ai soli carichi gravitazionali, senza perciò considerare le azioni indotte dal sisma. Gli elementi strutturali di tali edifici presentano generalmente una sezione trasversale sotto dimensionata che, quando sottoposta a grandi deformazioni trasversali e/o cicliche, subisce rotture per espulsione del copriferro con conseguente fenomeno di buckling delle armature longitudinali. Infatti, durante inversioni di carico il calcestruzzo nella zona compressa impedisce lo sviluppo di elevate deformazioni di compressione nell'acciaio, ma quando il calcestruzzo perde la sua resistenza, come nel caso di espulsione del copriferro, è probabile lo sviluppo di alte deformazioni di compressione nelle armature con conseguente rottura per buckling. L'unico fattore che si oppone all'inarcamento delle armature longitudinali sono le staffe trasversali che, se presenti, non devono però avere passi troppo elevati per essere efficienti.

Nelle analisi non lineari agli elementi finiti il buckling delle armature può essere colto in diversi modi, ricorrendo ad esempio ad una modellazione dell'armatura discreta, inserendo elementi di interfaccia acciaio- calcestruzzo e considerando la non linearità geometrica. Nel caso di modelli fessurativi, come il modello PARC\_CL 2.1, risulta invece necessario adottare un legame costitutivo per l'acciaio che sia in grado di considerare gli effetti indotti dal buckling.

Il confronto delle evidenze sperimentali con i risultati ottenuti dalle analisi non lineari agli elementi finiti condotte con il modello fessurativo PARC\_CL 2.1 ha dimostrato l'efficienza e le potenzialità del modello proposto. Futuri sviluppi saranno necessari per l'applicazione del modello alla valutazione del comportamento sismico di strutture degradate.

# List of Symbols

---

## Roman lower case letters

$a_m$	average crack spacing;
$b$	strain hardening ratio in Menegotto-Pinto model;
$b^+$	hardening ratio in tension, defined in Monti-Nuti model;
$b^-$	hardening ratio in compression, defined in Monti-Nuti model;
$b_0$	length of the control perimeter;
$d$	effective depth;
$d_g$	aggregate size;
$d_{max}$	maximum aggregate size;
$f_c$	cylinder compressive strength of concrete;
$f_{cf}$	flexural tensile strength;
$f_{cm}$	mean value of compressive strength of concrete;
$f_t$	axial tensile strength of concrete;
$f_{yi}$	yield strength of $i$ th order of reinforcing steel;
$f_{yi}^t$	yield strength of $i$ th order of reinforcing steel in tension;
$f_{yi}^c$	yield strength of $i$ th order of reinforcing steel in compression;
$f_{ui}$	ultimate strength of $i$ th order of reinforcing steel;
$h$	overall depth of member;
$h_{eq}$	crack band width of the finite element;
$l_x, l_y$	finite element dimensions in the $x, y$ -directions;
$l_{s,max}$	length over which the slip between concrete and steel occurs;
$s$	slip (relative displacement between steel and concrete cross-section);
$s_i$	bar spacing;
$t$	finite element thickness;
$v$	crack sliding;
$w$	crack width;

$w_{ctu}$	maximum crack opening;
$z$	internal level arm.

**Roman upper case letters**

$A_c$	area of concrete cross section;
$A_s$	area of reinforcement;
$D$	Longitudinal diameter;
$E_b$	initial unloading stiffness in case of unloading from compression to tension, defined in Kashani et al. model;
$E_c$	modulus of elasticity of concrete;
$E'_{c1}$	tangent stiffness modulus of concrete in 1-direction;
$E'_{c2}$	tangent stiffness modulus of concrete in 2-direction;
$E_e$	age-adjusted effective modulus;
$E_{hi}$	hardening modulus of the $i$ th order of bars;
$E_{si}$	modulus of elasticity of the $i$ th order of bars;
$E'_{si}$	tangent stiffness modulus of the $i$ th order of bars;
$E_{sec}$	unloading stiffness of steel in case of unloading from tension to compression, defined in Kashani et al. model;
$E_{un}$	initial unloading stiffness of steel in case of unloading from tension to compression, defined in Kashani et al. model;
$G$	elastic shear modulus of concrete in the un-cracked phase;
$G'_{12}$	tangent shear modulus of concrete in the 1,2-coordinate system;
$G_C$	fracture energy of concrete in compression;
$G_{cr}$	secant shear modulus of concrete in the cracked phase;
$G^*_{cr}$	secant shear modulus of concrete associated to the first linear branch in the cracked phase;
$G_{eq}$	equivalent overall shear modulus;
$G_F$	fracture energy of plain concrete in tension;
$G_F^{RC}$	fracture energy of reinforced concrete in tension;
$L$	computational length;
$P_{cr}$	cracking load;
$P_{cr,sh}$	cracking load in case of shrinkage;
$R$	curve transition parameter defined in Menegotto-Pinto model;
$R_0$	initial curve transition value defined in Menegotto-Pinto model;



---

$U_s$	bar perimeter;
$V_{Rm,c}$	design shear resistance of member without shear reinforcement.

### Greek symbols

$\alpha$	mass-proportional damping coefficient for Rayleigh damping;
$\alpha_i$	angle between the $x_i$ -direction and the $l$ -direction;
$\beta$	stiffness-proportional damping coefficient for Rayleigh damping;
$\gamma_{12}$	biaxial shear strain of concrete in the $l,2$ -coordinate system;
$\dot{\gamma}_{12}$	shear strain increment with respect to the time of concrete in the $l,2$ -coordinate system;
$\bar{\gamma}_{12}$	uniaxial shear strain of concrete in the $l,2$ -coordinate system;
$\gamma_{12,cr}$	shear strain in the cracked phase of the concrete;
$\gamma_{12,el}$	shear elastic strain;
$\gamma_p^n$	additional plastic excursion, defined in Monti-Nuti model;
$\gamma_s$	normalized superposition length, representing the distance between the tensile curve and the monotonic compressive curve after the yield point, defined in Monti-Nuti model;
$\gamma_{xy}$	shear strain in the $x,y$ -coordinate system;
$\delta$	shape parameter, defined in Kashani et al. model;
$\varepsilon^*$	normalized strain in Menegotto-Pinto model;
$\varepsilon_0^n$	steel strain corresponding to the yield point of the $n$ half cycle;
$\varepsilon_1$	biaxial strain of concrete along $l$ -direction;
$\bar{\varepsilon}_1$	uniaxial strain of concrete along $l$ -direction;
$\dot{\varepsilon}_1$	strain increment with respect to the time of concrete along $l$ -direction;
$\varepsilon_2$	biaxial strain of concrete along 2-direction;
$\bar{\varepsilon}_2$	uniaxial strain of concrete along 2-direction;
$\dot{\varepsilon}_2$	strain increment with respect to the time of concrete along 2-direction;
$\varepsilon_{c,cr}$	concrete strain corresponding to the peak stress in compression;
$\varepsilon_{cf}$	concrete strain caused by stress;
$\varepsilon_{c,pl}$	plastic compressive strain in the compressive domain;

$\varepsilon_{c,re}$	experienced minimum compressive strain by concrete on the monotonic curve;
$\varepsilon_{c,u}$	ultimate crushing strain;
$\varepsilon_h$	strain of the hyperbolic curve of steel, defined in Kashani et al. model;
$\varepsilon_p$	plastic strain amplitude of steel, defined in Kashani et al. model;
$\varepsilon_r^n$	steel strain corresponding to the reversal point;
$\varepsilon_{sf}$	steel strain caused by stress;
$\varepsilon_{sh}$	free shrinkage strain of concrete;
$\varepsilon_{sh,0}$	shrinkage strain of reinforced concrete;
$\varepsilon_{t,cr}$	cracking strain;
$\varepsilon_{t,pl}$	plastic compressive strain in the tensile domain;
$\varepsilon_{t,re}$	experienced maximum tensile strain by concrete on the monotonic curve;
$\varepsilon_{t,u}$	ultimate cracking strain;
$\varepsilon_x$	strain along $x$ -direction;
$\varepsilon_{x_i}$	strain of the $i$ th order of bars along $x_i$ -direction;
$\dot{\varepsilon}_{x_i}$	strain increment with respect to the time of the $i$ th order of bars in $x,y$ -coordinate system;
$\varepsilon_y$	strain along $y$ -direction;
$\zeta$	softening coefficient of concrete;
$\eta$	amplification coefficient of the seismic acceleration time history;
$\theta_i$	angle between the direction of the $i$ th order of bars and the $x$ -direction;
$\lambda$	computational slenderness;
$\lambda_{cr}$	critical slenderness ratio;
$\mu$	strain hardening ratio defined in Kashani et al. model;
$\nu$	Poisson's ratio;
$\xi_{max}^n$	maximum plastic strain hardening of previous half cycles, defined in Monti-Nuti model;
$\xi_p^n$	plastic strain hardening at the $n$ th half cycle, defined in Monti-Nuti model;
$\rho_i$	reinforcement ratio related to the $i$ th order of bars;
$\sigma^*$	asymptotic value of the compressive stress of steel, defined in Kashani et al. model;

---

$\sigma_0^n$	steel stress corresponding to the yield point of the $n$ half cycle;
$\sigma_1$	concrete stress along $1$ -direction;
$\sigma_2$	concrete stress along $2$ -direction;
$\sigma_{cl,cr}$	concrete close cracking residual bond stress;
$\sigma_h$	stress of the hyperbolic curve defined in Kashani et al. model;
$\sigma_{min}$	minimum stress value reached by steel in compression in case of buckling, defined in Kashani et al. model;
$\sigma_r^n$	steel stress corresponding to the reversal point;
$\sigma_s^*$	normalized stress in Menegotto-Pinto model;
$\sigma_{tmin}$	minimum stress value reached by steel in compression in case of absence of buckling, defined in Kashani et al. model;
$\sigma_{x_i}$	stress of the $i$ th order of bars along $x_i$ -direction;
$\sigma_{yc}$	updated value of the buckling stress, defined in Kashani et al. model;
$\sigma_\infty$	asymptotic value of the compressive stress of steel, defined in Monti-Nuti model;
$\tau_{1,2}$	shear stress of concrete in the $1,2$ -coordinate system;
$\bar{\tau}_{ts}$	average bond stress along the segment;
$\tau$	bond stress;
$\phi$	nominal diameter of bar;
$\Psi$	angle between the $1$ -direction and the $x$ -direction;
$\Phi_p^n$	plastic work of $n$ th half cycle, defined in Monti-Nuti model;
$\Delta\sigma_I^n$	stress variation due to isotropic strain hardening at $n$ th half cycle, defined in Monti-Nuti model;
$\Delta\sigma_{KM}^n$	stress variation due to kinematic strain hardening and memory rule in presence of buckling at $n$ th half cycle, defined in Monti-Nuti model;
$\Delta\sigma_{KIM}^n$	stress variation due to kinematic and isotropic hardening and memory rule in presence of buckling at $n$ th half cycle, defined in Monti-Nuti model.

### Matrices and vectors

$\{\epsilon_{1,2}\}$	biaxial strain field for concrete in $1,2$ -coordinate system;
$\{\bar{\epsilon}_{1,2}\}$	uniaxial strain field for concrete in $1,2$ -coordinate system;

---

$\{\boldsymbol{\varepsilon}_c\}$	strain field of concrete in $x,y$ -coordinate system;
$\{\boldsymbol{\varepsilon}_{cf}\}$	strain field of concrete in $x,y$ -coordinate system caused by external force;
$\{\boldsymbol{\varepsilon}_s\}$	strain field of steel in $x,y$ -coordinate system;
$\{\boldsymbol{\varepsilon}_{sf}\}$	strain field of steel in $x,y$ -coordinate system caused by external force;
$\{\boldsymbol{\varepsilon}_{sh}\}$	shrinkage strain field in $x,y$ -coordinate system;
$\{\boldsymbol{\varepsilon}_{x,y}\}$	strain field in $x,y$ -coordinate system;
$\{\boldsymbol{\varepsilon}_{x_i,y_i}\}$	strain field in $x_i,y_i$ -coordinate system;
$\{\boldsymbol{\sigma}_{1,2}\}$	stress field of concrete in $1,2$ -coordinate system;
$\{\boldsymbol{\sigma}_{1,2}\}_{damp}$	damping contribute to the stress vector of concrete in $1,2$ -coordinate system;
$\{\boldsymbol{\sigma}_{x,y}\}$	overall stress field, considering the contribution of both concrete and bars, in $x,y$ -coordinate system;
$\{\boldsymbol{\sigma}_{x_i,y_i}\}$	stress field for the $i$ th order of bars in $x_i,y_i$ -coordinate system;
$\{\boldsymbol{\sigma}_{x_i,y_i}\}_{damp}$	damping contribute to the stress vector of the $i$ th order of bars;
$\{\boldsymbol{\sigma}_{x,y}\}_c$	stress field for concrete in $x,y$ -coordinate system;
$\{\boldsymbol{\sigma}_{x,y}\}_{s,i}$	stress field for the $i$ th order of bars in $x,y$ -coordinate system;
$[C]$	Rayleigh damping matrix;
$[D_{1,2}]$	Jacobian matrix of concrete in $1,2$ -coordinate system;
$[D_{x,y}]$	overall Jacobian matrix, considering the contribution of both concrete and bars, in $x,y$ -coordinate system;
$[D_{x_i,y_i}]$	Jacobian matrix of the $i$ th order of bars in $x_i,y_i$ -coordinate system;
$[K]$	stiffness matrix;
$[M]$	mass matrix;
$[T_\psi], [T_{\vartheta_i}]$	transformation matrices;
$[T_\psi]^t, [T_{\vartheta_i}]^t$	transpose of the transformation matrices.

# Contents

---

Summary

Sommario

List of Symbols

<b>1</b>	<b>General Introduction .....</b>	<b>1</b>
1.1	Context of the Research Topic .....	2
1.2	Research Scope and Methodology .....	5
1.2.1	Lacunae in Current Knowledge.....	7
1.2.2	Research Objectives .....	8
1.2.3	Thesis Outline.....	8
1.3	References .....	10
<b>2</b>	<b>The PARC_CL 2.1 Crack Model.....</b>	<b>13</b>
2.1	Overview .....	13
2.2	Material Constitutive Models Implemented in PARC_CL 2.1 .....	17
2.2.1	Strain Fields.....	17
2.2.2	Stress Fields.....	19
2.2.3	Rayleigh Stiffness Proportional Damping.....	20
2.2.4	Stiffness Matrix and Numerical Solution Procedure.....	21
2.2.5	Cyclic Uniaxial Constitutive Law for Concrete .....	23
2.2.6	The Aggregate Interlock Effect.....	27
2.2.7	Cyclic Uniaxial Constitutive Law for Embedded Mild Steel Bars .....	30
2.3	Applications of the PARC_CL 2.1 Model to RC Members.....	32
2.3.1	Cyclic Analyses of RC Panels.....	32
2.3.1.1	PARC_CL 2.1 versus Other Crack Models .....	41
2.3.2	The CASH Benchmark Phase 2 .....	46
2.3.2.1	Diaphragm Effects .....	58
2.3.3	Analyses of RC Deck Slabs of Hollow Box Bridges .....	62
2.3.3.1	Evaluation of the Transverse Shear Resistance attributed to the Concrete .....	66
2.3.3.2	Interaction between Longitudinal Bending Moment and Transverse Shear Strength .....	70
2.4	Concluding Remarks .....	73
2.5	References .....	74
<b>3</b>	<b>Shrinkage Effect in the PARC_CL 2.1 Crack Model.....</b>	<b>79</b>
3.1	Shrinkage Effect on a Uniaxial Tension Member .....	80
3.1.1	Simplified Model for the Calculation of Uniform Shrinkage Strain.....	83

---

3.2	Implementation of the Shrinkage Effect in the PARC_CL 2.1 Model .....	87
3.3	Validation of the Implemented Formulation .....	88
3.3.1	Simulation of Uniaxial Tension Members .....	88
3.3.1.1	Analytical Calculations .....	89
3.3.1.2	NLFEA Results .....	90
3.4	Concluding Remarks .....	94
3.5	References .....	95
<b>4</b>	<b>Tension Stiffening Effect in the PARC_CL 2.1 Crack Model.....</b>	<b>97</b>
4.1	Implementation of a Tension Stiffening Model for RC elements .....	98
4.2	Effects of Shrinkage on Tension Stiffening .....	104
4.2.1	Uniaxial Tension Members .....	104
4.2.2	Simulation of RC Beams .....	108
4.2.2.1	T 12-70-00 Beam .....	112
4.2.2.2	T 25-70-00 Beam .....	117
4.2.3	Simulation of RC Continuous Slabs.....	121
4.2.3.1	Membrane Action Effects on Punching Shear Resistance.....	123
4.2.3.2	Membrane Action Dependency on Boundary Conditions .....	126
4.2.3.3	Moment Redistribution Effect .....	130
4.3	Concluding Remarks .....	131
4.4	References .....	132
<b>5</b>	<b>PARC_CL 2.1 Crack Model for Existing RC Members .....</b>	<b>137</b>
5.1	The Buckling Phenomenon .....	139
5.2	Implementation of Steel Constitutive Laws Including Buckling .....	143
5.2.1	Implementation of Monti and Nuti (1992) Model.....	144
5.2.1.1	Monotonic Behaviour .....	144
5.2.1.2	Cyclic Behaviour.....	146
5.2.2	Implementation of Kashani et al. (2015) Model .....	154
5.2.2.1	Tensile Envelope TE.....	156
5.2.2.2	Compressive Envelope CE.....	157
5.2.2.3	Unloading Reloading from Tension to Compression URTC..	159
5.2.2.4	Unloading Reloading from Compression to Tension URCT..	160
5.2.2.5	Incomplete Unload-Reload Cycles IURC.....	162
5.3	Validation of the Implemented Formulations .....	164
5.3.1	Simulation of Bare Bars .....	164
5.3.2	Simulation of RC Elements.....	168
5.3.3	Simulation of an Existing RC Column.....	171
5.3.3.1	NLFEA by means of PARC_CL 2.1 crack model.....	173
5.4	Concluding Remarks .....	189
5.5	References .....	191
<b>6</b>	<b>General Conclusions and Recommendations .....</b>	<b>197</b>
6.1	Recommendation for Future Research .....	199
6.2	References .....	202
<b>7</b>	<b>Curriculum Vitae.....</b>	<b>207</b>
<b>8</b>	<b>List of Publications .....</b>	<b>209</b>

# General Introduction

---

# 1

Advanced non-linear finite element analysis (NLFEA) has become an increasingly widespread tool for the design of new buildings and assessment of existing structures. Indeed, by means of NLFEA it is possible to assess safety using realistic descriptions of the material behaviour able to take into account hidden structural capacities.

In the Level of Approximation framework, suggested by *fib* Model Code 2010 (*fib*, 2013) for new reinforced concrete (RC) structures, NLFEA can be used to achieve the highest level-of-approximation. The idea behind this concept is that the higher the level-of-approximation, the more sophisticated are the analysis and the estimation of safety, together with the possibilities of finding more realistic structural capacities. On the other hand, the chance of avoiding over-conservative designs and reassessments increases the probability of avoiding unnecessary costs. Depending on the stage of the project, several levels of design expressions and design methods are distinguished. The lower levels-of-approximations are well-described in *fib* (2013) by means of clear expressions whereas the situation is remarkably different when it comes to using non-linear finite element analysis. Moreover, the *fib* Model Code provides safety formats to be used in correlation with non-linear finite element analysis by defining safety factors for the material properties and the global structural resistance.

If the *fib* Model Code suggested design concepts and strategies for *new* RC structures, the reference code for *existing* RC structures is Eurocode 8 - part 3 (EN 1998-3:2005). Indeed, one of the main objective of Eurocode 8 - part 3 (EN 1998-3:2005) is to provide criteria for the evaluation of the seismic performance of existing individual building structures. More specifically, Eurocode 8 - part 3 indicates that the seismic action effects may be evaluated using, for example, non-linear static analysis (pushover) and non-linear time history dynamic analysis.

It is beyond doubt that the results of non-linear finite element analysis can be substantially influenced by the adopted model and human factors. NLFEA can be a powerful design tool that, during the design process, can offer a refined verification by simulating the structural response under design actions. However, NLFEA reliability depends on the analyst's experience and awareness. A possible strategy is to verify NLFE programs by calibrating them, using selected test results. In this way, the accuracy of the prediction can be optimized before its use for design and assessment of similar types of members. Furthermore, NLFEA guidelines are important to reduce the sensibility or the scatter of analysis and most of all analyst's errors. Useful examples are the Guidelines for Non-linear Finite Element Analysis of Concrete Structures for static analyses published by the Dutch Ministry of Public Works (Hendriks et al., 2017).

## 1.1 Context of the Research Topic

In general, NLFEAs allow to consider realistic material modelling in order to obtain accurate structural behaviour. However, the results obtained from NLFEAs strongly depend on the modelling strategies. For this reason, attending blind predictions and round robin competitions is a fundamental step of NLFEA effectiveness check. The SMART 2013 international benchmark experience is an example of blind prediction in which the University of Parma took part.

Participants to the benchmark were invited to provide the response assessment of scaled RC nuclear structure facility, Figure 1.1a, tested under strong motion input (Richard et al., 2015). The aim of the research was to evaluate the predictive capacity of the modelling in terms of global and local response, in order to try to partially fill the gap between the need of non-linear calculation for large structures and the modelling technique. Figure 1.1 shows the different modelling approaches adopted by participant teams, that represent the main modelling strategies used in engineering practice.

Figure 1.1b-c is an example of frame approach using *beam elements*. The *beam elements* approach is particularly indicated for modelling frame structures (Yazgan and Dazio, 2011). By means of this approach the structure is modelled as an assembly of interconnected frame elements in which the non-linear flexural behaviour can be assessed using two different models: the *lumped plasticity* models allow to concentrate the non-linearity in some limited part of the



element. The *lumped plasticity* model is simpler and computationally lighter but, on the other hand, it requires a lot of experience by the operator to establish the non-linear behaviour and the characteristic length of the non-linear parts. On the contrary, the *distributed plasticity models* (also known as *fibre* models) allow capturing the spread of non-linearity through the whole member. The cross section of the element is discretized into smaller subregions referred to as fibres. A uniaxial cyclic stress-strain model is assigned to each fibre depending on the material it represents. The main advantages are related to the accuracy in the global response prediction and to the computational efficiency for the non-linear dynamic response analysis of structures with several hundred members (Spacone et al., 1996<sup>a</sup>; Spacone et al., 1996<sup>b</sup>). However, it is difficult to capture the shear failure (associated with the development of inclined crack) or phenomena associated with torsional effects.

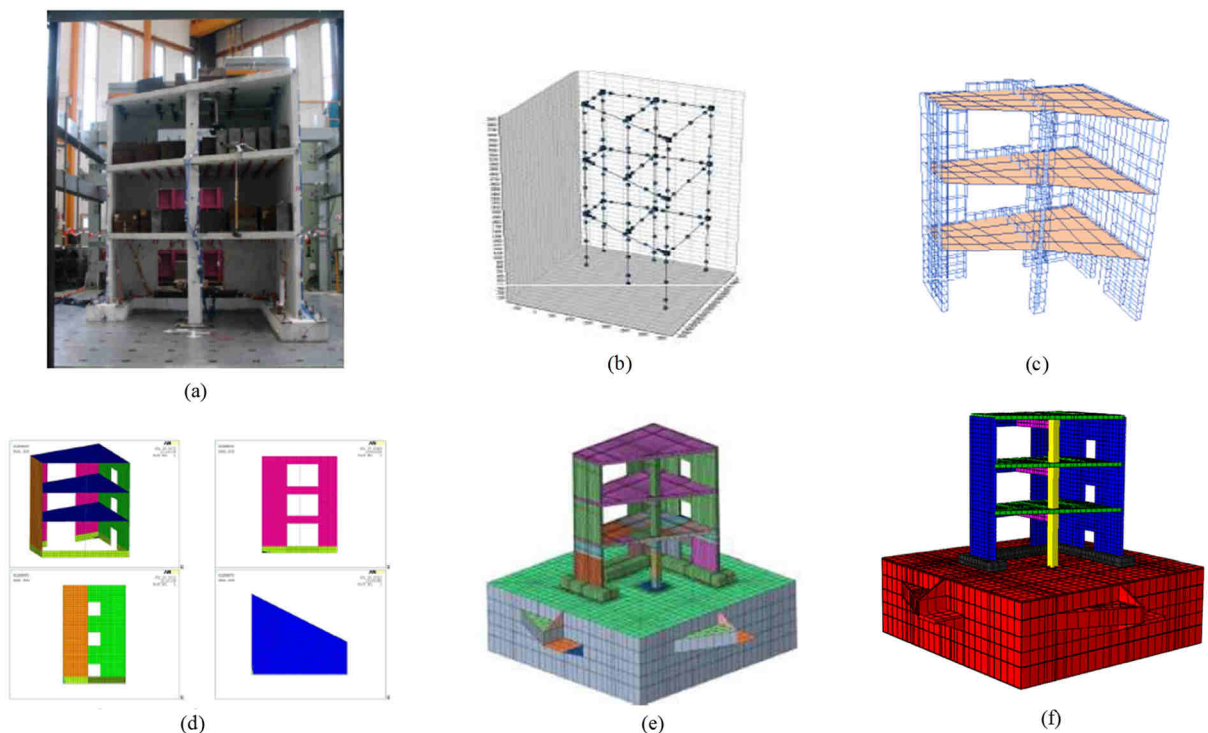


Figure 1.1: SMART2013 International Benchmark (Richard et al., 2018): (a) pictures of the RC specimen and modelling approaches adopted by participants: (b) lumped mass based models, (c) beam element based model, (d) plate and shell element model, (e) solid element model, (f) shell and solid elements.

Another modelling approach that can be adopted is the *solid elements* one, Figure 1.1e. In this case, the structural member is subdivided into three dimensional (3-D) finite elements characterized at each node by translational degrees of freedom. This approach can describe the geometry of the structure, especially the connection of adjacent members (e.g. walls and slabs),

more accurately than beam or shell element models. Moreover, due to the fact that these elements are defined in the 3-D space, they can capture different failure modes, related to flexural and shear behaviour both in-plane and out-of-plane. However, prediction of the non-linear response of the structure, modelled using *brick elements*, is high time and memory demanding; convergence issues are usually affecting the NLFEA solutions and the response is strongly dependent on material models which requires a 3D formulation. *Solid elements* have the tendency to produce large systems of equations and for this reason are usually applied when other approaches are unsuitable or would produce inaccurate analysis results.

Figure 1.1d-f is an example of modelling using *2D elements*. In particular Figure 1.1f shows the modelling strategies adopted by the team from the University of Parma using *shell elements* (of which the author of this Ph.D. thesis takes part), (Belletti et al., 2017). *Shell elements* can be considered as a simplification, with respect to *solid element*, based on two main hypotheses. The first one is that a plane section remains a plane before and after deformation. The second consideration is that stresses, acting normal to the mid-surface of the shell elements, are negligible (Maekawa et al., 2003)

Within the same modeling approach is also possible to assign the non-linear behaviour of materials in different ways. For example, during the CASH benchmark (organized by OECD-NEA - Nuclear Energy Agency), to which the University of Parma participated, most of the participants have been using *shell elements* to assess the capacity of full scale RC walls extracted from a nuclear power plants (NPP) building subject to various seismic loading intensities. The non-linearity at the integration points of shell elements has been assigning by means of different strategies: *plasticity models*, *damage mechanics models*, and *non-linear elastic models*.

Stress-based *plasticity models* are useful for modelling concrete subjected to triaxial stress states (Grassl et al., 2002; Cervenka and Papanikolaou, 2008). In these models, the elastic part of the strain is separated from the plastic one in order to realistically represent the observed deformations in confined compression. However, *plasticity models* are not able to describe the reduction of the unloading stiffness, experimentally observed.

Conversely, strain based *damage mechanics models* are able to consider the gradual reduction of the elastic stiffness (Mazars and Pijaudier-Cabot, 1989). On the other hand, isotropic *damage mechanics models* are often unable to describe irreversible deformations

observed in experiments and are mainly limited to tensile and low confined compression stress states.

For this reason, combinations of isotropic damage and plasticity are widely used to model both tensile and compressive failure (Grassl and Jirasek, 2006). These kinds of constitutive laws allow a physical description of crack initiation and development but are less useful in case of severe loadings.

A different approach is based on *non-linear elastic models* (discrete crack models or smeared crack models, described in *Chapter 2*). The smeared crack approach is the procedure most commonly employed. The basic assumption is that the first crack is developed perpendicular to the principal tensile direction. After cracking, the material can be described with an orthotropic model. In this context, this Ph.D. thesis is placed. A smeared crack model for the prevision of RC elements subjected to cyclic and dynamic loading is proposed.

## 1.2 Research Scope and Methodology

The non-linear behaviour of RC structures is related to the highly non-linear response of material to cyclic loading, in particular seismic one. For this reason, realistic cyclic constitutive models are required to obtain reasonably accurate simulations of RC members.

Existing commercial finite-element codes often have limitations in representing cyclic behaviour, due to idealizations in material models, or due to the fact that they are not able to consider particular failure modes, for example, those associated to existing buildings.

The need to handle every single constitutive law and to add, as needed, different contributions led to the creation of a new crack model for reinforced concrete elements, called PARC\_CL 2.1 (Physical Approach for Reinforced Concrete under Cyclic Loading condition). The PARC\_CL 2.1 model is a smeared and fixed crack model for the cyclic and dynamic response prevision of RC structures, able to consider plastic and irreversible deformation occurring during the unloading/reloading phases. The PARC\_CL 2.1 crack model is implemented as a user subroutine, written in the fortran language, for the Abaqus software.

In the PARC\_CL 2.1 crack model, the quantities that control the problem are the opening and the sliding of the crack lips, as well as the strain of the concrete struts that are located between cracks. Applied to a local analysis of cracked reinforced concrete, the above variables

allow for the effective modeling of compatibility and equilibrium conditions and take into account phenomena such as aggregate interlock, tension stiffening, and buckling.

Once the knowledge of the behaviour of a single element is reached, it is easily possible to study entire structures as an assemblage of many elements, Figure 1.2.

More specifically, the user subroutine is created for the application to *multi-layered shell* elements. The advantages of *multi-layered shell* finite element modelling are many, including the ability to consider the interaction between the stresses acting both in the plane and out of the element's main plane.

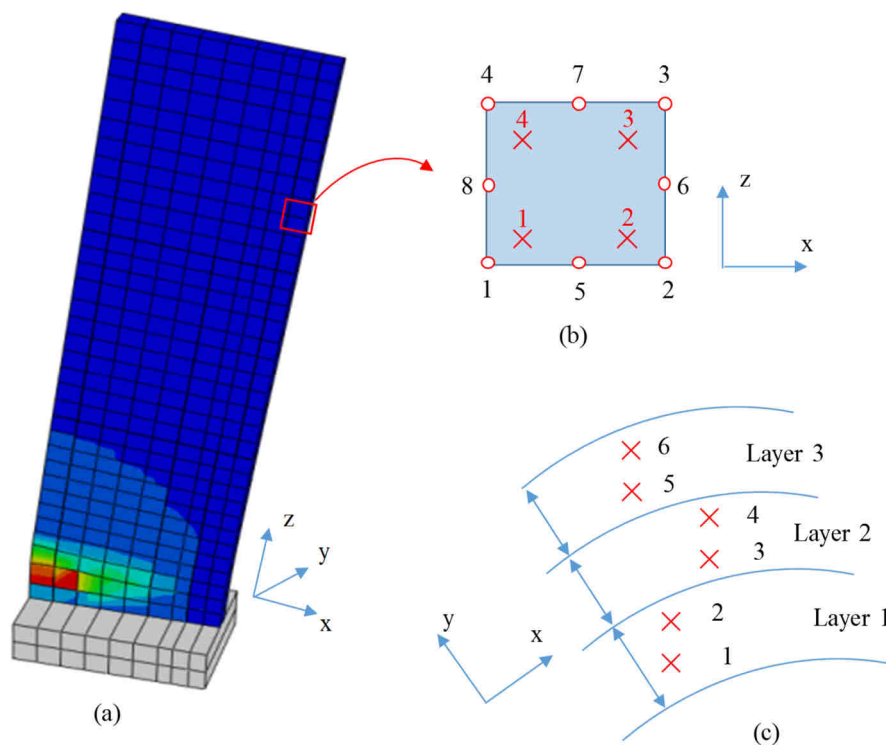


Figure 1.2: (a) Entire structure considered as the assembly of multi-layered shell elements: (b) shell element in plane and (c) shell section.

The thesis presents formulations implemented in the PARC\_CL 2.1 and demonstrates the reliability of the model through the methodical comparison with the experimental results of different types of structural elements. After demonstrating the efficiency of the model for the prediction of the structural response of new buildings, it was possible to extend the formulation to existing buildings as well. This interest arises from the need for a correct analysis of the vulnerability of existing structures, in which unexpected local and global mechanisms may develop, linked to lack of details and often accompanied by poor material characteristics.

Herein lies the true peculiarity of the PARC\_CL 2.1 model. The knowledge of such mechanisms would lead to great advantages in the "conceptual design" of the seismic assessment, so as to maximize its effectiveness. This procedure is essential for the safeguard and development of the existing building.

The buckling failure mode due to the instability of the vertical bars, often anticipated by corrosive phenomena, turns out to be pernicious for existing RC structures characterized by a lack of detail. For this reason, the first step to extend the model to existing buildings concerned the study of buckling of longitudinal rebars.

The aim of the thesis is therefore to develop a model for RC elements capable of evolving according to the type of problem that needs to be explored, in order to overcome the limits imposed by the commercial programs.

### 1.2.1 Lacunae in Current Knowledge

This research aims to provide a contribution to a correct methodological and engineering approach to the problem of predictive evaluation of the collapse mechanisms typical of new and existing structures. In fact, there is only limited research available that combines deterioration modelling with numerical analyses of the member resistance of existing structures.

Some collapse mechanisms typical of existing structures are not observed in new buildings, such as the buckling of longitudinal reinforcements caused by insufficient stirrups. This is due to the fact that reinforced concrete structures, built before the modern seismic codes, were designed only for gravitational loads, without considering the horizontal actions induced by earthquakes. The elements of these structures generally have a sub-dimensioned cross-section which, when subjected to large transverse and/or cyclic deformations, fail for spalling of concrete cover with consequent buckling of the longitudinal reinforcement.

There are currently a very limited models able to predict the non-linear response of RC elements accounting for the combined effect of inelastic buckling and cycle fatigue degradation. This aspect led to extend the PARC\_CL 2.1 formulation to existing RC structures. The first step of this work was the implementation of constitutive models able to take into account for buckling effect.

### 1.2.2 Research Objectives

This Ph.D. research focuses on the following main objectives:

- Develop a new crack model, called PARC\_CL 2.1, for the response prevision of RC elements or structures subjected to static and dynamic loading;
- Develop a numerical model to assess the contribute given by bond-slip mechanism between steel and concrete and shrinkage effects;
- Validate the PARC\_CL 2.1 model by means of comparison, both in terms of global and local response, with experimental data available in literature;
- Extend the PARC\_CL 2.1 crack model to the structural response assessment of existing RC structures. In this sense the first step consists in the implementation of constitutive laws for steel accounting for buckling of the longitudinal rebars;
- Develop a numerical model capable of evolving according to the type of problem that needs to be explored.

### 1.2.3 Thesis Outline

This thesis work is divided into six chapters each of which is organized in the following way, Figure 1.3:

- introduction to literature background;
- presentation of the implemented formulation;
- validation of the PARC\_CL 2.1 model by means of comparison with experimental tests inherent the implemented contribute;
- conclusion and remarks about potentiality and possible improvements of the PARC\_CL 2.1 crack model.

This methodology of work has allowed to create a cracking model increasingly more complex and able to grasp various aspects that affect the RC structures. For clarifying the versatility of the proposed model, the systematic verification is carried out through comparison with some experimental test.

In *Chapter 2* the concepts underlying the different theoretical approaches will be described, highlighting the peculiarities of the proposed model and the common aspects to other approaches. It will thus be possible to place the proposed model more accurately within the studies carried out by other authors on RC elements subject to in-plane stresses. Furthermore,

the main formulations for RC elements subjected to cyclic loading are presented and the comparison with the results obtained by another NLFEA program are shown.

*Chapter 3* presents a proper numerical modelling able to consider the concrete shrinkage effect. Shrinkage is an important contribute because it affects the cracking resistance of structural elements, as well as their deformations even under short-term loading. To this aim, concrete shrinkage is explicitly considered by treating it as a prescribed deformation. This permits to avoid inaccurate predictions of structural performances at serviceability conditions.

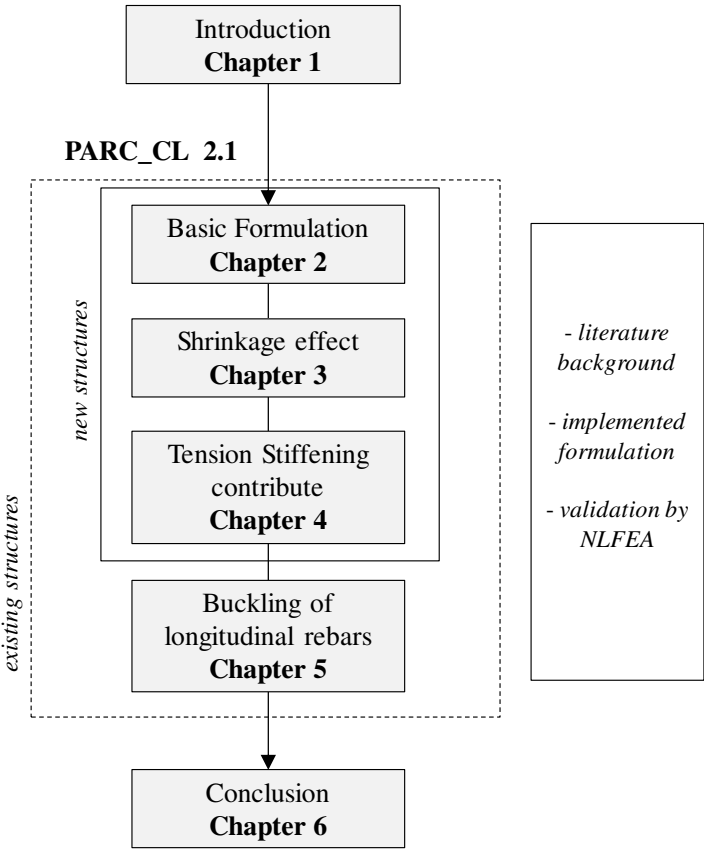


Figure 1.3: Thesis outline.

The combined effect of shrinkage deformations and tension-stiffening will be treated in *Chapter 4*. In fact, shrinkage causes time-dependent cracking and gradually reduces the beneficial effects of tension stiffening. On the other hand, the tension stiffening is the effect induced by the interaction between concrete and steel after cracking: concrete between cracks of RC elements carries tensile stress due to the bond between the reinforcing bars and the surrounding concrete. Moreover, the modeling of the tension stiffening will allow taking into

account splitting failure and the sliding of the bars due to debonding, caused by lack of details as bad anchoring of the bars.

*Chapter 5* presents the first development of the PARC\_CL 2.1 model to RC existing structures. Existing structures, designed and built before seismic codes, are characterized by lack of details, often associated with high stirrups spacing. This aspect is relevant above all in Italy where there is a high building heritage dating back to the 60s and 70s, a period of great building growth. The first step of this study consists in the implementation of the buckling of longitudinal rebars. The constitutive laws chosen for steel offer the possibility to be extended also to corrosion.

Eventually, major findings and conclusions together with suggesting for further developments are exposed in *Chapter 6*.

### 1.3 References

- Abaqus 6.12* (2012). User's and theory manuals; 2012 <<http://www.3ds.com/>> [1 June 2016].
- Belletti B., Stocchi A., Scolari M., Vecchi F.* (2017). Validation of the PARC\_CL 2.0 crack model for the assessment of the nonlinear behaviour of RC structures subjected to seismic action: SMART 2013 shaking table test simulation. *Engineering Structures*, 150:759-773.
- Cervenka J., Papanikolaou V.K.* (2008). Three-dimensional combined fracture-plastic material model for concrete. *International Journal of Plasticity* 24:2192–2220.
- EN 1998-3:2005. Eurocode 8 - Design of structures for earthquake resistance - Part 3: Assessment and retrofitting of buildings
- fib* – International federation for structural concrete. *fib model code for concrete structures* 2010. 431 Ernst & Sohn; 2013; 434 p.
- Grassl P., Lundgren K., Gylltoft K.* (2002). Concrete in compression: a plasticity theory with a novel hardening law. *International Journal of Solids and Structures* 39:5205–5223.
- Grassl P., Jirasek M.* (2006). Damage-plastic model for concrete failure. *International Journal of Solids and Structures* 43:7166–7196.



- 
- Hendriks M.A.N., De Boer A., Belletti B.* Guidelines for Nonlinear Finite Element Analysis of 506 Concrete Structures. Rijkswaterstaat Centre for Infrastructure, Report RTD:1016-1:2017, 2017.
- Maekawa K., Okamura H., Pimanmas A.* (2003). Non-Linear Mechanics of Reinforced Concrete. CRC Press, pages 768.
- Mazars J., Pijaudier-cabot G.* (1989). Continuum damage theory—application to concrete. *Journal of Engineering Mechanics*, 115(2):345-365.
- N005\_A469\_2014\_EDF\_B. THECNICAL REPORT. Presentation of the cash benchmark phase 2. <http://benchmark-cash.org/>
- Richard B., Cherubini S., Voltaire F., Charbonnel P.E., Chaudat T., Abouri S., et al.* (2015). SMART 2013: Experimental and numerical assessment of the dynamic behavior by shaking table tests of an asymmetrical reinforced concrete structure subjected to high intensity ground motions. *Eng Struct*; 109:99–116. <http://dx.doi.org/10.1016/j.engstruct.2015.11.029>.
- Richard B., Voltaire F., Fontan M., Mazars J., Chaudat T., Abouri S., Bonfils N.* (2018). SMART 2013: Lessons learned from the international benchmark about the seismic margin assessment of nuclear RC buildings. *Engineering Structures* 161:207-222.
- Spacone E., Filippou F.C., Taucer F.F.* (1996<sup>a</sup>). Fibre beam–column model for non-linear analysis of R/C frames: Part I. Formulaion. *Earthquake Engineering & Structural Dynamics*, 25( 7):711-725.
- Spacone E., Filippou F.C., Taucer F.F.* (1996<sup>b</sup>). Fibre beam–column model for non-linear analysis of R/C frames: Part II. Applications. *Earthquake Engineering & Structural Dynamics*, 25( 7):727-742.
- Yazgan U., and Dazio A.* (2011). Simulating Maximum and Residual Displacements of RC Structures: I. Accuracy. *Earthquake Spectra*, 27(4):1187–1202.



# The PARC\_CL 2.1 Crack Model

---

# 2

## 2.1 Overview

The description of cracking and failure mechanisms of RC structures within finite element analysis has led to two fundamentally different approaches: the discrete and the smeared one. The *smeared model* was first introduced by Rashid (1968) and Červenka and Gerstle (1971,1972). It considers the cracked solid as a continuum by reducing stiffness properties and considering cracks smeared over a distinct area, typically finite element or an area corresponding to an integration point of the finite element, Figure 2.1a. The *smeared approach* permits a description in terms of stress-strain relations passing from an isotropic constitutive law to an orthotropic law after the crack formation. This approach maintains the original mesh and does not impose restrictions on cracks inclination.

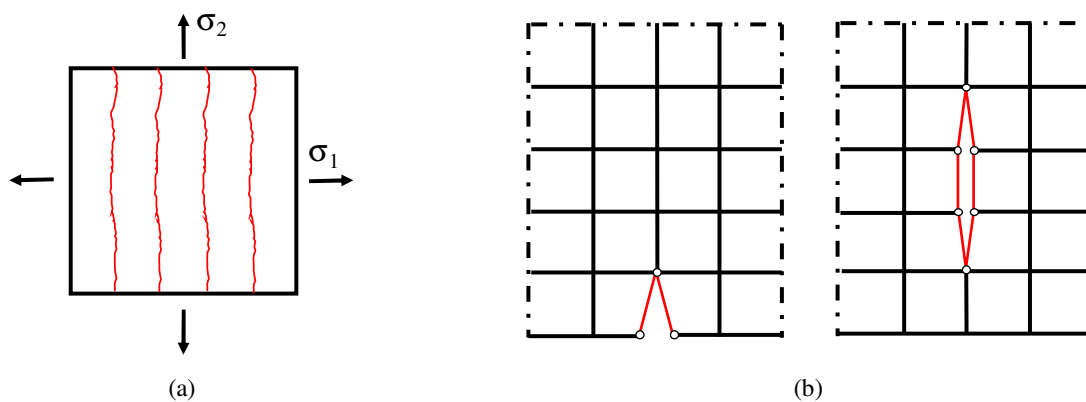


Figure 2.1: Example of (a) *smeared* crack model and (b) *discrete* crack model.

On the contrary, *discrete crack models* represent cracks as a geometrical discontinuity using, for example, interface elements. The first introduction to concrete structures has been made by Saouma and Ingrassia (1981). This method is theoretically more suitable to capture the failure localization. On the other hand, an adaptive re-meshing technique is required to account for phenomena such as progressive failure, Figure 2.1b. Furthermore, the crack is constrained to follow a predefined path, so it is a more suitable method to simulate the behavior of a structure dominated by the presence of one or few cracks. The main disadvantage of the discrete crack concept is the need of more specialized software and it is the main reason why the smeared method has become more widespread.

A further distinction can be done between the *smeared rotating crack* model (Rots and Blaauwendraad, 1989) and *smeared fixed crack* model. The first one assumes that, during loading, the crack pattern should change direction and for this reason the shear stresses are not considered (Stevens et al., 1991; Palermo and Vecchio, 2004; He et al., 2008); the second one hypothesizes the starting crack pattern as fixed (Okamura et al., 1991; Sittipunt and Wood, 1995). In this last case, the prediction of shear stresses generated along the cracks become very important, most of all when the structural behaviour is dominated by aggregate interlock phenomena.

More recently, a new strategy based on *embedded discontinuities* is developed (Belytschko et al. 1988; Dvorkin et al. 1990; Dias-da-Costa et al. 2009). By means elements with embedded discontinuities, the explicit remeshing is obtained by additional degrees of freedom that capture the jump in the displacement field inside the element. The partition-of-unity-based methods exploit the properties of the finite-element shape functions so that the extra degrees of freedom are overlaid to the regular nodes in the domain subjected to the enrichment.

With the advent of the new seismic codes, the interest in more realistic predictions of the non-linear behaviour of RC structures has increased. In fact, one of the main characteristics of RC structures is the highly non-linear response to cyclic loading, in particular seismic one. For this reason, realistic cyclic constitutive models are required to obtain reasonably accurate simulations of RC members. Nevertheless, if numerous are the constitutive models applied for monotonic loading case, as summarized by Bažant (2002) and de Borst (2002), the cyclic ones are less common in literature.

Existing commercial finite-element codes often have limitations in representing cyclic behavior, due to idealizations in material models. For example, to solve convergence problems, the tensile behaviour of concrete is commonly assumed to be secant in the unloading/reloading

phases, Figure 2.2a, even if the experimental evidence demonstrates that irrecoverable tensile strains remain in concrete (Gopalaratnam and Shah, 1985; Yankelevsky and Reinhardt, 1987). Furthermore, the crack closing process implies that the concrete path does not pass through the origin (Mansour and Hsu, 2005), Figure 2.2b. Indeed, under reversed cyclic loading, concrete may repeatedly experience crack closing and reopening. During this process, due to the aggregate interlock and the bond between steel and concrete, the compressive stress can be still transferred through the crack before it is fully closed. More complexities, as stiffness degradation in concrete and the Bauschinger effect of steel bars, are introduced by cyclic loads.

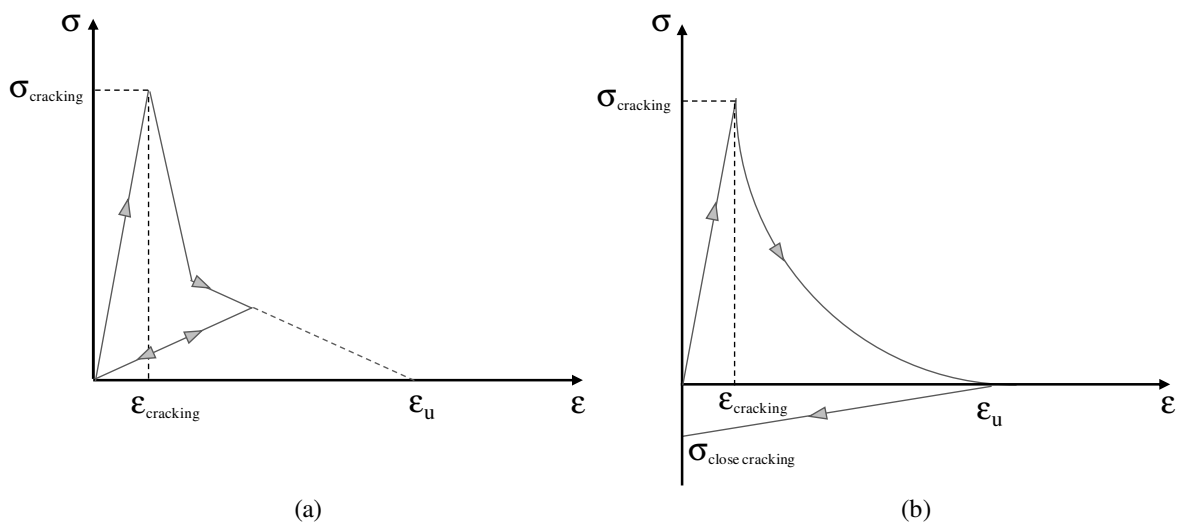


Figure 2.2: Tensile behaviour for concrete: (a) secant unloading/reloading phases; (b) crack closing process.

For all these reasons, a reliable numerical model able to catch these types of non-linearity and characterized by sufficiently accurate response predictions and simplicity in formulation is necessary. Therefore, a Physical Approach for Reinforced Concrete under Cyclic Loading condition (PARC\_CL 2.1) is proposed in this Ph.D. research.

The PARC model, Figure 2.3, was proposed in 2001 for the analysis of the behavior of reinforced-concrete membranes, subjected to plane stresses and monotonically loaded up to failure, (Belletti et al. 2001). The applications of the PARC model demonstrated the reliability of the obtained results; however, even a structure subjected to monotonic loading could experience unloading/reloading cycles due to the redistribution of internal actions (think for example to crack opening and closing). Therefore, it is useful to implement appropriate formulations that consider the possibility of loading and reloading branches. Furthermore, for the design of RC structures in seismic areas, the availability of cyclical constitutive laws becomes essential in order to conduct non-linear dynamic analyses. For all these reasons, the

model PARC\_CL 1.0 was proposed as an extension to cyclic loads (Belletti et al., 2013<sup>a</sup>), Figure 2.3. This release was characterised by secant unload/reload path not permitting to consider the real hysteretic behaviour of RC structures, (Belletti et al., 2013<sup>b</sup>; Damoni et al., 2014). To overcome this limit a new version called PARC\_CL 2.1, developed by the author of this research, is proposed. The PARC\_CL 2.1 permits to take into account hysteretic cycles and plastic strains in the unloading phase. The model is implemented in a user subroutine UMAT for the analyses of RC members by means of ABAQUS code. More specifically, it is possible to assess the static, cyclic and dynamic behavior of slabs, structural walls buildings, and floors by means of multi layered shell or membrane elements, Belletti et al. (2017<sup>b</sup>) and Belletti et al. (2018). PARC\_CL 2.1 is an improvement of PARC\_CL 2.0 (Belletti et al., 2017<sup>a</sup>), in which some modification in the cyclic concrete formulation and some important contribution like shrinkage, tension stiffening, and buckling effect are added.

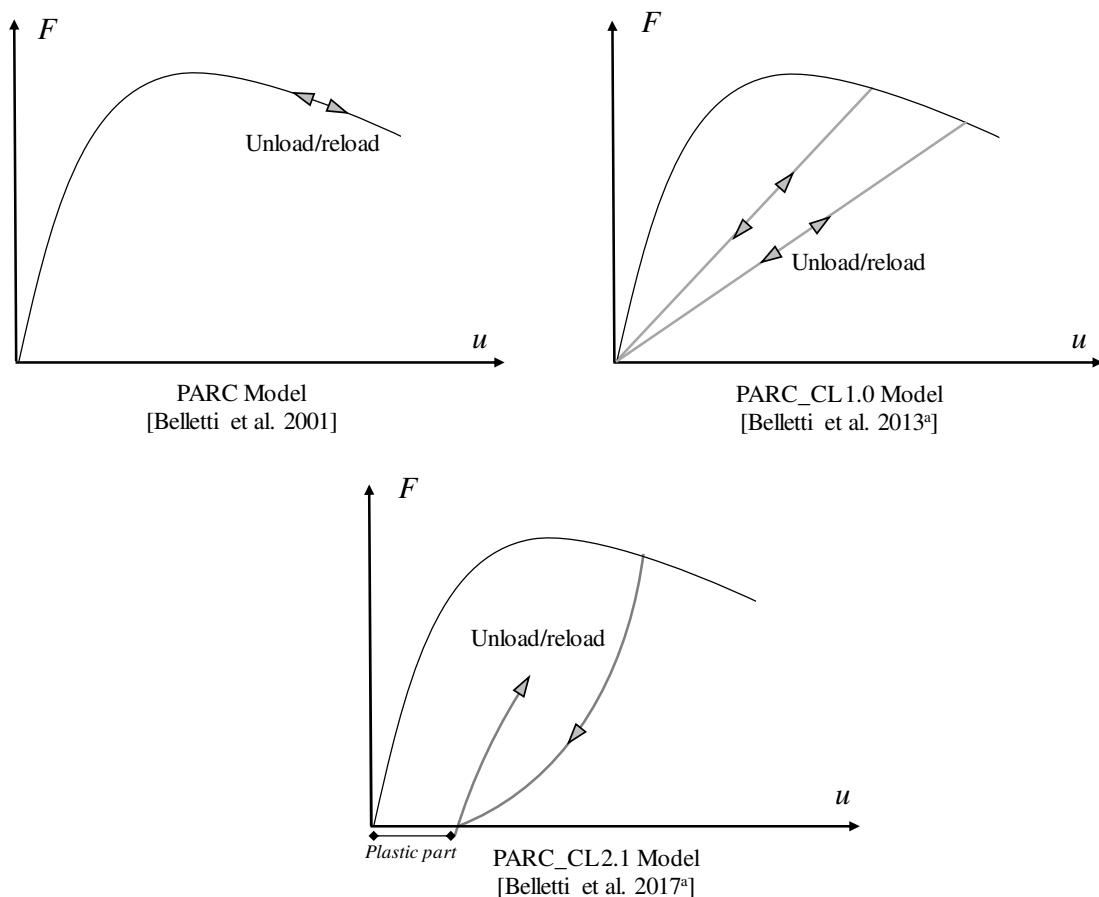


Figure 2.3: PARC model evolution.

## 2.2 Material Constitutive Models Implemented in PARC\_CL 2.1

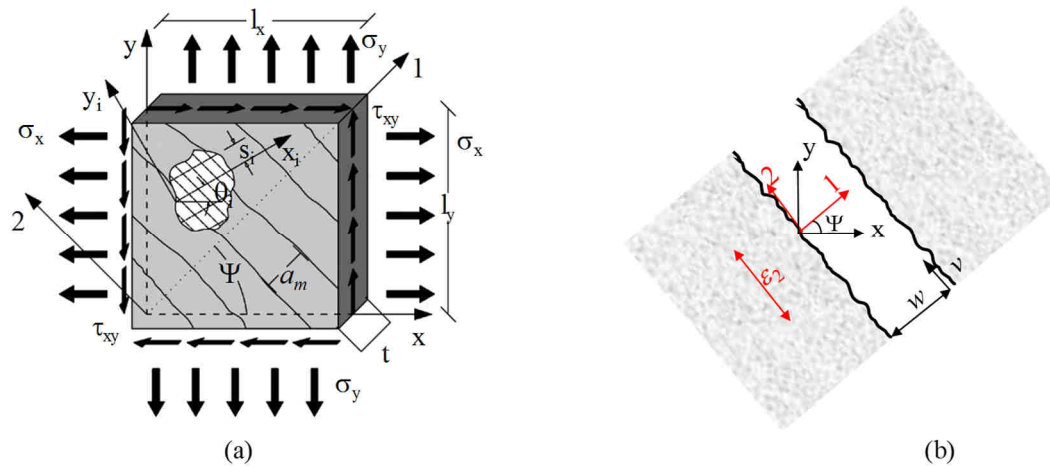


Figure 2.4: PARC\_CL 2.1 crack model: (a) RC membrane element subject to plane stress state, (b) crack parameters.

The proposed PARC\_CL 2.1 model is based on a total strain fixed crack approach, in which at each integration point two reference systems are defined: the local  $x, y$ -coordinate system and the  $1, 2$ -coordinate system along the principal stress directions. The angle between the  $1$ -direction and the  $x$ -direction is denoted as  $\psi$ , whereas  $\theta_i$  is the angle between the direction of the  $i$ th order of bars and the  $x$ -direction;  $\alpha_i = \theta_i - \psi$  is the direction of the  $i$ th bars with respect to direction  $1$ .

The element begins to crack when the principal tensile strain in concrete exceeds the concrete tensile limit strain  $\epsilon_{i,cr}$ . Since the formation of the first crack, the  $1, 2$ -coordinate system remains fixed, Figure 2.4a. The cracking is assumed as being uniform, the orientation of the cracks remains fixed upon further loading and the crack spacing  $a_m$  is assumed to be constant. The main quantities that govern the problem are the crack opening  $w$  and the crack slip  $v$ , Figure 2.4b.

### 2.2.1 Strain Fields

The concrete behavior is assumed orthotropic both before and after cracking and the total strains at each integration point are calculated in the orthotropic  $1, 2$ -system, Eq.(2.1):

$$\{\epsilon_{1,2}\} = [T_\psi] \cdot \{\epsilon_{x,y}\} \quad (2.1)$$

where  $[T_\psi]$  is the transformation matrix given by Eq.(2.2):

$$[T_\psi] = \begin{bmatrix} \cos^2 \psi & \sin^2 \psi & \cos \psi \cdot \sin \psi \\ \sin^2 \psi & \cos^2 \psi & -\cos \psi \cdot \sin \psi \\ -2 \cdot \cos \psi \cdot \sin \psi & 2 \cdot \cos \psi \cdot \sin \psi & \cos^2 \psi - \sin^2 \psi \end{bmatrix} \quad (2.2)$$

$\{\varepsilon_{1,2}\}$  and  $\{\varepsilon_{x,y}\}$  represent respectively the biaxial strain fields in  $1,2$ -system and  $x,y$ -system, as shown in Eq.(2.3) and Eq.(2.4).

$$\{\varepsilon_{1,2}\} = \{\varepsilon_1 \quad \varepsilon_2 \quad \gamma_{12}\}^T \quad (2.3)$$

$$\{\varepsilon_{x,y}\} = \{\varepsilon_x \quad \varepsilon_y \quad \gamma_{xy}\}^T \quad (2.4)$$

The stress-strain behavior presented herein is calculated on the base of the uniaxial strains ( $\bar{\varepsilon}_1, \bar{\varepsilon}_2, \bar{\gamma}_{12}$ ) in the  $1,2$ -coordinate system, according to Eq.(2.5)-(2.7).

$$\bar{\varepsilon}_1 = \frac{1}{1-\nu^2} \varepsilon_1 + \frac{\nu}{1-\nu^2} \varepsilon_2 \quad (2.5)$$

$$\bar{\varepsilon}_2 = \frac{\nu}{1-\nu^2} \varepsilon_1 + \frac{1}{1-\nu^2} \varepsilon_2 \quad (2.6)$$

$$\bar{\gamma}_{12} = \gamma_{12} \quad (2.7)$$

After the first crack, the Poisson's ratio  $\nu$  is assumed to be zero. As consequence, biaxial strains coincide with uniaxial strains.

The reinforcement is assumed smeared in concrete. The steel strain field along the reference system of each bar  $\{\varepsilon_{x_i, y_i}\}$  is obtained rotating the strains in the  $x,y$ -system  $\{\varepsilon_{x,y}\}$ , as shown in Eq.(2.8):

$$\{\varepsilon_{x_i, y_i}\} = [T_{\theta_i}] \cdot \{\varepsilon_{x,y}\} \quad (2.8)$$

where  $[T_{\theta_i}]$  is the transformation matrix given by Eq.(2.9):

$$[T_{\theta_i}] = \begin{bmatrix} \cos^2 \theta_i & \sin^2 \theta_i & \cos \theta_i \cdot \sin \theta_i \\ \sin^2 \theta_i & \cos^2 \theta_i & -\cos \theta_i \cdot \sin \theta_i \\ -2 \cdot \cos \theta_i \cdot \sin \theta_i & 2 \cdot \cos \theta_i \cdot \sin \theta_i & \cos^2 \theta_i - \sin^2 \theta_i \end{bmatrix} \quad (2.9)$$



### 2.2.2 Stress Fields

The concrete stress field in the  $1,2$ -coordinate system  $\{\sigma_{1,2}\}$  is given by Eq.(2.10):

$$\{\sigma_{1,2}\} = \begin{Bmatrix} \sigma_1 \\ \sigma_2 \\ \tau_{12} \end{Bmatrix} \quad (2.10)$$

where  $\sigma_1$  and  $\sigma_2$  represent the normal stresses in concrete along  $1$  and  $2$  directions calculated following the relation presented in §2.2.5, whereas  $\tau_{12}$  is the shear stress in concrete calculated according to the aggregate interlock model, §2.2.6.

The steel stress field  $\{\sigma_{x_i,y_i}\}$ , defined for each  $i$ th order bars in the  $x_i,y_i$ -system, is given by Eq.(2.11):

$$\{\sigma_{x_i,y_i}\} = \begin{Bmatrix} \sigma_{x_i} \\ \sigma_{y_i} \\ \tau_{x_i,y_i} \end{Bmatrix} = \begin{Bmatrix} \sigma_{x_i} \\ 0 \\ 0 \end{Bmatrix} \quad (2.11)$$

where  $\sigma_{x_i}$  represents the stress along the axis of the  $i$ th order of bar and it can be calculated following the Menegotto-Pinto's procedure explained in §2.2.7. The dowel action phenomenon is not considered yet in the model; for this reason, in Eq.(2.11) there are not stresses in the direction perpendicular to the axis of the bar.

Both the concrete stress field  $\{\sigma_{x,y}\}_c$  and the steel stress fields  $\{\sigma_{x,y}\}_{s,i}$  can be transformed from their local coordinate system to the overall global  $x,y$  coordinate system using respectively Eq.(2.12) and Eq.(2.13):

$$\{\sigma_{x,y}\}_c = [T_\psi]^t \cdot \{\sigma_{1,2}\} \quad (2.12)$$

$$\{\sigma_{x,y}\}_{s,i} = [T_{\theta_i}]^t \cdot \{\sigma_{x_i,y_i}\} \quad (2.13)$$

Finally the total stress field in the  $x,y$ -system is obtained by assuming that concrete and reinforcement behave like two springs placed in parallel, Eq.(2.14):

$$\{\sigma_{x,y}\} = \{\sigma_{x,y}\}_c + \sum_{i=1}^n \rho_i \{\sigma_{x,y}\}_{s,i} \quad (2.14)$$

where  $\rho_i$  is the reinforcement ratio related to the  $i$ th order of bars.

### 2.2.3 Rayleigh Stiffness Proportional Damping

Damping is a peculiar energy dissipation mechanism, which happens during structure vibration.

The matrix equation of motion takes the well-known form of Eq.(2.21):

$$[M] \cdot \{\ddot{u}(t)\} + [C] \cdot \{\dot{u}(t)\} + [K] \cdot \{u(t)\} = \{F\} \quad (2.15)$$

More specifically, the most widely used Rayleigh damping  $[C]$  is investigated, Eq.(2.16):

$$[C] = \alpha \cdot [M] + \beta \cdot [K] \quad (2.16)$$

Thus, the matrix  $[C]$  consists of a mass-proportional term  $[M]$  and a stiffness-proportional term  $[K]$ .

ABAQUS code (Abaqus, 2012) allows the definition of the mass-proportional damping,  $\alpha$ , as an input value for the non-linear finite element analysis whereas the definition of the stiffness-proportional damping,  $\beta$ , depends to the stiffness matrix, which is defined in the user subroutine. Therefore, the stiffness-proportional damping contribute is introduced in the user subroutine by modifying the stiffness matrix.

The damping contributes to the concrete stress field  $\{\sigma_{1,2}\}_{damp}$  can be calculated using Eq.(2.17).

$$\{\sigma_{1,2}\}_{damp} = \begin{Bmatrix} \beta \cdot E'_{c1} \cdot \dot{\epsilon}_1 \\ \beta \cdot E'_{c2} \cdot \dot{\epsilon}_2 \\ \beta \cdot G'_{12} \cdot \dot{\gamma}_{12} \end{Bmatrix} \quad (2.17)$$

In the same way, the damping contributes to the steel stress field  $\{\sigma_{x_i,y_i}\}_{damp}$  can be calculated as follow, Eq.(2.18):

$$\{\sigma_{x_i,y_i}\}_{damp} = \begin{Bmatrix} \beta \cdot E'_{si} \cdot \dot{\epsilon}_{xi} \\ 0 \\ 0 \end{Bmatrix} \quad (2.18)$$

When the damping contribute is needed, the  $\{\sigma_{1,2}\}$  concrete stress field is updated and calculated as the sum of the static contribution of the material  $\{\sigma_{1,2}\}_{static}$ , defined in Eq.(2.10) and the damping contribution  $\{\sigma_{1,2}\}_{damp}$ , calculated according to Eq.(2.19). The final concrete stress field is given in Eq.(2.19):

$$\{\sigma_{1,2}\} = \{\sigma_{1,2}\}_{static} + \{\sigma_{1,2}\}_{damp} \quad (2.19)$$

The same procedure is adopted for the calculation of the steel stress field in Eq.(2.20):

$$\{\sigma_{x_i, y_i}\} = \{\sigma_{x_i, y_i}\}_{static} + \{\sigma_{x_i, y_i}\}_{damp} \quad (2.20)$$

#### 2.2.4 Stiffness Matrix and Numerical Solution Procedure

The proposed PARC\_CL 2.1 model is based on a tangent approach, in which the Jacobian matrix in the local coordinate system of each material is composed by derivatives as shown in Eq.(2.21) for concrete and in Eq.(2.22) for each  $i$ th order of bars.

$$[D_{1,2}] = \begin{bmatrix} \frac{\partial \sigma_1}{\partial \varepsilon_1} \frac{1}{(1-\nu^2)} & \frac{\partial \sigma_1}{\partial \varepsilon_2} \frac{\nu}{(1-\nu^2)} & 0 \\ \frac{\partial \sigma_2}{\partial \varepsilon_1} \frac{\nu}{(1-\nu^2)} & \frac{\partial \sigma_2}{\partial \varepsilon_2} \frac{1}{(1-\nu^2)} & 0 \\ 0 & 0 & \frac{\partial \tau_{12}}{\partial \gamma_{12}} \end{bmatrix} \quad (2.21)$$

$$[D_{x_i, y_i}] = \begin{bmatrix} \frac{\partial \sigma_{x_i}}{\partial \varepsilon_{x_i}} & 0 & 0 \\ 0 & 0 & 0 \\ 0 & 0 & 0 \end{bmatrix} \quad (2.22)$$

To avoid numerical problems (i.e. negative value in the stiffness matrix), the stiffness contributes of concrete became secant in softening branches. When, after the first crack the Poisson's ratio is assumed to be zero, the terms out of the diagonal become zero. The stresses presented herein are calculated according to Eq.(2.24), (2.25) and (2.30) for concrete and Eq.(2.38) for steel.

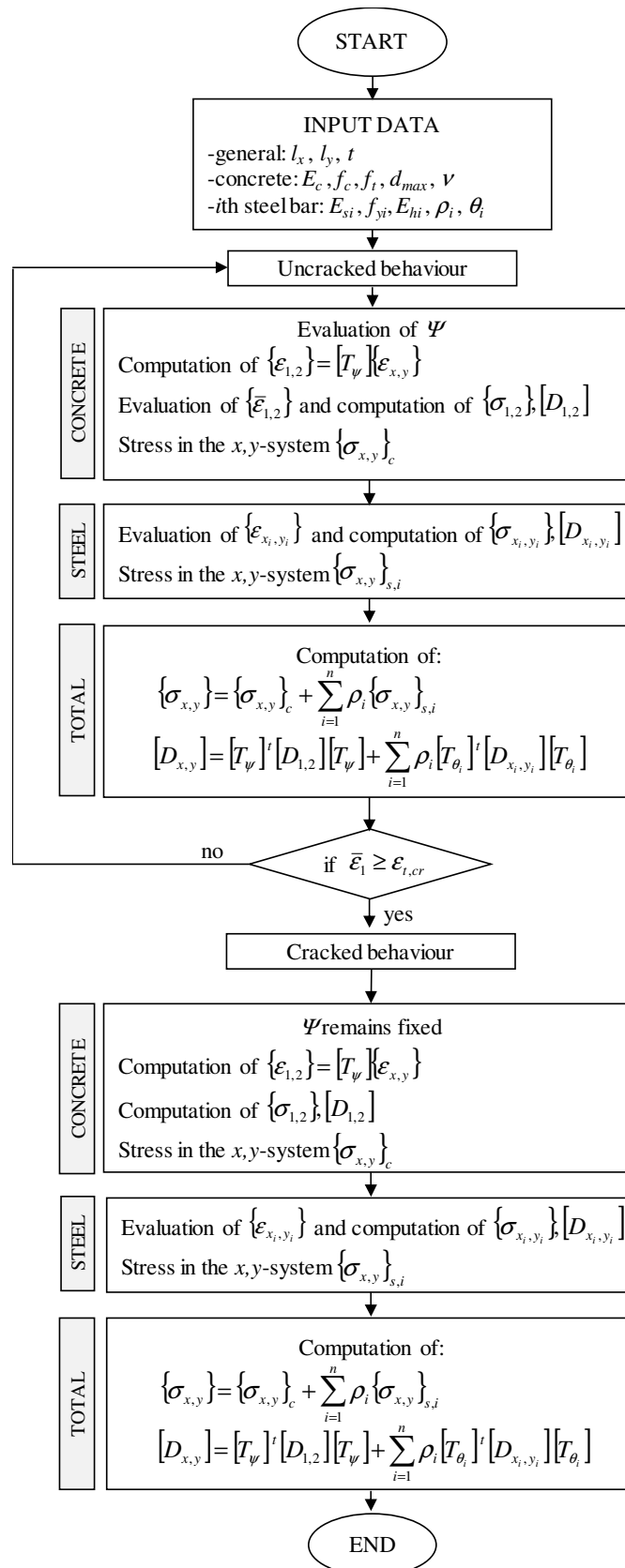


Figure 2.5: Flowchart of main steps of PARC\_CL 2.1 crack model.

The global stiffness matrix in  $x,y$ -coordinate system  $[D_{x,y}]$  is obtained by Eq.(2.23):

$$[D_{x,y}] = [T_\psi]^t \cdot [D_{1,2}] \cdot [T_\psi] + \sum_{i=1}^n \rho_i [T_{\theta_i}]^t \cdot [D_{x_i,y_i}] \cdot [T_{\theta_i}] \quad (2.23)$$

The stiffness matrix is updated until a solution is closely approximated. The main steps of the implemented algorithm are given in the flowchart reported in Figure 2.5. An iterative procedure was performed until all the equilibrium, compatibility and constitutive equations were satisfied.

## 2.2.5 Cyclic Uniaxial Constitutive Law for Concrete

The tensile envelope curve, presented in Eq.(2.24) and shown in Figure 2.6a, is characterized by a bilinear stress-strain relation Model Code 2010 (*fib*, 2013) prior to cracking; after cracking the softened trend is represented by an exponential law (Cornellissen et al., 1986).

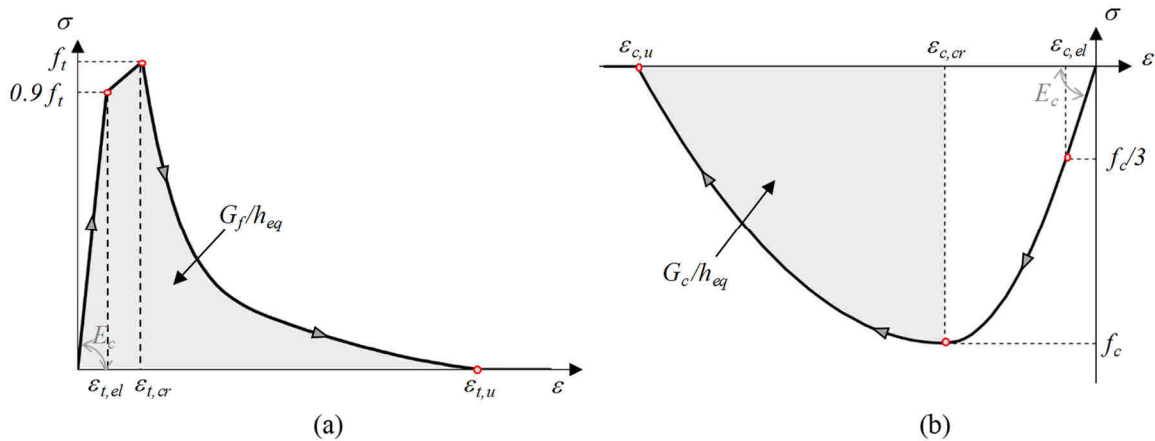


Figure 2.6: Constitutive law for concrete: (a) tension and (b) compression.

$$\sigma = \begin{cases} E_c \cdot \varepsilon & 0 \leq \varepsilon < \varepsilon_{t,el} \\ 0.9 \cdot f_t + 0.1 \cdot f_t \left( \frac{\varepsilon - \varepsilon_{t,el}}{\varepsilon_{t,cr} - \varepsilon_{t,el}} \right) & \varepsilon_{t,el} \leq \varepsilon < \varepsilon_{t,cr} \\ f_t \left\{ \left[ 1 + \left( c_1 \cdot \frac{\varepsilon - \varepsilon_{t,cr}}{\varepsilon_{t,u} - \varepsilon_{t,cr}} \right)^3 \right] \cdot \exp \left( -c_2 \cdot \frac{\varepsilon - \varepsilon_{t,cr}}{\varepsilon_{t,u} - \varepsilon_{t,cr}} \right) - \frac{\varepsilon - \varepsilon_{t,cr}}{\varepsilon_{t,u} - \varepsilon_{t,cr}} \cdot (1 + c_1^3) \cdot \exp(-c_2) \right\} & \varepsilon_{t,cr} \leq \varepsilon < \varepsilon_{t,u} \\ 0 & \varepsilon \geq \varepsilon_{t,u} \end{cases} \quad (2.24)$$

where:

- $E_c$  and  $f_t$  are the Young's modulus and the uniaxial tensile strength of concrete;
- $\varepsilon_{t,el} = 0.9 \cdot f_t / E_c$  is the elastic strain in tension;
- $\varepsilon_{t,cr} = 0.00015$  is the initial cracking strain;
- $\varepsilon_{t,u} = \varepsilon_{t,cr} + 5.136 \cdot G_F / (h_{eq} \cdot f_t)$  is the ultimate cracking strain;
- $c_1=3$  and  $c_2=6.93$  are material constants.

The compressive envelope curve presented in Eq.(2.25) and shown in Figure 2.6b, is characterized by a first elastic part followed by a parabolic formulation, proposed by Feenstra (1993):

$$\sigma = \begin{cases} E_c \cdot \varepsilon & \varepsilon_{c,el} < \varepsilon \leq 0 \\ \frac{f_c}{3} \cdot \left[ 1 + 4 \left( \frac{\varepsilon - \varepsilon_{c,el}}{\varepsilon_{c,cr} - \varepsilon_{c,el}} \right) - 2 \left( \frac{\varepsilon - \varepsilon_{c,el}}{\varepsilon_{c,cr} - \varepsilon_{c,el}} \right)^2 \right] & \varepsilon_{c,cr} < \varepsilon < \varepsilon_{c,el} \\ f_c \cdot \left[ 1 - \left( \frac{\varepsilon - \varepsilon_{c,cr}}{\varepsilon_{c,u} - \varepsilon_{c,cr}} \right)^2 \right] & \varepsilon_{c,u} < \varepsilon < \varepsilon_{c,cr} \\ 0 & \varepsilon \leq \varepsilon_{c,u} \end{cases} \quad (2.25)$$

where:

- $f_c$  is the uniaxial compressive strength of concrete;
- $\varepsilon_{c,el} = f_c / (3 \cdot E_c)$  is the elastic strain in compression;
- $\varepsilon_{c,cr} = 5 \cdot \varepsilon_{c,el}$  is the strain corresponding to the maximum concrete strength in compression;
- $\varepsilon_{c,u} = \varepsilon_{c,cr} - 1.5 \cdot G_C / (h_{eq} \cdot f_c)$  is the ultimate crushing strain.

The value of  $h_{eq}$  in the PARC\_CL 2.1 crack model is fixed equal to the square root of the average element area, according to Hendricks et al. (2012). The value of the fracture energy of concrete in tension  $G_F$  (Figure 2.6a) is evaluated according to Model Code 1990 (1993) and it is the energy required to propagate a tensile crack in a unit area of concrete. In order to pass from the dissipated energy by a single macro-crack in concrete,  $G_F$ , to the energy dissipated by several macro-crack in RC,  $G_F^{RC}$ , Eq.(2.26) is needed:

$$G_F^{RC} = G_F \left( 1 + \frac{h_{eq}}{a_m} \right) \tag{2.26}$$

where  $a_m$  is the average crack spacing, assumed to be constant during the analysis. Its value is evaluated on the base of the length over which the slip between concrete and steel occurs,  $l_{s,max}$  as defined in Model Code 2010 (*fib*, 2013).

The value of the fracture energy of concrete in compression  $G_C$  (Figure 2.6b) is assumed equal to  $250G_F$  according to Nakamura and Higai (2001).

As stated in the introduction, the PARC\_CL 2.1 crack model allows considering plastic and irreversible deformations in the unloading phase., More specifically, the unloading paths in tension are simplified by a straight line with slope  $E_c$  from the experienced maximum tensile strain on the monotonic curve ( $\epsilon_{t,re}$ ) to the plastic tensile strain ( $\epsilon_{t,pl}$ ), as shown in Figure 2.7.

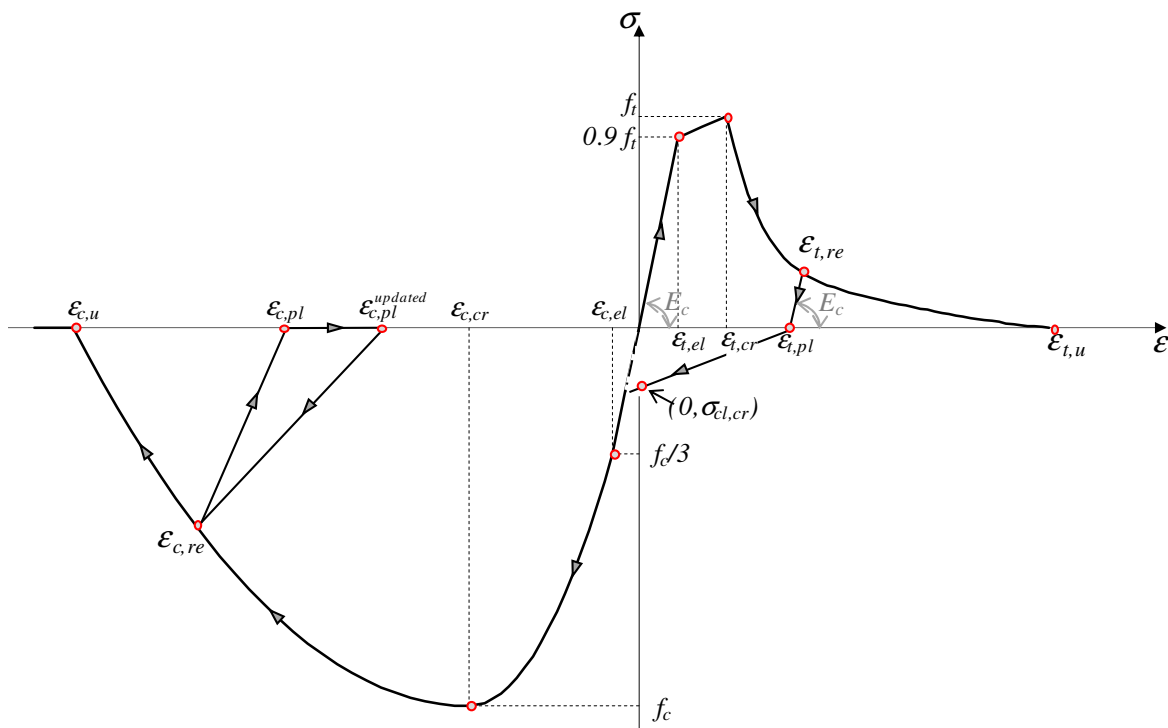


Figure 2.7: Cyclic behaviour of concrete (not to scale).

Passing from tension to compression it is necessary to determinate the stress with no deformation  $\sigma_{cl,cr}$ , called the residual bond stress by Okamura and Maekawa (1991), as reported in Eq.(2.27).

$$\sigma_{cl,cr} = -f_t \left( 0.05 + \frac{0.03 \varepsilon_{t,re}}{\varepsilon_{t,pl}} \right) \quad (2.27)$$

In compression, the unloading paths are characterized by a straight line, with variable slope, from the experienced minimum compressive strain on the monotonic curve ( $\varepsilon_{c,re}$ ) to the plastic compressive strain ( $\varepsilon_{c,pl}$ ), Eq.(2.28). The passage from compression to tension is with zero stress.

$$\varepsilon_{c,pl} = \varepsilon_{c,re} - \frac{20 \cdot \varepsilon_{c,cr}}{7} \cdot \left( 1 - \exp\left(-0.35 \frac{\varepsilon_{c,re}}{\varepsilon_{c,cr}}\right) \right) \quad (2.28)$$

The biaxial state of concrete in compression, due to transverse cracking, is also taken into account, according to Vecchio and Collins (1993), by reducing the compressive stress  $f_c$  and the compressive peak strain  $\varepsilon_{c,cr}$  with the  $\zeta$  coefficient, Eq.(2.29):

$$\zeta = \frac{1}{(0.85 - 0.27 \cdot \varepsilon_{\perp}/\varepsilon)}, \quad 0.4 \leq \zeta \leq 1 \quad (2.29)$$

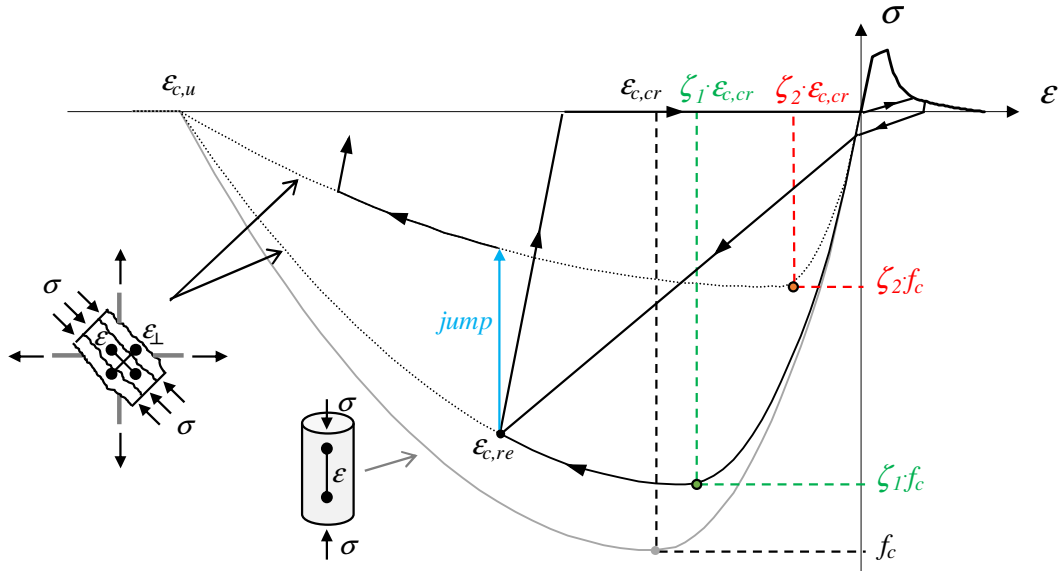


Figure 2.8: Cyclic behaviour considering the biaxial state of concrete.

The effect is applied only on the envelope curve, as shown in Figure 2.8. During the unloading-reloading steps, the coefficient  $\zeta$  is maintained fixed until the compressive



deformation of concrete reaches the minimum compressive strain of the previous cycle  $\varepsilon_{c, re}$ . In Figure 2.8 is shown an example of the cyclic behaviour in which the concrete pass from a biaxial envelope curve with  $\zeta_1$  coefficient to a biaxial curve with  $\zeta_2$  coefficient, where  $\zeta_2 < \zeta_1$ .

### 2.2.6 The Aggregate Interlock Effect

The PARC\_CL 2.1 is a *smearred fixed crack* model. For this reason, the prediction of shear stresses generated along the cracks become fundamental and an aggregate interlock relation is necessary to be defined.

Starting from the Gambarova (1983) formulation, Eq.(2.30), the aggregate interlock effect is evaluated on the basis of the crack width,  $w$ , and the crack sliding,  $v$ , Figure 2.9a:

$$\tau_{12} = \bar{\tau} \left( 1 - \sqrt{\frac{2w}{d_{\max}}} \right) \frac{a_3 + a_4 \left| \frac{v}{w} \right|^3}{1 + a_4 \left( \frac{v}{w} \right)^4} \frac{v}{w} \quad (2.30)$$

where  $\bar{\tau} = 0.27 \cdot f_c$ ;  $a_3 = 2.45/\bar{\tau}$ ;  $a_4 = 2.44 \cdot (1 - 4/\bar{\tau})$  and  $d_{\max}$  is the maximum aggregate size.

The passage from  $\tau_{12} - \gamma_{12, cr}$  to  $\tau_{12} - v$  is possible considering that  $v = \gamma_{12, cr} \cdot a_m$ , Figure 2.9b. The crack width,  $w$ , is obtained by multiplying the plastic part of the tensile strain by  $a_m$ .

To simplify the previous relation, it is possible to schematized Eq.(2.30) with a bilinear curve Figure 2.9a. In this case the endpoint of the elastic part P( $\gamma_{cr}^*$ ,  $\tau^*$ ) has coordinates equal to Eq.(2.31) and (2.32). If the value of  $w$  increases, the peak value reached by the point P diminishes, Figure 2.9c.

$$\gamma_{cr}^* = v^* / a_m \quad (2.31)$$

$$\tau^* = \bar{\tau} \left( 1 - \sqrt{\frac{2w}{d_{\max}}} \right) \frac{a_3 + a_4 \left| \frac{v^*}{w} \right|^3}{1 + a_4 \left( \frac{v^*}{w} \right)^4} \frac{v^*}{w} \quad (2.32)$$

where  $v^* = f_c \cdot w / a_5 + a_6$ ;  $a_5 = 0.366 \cdot f_c + 3.333$ ;  $a_6 = f_c / 110$ .

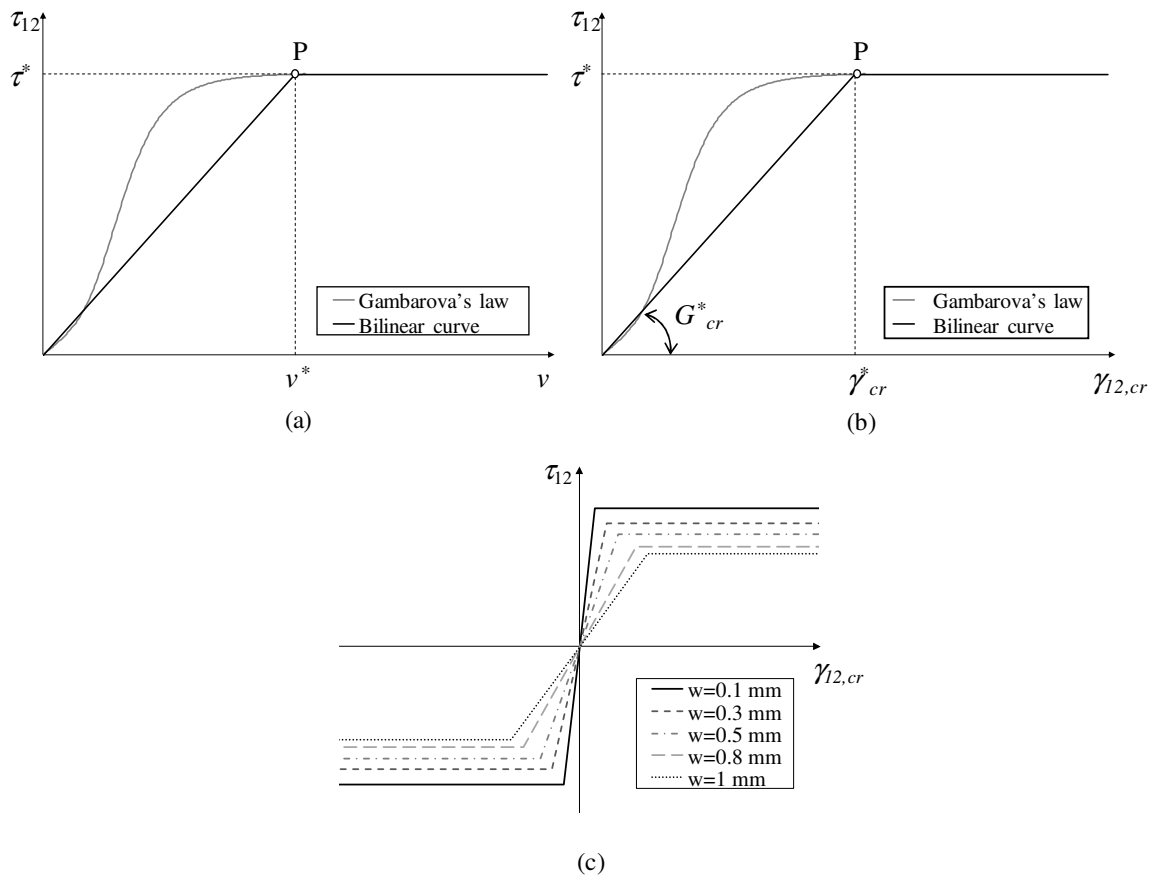


Figure 2.9: (a) Linearization of Gambarova's relation for a given crack width; (b) shear stress-strain relation for a fixed value of  $w$ ; (c) influence of  $w$  on  $\tau_{12}$ - $\gamma_{12,cr}$  curve.

Before cracking the shear stress-strain relation is defined by a straight line with a slope equal to the shear modulus  $G$ . After cracking a bilinear curve is used to define the stress-strain relationship between the shear stress  $\tau_{12}$  and the shear strain  $\gamma_{12,cr}$  in the cracked phase of the concrete, Figure 2.9-a. In this phase, the shear modulus,  $G_{cr}$ , is derived by Eq.(2.33):

$$G_{cr} = \begin{cases} \frac{\tau_{12}}{\gamma_{12,cr}} = \frac{\tau^*}{v^*} \cdot a_m = G_{cr}^* \cdot a_m & \text{if } \gamma_{12,cr} \leq \gamma_{cr}^* \\ \frac{\tau_{12}}{\gamma_{12,cr}} = \frac{\tau^*}{\gamma_{12,cr}} & \text{if } \gamma_{12,cr} > \gamma_{cr}^* \end{cases} \quad (2.33)$$

where  $G_{cr}^*$  represents the secant shear modulus associated with the first linear branch in the cracked phase, Figure 2.9b.

The  $\tau_{12}$ - $\gamma_{12}$  curve, including the elastic part, is shown in Figure 2.10b, where  $\gamma$  corresponds to the shear strain at the onset of concrete cracking and  $\gamma^*$  defines the point after which the shear strain remains constant, Eq.(2.34).

$$\gamma^* = \gamma_{cr}^* + \gamma_f \tag{2.34}$$

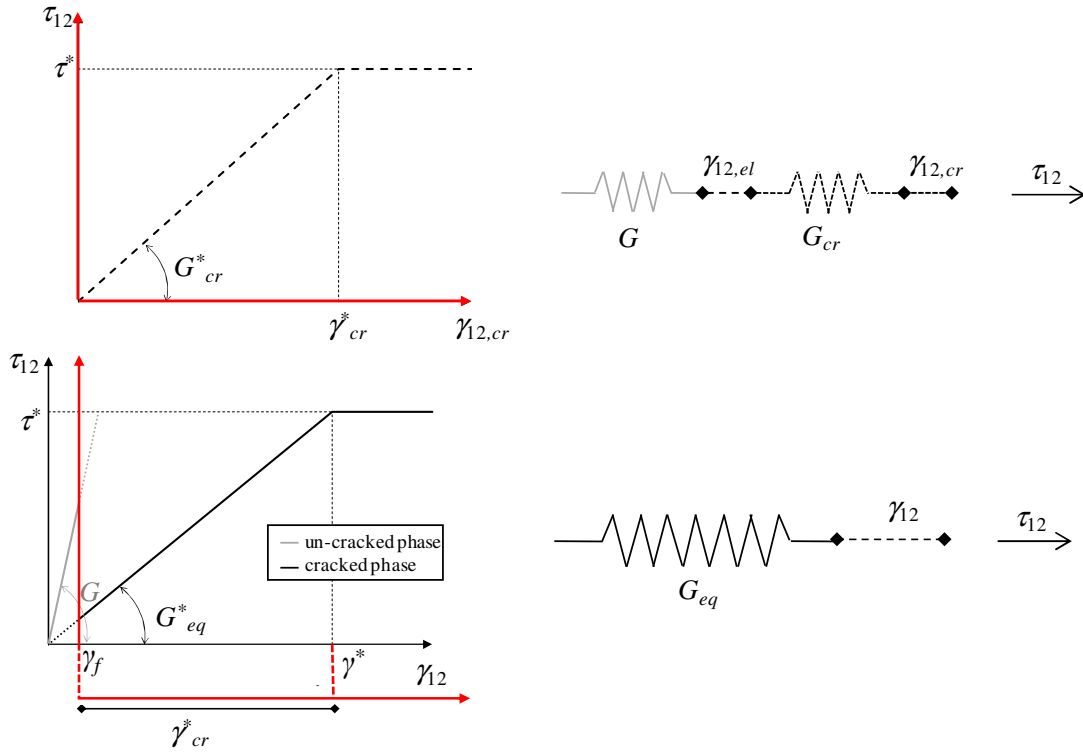


Figure 2.10: Aggregate interlock effect. Overall behavior  $\tau_{12}$ - $\gamma_{12}$  based on the total strain assumption.

According to the total strain concept, the PARC\_CL 2.1 crack model assumes that the un-cracked concrete, characterized by the elastic deformation  $\gamma_{2,el}$ , and the cracked concrete, characterized by the cracking deformation  $\gamma_{2,cr}$ , behave like two springs in series, Figure 2.10. Therefore, the equivalent overall shear modulus,  $G_{eq}$ , in the cracked phase can be calculated according to Eq.(2.35).

$$G_{eq} = \frac{G \cdot G_{cr}}{G + G_{cr}} \tag{2.35}$$

where  $G$  is the elastic shear modulus, Eq. (2.36), and  $G_{cr}$  is calculated according to Eq. (2.33).

$$G = \frac{E_c}{2 \cdot (1 + \nu)} \tag{2.36}$$

Combining the cracked shear modulus,  $G_{cr}$ , with the elastic shear modulus,  $G$ , using Eq.(2.35), the overall  $\tau_{12}$ - $\gamma_{12}$  behavior can be derived, as reported in Eq.(2.37) and in Figure 2.10.

$$\tau_{12} = \begin{cases} G \cdot \gamma_{12} & \text{if } \gamma_{12} \leq \gamma_f \\ G_{eq}^* \cdot \gamma_{12} & \text{if } \gamma_f < \gamma_{12} \leq \gamma^* \\ \tau^* & \text{if } \gamma_{12} > \gamma^* \end{cases} \quad (2.37)$$

where  $G_{eq}^*$  is calculated using Eq.(2.35) by substituting  $G_{cr}$  with  $G^*$ .

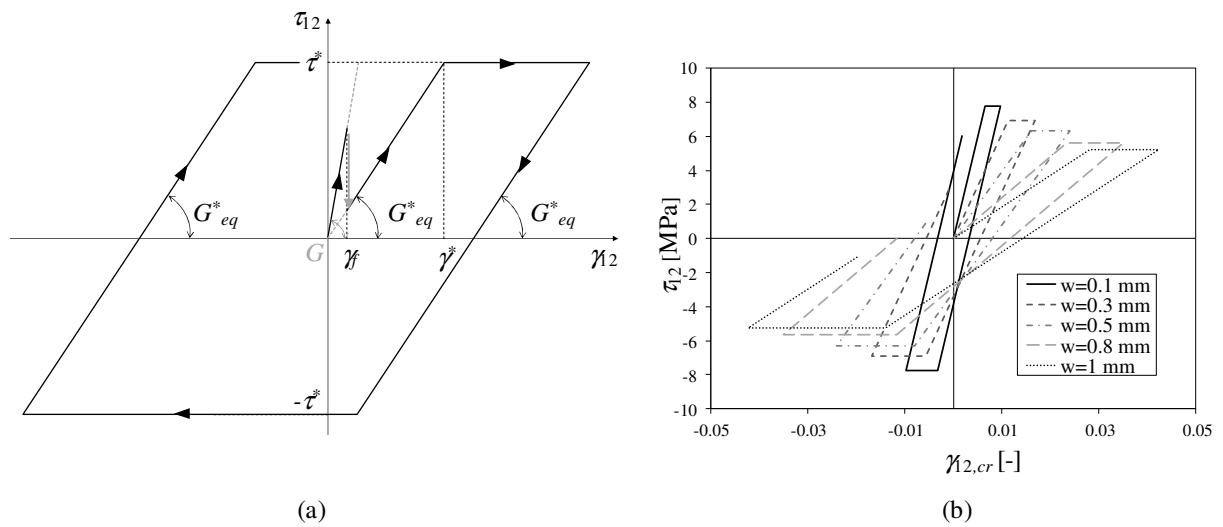


Figure 2.11: Aggregate interlock effect. Cyclic behaviour: (a)  $\tau_{12}$ - $\gamma_{12,cr}$  curve with loading and unloading phase, (b) influence of crack width on  $\tau_{12}$ - $\gamma_{12,cr}$  cyclic curves.

The overall behaviour in case of cyclic loading is presented in Figure 2.11 a as an extension, made by the author of this Ph.D. thesis, of the Gambarova's formulation. In the unloading phase, a branch with slope  $G_{eq}^*$ , as illustrated in Figure 2.11 a, has been defined. Changing the crack width,  $w$ , the value of  $G_{eq}^*$  changes and, as a consequence of this, different cyclic curves can be derived as shown in Figure 2.11 b.

### 2.2.7 Cyclic Uniaxial Constitutive Law for Embedded Mild Steel Bars

The constitutive relation for steel is based on Menegotto and Pinto (1973) model and allows to consider the hysteretic stress-strain behaviour of reinforcing steel bar also including yielding, strain hardening, and Bauschinger effect, Figure 2.12.

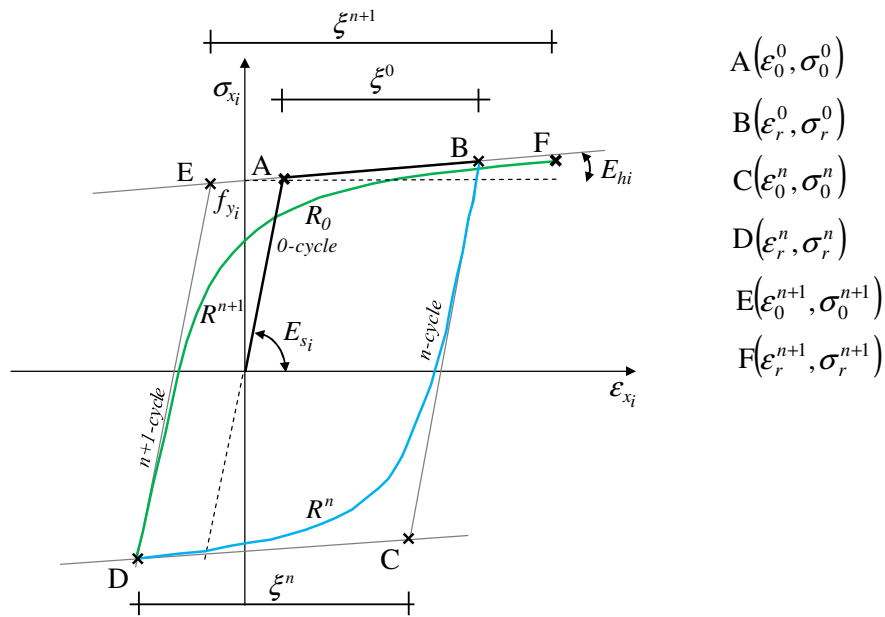


Figure 2.12: Hysteretic model for steel.

The Menegotto-Pinto formulation, applied axially to the bar, can be expressed following Eq.(2.38).

$$\sigma_{x_i} = \sigma_s^* \cdot (\sigma_0^n - \sigma_r^{n-1}) + \sigma_r^{n-1} \quad (2.38)$$

where:

$$\sigma_s^* = b\varepsilon^* + \frac{(1-b)\varepsilon^*}{\left[1 + (\varepsilon^*)^{R^n}\right]^{1/R^n}} \quad (2.39)$$

$$\varepsilon^* = \frac{\varepsilon_{x_i} - \varepsilon_r^{n-1}}{\varepsilon_0^n - \varepsilon_r^{n-1}} \quad (2.40)$$

Eq.(2.38) consists in a curved transition from a straight line asymptote with slope  $E_{s_i}$  (from the origin to the point A) to another asymptote with slope  $E_{h_i}$  (A-B line). The stress  $\sigma_0$  and the strain  $\varepsilon_0$  define the intersection point of the two asymptotes of the branch considered (e.g. point A in Figure 2.12); similarly,  $\sigma_r$  and  $\varepsilon_r$  are the stress and the strain in the point where the last strain reversal occurs (e.g. point B in Figure 2.12). As shown in Figure 2.12,  $(\sigma_0, \varepsilon_0)$  and  $(\sigma_r, \varepsilon_r)$  are updated after each strain reversal.  $b$  is the strain-hardening ratio and can be calculated as in Eq. (2.41):

$$b = \frac{E_{h_i}}{E_{s_i}} \quad (2.41)$$

$$R^n = R_0 - \frac{a_1 \cdot \xi^{n-1}}{a_2 + \xi^{n-1}} \quad (2.42)$$

$R^n$  is the parameter that influences the shape of the transient curve and it allows to consider the Bauschinger effect, (2.42).  $R_0$  is the value of the parameter  $R^n$  during the first loading cycle.

$\xi^n$  is updated following the strain reversal, Eq.(2.43), and its value does not change when reloading occurs after partial unloading, Figure 2.12.

$$\xi^n = \varepsilon_r^n - \varepsilon_0^n \quad (2.43)$$

It is assumed that  $R_0=20$ ,  $a_1=18.45$  and  $a_2=0.001$  according to Gomes and Appleton (1997).

## 2.3 Applications of the PARC\_CL 2.1 Model to RC Members

In order to assess the efficiency of the proposed PARC\_CL 2.1 model under monotonic, cyclic and dynamic loading the above described procedure, as well as of its correct implementation into a commercial finite element (FE) code (ABAQUS), is verified herein through comparisons with different case studies. The first validation consisted of simple RC panels subjected to cyclic static loading. In the next paragraphs, more complex case studies will be analysed, and the results obtained for RC multi-storey walls and deck slabs will be presented.

### 2.3.1 Cyclic Analyses of RC Panels

8 out of 12 specimens referred to Mansour and Hsu (2005) are selected to validate the PARC\_CL 2.1 model comparing the experimental results with the NLFEA results.

The panels were performed using the “Universal Element Tester” facility at the University of Houston and it consists of 12 panel specimens tested under reversed cyclic shear stresses, (Figure 2.13). All panels were 1398x1398x178 mm in size, except panels CE4, CA4, and CB4, which were 1398x1398x203 mm in size. The specimens were reinforced with two parallel steel grids placed at angles of 45° (CA and CB-series Figure 2.13a) and 0° (CE-series Figure 2.13b) to the  $x$ -direction. The properties of the panels are summarized in Table 2.1.

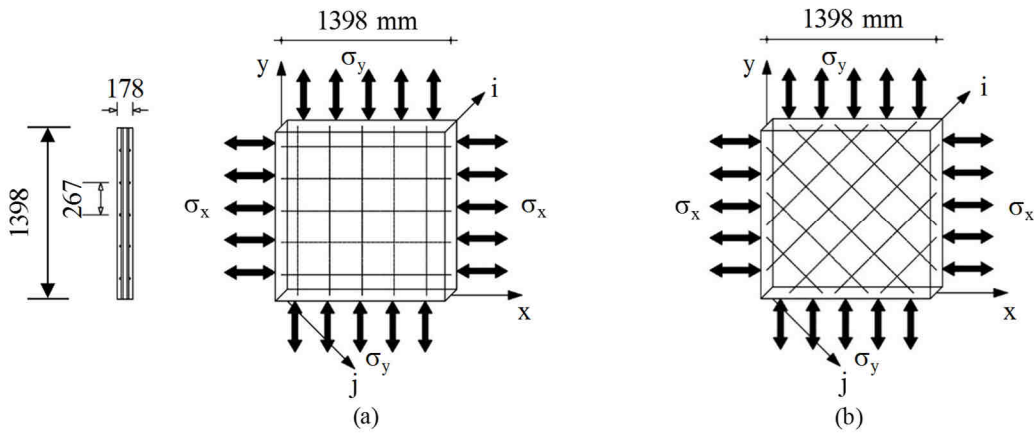
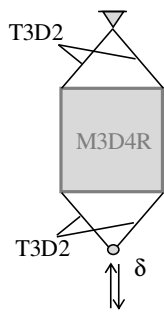


Figure 2.13: Steel bar orientations in test panels: (a) Panels of CE-series ( $\theta_i=0^\circ$ ) and (b) CA- and CB-series ( $\theta_i=45^\circ$ ).

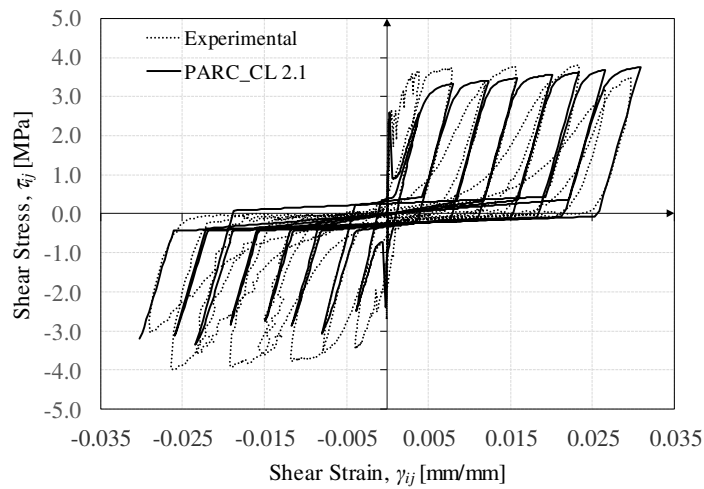
Table 2.1: Material properties and steel bar arrangement of test panels.

Series	Panel	Concrete			Steel in $x$ - $i$ direction		Steel in $y$ - $i$ direction		$\theta$ [degrees]
		$f_c$ [MPa]	$G_F$ [N/mm]	$G_C$ [N/mm]	$\rho_{x-i}$ [%]	$f_y$ [MPa]	$\rho_{y-i}$ [%]	$f_y$ [MPa]	
CE	CE2	49	0.147	36.78	0.54	424.1	0.54	424.1	0
	CE3	50	0.148	36.90	1.20	425.4	1.20	425.4	0
	CE4	47	0.146	36.50	1.90	453.4	1.90	453.4	0
CA	CA2	45	0.145	36.20	0.77	424.1	0.77	424.1	45
	CA3	44.5	0.145	36.20	1.70	425.4	1.70	425.4	45
	CA4	45	0.145	36.20	2.70	453.4	2.70	453.4	45
CB	CB3	48	0.147	36.63	1.70	425.4	0.77	424.1	45
	CB4	47	0.146	36.50	2.70	453.4	0.67	424.1	45

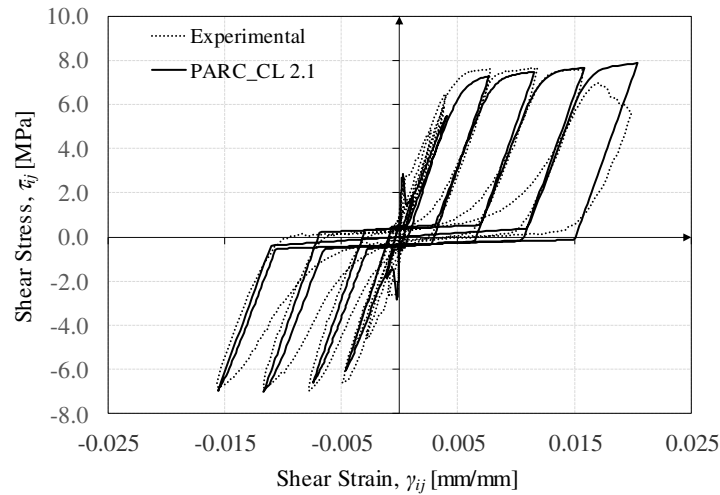
NLFEA SET-UP



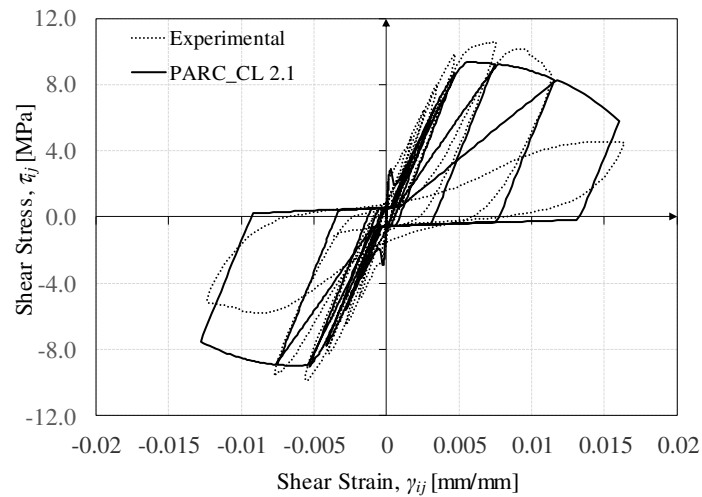
(a)



(b)



(c)

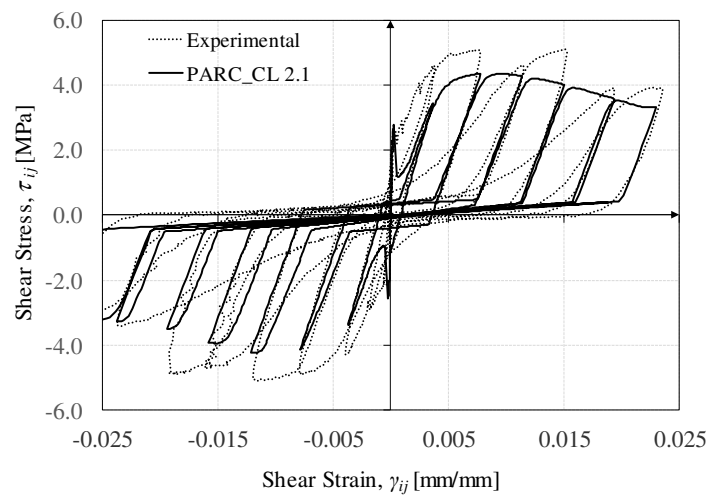


(d)

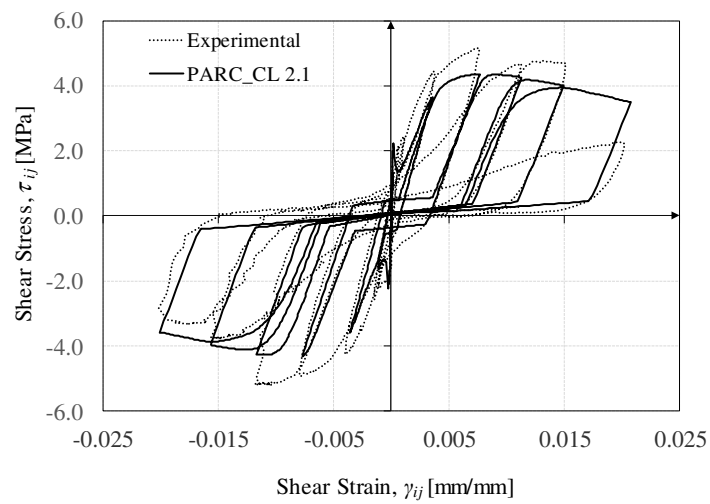
Figure 2.14: Comparison of measured and predicted shear-stress versus shear-strain curves in the  $i,j$ -system for the CA-series:(a) Modeling of the test setup; (b) CA2-panel; (c) CA3-panel; (d) CA4-panel.

A single 4-node membrane element with reduced integration scheme (defined M3D4R in Abaqus) was used to carry out NLFEA. An external frame was modelled using truss elements in Abaqus (2012) to simulate the same loading condition (Figure 2.14a). At the frame's end, the cyclic displacement time history was imposed.



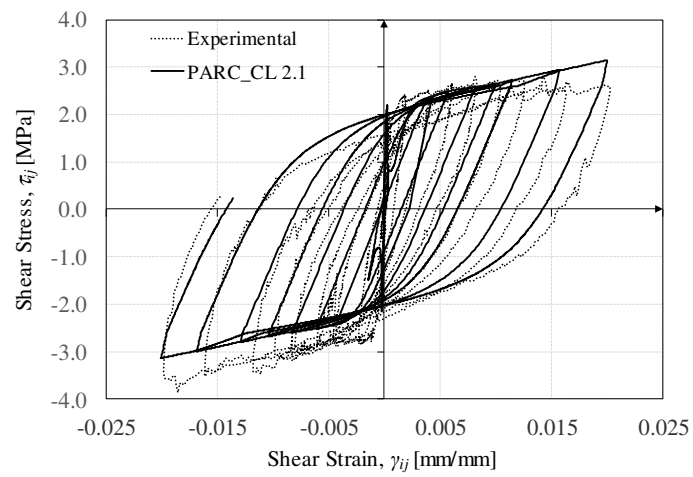


(a)

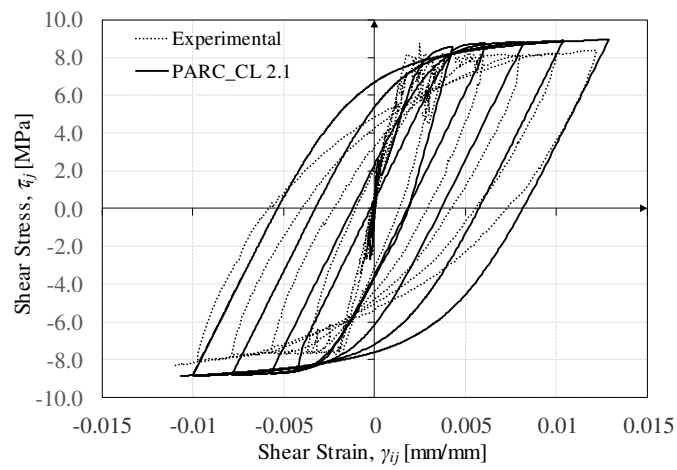


(b)

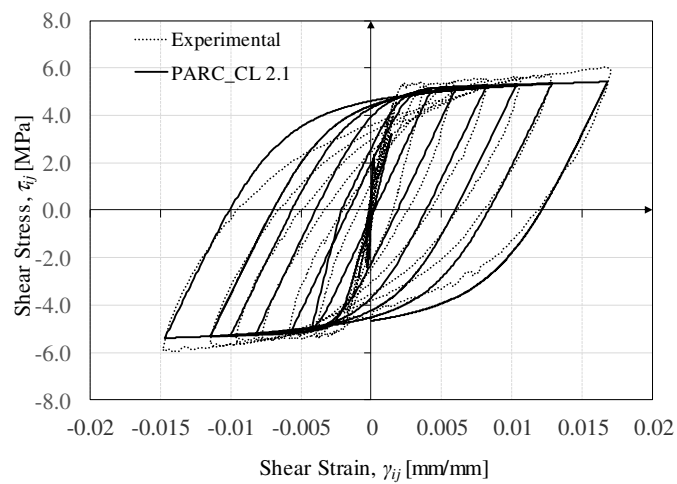
Figure 2.15: Comparison of measured and predicted by NLFEA shear-stress versus shear-strain curves in the  $i,j$ -system for the CB-series: (a) CB3-panel; (b) CB4-panel.



(a)



(b)



(c)

Figure 2.16: Comparison of measured and predicted shear-stress versus shear-strain curves in the  $i,j$ -system for the CE-series: (a) CE2-panel; (b) CE3-panel and (c) CE4-panel.

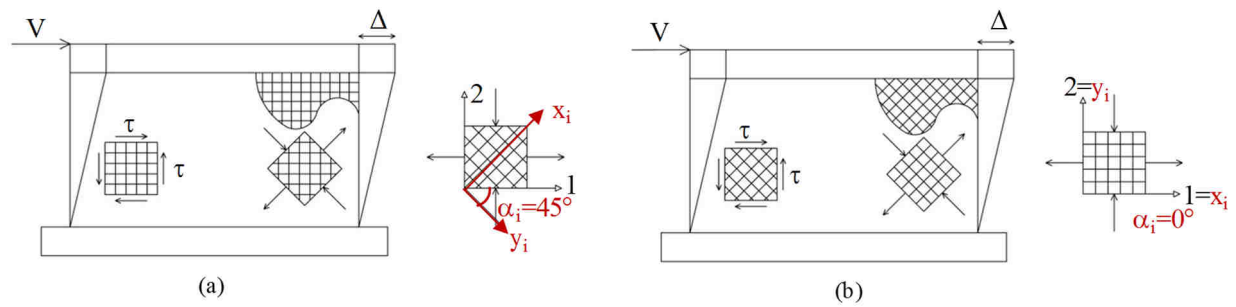


Figure 2.17: Squat walls and relative 2-D panel element (Hsu and Mo, 2010): (a) conventional horizontal and vertical steel bars configuration and (b) diagonal steel bars configuration.

One of the main purposes of the experimental tests carried out by Mansour and Hsu (Pang and Hsu, 1995; Hsu and Mo, 2010) was to investigate the effect of the steel bar orientation on the cyclic behaviour. Indeed, the steel bar orientation produces different cyclic response of the shear members: this becomes evident comparing the hysteretic loops of two RC panels with symmetrical reinforcement, CA3-panel (Figure 2.14c) and CE3-panel. In order to explain these different behaviours and to check the PARC\_CL 2.1 validity, a detailed study is conducted according to Hsu and Mo (2010).

In Figure 2.14-Figure 2.16 the experimentally-measured shear stress vs. shear strain responses, in the  $i,j$  system (Figure 2.13), for CA, CB and CE-series are compared with the PARC\_CL 2.1 model predictions. An acceptable level of agreement is observed between model and test results in terms of shear stress capacity, stiffness, ductility, shape of the unloading/reloading loops and pinching characteristics of the response.

Each tested panel can represent an element taken from the web of a squat wall subject to horizontal load  $V$ . Figure 2.17a can represent the case of the CA-panel, in which the angle  $\alpha_i$  is  $45^\circ$ , is shown; whereas Figure 2.17b can refer to the CE-panel, in which the  $\alpha_i$  angle is  $0^\circ$ , is presented.

To better explain how the response of the panels changes in function of different steel bar orientations it is necessary to study the materials behaviour. For example, the concrete and steel behaviour for CA3 and CE3-panels are reported in Figure 2.18. A reduction in the maximum attained compressive strengths of concrete is registered: panel CA3 reaches a value of  $f_c$  of almost 15 MPa (33% of its maximum compressive strength). This is due to the presence of cracks in the orthogonal direction that causes the biaxial state of concrete in compression, Figure 2.8, Eq.(2.29). Instead, CE3 element remains mainly in tension, reaching a  $f_c$  value of 3

MPa. In CA3-panel, bars remain in the tensile domain, Figure 2.18c, because of compressive stresses are resisted by concrete. Instead, steel bars in the CE3 panel are subjected to tension and compression stresses (Figure 2.18d): it is due to the steel bars orientation that are set parallel to the externally applied stresses. These observations lead to different global response (in terms of shear strain and stresses) as shown in Figure 2.14c and Figure 2.16b. More specifically, the steel bar orientation produces differences in terms of shear ductility and energy dissipation capacity. When the steel bars are oriented in the  $I,2$ -system, the hysteretic loops are fully rounded and the behavior is ductile; whereas when they are oriented at  $45^\circ$  (CA3-panel), the behavior is much less ductile. The PARC\_CL 2.1 model is able to predict the pinched shape as well as the fully rounded of the hysteretic loops. In fact, the obtained curve for the CA3-panel (and of the CA series in general) is severely ‘pinched’ near the origin, whereas the CE-series is fully rounded.

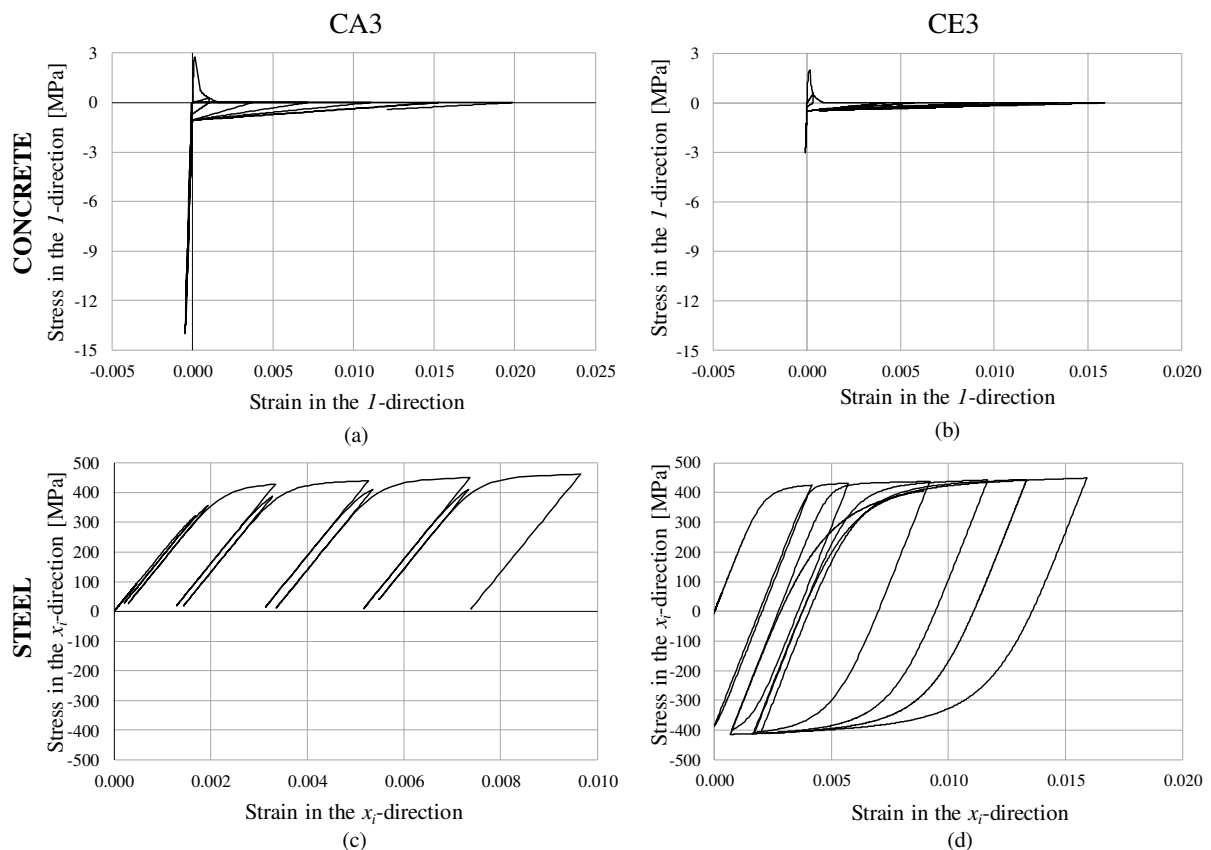


Figure 2.18: Cyclic stress-strain curves by means PARC\_CL 2.1: (a) and (c) CA3 panel; (b) and (d) CE3 panel.

To better clarify the pinching mechanism, the first hysteretic cycle after yielding for CA3 and CE3-panels, obtained by means PARC\_CL 2.1, is studied (Figure 2.19 and Figure 2.20).

Four points A, B, C, D are chosen to show the correlation between the shear stresses and strain and the corresponding stresses and strain in steel and concrete.

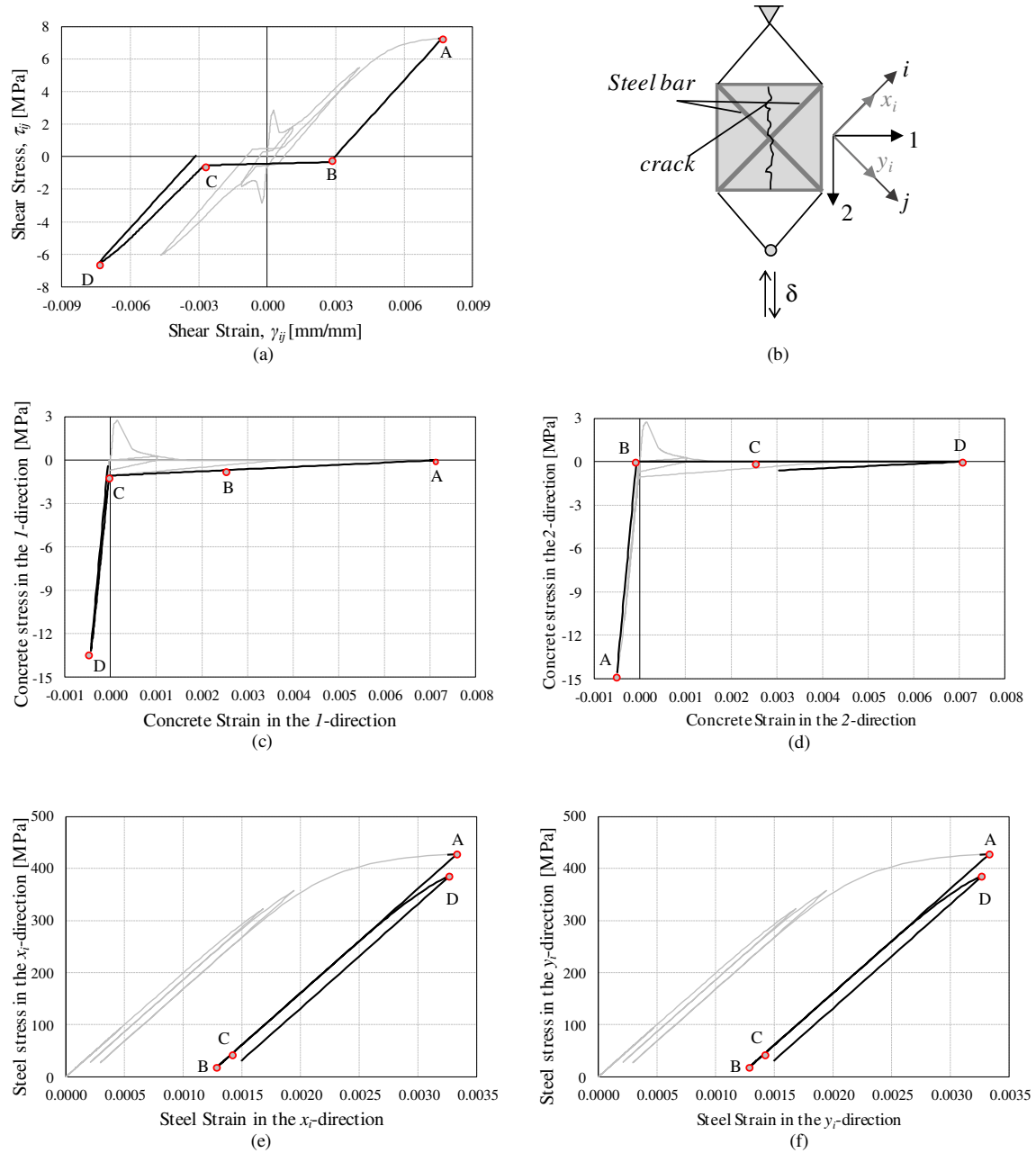


Figure 2.19: One hysteretic cycle for CA3-panel: (a) shear stress vs. strain curve, (b) element configuration, (c) and (d) stress-strain curve for concrete, (e) and (f) stress-strain curve for steel.

For CA3-panel, point A is the last point of the shear loading; point B is the minimum shear stress in the positive strain domain whereas C is the corresponding point in the negative strain domain and they delimit the pinching zone. Point D is the minimum stress point. When the element is unloaded from point A to point B, also the steel stress is reduced (Figure 2.19-e,f):

the behavior of the steel is equal in the  $x_i$ -direction and  $y_i$ -direction because of the same reinforcement ratio. Consequently, the concrete in the  $l$ -direction reduces its strain and vertical cracks start to close. At point B, shear stress, steel stresses, and concrete stresses are close to zero. Proceeding from point B to point C the vertical cracks in one direction are fully closed and horizontal cracks start to open: this region, with a very small shear resistance, is called pinching zone. Finally, from point C to point D the vertical strain increases and produces reloading of the steel bars; consequently, the shear stiffness increases.

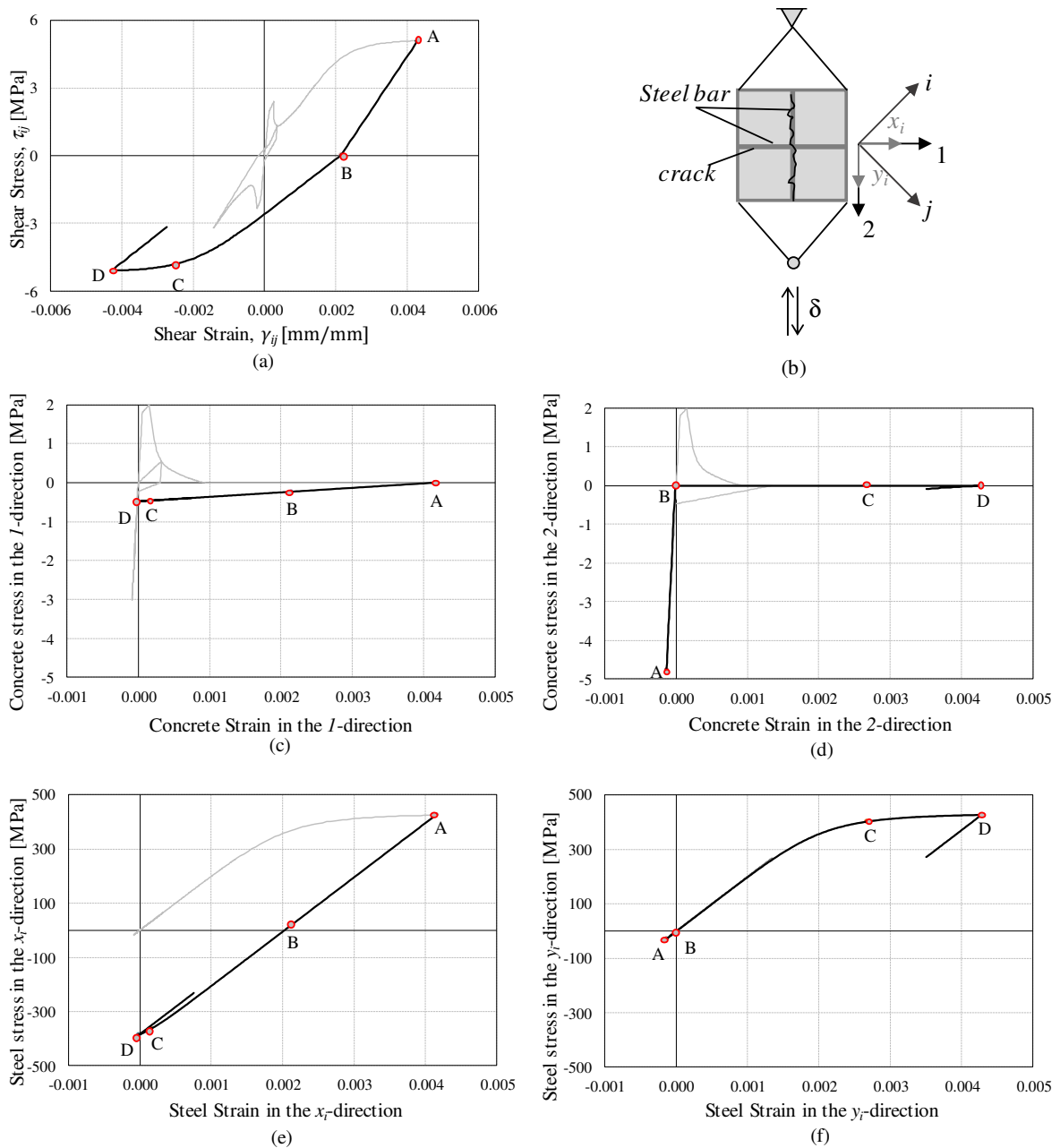


Figure 2.20: One hysteretic cycle for CE3-panel: (a) shear stress vs. strain curve, (b) element configuration, (c) and (d) stress-strain curve for concrete, (e) and (f) stress-strain curve for steel.

The PARC\_CL 2.1 results for the CE3 panel are illustrated in Figure 2.20: steel bars are oriented in the direction of the applied stresses so the pinching mechanism is absent. As in the previous panel in the first cycle after yielding is presented: with the help of 4 points, it is remarked the correlation between materials. Point A represents the maximum shear strain of the cycle; point B is the minimum shear stress in the positive domain, point C is in the negative strain region and it represents the moment in which the steel in the  $y_i$ -direction reaches yielding (Figure 2.20-f). Point D is the minimum shear strain reached by the panel. When the element is unloaded from point A to point D the panel is subject to compressive stress in the horizontal direction ( $1$ -axis) and to tensile stress in the perpendicular direction ( $2$ -axis) as demonstrated to the concrete behaviour. Consequently, also the bars are subject to the same type of load: the bars along the compressive direction ( $x_i$ ) reduces the stress whereas the steel in the perpendicular direction ( $y_i$ ) is subject to tensile load. The reinforcement is offering a high shear stiffness from point B to point C.

### ***2.3.1.1 PARC\_CL 2.1 versus Other Crack Models***

It is in the Author's opinion that, for the validation of a new model it is necessary to make comparisons not only with experimental results but also with models of proven validity. This is even more significant if done on simple elements, whose theoretical behavior and failure mode is known.

For these reasons, the results obtained with the PARC\_CL 2.1 are compared to those obtained with a commercial software, DIANA 10.0 (Manie 2015).

Two panels with different failure mode are selected: the CE4-panel and the CB4-panel. CE4-panel, Figure 2.13, is characterized by reinforcements placed in parallel to the applied principal stresses with the same reinforcement ratios in the  $x_i$ - $y_i$  directions and its response in terms of shear stress-strain curve is dominated by the stiffness offered by the reinforcements. The CB4-panel is characterized instead by two parallel steel grids placed at angles of  $45^\circ$  with different steel ratio. This last case study is dominated by the aggregate interlock effect so it is very interesting to compare the aggregate interlock cyclic formulation implemented in the PARC\_CL 2.1 crack model with other approaches available in the DIANA software.

The DIANA's concrete modeling is based on a total strain rotating crack model with exponential softening in tension and parabolic behavior in compression. The tensile softening of concrete depends on the tensile fracture energy,  $G_F$ , whereas the compressive softening

depends on the compressive fracture energy,  $G_C$  (Hendriks et al. 2012). The reduction of compressive strength of concrete due to lateral cracking is taken into account and, accordingly to the PARC\_CL 2.1 crack model, the lower limit was set at 0.4. Furthermore, a variable Poisson's ratio of concrete is assumed. Both in tension and in compression the cyclic behaviour of concrete is defined with unloading-reloading paths secant to the origin. The Menegotto-Pinto model is assumed for reinforcement bars assuming the same parameters adopted in the PARC\_CL 2.1 model.

For concrete 4-node membrane element (Q8MEM, Belletti et al. 2013<sup>c</sup>) is used for meshing the panel with a full Gauss integration scheme (2×2). The reinforcement bars are modelled with embedded truss elements with two Gauss integration points along the axis of the element. Perfect bond is assumed.

The CE4-panel is modeled using the *fixed crack model* available in DIANA software (Manie 2015). The shear stiffness after cracking  $G_{cr}$  is reduced using a constant shear retention factor  $\beta_{const}$  as in Eq.(2.44).

$$G_{cr} = \beta_{const} \cdot G = 0.03 \cdot G \quad (2.44)$$

Figure 2.21a shows that the DIANA result reaches the experimental shear stress value only in the first cycle than the model presents a lower resistance. Even if the same Menegotto-Pinto parameter have been used, DIANA results seem to present a low strength than PARC\_CL 2.1, Figure 2.21b.

As mention before, to validate the aggregate interlock formulation presented in §2.2.6 the CB4-panel is chosen. Figure 2.22 shows the results obtained using different approaches presented in the DIANA material library, compared with the results obtained using PARC\_CL 2.1 crack model.

The comparison between PARC\_CL 2.1 *fixed crack model* and DIANA *rotating crack model* is presented in Figure 2.22a: in the first cycles, DIANA results better reproduce the experimental ones, reaching higher values of shear stress than PARC\_CL 2.1. However, the last cycles do not capture the softening of the experimental curve.



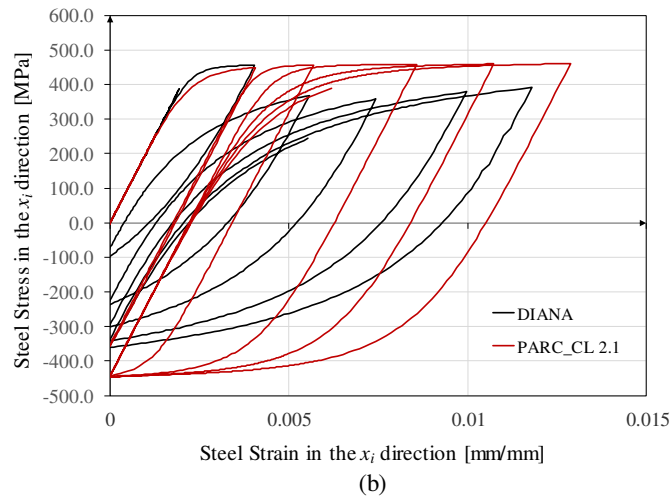
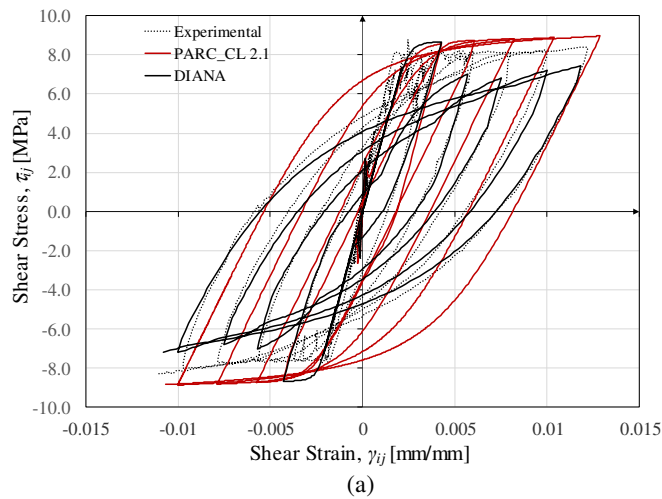


Figure 2.21: (a) comparison between experimental shear-stress versus shear-strain curves in the  $i,j$ -system and DIANA and PARC\_CL 2.1 results for the CE4 panel; (b) comparison between DIANA and PARC\_CL 2.1 stress-strain curve for steel.

Furthermore, the same panel is modeled using different *fixed crack models* available in the DIANA library:

1) *constant shear retention factor*; the elastic shear modulus of concrete  $G$  is multiplied for a constant coefficient  $\beta$ , as presented in Eq.(2.44) with  $\beta_{const} = 0.01$ . Figure 2.22b shows that the response prediction obtained using a constant shear retention factor result presents an increasing curve not able to capture the softening of the shear stress.

2) *damage based shear retention factor*; the shear stiffness  $G_{cr}$  decays similarly to the normal stiffness after the crack, Eq.(2.45):

$$G_{cr} = \frac{E^*}{2 \cdot (1 + \nu^*)} \quad (2.45)$$

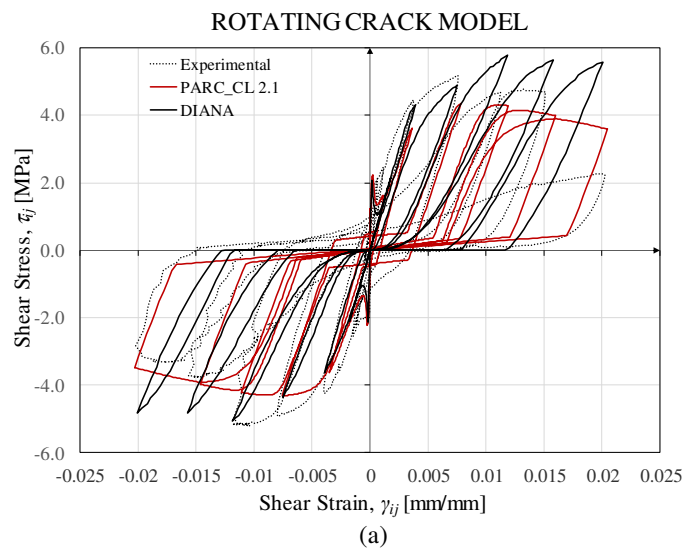
where  $E^*$  and  $\nu^*$  are the reduced stiffness and Poisson's ratios respectively. In Figure 2.22c DIANA result presents a lower resistance due to a shear modulus underestimation. For positive strains, the cycles are full, whereas for negative strains the cycles are slimmer, maybe due to the different behaviour of steel in tension and in compression.

3) *aggregate size based shear retention factor*; the shear stiffness diminishes with the crack opening. It is assumed that aggregate interlock equals zero for crack opening width values higher than half the maximum aggregate size. The linear decay of the shear retention is defined in Eq. (2.46):

$$G_{cr} = \beta_{\text{aggreg}} \cdot G \quad (2.46)$$

where  $\beta_{\text{aggreg}} = 1 - (2/d_{\text{max}}) \cdot \varepsilon_n \cdot a_m$  being  $\varepsilon_n$  the crack strain values (which are the plastic part of the maximum principal strain values). Since for low value of  $\varepsilon_n$  the shear retention factor is close to 1 the aggregate interlock model causes a strong overestimation of the shear stresses above all in correspondence of the first cycle, Figure 2.22d.

Differently to PARC\_CL 2.1 model, the adopted aggregate interlock modeling implemented in DIANA software, Figure 2.22, depends only to the crack opening  $w$  and not to the crack sliding  $v$ . Figure 2.22 demonstrates that aggregate interlock modeling implemented in PARC\_CL 2.1 leads a better prediction of the results thanks to the plastic strains.



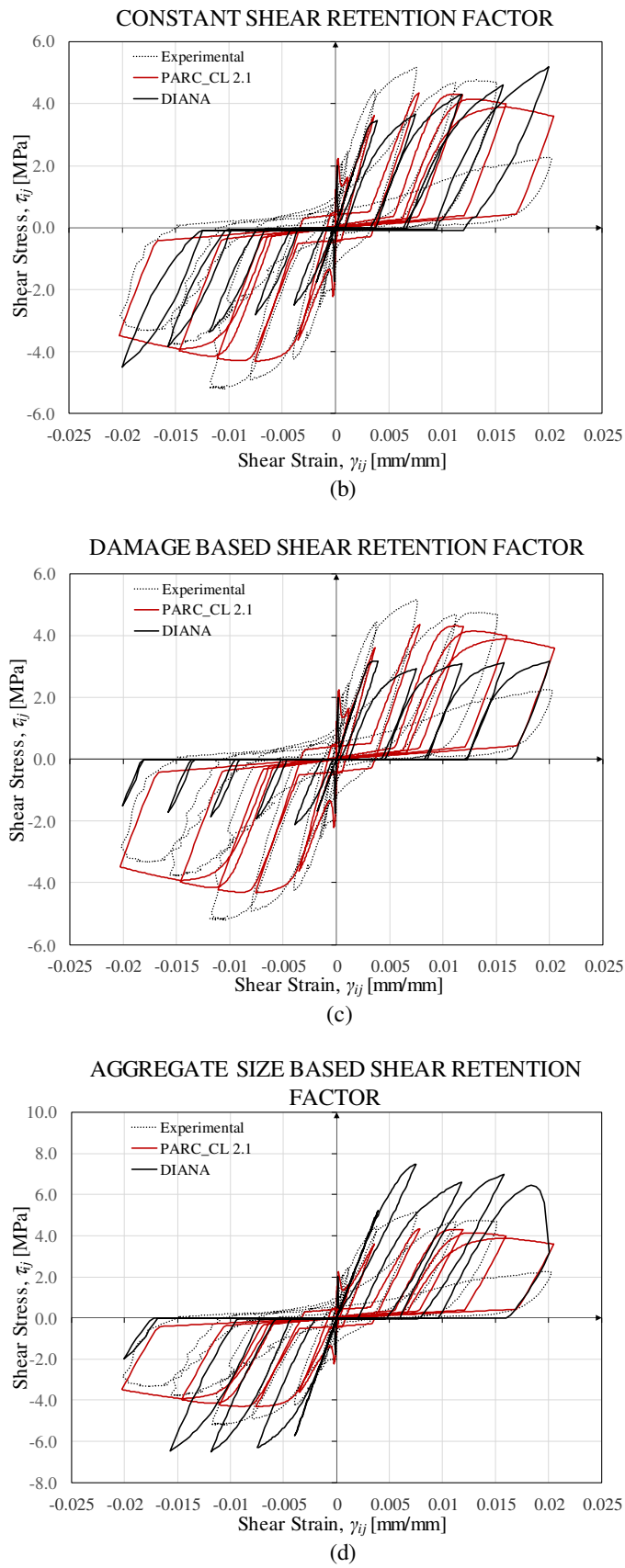


Figure 2.22: CB4 panel: comparison between experimental results, PARC\_CL 2.1 results and DIANA results using different aggregate interlock models.

### 2.3.2 The CASH Benchmark Phase 2

In 2017, an international benchmarking program called CASH-phase 2 on the beyond design seismic capacity of RC shear walls was organized by OECD-NEA (Nuclear Energy Agency) (N005\_A469\_2014\_EDF\_B). Participants were invited to carry out pushover and dynamic analyses to assess the capacity of two full scale RC walls extracted from a nuclear power plants (NPP) building. The main objective of the CASH benchmark was the evaluation not only of the reliability of finite element commercial software but also of the ability, in current engineer practice, to calculate the resistance of RC walls subject to various seismic loading.

Comparison between Phase 2 results, obtained from various teams coming from academia, industry and nuclear research organizations, were presented during the workshop organised in Paris 1-2 of June 2017. The predictions of about half of the participants were in good agreement. The strong differences recorded by other teams were due to modelling errors or to the use of unsuitable software for the required analysis.

The used software were both commercial like ATHENA, ABAQUS, SOFISTIK, SOLVIA, Ls-Dyna and open access like CAST3M, Code, Aster, VecTor2. NLFEA have been carried out using plasticity-based model or crack models available in the software material libraries; only the team from the University of Toronto and the team from the University of Parma adopted crack models self-implemented in user subroutines. In this paragraph, the results obtained by the University of Parma team are presented.

The work was organized in three different tasks with increasing complexity to check, improve and assess the modelling technique of participants. Before to start, Cash benchmark organizers required to provide the non-linear material behaviour of a single finite element subject to cyclic loading. Four nodes membrane element with a single integration Gaussian point was used by the team from the University of Parma for the description of the non-linear material behavior. The concrete response to cyclic tension-compression loads and alternated shear cycles is illustrated in Figure 2.23. As shown in Figure 2.23b, the reduced shear strain level imposed by the organizers does not allow to appreciate the hysteretic behavior implemented in the PARC\_CL 2.1 and explained in §2.2.6.

Figure 2.24 illustrates the cyclic behavior of steel obtained by using the implemented Menegotto-Pinto formulation, presented in §2.2.7.

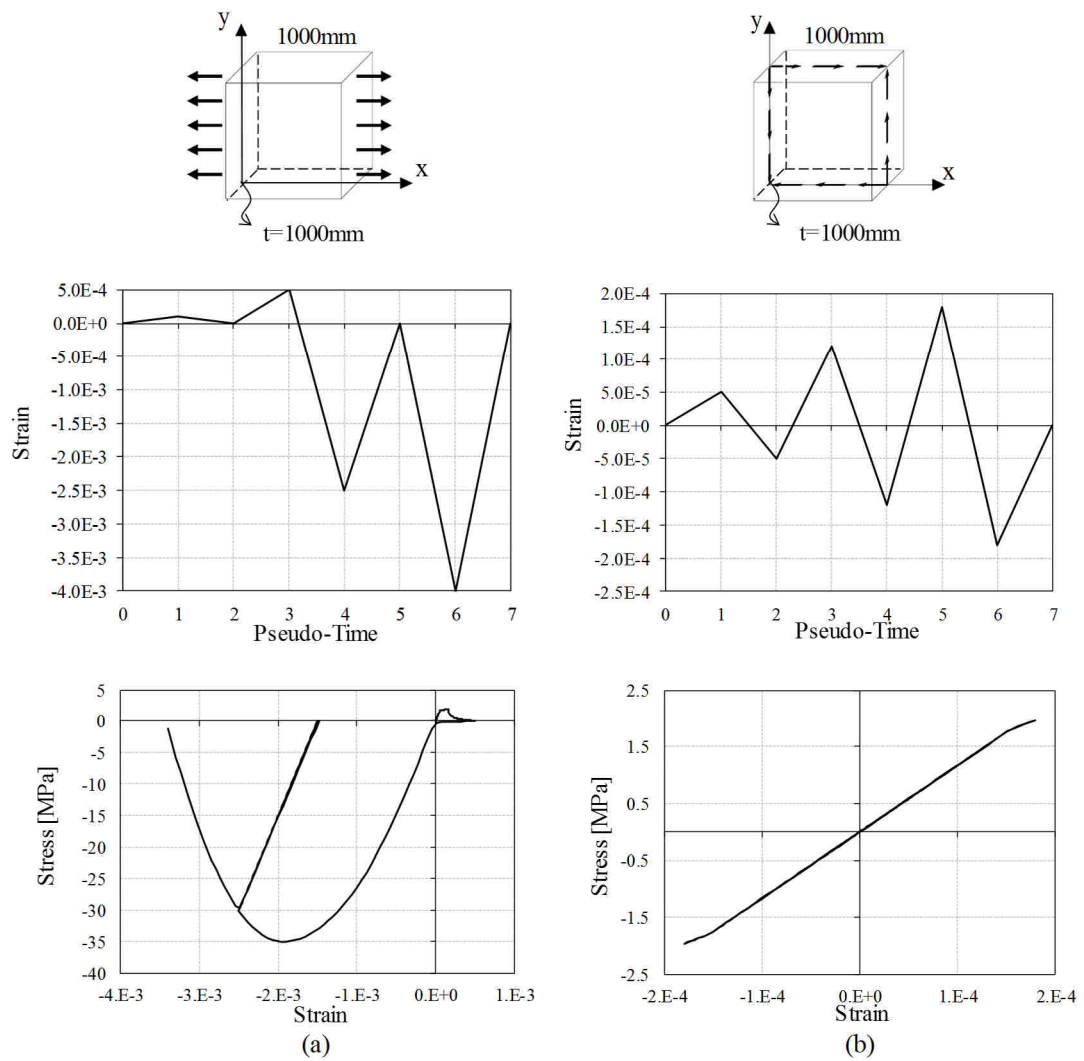


Figure 2.23: Concrete response under (a) tension and compression cyclic loading and (b) cyclic shear loading.

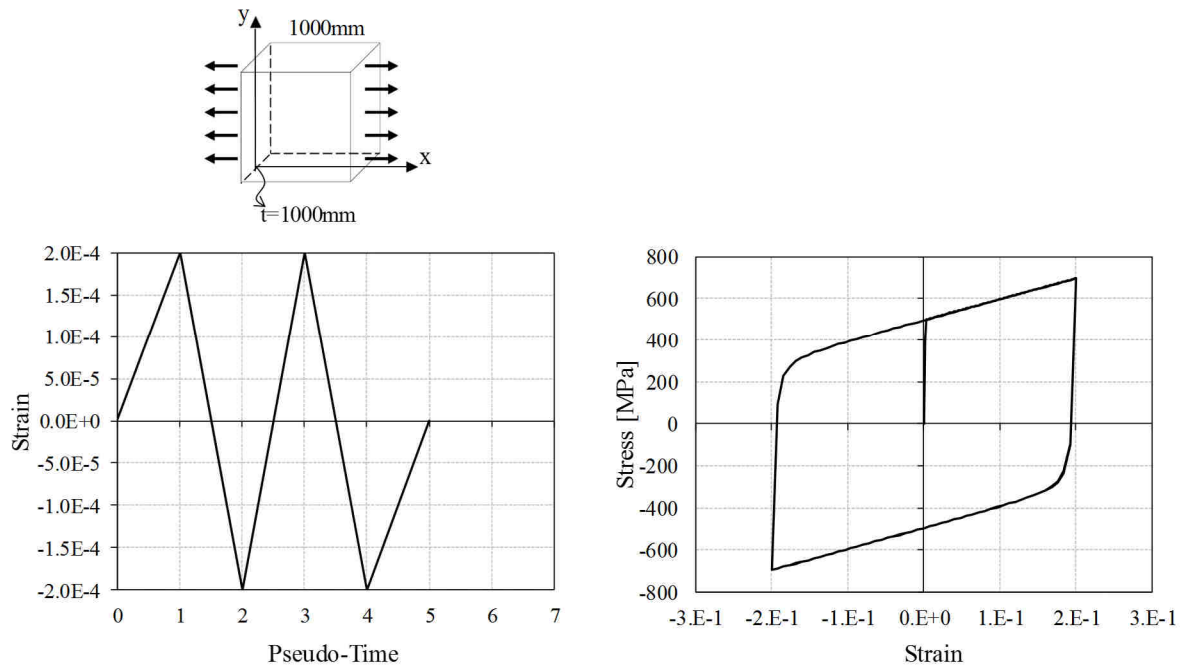


Figure 2.24: Steel response under tension and compression cyclic loading.

After the calibration of the constitutive laws, two full scale four floors and two bays RC walls are analysed. The total height of the walls is 16 meters, the width is 12 meters and the thickness is 0.4 meters, Figure 2.25. The irregular wall differs from the regular one due to the absence of the shear wall on Level 2 at the second bay. An interior column of 0.4x0.4m is located in the middle of the structure. To simulate the presence of perpendicular walls and floor slabs, two lateral flanges 0.4x1.0m and interstorey beams 0.4x1.0m have been added to the walls, respectively. This aspect is of particular interest because in nuclear power plants (NPP) building RC walls are connected to the RC floor slab at every floor level. During earthquake shaking, the non-linear behavior of wall-to-slab connections and slabs are particularly important because they affect the seismic load distribution and the damage pattern in the structural members of the system (Pantazopoulou et al. 1992). Nevertheless, even if the in-plane non-linear behavior of individual RC walls (Belletti et al., 2014<sup>a</sup>) and floor slabs (Qadeer et al., 1969; Paulay et al., 1981) is well documented in literature, an exhaustive investigation on the response of RC walls systems and on the behaviour of slab-wall junction under earthquake motion is not nowadays achieved (Kaushik, 2017). Therefore, there are still several uncertainties regarding both demand and capacity assessment., Figure 2.25.

Table 2.2 shows the mean values of the mechanical properties of concrete and steel. Shear walls, beams, and columns reinforcements are indicated in Figure 2.26 as reinforcement ratio

$\rho$ ; these quantities are obtained by Cash benchmark organizers from the design study, considering a determined seismic ground motion.

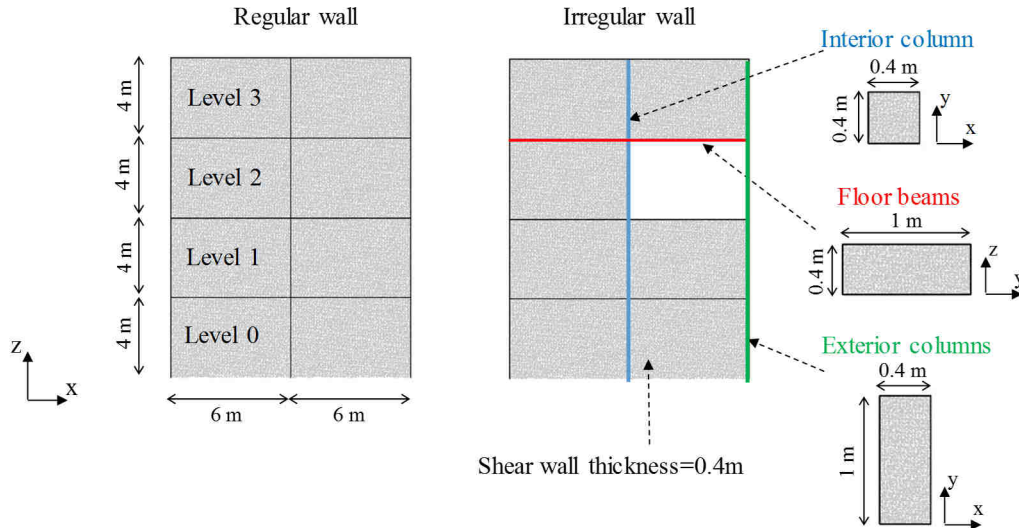


Figure 2.25: Geometry description.

Table 2.2: Mechanical properties of concrete and steel.

Concrete					Steel			
$f_c$ [MPa]	$E_c$ [MPa]	$f_t$ [MPa]	$\nu$	density [kg/m <sup>3</sup> ]	$f_y$ [MPa]	$E_s$ [MPa]	$E_h$ [MPa]	density [kg/m <sup>3</sup> ]
35.0	30000.0	2.0	0.2	2300.0	500.0	200000.0	1000.0	7500.0

The loads consist of self-weight of structural elements, vertical masses applied on the floors to model the live loads (per floor  $M_z = 60$  t) and horizontal masses applied on the floors to adjust the first horizontal frequency (per floor  $M_h = 500$  t).

The adopted FEM model is reported in Figure 2.27. 864 nodes and 644 multi-layered shell elements with 4 nodes and full integration scheme, with average element size equal to 550 mm, have been used to model the walls. The mesh allows running non-excessive time consuming analysis for the adopted computer (3.20 GHz CPU with 16 GB RAM). The self-weight of structural members has been applied as density whereas the horizontal and vertical masses as lumped mass elements. The wall structure is clamped at the base and the out of plane displacements are prevented in all nodes.

The analyses were conducted using the ABAQUS 6.12 software by means the PARC\_CL 2.1 crack model.

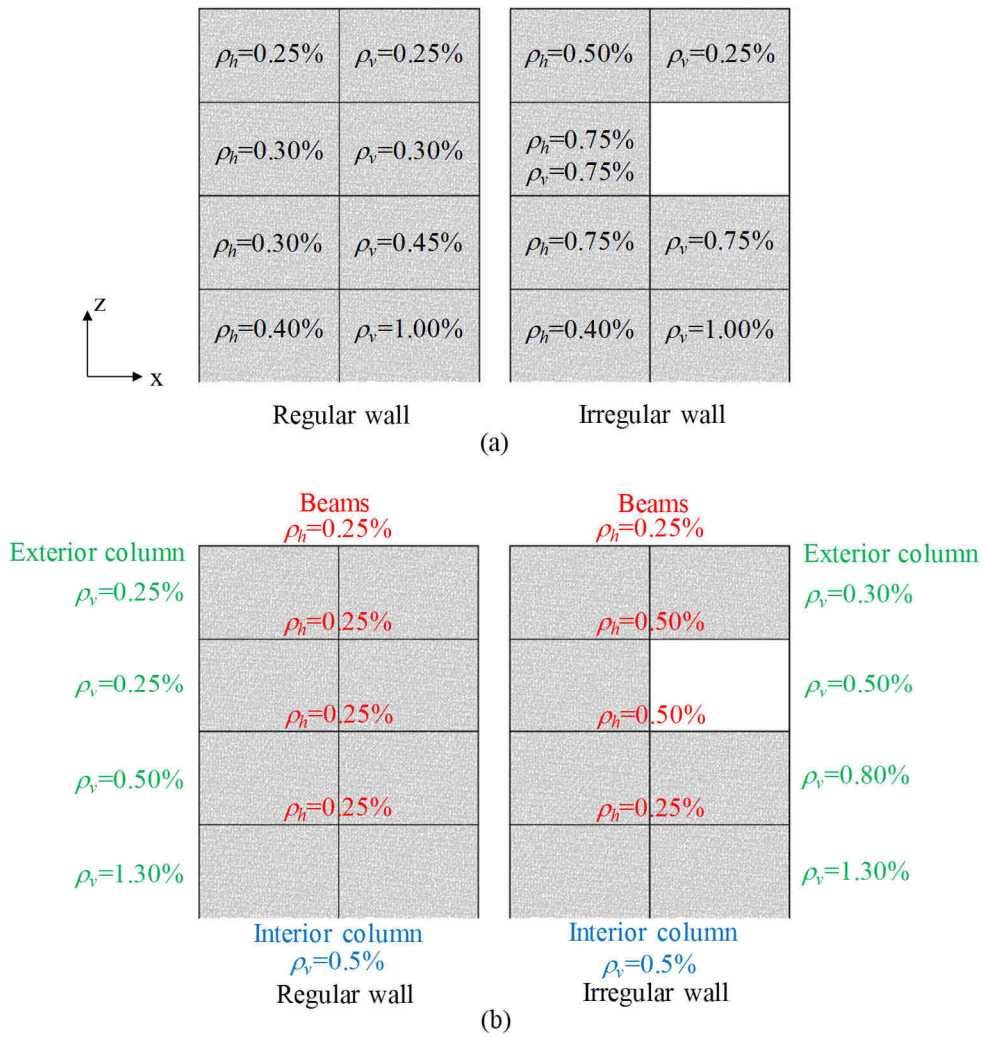


Figure 2.26: Reinforcement ratio of (a) shear walls and (b) columns and beams.

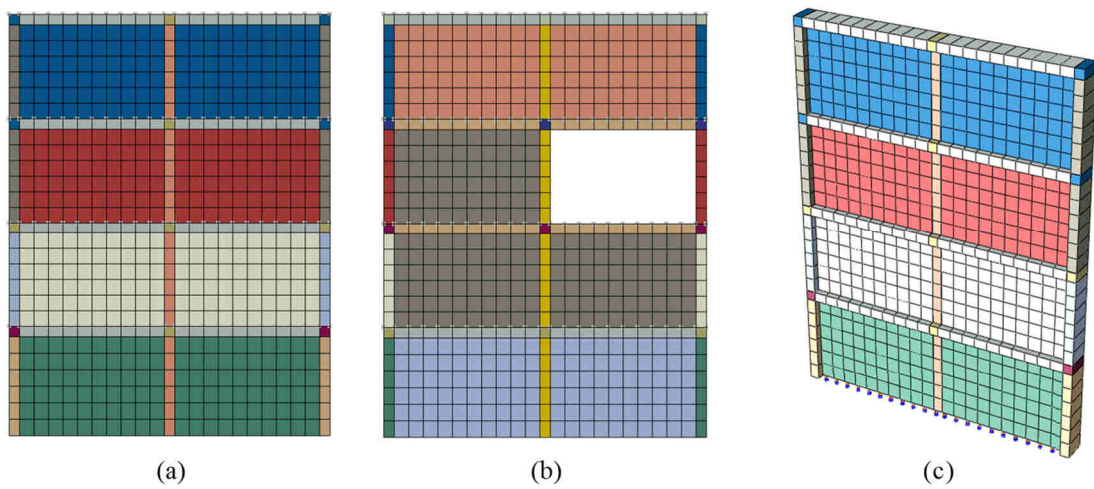


Figure 2.27: Adopted finite element mesh for (a) regular wall, (b) irregular wall. (c) Shell elements thickness.



The Newton-Raphson method has been adopted as a convergence criterion. For dynamic analyses the default Abaqus/Standard Hilber-Hughes-Taylor time integration has been used.

For Task 1 the principal vibration modes and the spectral analysis response from the entire modelling of the multi-storey RC walls are expected. The acceleration spectrum is given in Figure 2.28. A viscous damping ratio  $\xi$  equal to 7% has been adopted for spectral analyses as well as a reduced Young modulus  $E_c/2$  for concrete.

Figure 2.29 shows the first mode deflected shape for the regular and irregular wall having frequencies  $f$  respectively equal to 4.02 Hz e 3.42 Hz, in good agreement with the values provided in Table 2.3 by the benchmark organizers.

Figure 2.30 illustrates the diagram of the shear force, the bending moment and the inter-storey drift for the regular and the irregular wall, obtained by spectral analysis and considering only the first vibration mode. Figure 2.30c highlights the substantial difference between the deformed shape of the irregular wall and the regular one due to the presence of the opening at Level 2.

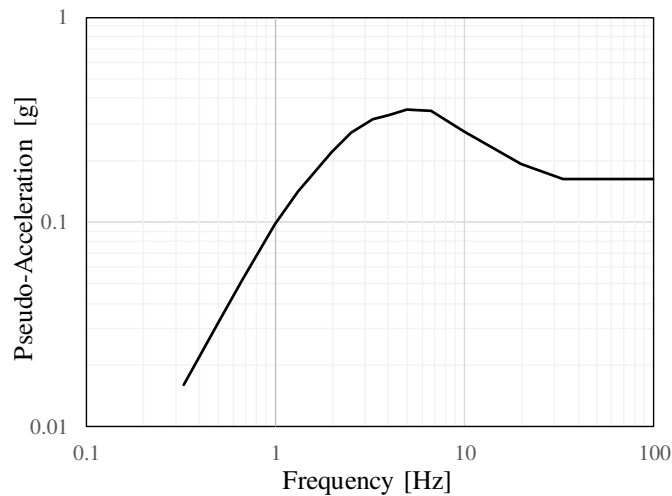


Figure 2.28: Elastic Response Spectrum.

Table 2.3: Rayleigh coefficient

Wall	Analysis	$f_1$ [Hz]	$\xi_1$	$f_2$ [Hz]	$\xi_2$	$\alpha$	$\beta$
Irregular	Non-linear	5.2	2%	35	2%	1.138	1.584E <sup>4</sup>
	Linear	3.68	7%	35	7%	2.927	5.761E <sup>4</sup>
Regular	Non-linear	6.2	2%	35	2%	1.324	1.545E <sup>4</sup>
	Linear	4.38	7%	35	7%	3.427	5.658E <sup>4</sup>

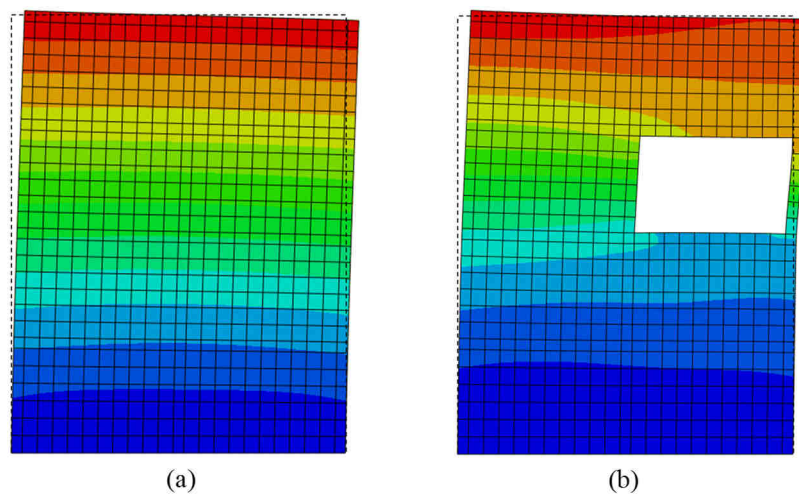


Figure 2.29: First mode deflected shape for (a) regular wall and (b) irregular wall.

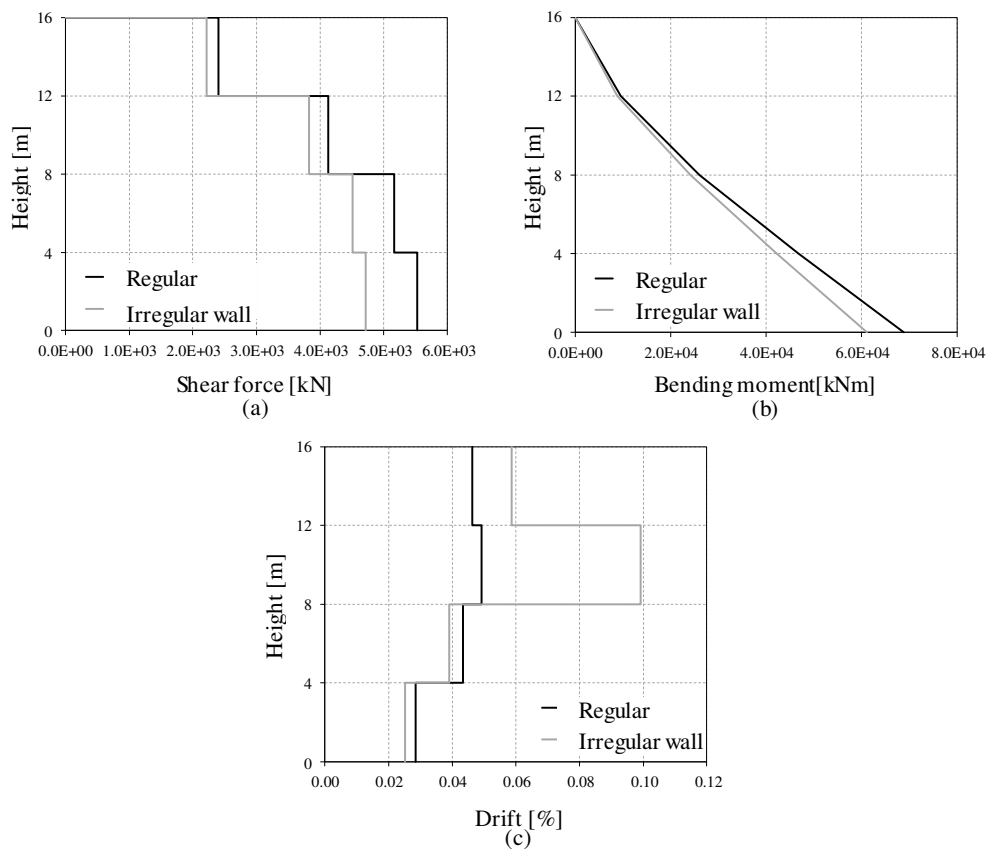


Figure 2.30: Spectral analysis results obtained for regular and irregular wall: (a) shear force, (b) bending moment and (c) inter-storey drift diagrams.

The aim of Task 2 was the evaluation of the non-linear response of the specimens up to their ultimate capacity. Non-linear Pushover analyses have been conducted in load control applying a first mode proportional distribution of horizontal forces, as indicated in Figure 2.31a and in Eq.(2.47).

$$F = [M] \cdot \{\phi\} \quad (2.47)$$

Only horizontal mass per floor  $[M]$  has been taken into account and the horizontal force has been applied to each floor along the wall/slab interface. The normalized force distribution at each level is (0.15, 0.43, 0.72, 1) for the regular wall and (0.09, 0.31, 0.73, 1) for the irregular wall. The full elastic modulus has been used.

Figure 2.31b shows the shear base–P4B displacement curve for the regular and irregular wall. For the irregular wall, the pushover analysis has been conducted in direction  $+x$  and  $-x$ . The analyses have been interrupted when material strains achieved an assumed threshold limit equal to 3.5‰ for concrete and 0.4‰ for steel (as suggested by Cash benchmark organisers). The capacity, in terms of resistance and ductility, of the irregular wall is lower than the capacity of the regular wall because of the presence of the opening. Furthermore, the irregular one presents a lower capacity if the forces are applied in  $-x$  direction again due to the presence of the opening.

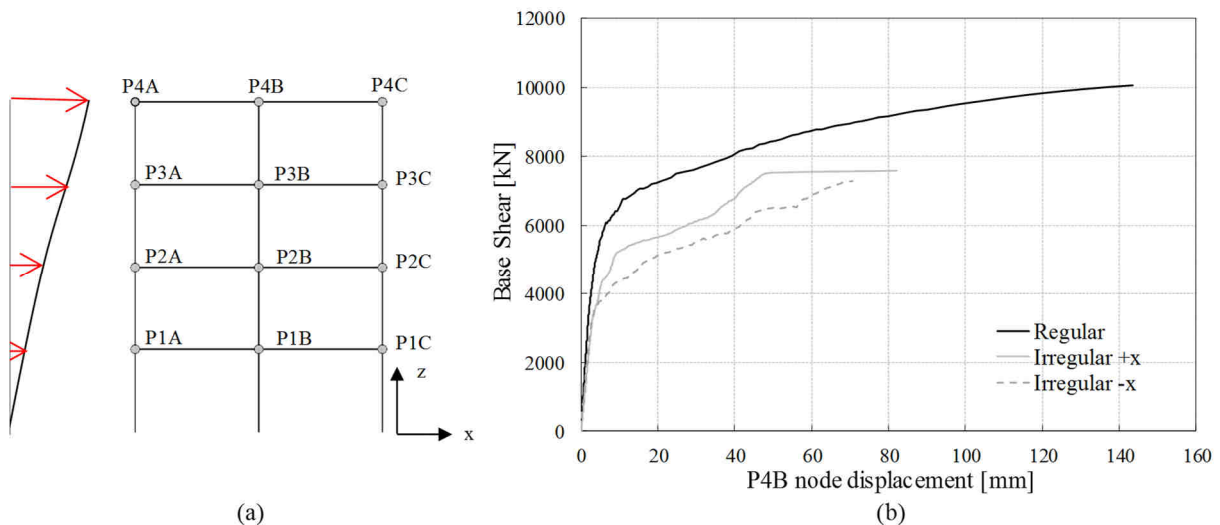


Figure 2.31: (a) Pushover force and node groups; (b) Pushover analysis for the regular and irregular wall.

Figure 2.32 shows the contour plot of longitudinal reinforcement strain values for different levels of displacement of the P4B point for the regular and the irregular walls (in grey the longitudinal reinforcement strain values higher than the steel yielding strain). Observing Figure 2.32 it is possible to note that the failure occurs after the yielding of the longitudinal rebars in correspondence of the lateral flanges. This phenomenon appears particularly localized at Level 2 both for the regular and irregular wall. Furthermore, the irregular wall presents high values of crack width and strain both of longitudinal and horizontal rebars at the corners.

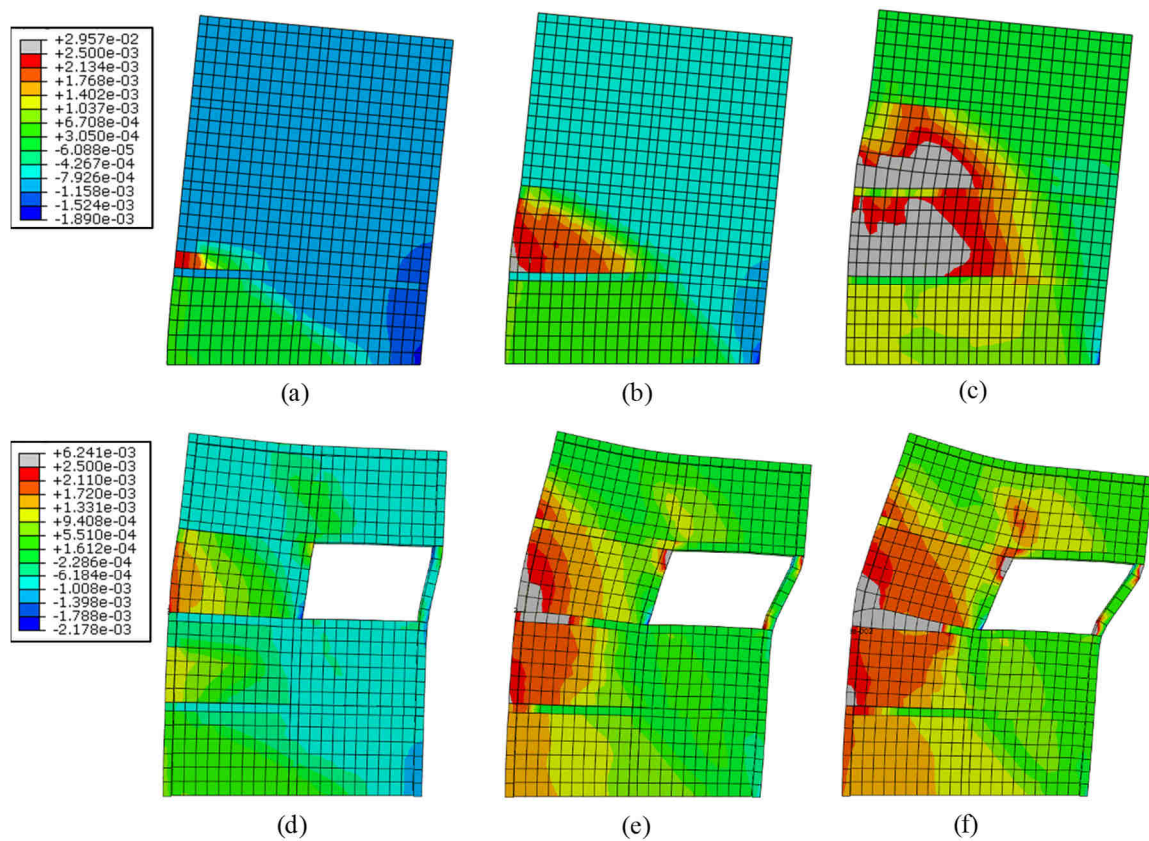


Figure 2.32: Longitudinal reinforcement strain values for the regular wall in correspondence of P4B node for displacement equal to: (a) 10 mm, (b) 25 mm, (c) 50 mm; for the irregular wall at (d) 25 mm, (e) 50 mm, (f) 80 mm.

Finally, Task 3 required linear and non-linear incremental dynamic analysis. Figure 2.33a shows the seismic acceleration time history to be amplified by a coefficient  $\eta$  (according to incremental dynamic analysis) and applied only in the  $x$  direction (no excitation is applied along the vertical direction). More specifically,  $\eta$  equal to 1 is used for the prediction of quasi-elastic behaviour (i.e. slight levels of damage),  $\eta$  equal to 2 scales the accelerogram to simulate an earthquake that causes high levels of damage to structures.  $\eta$  value equal to  $\eta_5$  has to be determined as the accelerogram scaling multiplier value that causes an inter-storey drift equal to 5‰.

Table 2.3 shows the Rayleigh coefficients  $\alpha$  and  $\beta$ , to be used in the input file to obtain a damping ratio  $\xi$  of 7% for linear dynamic analysis and 2% for non-linear dynamic analyses. These coefficients have been fixed by benchmark organizers on the base of their estimated frequencies  $f_1$  and  $f_2$  and correspond to typical values for nuclear industry practice.

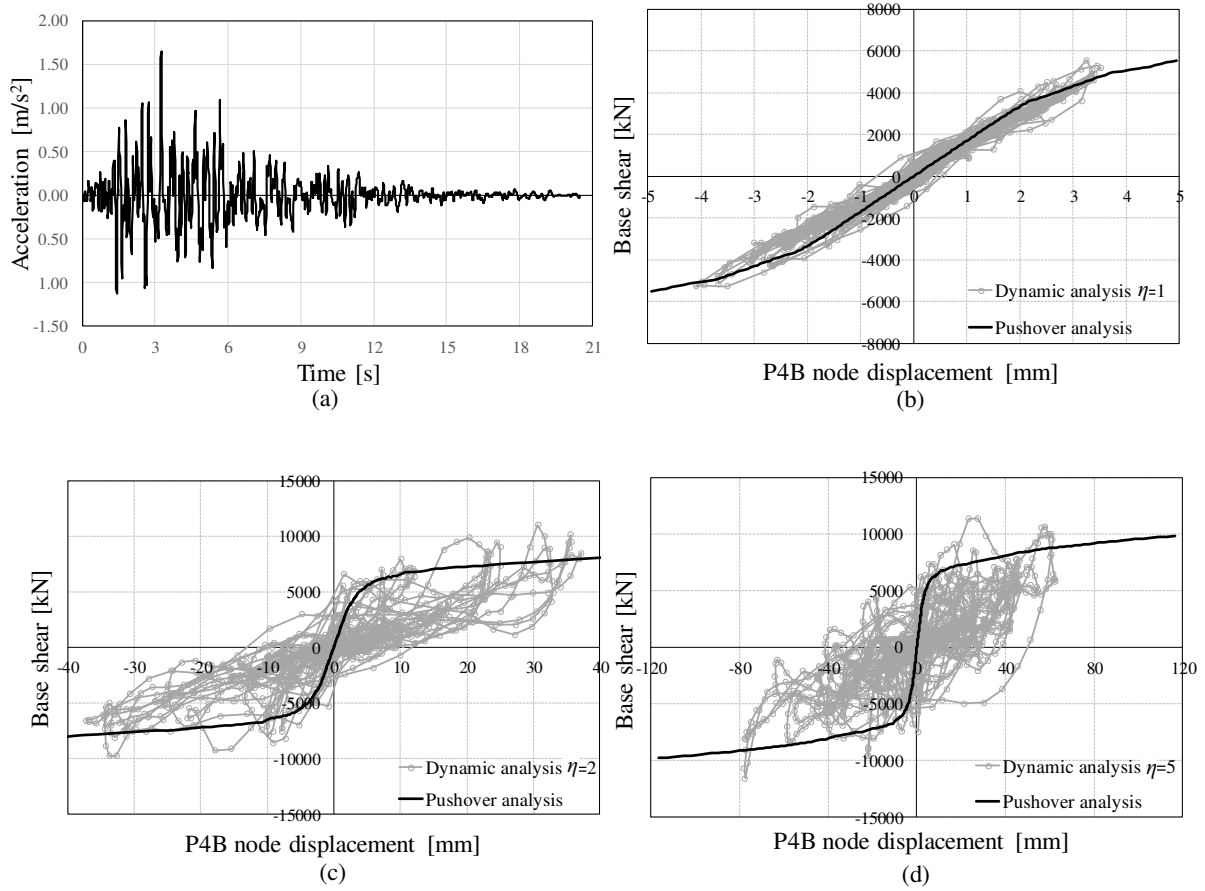


Figure 2.33: (a) Seismic acceleration time history ( $\eta = 1$ ); Regular wall base shear-P4B node displacement for accelerogram multiplier equal to: (b)  $\eta=1$ , (c)  $\eta=2$ , (d)  $\eta=5$ .

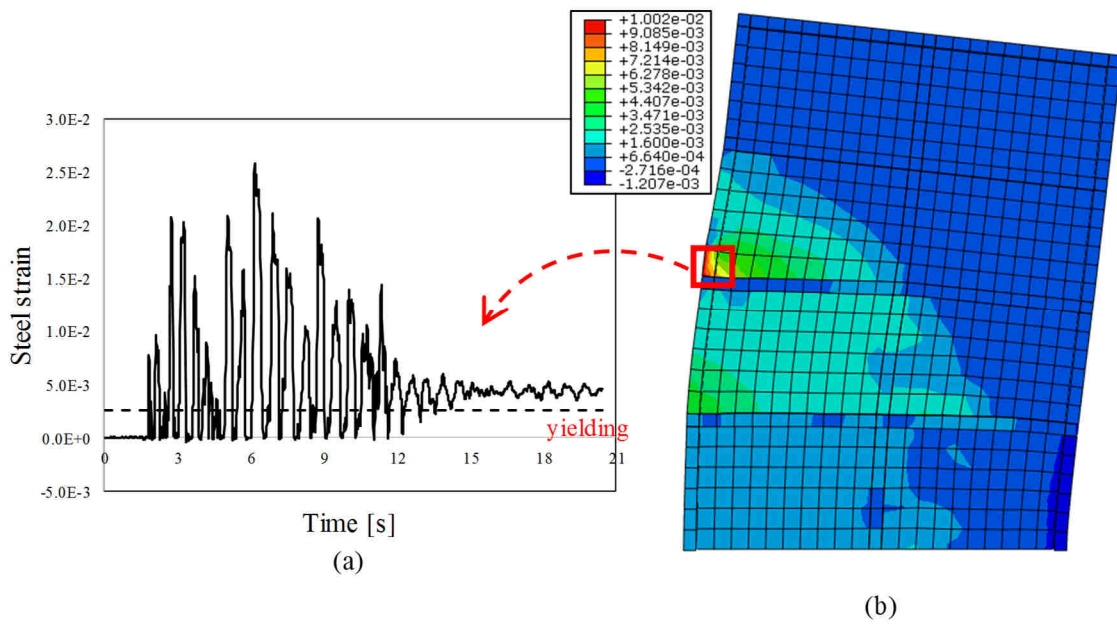


Figure 2.34: Regular wall: (a) longitudinal reinforcement strain-time curve for the highlighted element when a scaled factor of  $\eta=2$  is used; (b) longitudinal reinforcement strains at the maximum horizontal displacement occurring at 5 seconds.

Figure 2.33 and Figure 2.36 show, for regular and irregular wall respectively, the shear base–P4B node displacement curve for accelerogram multiplier equal to  $\eta=1$ ,  $\eta=2$  and  $\eta=5$  respectively. More specifically, Figure 2.33a and Figure 2.36a show that if the walls are loaded with the basic accelerogram, they remain in the quasi-elastic range.

As shown in Figure 2.34 for the regular wall and Figure 2.37 for the irregular wall, when the walls are subject to a scaled accelerogram ( $\eta=2$ ) they experience major damage and the yield of the longitudinal bars is reached.

Figure 2.35 and Figure 2.38 illustrate the inter-storey drift recorded for a scaled accelerogram ( $\eta=5$ ). The maximum interstorey-drift, fixed by the benchmark organizers equal to 5‰, was reached at Level 2 both for the regular and irregular wall.

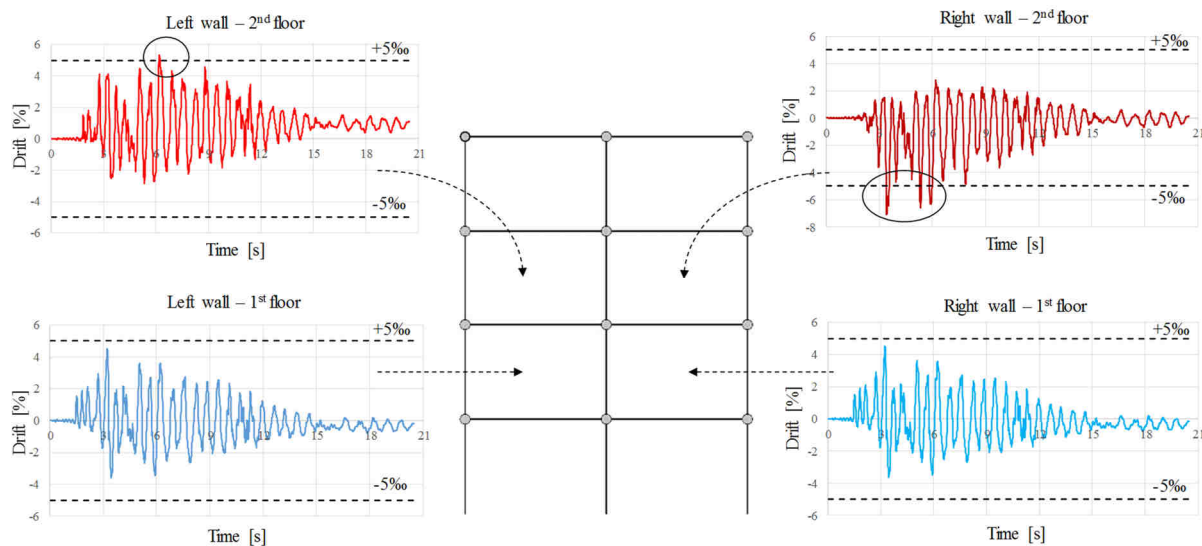


Figure 2.35: Regular wall: drift vs time curve for an accelerogram scaled of a value  $\eta=5$ .

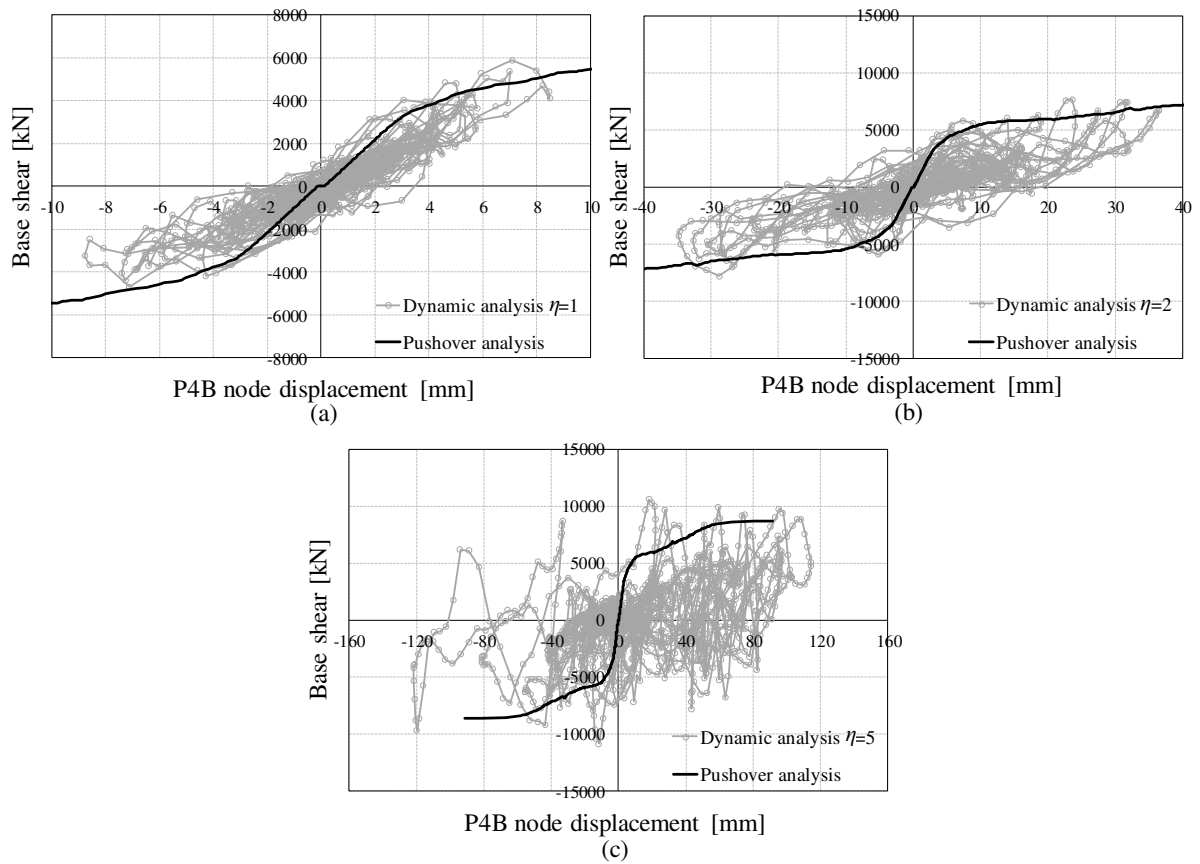


Figure 2.36: Irregular wall base shear-P4B node displacement for accelerogram multiplier equal to (a)  $\eta=1$ , (b)  $\eta=2$ , (c)  $\eta=5$ .

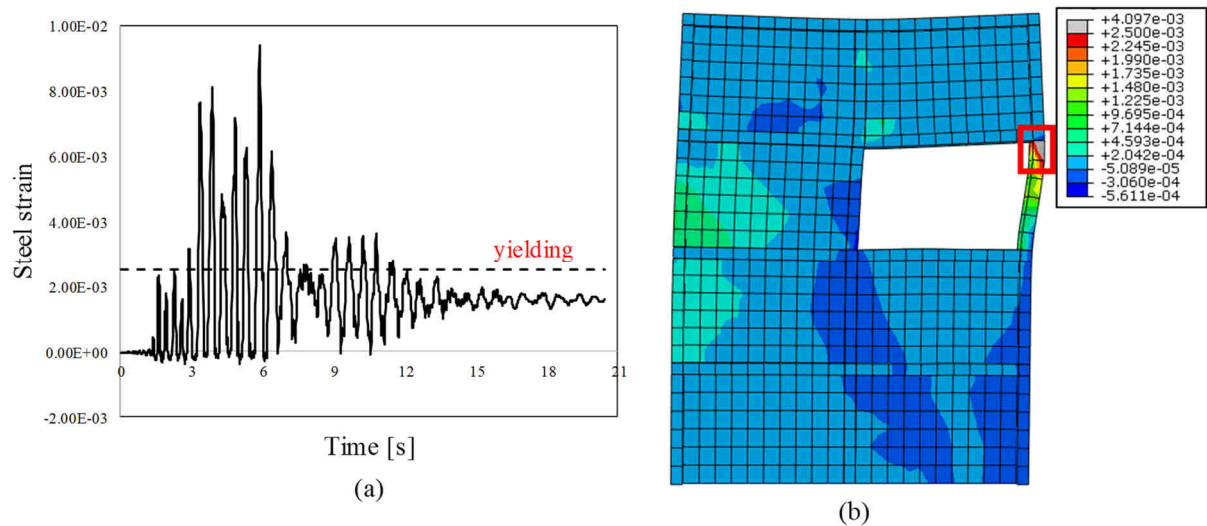


Figure 2.37: Irregular wall: (a) longitudinal reinforcement strains vs time curve for the highlighted element when a scaled factor of  $\eta=2$  is used; (b) longitudinal reinforcement strains at the maximum horizontal displacement occurring at 6 seconds.

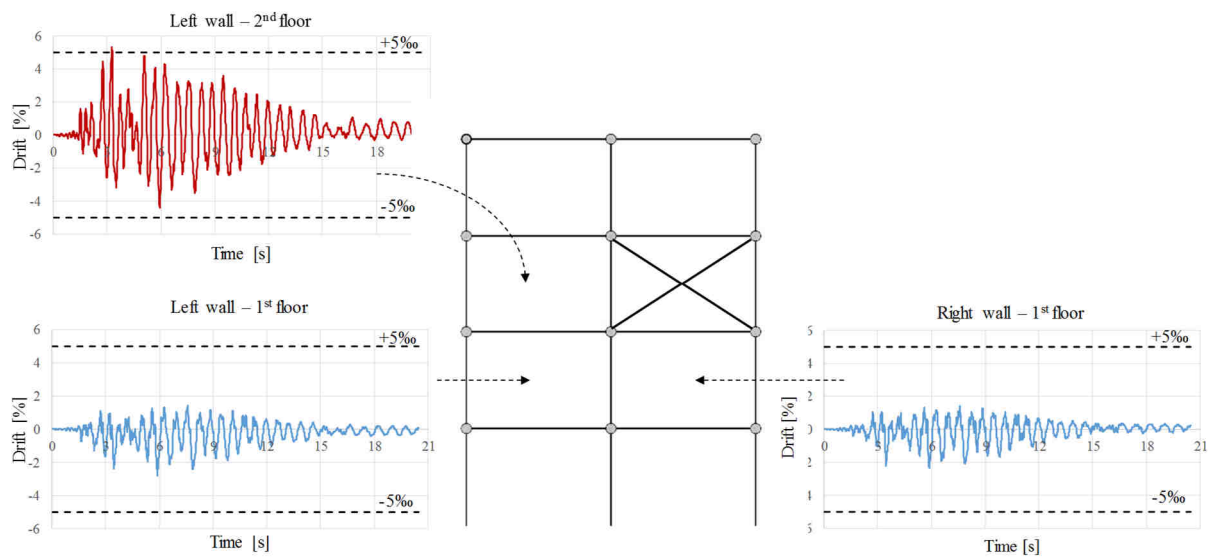


Figure 2.38: Irregular wall: drift vs time curve for an accelerogram scaled of a value  $\eta=5$ .

### 2.3.2.1 Diaphragm Effects

Stiffness, resistance, and ductility of RC multi-storey walls depends on diaphragm effects, which reduces free rotation of walls in correspondence of floors and wall-to-slab connections. From the past experimental research on a single storey slab-wall system (Pantazopoulou et al., 1992), it was observed that the shear wall-slab junction experienced large stress concentration under combined axial and cyclic lateral loading. Although various studies have been carried out on coupling action of the beam and floor slab in building with shear walls, the failure modes of shear wall-floor slab junction and their possible implications on the seismic design of walls have not been studied extensively. However, none of the past studies has focused on the detailed investigation of the behavior of floor slab and shear wall junction under earthquake shaking. Furthermore, the interaction between these two systems is usually ignored by designers for simplicity.

In order to consider the presence of the diaphragm, beams (1 meter width) have been introduced at each level by the organizer of CASH-phase 2 benchmark. Since these beams are free to deform, it is authors opinion that the stiffening effect provided by RC slabs at each level could be more pronounced than the stiffening effect provided by the modelled beams. Furthermore, the actual geometry of RC slabs, properly modelled, could lead to a different distribution of internal stresses on RC multi-storey walls. To maximize the stiffening effect provided by diaphragms, the regular wall has been modelled assuming a shear type behavior by preventing beam rotations. Even if the shear type static scheme is not representative of the



actual stiffening effect provided by diaphragms, it represents the opposite circumstance with respect to the modelling of the multi-storey wall carried out in the benchmark, where nodes are free to rotate in correspondence of floor, determining a cantilever static scheme for the analysed multi-storey wall. Since the detected non-linear behavior of the regular wall and the regular wall – Shear type are, as expected, very different, it means that the modelling of the actual geometry of the diaphragms deserves to be modelled in future development of this research.

Figure 2.39 shows the first mode deflected shape for the regular wall - shear type model having a natural frequency equal to 6.47 Hz much higher than the natural frequency of the regular wall analysed in the benchmark equal to 4.02 Hz. Considering the response spectrum illustrated in Figure 2.28, seismic actions applied to RC multi-storey walls could increase significantly if the stiffening effect provided by diaphragms is taken into account.

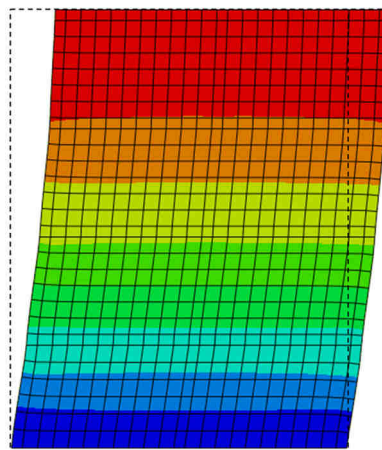


Figure 2.39: First mode deflected shape for the regular wall with shear type behaviour.

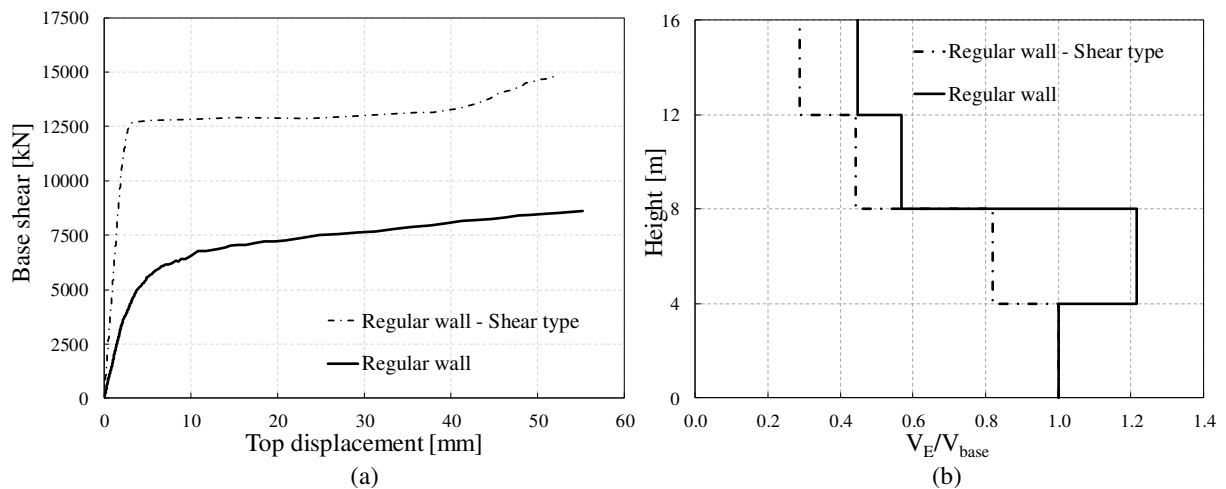


Figure 2.40: Comparison between pushover results obtained for regular wall and regular wall – Shear type models.

A pushover analysis has been carried out on the regular wall - shear type model by applying a first mode proportional distribution profile of horizontal forces characterized by a normalized force distribution equal to (0.35, 0.65, 0.87, 1).

Figure 2.40a shows the comparison between the shear base force vs top displacement curves obtained from the pushover analyses carried out on the regular wall and the regular wall - shear type model. Pushover curves are interrupted at the achievement of an interstorey-drift equal to 0.5%.

The crack pattern of the regular wall, illustrated in Figure 2.41, is governed by flexural mechanism, whereas at the contrary the crack pattern of the regular wall – Shear type model is governed by shear mechanisms. More specifically, for a horizontal displacement equal to 10 mm, Figure 2.41, the crack pattern is describing a shear mechanism of a squat wall at Level 1 limited by adjacent diaphragms. For horizontal displacement equal to 50 mm, Figure 2.41, the crack pattern is describing a shear mechanism of the entire wall governed by an inclined crack, formed perpendicularly to compressive stresses of the inclined strut, joining the top and left corner of the wall to the bottom right corner of the wall where the maximum value of compressive strain is achieved in concrete, Figure 2.41.

In Figure 2.41 it is also shown the contour plot of the horizontal reinforcement strain values. For a drift equal to 0.5% (critical value for nuclear power plants), corresponding to top displacement equal to 50mm, the yielding of the transversal reinforcement has been reached along the shear crack.

In conclusion:

- The response prediction of complex structures like a multi-storey wall with and without opening can be reliably obtained using NLFE tools both via pushover and incremental dynamic analyses.
- Considerable efforts are still needed to understand the behavior of seismic-resisting wall systems. Normative prescriptions are often based on a few experimental campaigns carried out on isolated elements. In order to better understand the non-linear behavior, numerical methods able to predict the response of seismic-resisting wall systems and their interaction with diaphragms and secondary structural elements are required hopefully supported by experimental evidence.
- Different hypotheses, used to simulate the presence of the RC slabs, lead to different failure mechanisms and distribution of strains in multi-storey walls. Future studies will be focalized on a more refined and realistic modelling of the diaphragm and wall-to-slab junction.

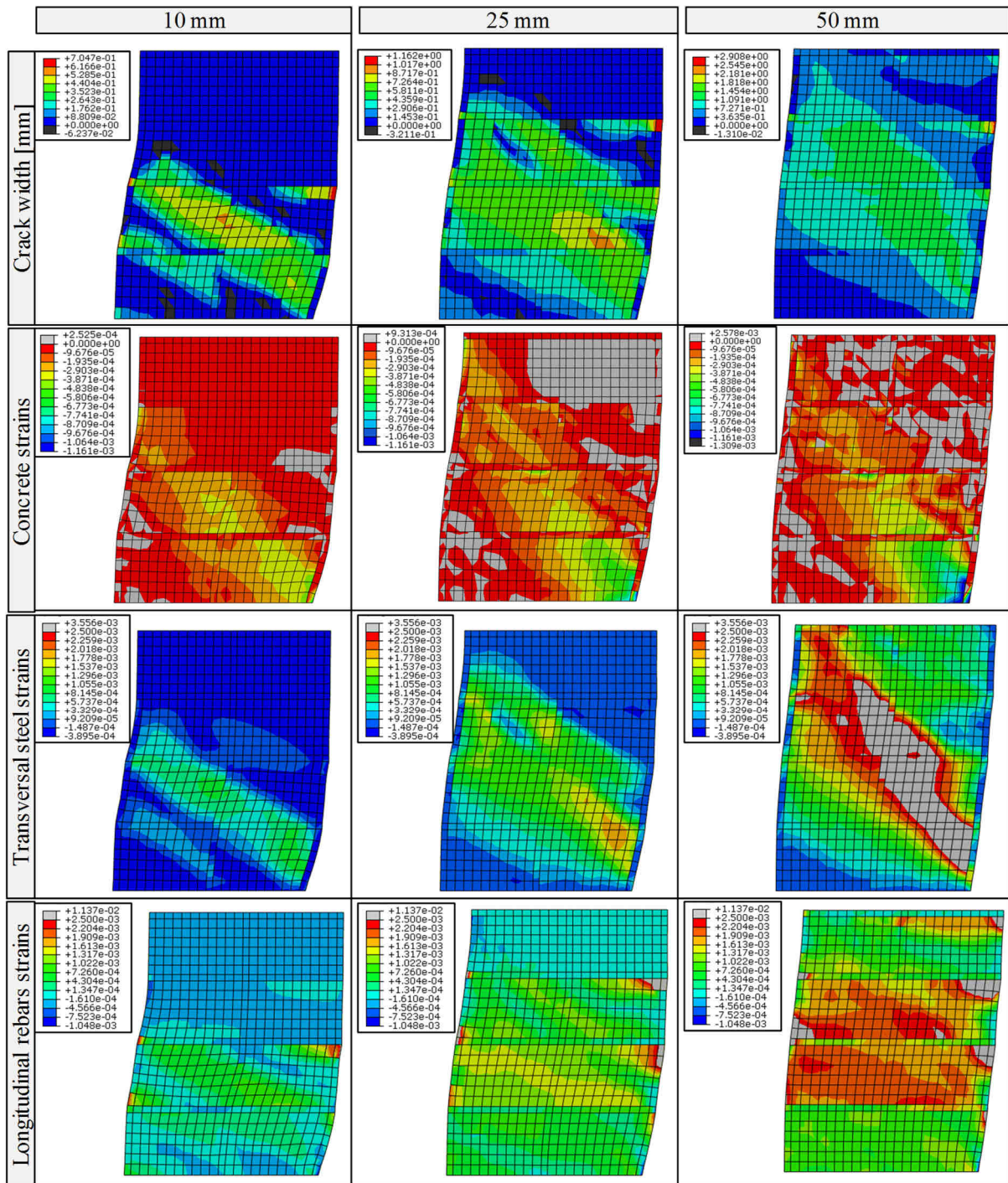


Figure 2.41: Contour plot for regular wall – Shear type.

### 2.3.3 Analyses of RC Deck Slabs of Hollow Box Bridges



Figure 2.42: Longitudinal view of the bridge.

Figure 2.42 shows a view of the typology of the viaduct analysed in this paragraph as case study. The dimensions and the reinforcement layout, assumed in this study, for the viaduct are not representative of a specific viaduct but representative of typical configurations of existing viaducts.

In the verification of bridges and viaducts, the longitudinal and transversal behavior are usually considered independent among them. Generally, concentrated loads are taken into account only in the verification of the cross section without considering the interaction between longitudinal moments and transverse shear resistance. The objective of this work, conducted with Ecole Polytechnique Fédérale de Lausanne, is to analyse the interaction between longitudinal bending moment and transverse shear strength.

The bridge has a 56.2m span, except for the first and last spans, which are 45 m long. The cross section and reinforcement details are reported in Figure 2.43. The bridge deck is characterized by a tapered section with thicknesses varying from 250mm to 400mm, whereas webs and bottom slab have constant thickness, respectively equal to 500mm and 600mm. The bridge deck is 11m wide, characterized by a 3.8m central top slab and two cantilevers 3.105m long. Table 2.4 reports the mean values of the mechanical properties.

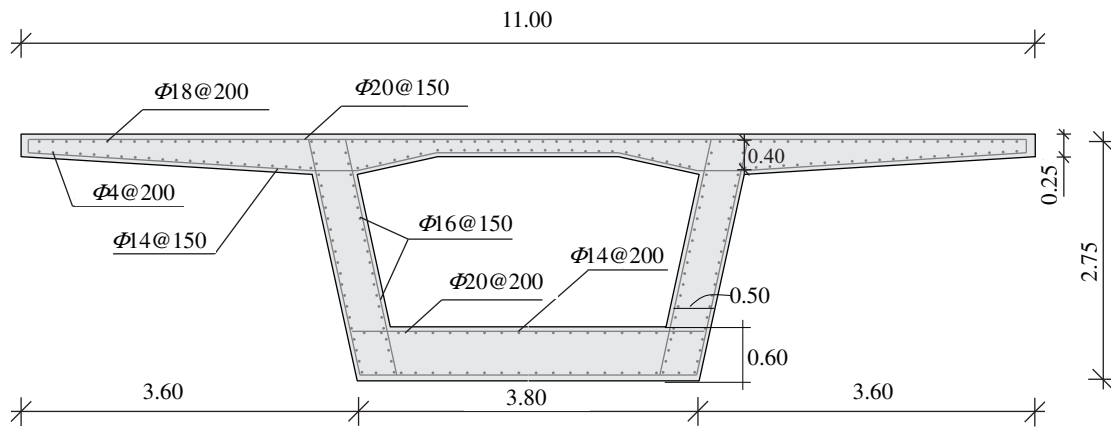


Figure 2.43: Transverse cross-section and reinforcement layout (dimensions in meters)

The shear resistance of the cantilever of the bridge deck has been evaluated considering the load case illustrated in Figure 2.44 (characterized by a distance  $a_v$  equal to  $2d$  which maximize the transversal shear at the web).

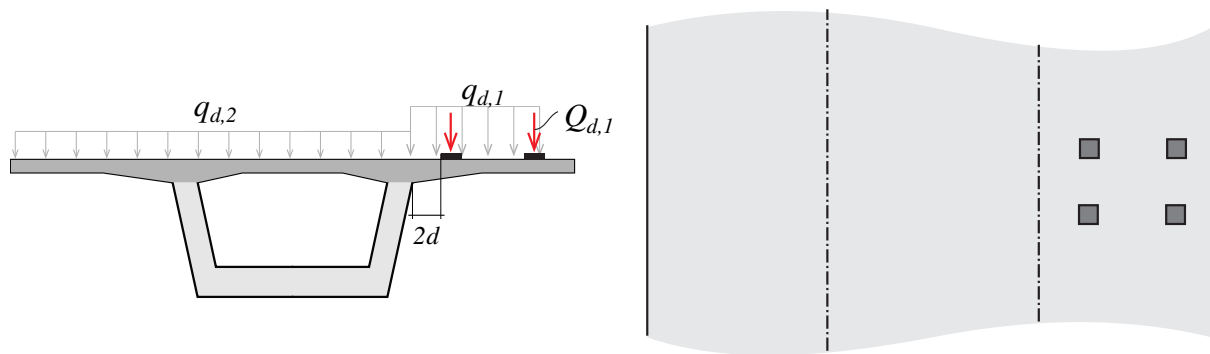


Figure 2.44: Loading arrangement according to EN 1991.

The interaction between longitudinal bending moment and transverse shear of the bridge deck has been accounted by applying a uniform profile of strains ranging from  $-0.3\text{‰}$  to  $+3.0\text{‰}$  along the bridge deck. The minimum compressive strain value corresponds to scenarios of maximum values of prestressing forces applied, whereas the maximum tensile strain value corresponds to yielding of longitudinal bars due to hogging moment occurring at supports of continuous span bridges.

Table 2.4: Mechanical properties of materials.

concrete					steel			
$f_c$	$E_c$	$f_t$	$G_f$	$G_c$	$f_y$	$f_u$	$E_s$	$E_h$
[MPa]	[MPa]	[MPa]	[Nmm/mm <sup>2</sup> ]	[Nmm/mm <sup>2</sup> ]	[MPa]	[MPa]	[MPa]	[MPa]
40	34130	3.02	0.142	35.45	550	687	210000	3678

The response prediction of the bridge deck has been evaluated using two different modelling strategies. In the first one, a portion of the bridge has been entirely modelled, Figure 2.45a, whereas in the second one, only the cantilever of the bridge deck has been modelled, Figure 2.45b.

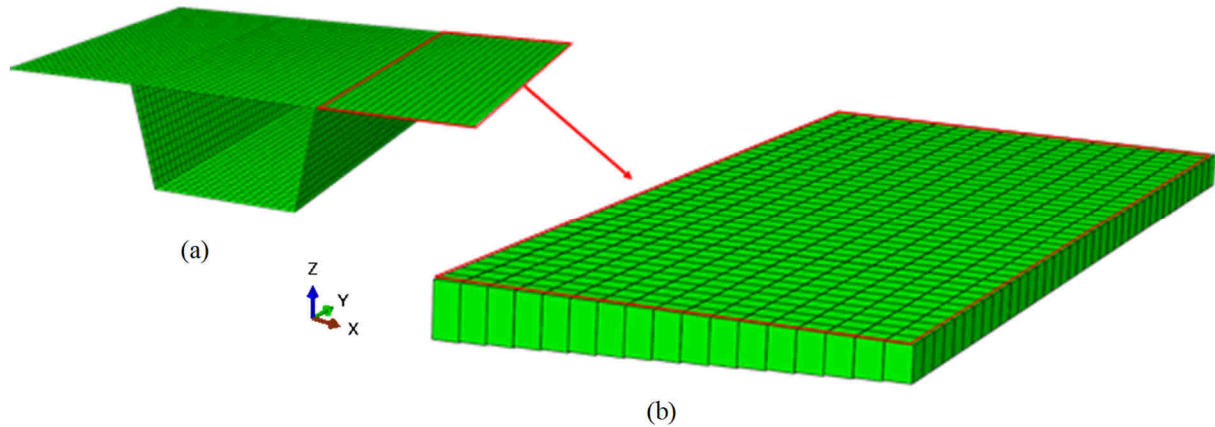


Figure 2.45: Modeling of (a) a portion of the bridge and (b) the cantilever.

In both cases, NLFEA has been carried out using multi-layered shell elements and the PARC\_CL 2.1 (Belletti et al., 2017<sup>a</sup>) crack model. Since PARC\_CL 2.1 crack model is suitable for plane stress analyses, the thickness of the slab is subdivided into layers. 7 layers have been used to model with good accuracy the position of longitudinal and transversal rebars at the top and bottom sides of the bridge deck. 4 Gauss integration points in the plane of eight-nodes shell element, and 3 Simpson integration points in the thickness of each layer have been adopted.

Since the adopted multi-layered shell elements are not able to predict the non-linear behaviour over the thickness of the slab, two post-processing approaches, based on the Critical Shear Crack Theory (Muttoni et al., 2008) and Model Code 2010 formulations (*fib*, 2013) have been used.

The symmetry of loading and boundary conditions has been exploited for both the modelling strategies by applying symmetric boundary conditions to one end, Figure 2.46.

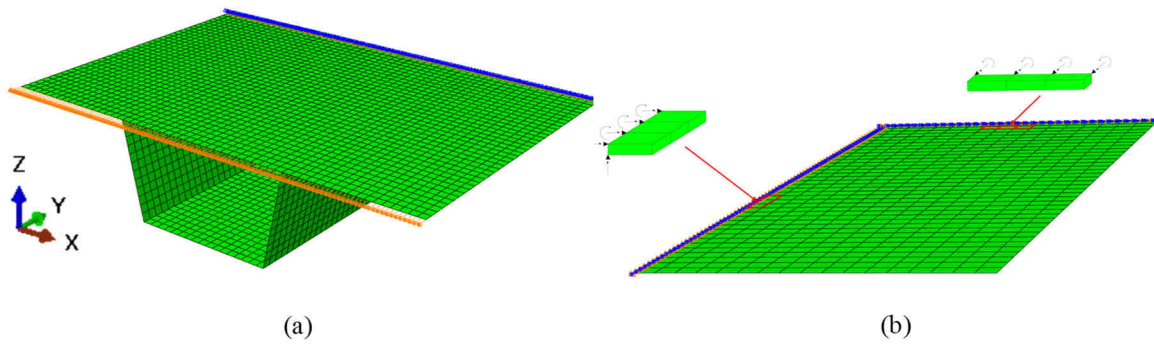


Figure 2.46: Boundary conditions applied to (a) a portion of the bridge and (b) the cantilever.

Therefore, compressive or tensile longitudinal strains have been imposed to the bridge deck in *load case 1* by applying longitudinal displacements to nodes of the opposite bridge deck end, Figure 2.47. Figure 2.47b shows that *load case 1* causes curvature of the transverse cross section in case of the modelling of the entire portion of the bridge that cannot be obviously observed in the case of the modeling of the cantilever. Therefore layers, subdividing the thickness of the bridge deck, will be subject to variable longitudinal strains along the thickness when the entire portion of the bridge is modelled whereas they will be subject to a constant value of longitudinal strains along the thickness when only the cantilever is modelled.

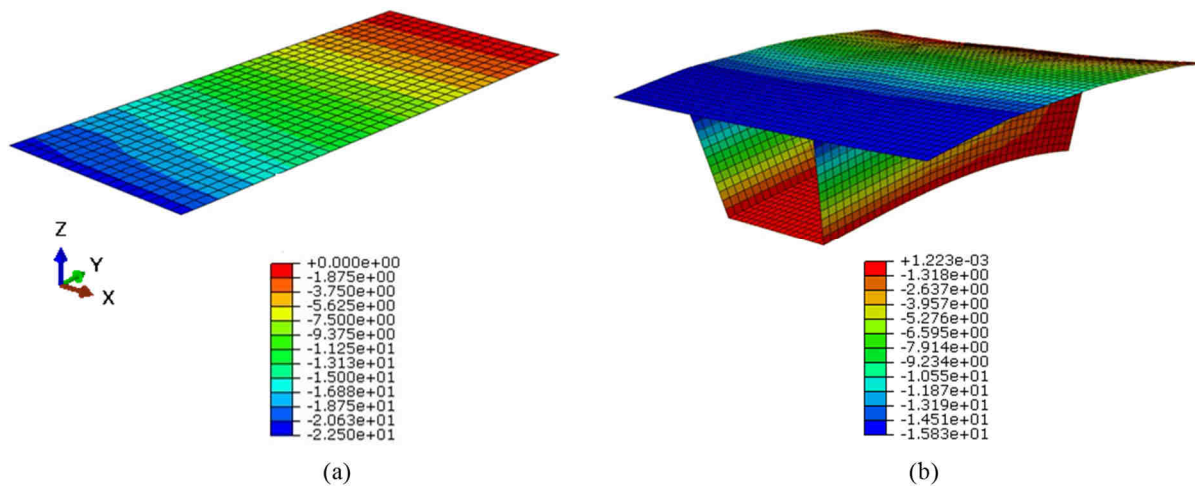


Figure 2.47: *Load case 1* for (a) the cantilever and (b) portion of the bridge.

*Load case 2* consisted in applying concentrated loads,  $Q$ , as pressure on the elements belonging to the loading areas having dimensions 0.4 m x 0.4 m (according to Load model 1 by EN 1991). Figure 2.48 shows *load case 2* applied to the modelled portion of the bridge. The same loading scheme has been applied to the cantilever.

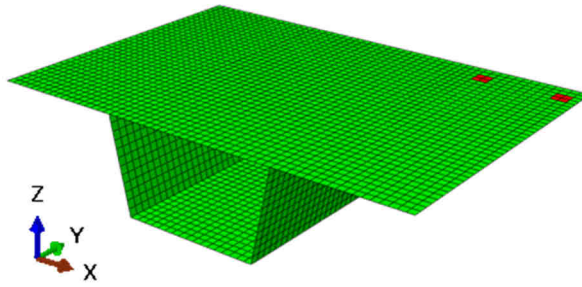


Figure 2.48: *Load case 2* applied to the modelled portion of the bridge.

The bridge deck response has been predicted with and without considering the geometrical non-linearity. The geometric non-linearity, which has to be set to evaluate membrane actions, is considered by adopting a Lagrangian formulation.

### 2.3.3.1 Evaluation of the Transverse Shear Resistance attributed to the Concrete

The transverse shear resistance of the bridge deck is evaluated according to Model Code 2010 (fib, 2013) and the Critical Shear Crack Theory (Natario et al., 2014).

#### 2.3.3.1.1 Model Code 2010

The shear resistance attributed to the concrete is calculated referring to the *control section* located at a distance equal to  $d$  from the face of supports having length  $b_{w2}$  or  $b_{w4}$  and effective depth,  $d$ , as illustrated in Figure 2.49. Table 2.5 reports all the geometrical quantities required for calculations.

Since the concentrated load is applied at a distance  $d < a_v \leq 2d$  from the edge of the support, an amplifier coefficient  $\beta$  for the design shear force,  $V_{Ed}$ , equal to 1 has been assumed. The design shear resistance of members without shear reinforcement,  $V_{Rm,c}$ , is given by Eq.(2.48):

$$V_{Rm,c} = k_v \frac{\sqrt{f_{cm}}}{\gamma_c} z b_w \quad (2.48)$$

where  $\gamma_c$  has been assumed equal to 1,  $z$  is the internal level arm, and  $b_w$  is the width of web. Coefficient  $k_v$  is calculated using Eq.(2.49) for Level of Approximation LoA II:

$$k_v = \frac{0.4}{1+1500\varepsilon_x} \cdot \frac{1300}{1000+k_{dg}z} \quad (2.49)$$

where  $\varepsilon_x$  is the axial strain,  $k_{dg}=32/(16+d_g) \geq 0.75$  with  $d_g$  equal to the maximum size of aggregate.



Table 2.5: Geometrical quantities at the critical section (in mm) and referred to Figure 2.49.

$h$	$d$	$c$	$a_v$	$z$	$b_{w2}=2a+b$	$b_{w4}=2c+b$
393.1	333.1	50	680	299.8	7080	3080

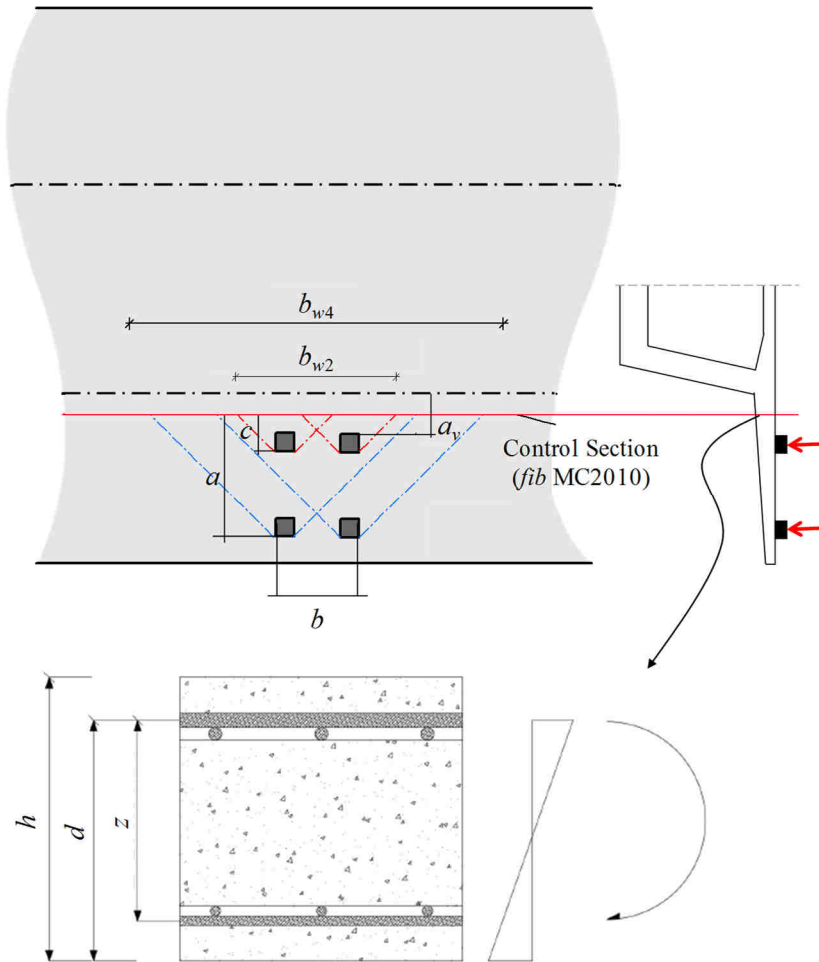


Figure 2.49: Geometrical quantities adopted for the transverse shear resistance evaluation (dimensions in meters).

Shear resistance according to LoA IV has been obtained by NLFEA results. Since the presented shell modelling approach cannot detect shear failures along the thickness of the bridge deck, a post-processing method of NLFE results has been carried out, Figure 2.51a. More specifically, the shear resistance per unit length,  $v_{Rm,c}$ , can be achieved at the intersection of the failure envelope given by Eq.(2.50) with the NLFEA curve, relating the shear stress values (averaged along the effective length), Figure 2.50a, to the mid-depth strain, calculated as shown in Figure 2.50b.

$$v_{Rm,c} = k_v \frac{\sqrt{f_{cm}}}{\gamma_c} z \quad (2.50)$$

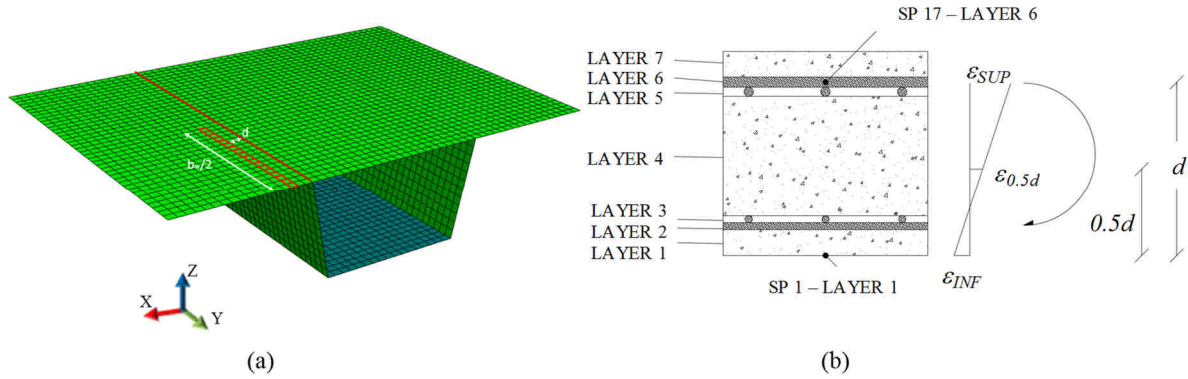


Figure 2.50: (a) Effective length for averaging shear stresses and (b) mid-depth strain.

### 2.3.3.1.2 Critical Shear Crack Theory

The Critical Shear Crack Theory (CSCT) allows determining the shear strength of slender one or two – way slabs on the basis of the opening of the critical shear crack (Muttoni et al., 2008). Muttoni et al. (2008) proposed a failure criterion in terms of one – way shear that estimates the maximum shear force for a given critical crack width. Such a parameter can be assumed proportional to the product of a reference longitudinal strain  $\epsilon$  times the effective depth  $d$ . CSCT formulation evaluates the shear strength in the critical section at  $0.5d$  from the point of maximum acting moment, Figure 2.50b. The reference longitudinal strain is assessed at  $0.6d$  from the outer compressive fibre considering a linear elastic behavior of concrete in compression, neglecting concrete tensile strength. Hence, taking into account the effects of the critical shear crack width, the aggregate size  $d_g$  and the concrete compressive strength  $f_c$ , the failure criterion is described by Eq.(2.51):

$$v_c(\epsilon) = \frac{d\sqrt{f_c}}{3} \frac{1}{1 + \frac{120 \cdot \epsilon \cdot d}{16 + d_g}} \quad (2.51)$$

The longitudinal strain  $\epsilon$  and the  $c_{flex}$  are defined by Eq.(2.52) and (2.53):

$$\epsilon = \frac{m}{d \cdot \rho \cdot E_s \left( d - \frac{c_{flex}}{3} \right)} \frac{0.6d - c_{flex}}{d - c_{flex}} \quad (2.52)$$

$$c_{flex} = d\rho \frac{E_s}{E_c} \sqrt{1 + \frac{2E_c}{\rho E_s}} - 1 \quad (2.53)$$

Experimental outcomes carried out by Natario et al. (2014) show for linearly supported slabs under concentrated loads clear and rather significant redistributions of the reactions.

Redistributions occur not only due to bending cracks but also for the development of the inclined shear cracks. Indeed, as the level of applied load increases, the reaction in the region close to the load enhances at a slower rate because load starts to be transferred to the adjacent regions, which are less affected by the shear crack. To account for this distribution of internal forces, a unitary average shear stress  $v_{avg,4d}$  is calculated along a distance  $4d$  from unitary shear stresses obtained by NLFEA. The reference longitudinal strain  $\varepsilon$  is calculated in correspondence of the maximum unitary acting moment  $m$ . Then, it is calculated the parameter  $k$ , as the ratio of the acting moment  $m_i$  to the average unitary shear  $v_{avg,4d}$  (both of them evaluated in the critical section). Hence, the ultimate shear failure value  $V_R$  is evaluated following an iterative procedure at the intersection with the failure criterion of Eq.(2.51). The main results are presented in Figure 2.51b.

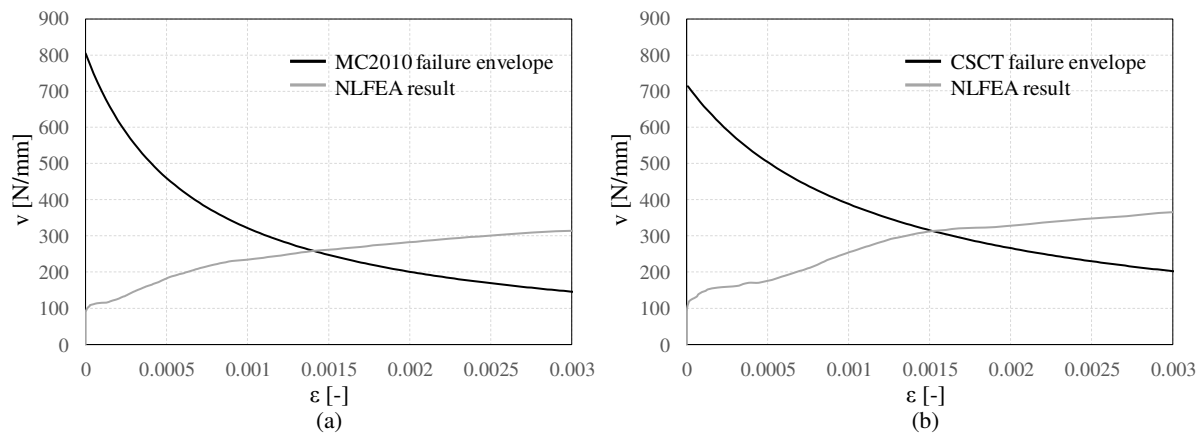


Figure 2.51: Shear resistance evaluation according to LoA IV and failure envelope evaluated using a) Model Code 2010 (*fib*, 2013) formulations and b) CSCT (Muttoni et al., 2008).

Table 2.6: Transverse shear resistance.

<i>fib</i> MC2010		CSCT
LoA II (kN)	LoA IV (kN)	LoA IV (kN)
1649.93	2054.57	1583.51

Table 2.6 reports the comparisons between transverse shear resistance values obtained using the previously explained approaches without considering longitudinal strains applied to the bridge deck, therefore without considering longitudinal moments applied to the bridge section.

### 2.3.3.2 Interaction between Longitudinal Bending Moment and Transverse Shear Strength

Parametric analyses have been carried out to investigate the interaction between longitudinal moment and transverse shear resistance by imposing longitudinal strains to bridge decks. Longitudinal strain values are ranging from compressive strain values due to self-weight and prestressing forces to tensile strain values corresponding to yielding of longitudinal bars due to hogging moment at supports of continuous span bridges. Therefore, the parametric analyses have been carried out by imposing longitudinal strain values equal to  $-0.3‰$ ,  $-0.2‰$ ,  $-0.1‰$ ,  $0.0‰$ ,  $+0.5‰$ ,  $+1.0‰$ ,  $+1.5‰$ ,  $+2.0‰$ ,  $+2.5‰$ ,  $+3.0‰$ .

Figure 2.52a and Figure 2.52b, together with Table 2.7, report the transverse shear resistances attributed to concrete against the applied longitudinal strain values evaluated, respectively, according to Model Code 2010 (*fib*, 2013) and CSCT failure criterion together with analytical calculations, which are neglecting the effects of longitudinal moments.

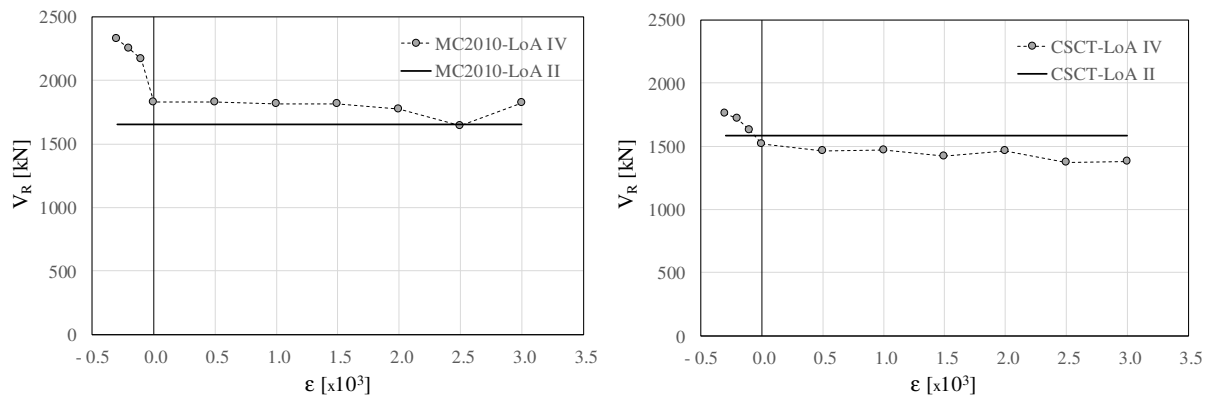


Figure 2.52: Transverse shear resistances values with respect to applied longitudinal strain.

Table 2.8 reports the corresponding maximum values of the resultant force of the load model that can be applied to the bridge deck. It results in an average increment, due to compressive strain applied to the bridge deck, equal to 20% using Model Code 2010 (*fib*, 2013) failure envelope and 11% using CSCT failure envelope. Moreover, an average decrease due to tensile strain equal to 11% using Model Code 2010 (*fib*, 2013) failure envelope and 25% using CSCT failure envelope have been obtained.

Therefore, the resultant force of tandem system assessment carried out by neglecting the effects of the longitudinal bending moment could be non-conservative.

The main reason for the interaction between longitudinal bending moment and transverse shear resistance can be attributed to the reduction or increment of compressive strength of

concrete due to the multi-axial state of stresses. Indeed, the cracking induced by the imposed longitudinal tensile strain causes a reduction of compressive strength of concrete (when the transverse bending behavior is observed) and therefore higher values of axial strains at mid-depth of the transverse cross section, Figure 2.53. Since the shear failure criterion attributed to concrete is dependent on axial strains at mid-depth of the transvers cross section, it results in a lower transvers shear resistance. On the other hand, when compressive strains are imposed, the confining effects increase the compressive strength of concrete and provide positive effects to the non-linear transverse behavior.

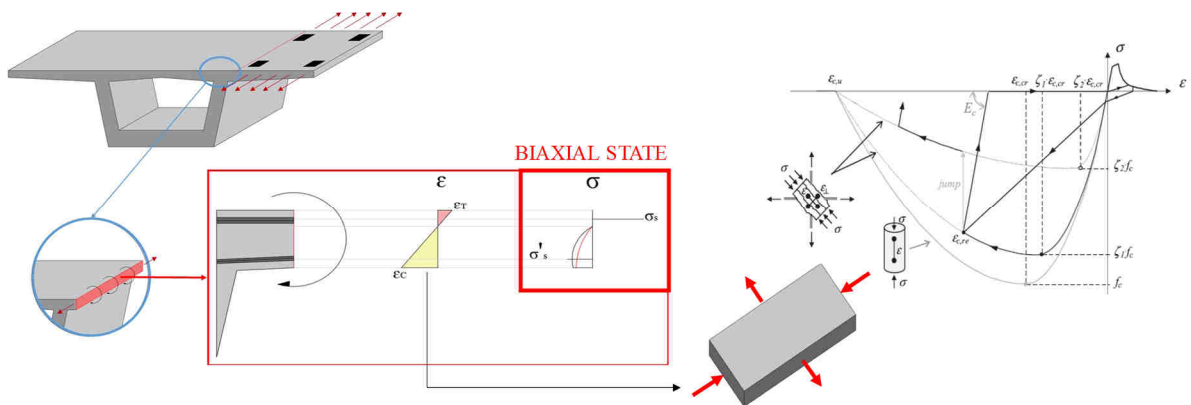


Figure 2.53: The cracking induced by the imposed longitudinal tensile strain causes a reduction of compressive strength of concrete.

Table 2.7: Transverse shear resistance values.

	$\epsilon$	Compressive strain			0	Tensile strain					
		-0.3‰	-0.2‰	-0.1‰		+0.5‰	+1‰	1.5‰	+2.0‰	+2.5‰	+3‰
Model Code 2010 - LoA IV	$V_{Rd}$ [kN]	2324.36	2253.56	2166.48	1828.76	1826.64	1816.02	1812.48	1776.46	1641.14	1819.56
CSCCT - LoA IV	$V_{Rd}$ [kN]	1758.22	1719.47	1625.02	1517.98	1464.21	1467.6	1424.01	1462.76	1375.58	1380.42

Table 2.8: Maximum values of external forces applied to the bridge deck.

	$\epsilon$	Compressive strain			0	Tensile strain					
		-0.3‰	-0.2‰	-0.1‰		+0.5‰	+1‰	1.5‰	+2.0‰	+2.5‰	+3‰
Model Code 2010 - LoA IV	$Q_{est}$ [kN]	2531.83	2500.07	2423.18	2054.57	1833.95	1805.94	1803.15	1818.67	1840.03	1816.53
CSCCT - LoA IV	$Q_{est}$ [kN]	1760.64	1763.86	1790.19	1583.51	1204.07	1196.49	1204.76	1173.02	1205.14	1106.42

Figure 2.54 reports the comparison between the transverse shear resistance values obtained from the portion of the bridge and cantilever modelling. Since longitudinal strains imposed to bridge deck cause inflections of the portion of the bridge modelling (Figure 2.47a), layers used to subdivide the slab thickness are subjected to different values of longitudinal and transverse strains. At the contrary, a constant value of longitudinal strain is imposed on the cantilever. Therefore, the transverse shear resistance obtained with the bridge modelling results lower than

the shear resistance obtained with the cantilever modelling. So, the modelling of the cantilever results non-conservative for this study.

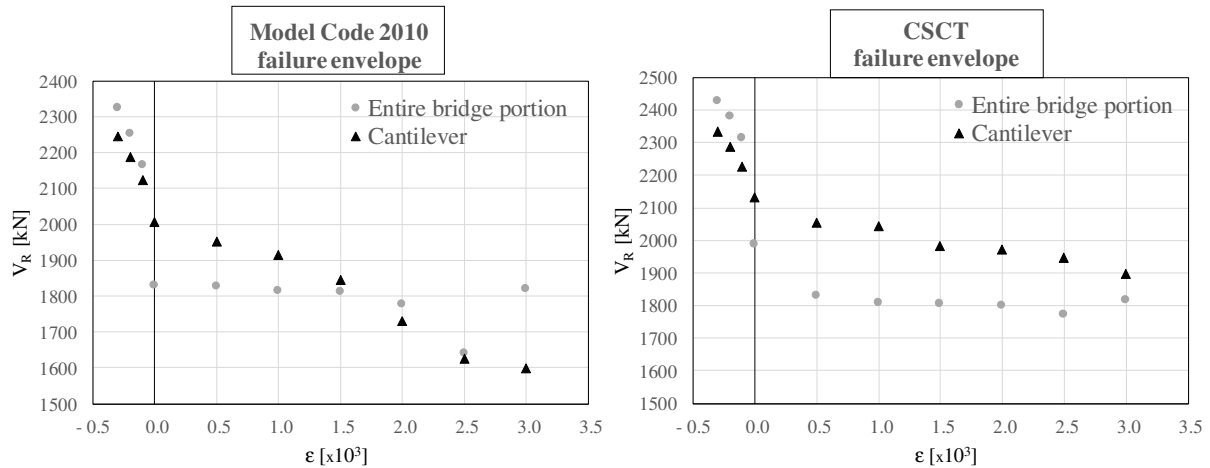


Figure 2.54: Transverse shear resistance values obtained from the portion of the bridge and cantilever modelling.

From Figure 2.55 it can be appreciated how membrane action effects can affect the transverse shear resistance assessment. Indeed, it is well known that when geometrical non-linearity and second order effects are considered, positive effects due to membrane action can be exploited.

In conclusion:

- the resultant force of tandem system assessment carried out by neglecting the effects of the longitudinal bending moment could be non-conservative;
- the modelling of an entire portion of the bridge results more conservative than the modelling of the cantilever, only for transverse shear resistance verifications;
- membrane action can play an important role in the transverse shear resistance assessment;
- future studies will be carried out with different values of transverse reinforcement ratios.

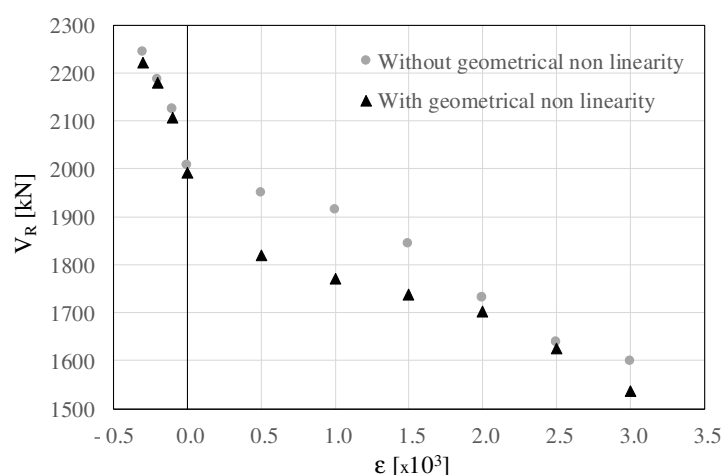


Figure 2.55: Membrane action effects on the transverse shear resistance assessment for the cantilever modelling.

## 2.4 Concluding Remarks

In this chapter the basic formulation of the PARC\_CL 2.1 model was presented and validated by means of simulation of different RC structural members

The PARC\_CL 2.1 crack model was primarily validated by means of comparison with experimental tests on simple RC panels carried out at the University of Houston (Mansour and Hsu, 2005). Furthermore, in order to verify the aggregate interlock law implemented in the PARC\_CL 2.1 model, the results obtained with the PARC\_CL 2.1 are compared to those obtained with the commercial software DIANA 10.0.

Subsequently, the PARC\_CL 2.1 was applied to more complex structural members, such as RC walls and deck slabs.

It has been demonstrated, through comparison with experimental tests, that the PARC\_CL 2.1 model is able of providing reasonably accurate predictions of the non-linear response of RC members subjected to cyclic and dynamic loading. In fact, thanks to the tangent approach is possible to take into account plastic strains.

It is in the author' opinion that the non-linear shell and membrane modeling using the PARC\_CL 2.1 crack model may be a powerful tool for the assessment of both local and global damage indicators (like crack width and displacements) which are strongly relevant in the seismic performances of RC structures.

The powerful of a self-implemented model is the chance, with respect to the standard models available in the libraries of the commercial finite element software products, to evaluate

for several mechanical phenomena in order to achieve a more refined response of the structural member.

New contributions, aimed to apply the PARC\_CL 2.1 to more generalized case studies, will be presented in the next chapters.

## 2.5 References

- Abaqus 6.12* (2012). User's and theory manuals; 2012 <<http://www.3ds.com/>> [1 June 2016].
- Bazant ZP.* (2002). Concrete fracture models: testing and practice. *Eng Fract Mech*, 69:165–205.
- Belletti B., Cerioni R., Iori I.* (2001). Physical approach for reinforced-concrete (PARC)membrane elements. *ASCE J Struct Eng*;127(12):1412–26.
- Belletti B., Esposito R., Walraven J.* (2013<sup>a</sup>). Shear Capacity of Normal, Lightweight, and High-Strength Concrete Beams according to ModelCode 2010. II: Experimental Results versus Nonlinear Finite Element Program Results. *ASCE Journal Of Structural Engineering*, 139(9), pp. 1600-1607.
- Belletti B., Damoni C., Gasperi A.* (2013<sup>b</sup>). Modeling approaches suitable for pushover analyses of RC structural wall buildings. *Eng Struct* 2013;57(12):327–38.
- Belletti B., Damoni C., den Uijl J.A, Hendriks M.A.N, Walraven J.C.* (2013<sup>c</sup>). Shear resistance evaluation of prestressed concrete bridge beams: fib Model Code 2010 guidelines for Level IV approximations. *Structural concrete*, 14(3): 242-249.
- Belletti B., Damoni C., Scolari M., Stocchi A.* (2014<sup>a</sup>). Simulation of RC walls seismic behaviour with shell elements and PARC\_CL modelling. 2ECEES, Istanbul(Turkey). August 25–29.
- Belletti B., Damoni C., Hendriks M.A.N, De Boer A.* (2014<sup>b</sup>) Analytical and numerical evaluation of the design shear resistance of reinforced concrete slabs. *Structural Concrete*, 15(3): 317-330.



- 
- Belletti B., Scolari M., Vecchi F.* (2017<sup>a</sup>). PARC\_CL 2.0 crack model for NLFEA of reinforced concrete structures under cyclic loadings. *Comput and Struct*; 199:165–79.
- Belletti B., Stocchi A., Scolari M., Vecchi F.* (2017<sup>b</sup>). Validation of the PARC\_CL 2.0 crack model for the assessment of the nonlinear behaviour of RC structures subjected to seismic action: SMART 2013 shaking table test simulation. *Engineering Structures*, 150:759-773.
- Belytschko T., Fish J., Engelmann B.E.* (1988). A finite element with embedded localization zones. *Computer Methods in Applied Mechanics and Engineering*, 70(1): 59-89.
- Cervenka V., Gerstle K.H.* (1972). Inelastic analysis of reinforced concrete panels: Experimental verification and application, IABSE Publications, 32-II:25-39.
- Cervenka V., Gerstle K.H.* (1971). Inelastic analysis of reinforced concrete panels: Theory, IABSE Publications, 31-II:32-45.
- Comité Euro-International du Béton and Fédération Internationale de la Précontrainte (CEB-FIP).* CEB-FIP Model Code 1990 (MC90), Bulletin d'information 213 and 214. London: Thomas Telford; 1993.
- Cornelissen H.A.W., Hordijk D.A., Reinhardt H.W.* (1986). Experimental determination of crack softening characteristics of normalweight and lightweight concrete. *Heron* 1986; 31:2.
- Damoni C., Belletti B., Esposito R.* (2014). Numerical prediction of the response of a squat shear wall subjected to monotonic loading. *Euro J Environ Civil Eng*;18(7):754–69.
- de Borst R.* (2002). Fracture in quasi-brittle materials: a review of continuum damage-based approaches. *Eng Fract Mech*; 69:95–112.
- Dias-da-Costa D., Alfaiate J., Sluys L.J., Júlio E.* (2009). A discrete strong discontinuity approach. *Engineering Fracture Mechanics*, 76(9):1176-1201.
- Dvorkin E., Cuiñiño A., Gioia G.* (1990). Finite elements with displacement interpolated embedded localization lines insensitive to mesh size and distortions. *International Journal for Numerical Methods in Engineering*, 30:541-564.

- Feenstra P.H.* (1993). Computational aspects of biaxial stress in plain and reinforced concrete [Ph.D. thesis]. Delft University of Technology.
- fib* – International federation for structural concrete. fib model code for concrete structures 2010. 431 Ernst & Sohn; 434 p.
- Gambarova P.G.* (1983). Sulla trasmissione del taglio in elementi bidimensionali piani di c.a. fessurati. In: Proceedings of Giornate AICAP; p. 141–56 [in Italian].
- Gomes A., Appleton J.* (1997). Nonlinear cyclic stress-strain relationship of reinforcing bars including buckling. *Eng Struct*; 19(10):822–6.
- Gopalaratnam V.S., Shah S.P.* (1985). Softening response of plain concrete in direct tension. *J Am Concr Inst* 1985;82(3):310–23.
- He W., Wu Y-F, Liew K.M.* (2008). A fracture energy based constitutive model for the analysis of reinforced concrete structures under cyclic loading. *Comput Meth Appl Mech Eng* 2008; 197:4745–62.
- Hendriks M.A.N., Uijl J.A., De Boer A., Feenstra P.H., Belletti B., Damoni C.* (2012). Guidelines for nonlinear finite element analyses of concrete structures. Rijkswaterstaat Technisch Document (RTD), Rijkswaterstaat Centre for Infrastructure, RTD 2012;1016:2012.
- Hsu T.C., Mo Y.L.* (2010). Unified theory of concrete structures. Wiley (editor); 2010.
- Kaushik S.* (2017). Influence of floor slab on seismic design of rectangular structural wall in RC frame-wall buildings. Ph.D. thesis, Indian institute of technology Guwahati.
- Manie J.* (2015). DIANA User's manual, Release 10. TNO DIANA.
- Mansour M, Hsu TTC.* (2005). Behavior of reinforced concrete elements under cyclic shear. II: theoretical model. *J Struct Eng, ASCE* 2005;131:44–53.
- Menegotto M, Pinto P.E.* (1973). Method of analysis for cyclically loaded R.C. plane frames including changes in geometry and non-elastic behaviour of elements under combined normal force and bending, Symposium on the Resistance and Ultimate Deformability of

Structures Acted on by Well Defined Repeated Loads. Lisbon (Portugal): International Association for Bridge and Structural Engineering (ABSE).

*Muttoni A., Fernández Ruiz M.* (2008). Shear strength of members without transverse reinforcement as function of critical shear crack width, *ACI Structural Journal*. 2008; 105(2):163 – 72.

N005\_A469\_2014\_EDF\_B. THECNICAL REPORT. Presentation of the cash benchmarck phase 2. <http://benchmark-cash.org/>

*Nakamura H, Higai T.* (2001). Compressive fracture energy and fracture zone length of concrete. In: Shing Benson P, editor. ASCE; 2001. p. 471–87.

*Natario F., Muttoni A. and Fernández Ruiz M.* (2014). Shear strength of RC slabs under concentrated loads near clamped linear supports, *Engineering Structures*. 2014; 76: 10 – 23.

*Okamura H., Maekawa K.* (1991). Nonlinear analysis and constitutive models of reinforced concrete. Tokyo (Japan): Gihodo-Shuppan Press.

*Palermo D., Vecchio F.J.* (2004). Compression field modeling of reinforced concrete subjected to reverse loading: verification. *ACI Struct J* 2004;101(2):155–64.

*Pang X., Hsu T.T.C.* (1995). Behavior of reinforced concrete membrane element shear. *ACI Struct J* 1995;92(6):665–79.

*Pantazopoulou S., Imran I.* (1992). Slab-Wall Connections Under Lateral Forces. *Structural Journal* 1992, 89(5):515-527.

*Paulay T., Taylor R.G.* (1981). Slab coupling of earthquake-resisting shear wall. *ACI Structural Journal*, 78(2):130-140.

*Qadeer A., Smith B.S.* (1969). The bending stiffness of slabs connecting shear walls. *ACI Structural Journal*, 66(6):464-473.

*Rashid Y.R.* (1968). Analysis of prestressed concrete pressure vessels. *Nuclear Engineering and Design* 7:334-344.

- Rots J.G., Blaauwendraad J.* (1989). Crack models for concrete: discrete or smeared? Fixed, multi-directional or rotating? HERON 1989;34(1):1–59.
- Saouma V.E., Ingraffea A.R.* (1981). Fracture Mechanics Analysis of discrete cracking, IABSE Colloquium on "Advanced Mechanics of Reinforced Concrete", Delft, 1981, pp. 413-436.
- Sittipunt W., Wood S.L.* (1995). Influence of web reinforcement on the cyclic response of structural walls. ACI Struct J 1995;92(6):745–56.
- Stevens N.J., Uzumeri S.M., Collins M.P.* (1991). Reinforced concrete subjected to reversed cyclic shear-experiments and constitutive model. ACI Struct J; 88(2):135–46.
- Yankelevsky D.Z., Reinhardt H.W.* (1987). Response of plain concrete to cyclic tension. ACI Mater J; 84(5):365–73.
- Vecchio F.J., Collins M.P.* (1993). Compression response of cracked reinforced concrete. ASCE J Struct Eng; 119(12):3590–610

# Shrinkage Effect in the PARC\_CL 2.1 Crack Model

---

# 3

It is well-known that concrete is a brittle material which cracks when the tensile stresses exceed the tensile strength of the material. Cracking in concrete can be a consequence of different contributions like thermal contraction, large differential temperatures within the concrete body, external or internal restraints, too large deformations, applied loads but, one of the most common reasons is shrinkage. Concrete is particularly prone to cracking at a very young age. Early-age cracking due to shrinkage can present a significant problem in concrete because the tensile strength of the material is still developing. In the meantime, volume changes are already taking place due to the combined effect of heat of hydration, the binder hydrating and the outer surfaces drying out. Restrained volume changes drive tensile stress development.

Another important question is related to RC members, where the presence of embedded reinforcement produces a restraining of concrete shrinkage, affecting the cracking resistance of structural elements, as well as their deformations even under short-term loading (Bischoff, 2001; Scanlon et al., 2008).

Nevertheless, in the design of RC members, creep and shrinkage effects are usually taken into account for the evaluation of long-term deflections and pre-stress losses, whereas on short-term response are often neglected (Gilbert, 2001; Gribniak et al., 2013). The phenomena of shrinkage and creep are linked: some models take this interdependence into account (Bažant and Baweja, 2000), whereas others assume that the two terms are independent and overlapped (Gilbert, 1988).

Eurocode 2 (1992) and Model Code 2010 (*fib*, 2013) provide analytical formulations for the evaluation of the average shrinkage deformation. These formulations are easy to use and, in general, assure the achievement of safety conditions. However, they are not always able to catch all the phenomena that involve the material in the non-linear phase, and they are not representative of the physical reality of the phenomenon.

The cracking of concrete may severely affect the durability performance and service life of structures since it contributes to the corrosion of the reinforcement, it aggravates freeze-thaw cycles, resulting in quick deterioration, and facilitates alkali-aggregate reactivity. Severe cracking often calls for costly measures to fix. As a result, research aiming at the prevention of shrinkage cracking and predicting early-age cracking risk has been on the rise (Holt, 2001; Holt and Leivo, 2004; Tongaroonsri, 2009).

In terms of NLFEA, a proper numerical modelling able to consider the shrinkage effect and able to avoid inaccurate predictions of structural performances at serviceability conditions is needed. To this aim, concrete shrinkage can be explicitly considered by treating it as a prescribed deformation or as a fictitious force in the analyses (Maekawa et al., 2006; Luo et al., 2015).

In this chapter, the shrinkage formulation implemented in PARC\_CL 2.1 model is presented, and the effectiveness of the proposed procedure is verified herein through the modelling of tensile members.

### 3.1 Shrinkage Effect on a Uniaxial Tension Member

For an uncracked and unreinforced concrete section, shrinkage would cause a free shortening equal to  $\varepsilon_{sh} \Delta x$ , Figure 3.1a (where  $\varepsilon_{sh}$  is the free shrinkage strain of the concrete). If reinforcement is provided, it restrains the free shrinkage of concrete, Figure 3.1b. The reinforcement would be subjected to a compressive force  $E_s \varepsilon_s A_s$  while an opposite tensile force would be applied to the concrete (denoted as  $\Delta T$  in Figure 3.1b). Due to this restraint to shrinkage, the shortening of the section changes  $\varepsilon_{sh,0} \cdot \Delta x$ . The value of the initial strain  $\varepsilon_{sh,0}$  is determined in Eq.(3.1) and it is less than  $\varepsilon_{sh}$  (Bischoff, 2001).

$$\varepsilon_{sh,0} = \varepsilon_{sh} \frac{1}{1 + \rho n} \quad (3.1)$$

where  $n = E_s / E_c$ .

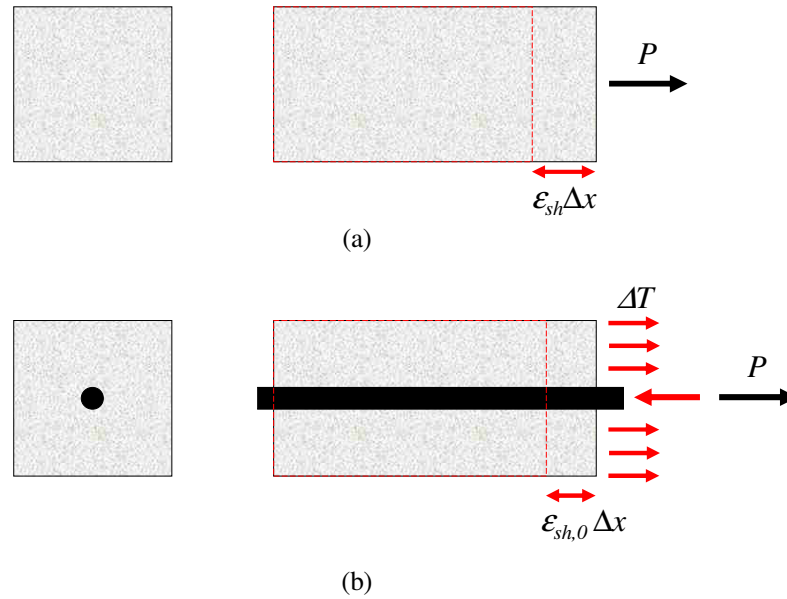


Figure 3.1: Shrinkage effect on (a) unreinforced element; (b) tension member.

Bischoff (2001) proposed to consider the initial uncracked member response by including the free shrinkage strain,  $\epsilon_{sh}$ , of the concrete as part of the relationship for the total concrete strain  $\epsilon_c$ , Eq.(3.2); whereas for the reinforcement is given by Eq.(3.3).

$$\epsilon_m = \epsilon_c = \epsilon_{cf} - \epsilon_{sh} \quad (3.2)$$

$$\epsilon_m = \epsilon_s = \epsilon_{sf} \quad (3.3)$$

where  $\epsilon_{cf}$  is the concrete strain caused by stress, equal to  $\sigma_c / E_c$  before cracking (i.e.  $\sigma_c < f_t$ ), and  $\epsilon_{sf}$  represents the stress strain caused by stress and equal to  $\sigma_s / E_s$ , for  $f_s < f_y$ . The elastic stresses in concrete and steel are given by  $\sigma_c$  and  $\sigma_s$  respectively. In both instances, the total concrete strain  $\epsilon_c$  and total steel strain  $\epsilon_s$  equal the member strain  $\epsilon_m$ . Substituting Eq.(3.2) and Eq.(3.3) and their corresponding linear elastic stress-strain relationship into the equilibrium equation it is possible to obtain the cracking load  $P$ , Eq.(3.4):

$$P = P_c + P_s = A_c \sigma_c + A_s \sigma_s = A_c E_c \epsilon_{cf} + A_s E_s \epsilon_{sf} \quad (3.4)$$

where  $P_c$  and  $P_s$  are the loads associate to the concrete and to the steel respectively.

Considering the condition of zero axial load ( $P=0$ ), the shortened member strain  $\epsilon_{m,i}$  and the initial strains in materials,  $\epsilon_{cf,i}$  and  $\epsilon_{sf,i}$ , are shown in Eq. (3.6) and (3.7):

$$\varepsilon_{m,i} = \varepsilon_{sh} \frac{1}{1 + \rho n} \quad (3.5)$$

$$\varepsilon_{cf,i} = -\varepsilon_{sh} \frac{\rho n}{1 + \rho n} \quad (3.6)$$

$$\varepsilon_{sf,i} = -\frac{\varepsilon_{cf,i}}{\rho n} \quad (3.7)$$

where the concrete shrinkage  $\varepsilon_{sh}$  has a negative value for shortening.

If the member is loaded, shrinkage of the concrete causes a significant change in the load-deformation response, as shown in Figure 3.2. Analyses of results from past work generally neglected to account for shrinkage, assuming in most cases that the response of a RC tension member starts off at zero deformation before the load is applied, curve **OAB**. However, concrete can experience significant amounts of shrinkage before testing.

Figure 3.2 shows the idealized instantaneous and time-dependent responses of a concentrically reinforced concrete member subjected to axial tension, both before and after cracking. The instantaneous response (curve **OAB**) is linear until the reaching of the first cracking (at  $P = P_{cr}$ ) and non-linear after cracking. The load at which cracking occurs depends on the tensile strength  $f_t$  of the concrete at the time of loading.

Observing the effect of the shrinkage on the response curve, **O'A'B'** in Figure 3.2, it is possible to conclude that before cracking:

- shrinkage causes the shortening of the member and, at low tensile loads, the load-deformation curve moves to the left, **O'A'** by a strain equal to  $\varepsilon_{sh,0}$ .
- Restraint to shrinkage causes a gradual build-up of tensile stress in the concrete that reaches an initial stress equal to  $\sigma_{c,0}$ , Eq.(3.28):

$$\sigma_{c,0} = -\varepsilon_{sh} E_c \frac{\rho n}{1 + \rho n} \quad (3.8)$$

- The initial stress causes a reduction of the cracking load from  $P_{cr}$  to  $P_{cr,sh}$ , Eq.(3.29):



$$P_{cr,sh} = A_c f_t + A_s \sigma_s = P_{cr} \left[ 1 - \varepsilon_{sh,0} \frac{A_s E_s}{A_c f_t + A_s n f_t} \right] \quad (3.9)$$

where  $P_{cr}$  is the cracking load in case of no shrinkage.

After the first crack is formed ( $P > P_{cr}$ ), cracking and the deterioration of bond result in a slip at the concrete-steel interface. These two physical mechanisms are primarily responsible for the reduction in tension stiffening due to restraint to shrinkage. In absence of cracks, the incremental increase of stress, caused by the restraint to shrinkage, would cause an increase in tension stiffening. The formation of new cracks and the resulting bond slip result in a subsequent overall (net) drop in tension stiffening.

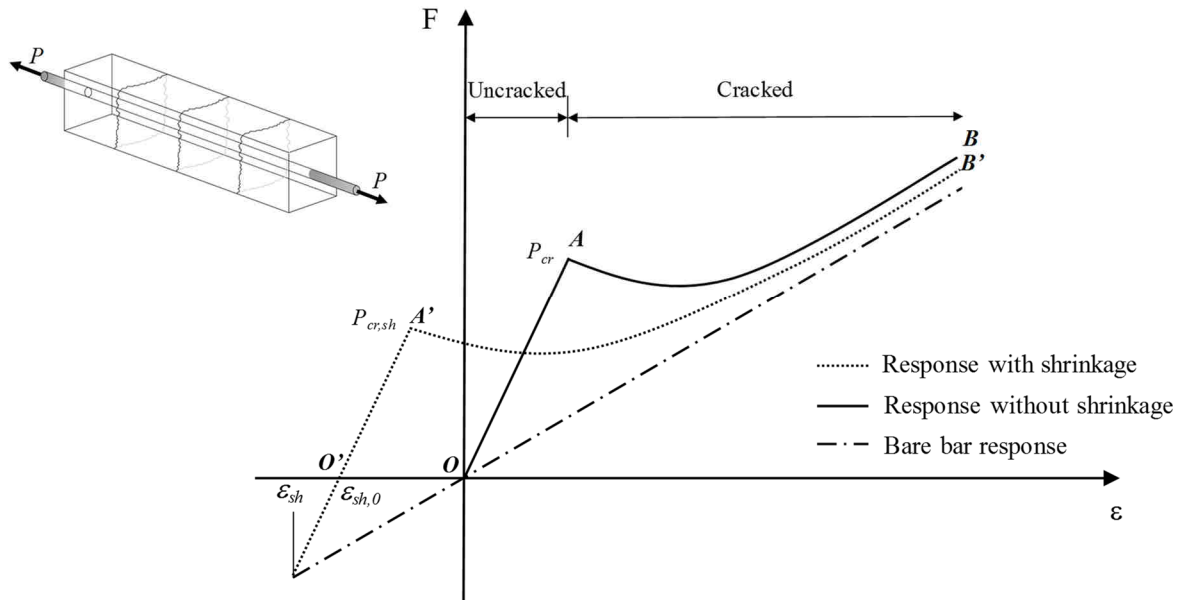


Figure 3.2: Response of an axially loaded tension member

### 3.1.1 Simplified Model for the Calculation of Uniform Shrinkage Strain

In order to apply the previously proposed formulations, it is necessary to know the initial value of the shrinkage strain. In fact, the shrinkage strain is not always given as data in the experimental campaigns. For this reason, it is necessary to rely on simplified analytical formulations, able to provide the initial value of shrinkage strain to be assigned. In this sense, the main codes provide simplified calculation models for the assessment of shrinkage strain. They adopt sectional approaches, reducing the effects of the phenomenon to an average deformation on the cross-section of the element. Starting from the hypothesis that the section remains plane, such formulations return only the final state of the effect. These models are

easily expendable in the design practice, as they simply return the effects of shrinkage in terms of deformation and critical load. Simplified models neglect the temporal and spatial evolution of the phenomenon and are based on the mechanical characteristics of the material and environmental conditions.

More specifically, Eurocode2 (EN 1992-1-1, 2002) defines the total shrinkage strain,  $\varepsilon_{cs}$ , as a sum of two components: the drying shrinkage strain,  $\varepsilon_{cd}$ , and the autogenous shrinkage strain,  $\varepsilon_{ca}$ , Eq.(3.10). The drying shrinkage strain develops slowly since it is a function of the migration of the water through the hardened concrete. The autogenous one develops during the hardening of the concrete: the major part, therefore, develops in the early days after casting. Autogenous shrinkage is a linear function of the concrete strength. It should be considered specifically when new concrete is cast against hardened concrete.

$$\varepsilon_{cs} = \varepsilon_{cd} + \varepsilon_{ca} \quad (3.10)$$

The development of the drying shrinkage strain in time,  $\varepsilon_{cd}(t)$ , follows from Eq.(3.11):

$$\varepsilon_{cd}(t) = \beta_{ds}(t, t_s) \cdot k_h \cdot \varepsilon_{cd,0} \quad (3.11)$$

where  $\beta_{ds}(t, t_s)$  is defined in Eq.(3.12),  $k_h$  is a coefficient depending on the notional size  $h_0$  according to Table 3.1 and  $\varepsilon_{cd,0}$  is the drying shrinkage strain at the initial time.

Table 3.1: Values for  $k_h$ , Eurocode2.

$h_0$	$k_h$
100	1.00
200	0.85
300	0.75
$\geq 500$	0.70

$$\beta_{ds}(t, t_s) = \frac{(t - t_s)}{(t - t_s) + 0.04\sqrt{h_0^3}} \quad (3.12)$$

where  $t$  is the age of the concrete at the moment considered (in days),  $t_s$  is the age of the concrete (days) at the beginning of drying shrinkage (or swelling);  $(t - t_s)$  represents the duration of drying in days.  $h_0$  is the notional size (mm) of the cross-section and equal to  $2A_c/u$ , where  $A_c$  is the concrete cross-sectional area and  $u$  is the perimeter of that part of the cross section which is exposed to drying.

The basic drying shrinkage strain  $\varepsilon_{cd,0}$  is calculated from Eq.(3.28):

$$\varepsilon_{cd,0} = 0.85 \left[ (220 + 110 \cdot \alpha_{ds1}) \cdot \exp\left(-\alpha_{ds2} \cdot \frac{f_{cm}}{f_{cmo}}\right) \right] \cdot 10^{-6} \cdot \beta_{RH} \quad (3.13)$$

$$\beta_{RH} = 1.55 \left[ 1 - \left( \frac{RH}{RH_0} \right)^3 \right] \quad (3.14)$$

where  $f_{cm}$  is the mean compressive strength (MPa),  $f_{cmo}$  is assumed equal to 10 MPa,  $\alpha_{ds1}$  and  $\alpha_{ds2}$  are coefficients which depend on the type of cement, Table 3.2;  $RH$  is the ambient relative humidity (%) and  $RH_0$  represents the saturation condition (100%).

Table 3.2: Value of  $\alpha_{ds1}$  and  $\alpha_{ds2}$  for different cement classes, Eurocode2.

Cement Class	$\alpha_{ds1}$	$\alpha_{ds2}$
S	3	0.13
N	4	0.12
R	6	0.11

The autogenous shrinkage strain follows from Eq.(3.15):

$$\varepsilon_{ca}(t) = \beta_{as}(t) \cdot \varepsilon_{ca}(\infty) \quad (3.15)$$

where:

$$\varepsilon_{ca}(\infty) = 2.5(f_{ck} - 10) \cdot 10^{-6} \quad (3.16)$$

$$\beta_{as}(t) = 1 - \exp(-0.2 \cdot t^{0.5}) \quad (3.17)$$

Also, Model Code 2010 (*fib*, 2013) proposes a formulation for total shrinkage deformation in which the two contributions for drying and autogenous are distinguished, in a similar form to the Eq.(3.10).

The autogenous shrinkage strain,  $\varepsilon_{cbs}$  is shown in Eq.(3.18):

$$\varepsilon_{cbs}(t) = \varepsilon_{cbs,0}(f_{cm}) \cdot \beta_{bs}(t) \quad (3.18)$$

where:

$$\varepsilon_{cbs,0}(f_{cm}) = -\alpha_{bs} \cdot \left( \frac{0.1 \cdot f_{cm}}{6 + 0.1 \cdot f_{cm}} \right)^{2.5} \cdot 10^{-6} \quad (3.19)$$

$$\beta_{bs}(t) = 1 - \exp(-0.2 \cdot \sqrt{t}) \quad (3.20)$$

The drying shrinkage  $\varepsilon_{cds}(t, t_s)$  is reported in Eq.(3.21) and it is calculated by means of the notional drying shrinkage coefficient  $\varepsilon_{cds,0}(f_{cm})$ , Eq.(3.22), the coefficient  $\beta_{RH}(RH)$ , Eq.(3.23), taking into account the effect of the ambient relative humidity and the function  $\beta_{ds}(t-t_s)$ , Eq.(3.24), describing the time development:

$$\varepsilon_{cds}(t, t_s) = \varepsilon_{cds,0}(f_{cm}) \cdot \beta_{RH}(RH) \cdot \beta_{ds}(t - t_s) \quad (3.21)$$

where:

$$\varepsilon_{cds,0}(f_{cm}) = [(220 + 110 \cdot \alpha_{ds1}) \cdot \exp(-\alpha_{ds2} \cdot f_{cm})] \cdot 10^{-6} \quad (3.22)$$

$$\beta_{RH} = \begin{cases} -1.55 \left[ 1 - \left( \frac{RH}{100} \right)^3 \right] & 40 \leq RH \leq 99\% \beta_{s1} \\ 0.25 & RH > 99\% \beta_{s1} \end{cases} \quad (3.23)$$

$$\beta_{ds}(t - t_s) = \left[ \frac{(t - t_s)}{0.035 \cdot h^2 + (t - t_s)} \right]^{0.5} \quad (3.24)$$

$$\beta_{s1} = \left( \frac{35}{f_{cm}} \right)^{0.1} \leq 1 \quad (3.25)$$

The  $\alpha_{bs}$ ,  $\alpha_{ds1}$  and  $\alpha_{ds2}$  coefficients depend on the type of cement as indicated in Table 3.3

Table 3.3: Coefficient used in Eq.(3.19) and Eq.(3.22), Model Code 2010 (*fib*, 2013).

Strength class of cement	$\alpha_{bs}$	$\alpha_{ds1}$	$\alpha_{ds2}$
32.5 N	800	3	0.013
32.5 R, 42.5 N	700	4	0.012
42.5 R, 52.5 N, 52.5 R	600	6	0.012

### 3.2 Implementation of the Shrinkage Effect in the PARC\_CL 2.1 Model

In the PARC\_CL 2.1 crack model the shrinkage effect is obtained in a simplified way, by implementing it as an average deformation, without resolving the solution of thermo-hygrometric problems and neglecting temporal and spatial evolution of the phenomenon. The aim of the model is to capture the shrinkage effects in terms of initial strain and critical load (Wu, 2008).

In the PARC\_CL 2.1 crack model, shrinkage is applied as an additional tensile strain, called free shrinkage strain  $\{\varepsilon_{sh}\}$ , Eq.(3.26), (Bernardi et al., 2016):

$$\{\varepsilon_{sh}\} = \begin{Bmatrix} \varepsilon_{sh} \\ \varepsilon_{sh} \\ 0 \end{Bmatrix} \quad (3.26)$$

The PARC\_CL 2.1 assumes perfect bond condition between concrete and steel; for this reason, the strain field of the RC element  $\{\varepsilon_m\}$  in the  $x,y$ -reference system is given by Eq.(3.27):

$$\{\varepsilon_m\} = \{\varepsilon_c\} = \{\varepsilon_s\} = \begin{Bmatrix} \varepsilon_x \\ \varepsilon_y \\ \gamma_{xy} \end{Bmatrix} \quad (3.27)$$

where  $\{\varepsilon_c\}$  is the strain vector of concrete and  $\{\varepsilon_s\}$  is the strain vector of steel in the  $x,y$ -reference system. Therefore, the linear elastic un-cracked response is modelled by including the free shrinkage strain  $\{\varepsilon_{sh}\}$  of the concrete in the total concrete strain field, Eq.(3.28):

$$\{\varepsilon_m\} = \{\varepsilon_c\} = \{\varepsilon_{cf}\} - \{\varepsilon_{sh}\} \quad (3.28)$$

where  $\{\varepsilon_{cf}\}$  is the concrete strain field caused by external force.

For the steel reinforcement the total strain is given by Eq.(3.29):

$$\{\varepsilon_m\} = \{\varepsilon_s\} = \{\varepsilon_{sf}\} \quad (3.29)$$

where  $\{\varepsilon_{sf}\}$  is the steel strain field caused by external force.

After the strain fields have been corrected, considering the strains induced by shrinkage, the PARC\_CL 2.1 is able to calculate the stress fields and the stiffness matrix as explained in §2.2.

### 3.3 Validation of the Implemented Formulation

Short-term uniaxial tension members, referred to Wu and Gilbert (2008), are selected to validate the shrinkage contribute implemented in the PARC\_CL 2.1 model. The main objectives of the experimental program were the quantification of tension stiffening in RC members under increasing load and the shrinkage effect on tension stiffening prior to cracking; moreover, the authors measured the effect of creep and shrinkage on the magnitude of tension stiffening and the effects of the time-dependent change in tension stiffening on the crack width and crack spacing. In this chapter, only the shrinkage effect will be taken into account in order to demonstrate the efficiency of the PARC\_CL 2.1 crack model in predicting the effects of shrinkage. The effects of shrinkage on tension stiffening will be deal with in §4.

#### 3.3.1 Simulation of Uniaxial Tension Members

Four specimens out of six referred to Wu and Gilbert (2008) experimental campaign are analysed in this paragraph.

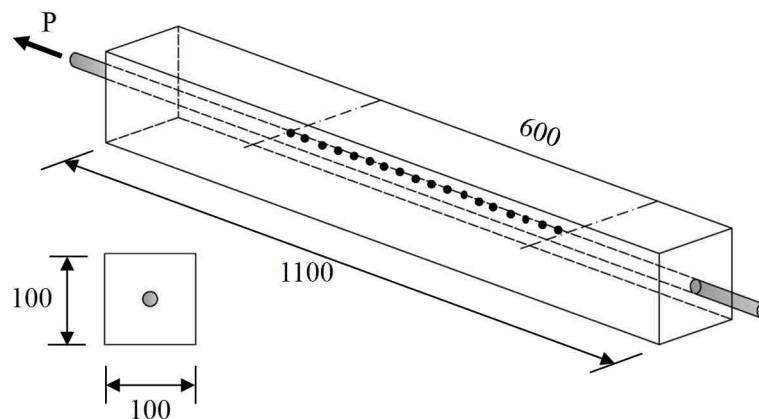


Figure 3.3: Specimen details of uniaxial tension members (all dimensions in mm), Wu and Gilbert (2008).

The specimens were characterised by a cross-section equal to 100 mm by 100 mm and length of 1100 mm, Figure 3.3. A single ribbed reinforcing bar was placed in the centre of the cross-section. The tensile axial force  $P$  was applied to the ends of the reinforcing bar. Over the middle 600 mm length of each specimen, 25 strain gauges were attached to the reinforcing bar at 25mm centres in order to monitor the local steel strains. In this work, only the specimens tested under short-term monotonically increasing load are analysed. The specimens are called STN12, STN16, STS12, and STS16. “ST” indicates the duration of the test, short-term. The third letter indicates if the specimen commenced drying and began to shrink prior to the

application of load; “S” if yes and “N” if no. The final number indicates the reinforcing bar diameter, either 12 mm or 16 mm. Two different diameters were chosen by the authors to investigate the influence of reinforcing ratio on tension stiffening.

The tests were undertaken in an Instron universal testing machine in displacement control. The corresponding tensile force was recorded by a pressure transducer connected to the machine grips. Loads, elongation and steel strains (strain gauges) were all recorded electronically using an HBM amplifier and stored in the computer hardware by a data logger.

All the short-term specimens (“ST”) were cast from the same batch of ready-mixed concrete and cured under wet burlap. Specimens “STN” were tested immediately after wet curing so that relatively little shrinkage had occurred at the time of testing. Specimens “STS” were uncovered and permitted to dry for a period of four weeks before testing.

Table 3.4: Reinforcing bar properties.

Bar	$\phi$ [mm]	$f_y$ [MPa]	$E_s$ [MPa]
<b>12</b>	12	500	200000
<b>16</b>	16	500	204000

Table 3.5: Concrete properties.

Specimen	$f_c$ [MPa]	$f_t$ [MPa]	$f_{cf}$ [MPa]	$E_c$ [MPa]
<b>STN12</b>	21.56	2.04	3.05	22400
<b>STN16</b>				
<b>STS12</b>	24.73	2.15	3.08	21600
<b>STS16</b>				

In Table 3.4 and Table 3.5 steel and concrete properties are reported respectively. In particular, the compressive strength  $f_c$  and the elastic modulus of concrete  $E_c$  were measured on standard 100 mm diameter concrete cylinders. The indirect concrete tensile strength was measured on standard cylinders using the Brazil tests and the flexural tensile strength,  $f_{cf}$  was measured on 100mm by 100mm by 600mm concrete prisms.

### 3.3.1.1 Analytical Calculations

Wu and Gilbert (2008) provided the free shrinkage strain  $\epsilon_{sh}$  for each specimen at the age of the test, 32 days for STN specimens and 57 days for STS specimens. However, shrinkage strains

are difficult to measure and therefore are not always provided. Alternatively, Eurocode2 and Model Code 2010 (*fib*, 2013) provide analytical formulation for estimating the shrinkage strain.

Briefly, the shrinkage strain values for the STS specimens (specimens subjected to shrinkage) obtained from the analytical calculations are compared with those experimentally measured, Table 3.6. The formulations proposed by Eurocode2 and Model Code 2010 (*fib*, 2013) do not depend on the reinforcement ratio. Therefore, only one value of  $\varepsilon_{sh}$  is obtained for STS12 and STS16 samples.

Table 3.6 shows that Eurocode2 slightly overestimates the shrinkage strain value, whereas Model Code 2010 (*fib*, 2013) provides values closer to the experimental ones.

Table 3.6: Value of  $\varepsilon_{sh}$  for STS specimens: comparison between the experimental value and analytical calculations.

	$\varepsilon_{sh} (10^{-6})$
<b>Experimental</b>	249.0
<b>Eurocode2</b>	294.0
<b>Model Code 2010</b>	239.0

### 3.3.1.2 NLFEA Results

Taking advantage by the symmetry of the problem, only one half of each specimen is simulated, by adopting an FE mesh constituted by quadratic, 4-node isoparametric membrane elements with 4 Gauss integration points (defined M3D4 in Abaqus). Similarly to test setup, numerical analyses are performed under displacement control, Figure 3.4.

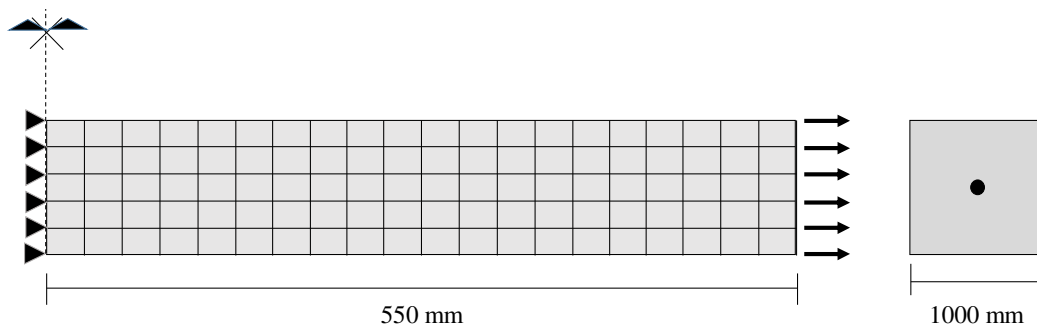


Figure 3.4: Adopted mesh, boundary conditions and applied loads.

STN specimens were tested at the age of 32 days. The measured drying shrinkage strains  $\varepsilon_{sh}$  in the unreinforced companion member were indicated in Table 3.7. Consequently, using



the formulation presented in §3.1, it is possible to calculate the value of the initial strain  $\varepsilon_{sh,0}$ , and the cracking load  $P_{cr,sh}$ , Table 3.7.

Table 3.7: Analytical calculation for specimens STN12 and STN16.

Specimen	$\varepsilon_{sh}$	$n$	$\rho$	$\varepsilon_{sh,0}$	$P_{cr,sh}$ [kN]
STN12	$-28 \times 10^{-6}$	8.93	0.0114	$-25.4 \times 10^{-6}$	20.8
STN16	$-28 \times 10^{-6}$	8.93	0.02	$-23.7 \times 10^{-6}$	22.3

STS specimens were identical to the respectively STN specimens except that they were tested at the age of 57 days. The drying properties are indicated in Table 3.8. At the time of the test the creep coefficient associated with the initial period of shrinkage was  $\varphi=1.13$ , and consequently the average strain in the specimen prior to loading (accounting for the restraint provided by the reinforcement) is calculated using the age-adjusted effective modulus method proposed by Gilbert (1988), Eq.(3.30):

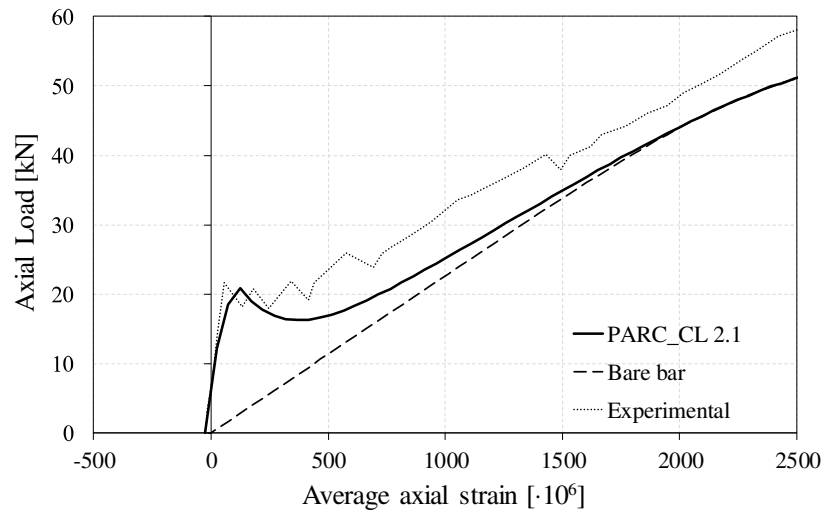
$$\varepsilon_{sh,0} = \varepsilon_{sh} \frac{1}{1 + \rho \bar{n}^*} \quad (3.30)$$

where  $\bar{n}^* = E_s / E_e$  and  $E_e = E_c / (1 + \chi\varphi)$ .

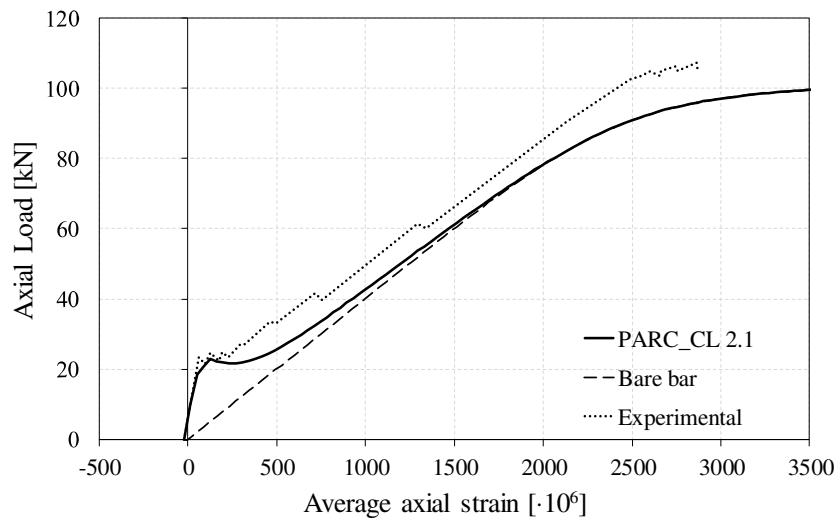
Figure 3.5 shows the comparison between the NLFEA results obtained by using PARC\_CL 2.1 crack model and the experimental ones for specimens STN12 and STN16, i.e. with a low value of shrinkage. The implemented formulation has demonstrated to be able to correctly calculate the response of the specimen in terms of initial shrinkage strain  $\varepsilon_{sh,0}$ , and the cracking load  $P_{cr,sh}$ , returning the expected values, Table 3.9. The bare bar curve in Figure 3.5 is obtained by using the Menegotto-Pinto formulation §2.2.7.

Table 3.8: Analytical calculation for specimens STS12 and STS16.

Specimen	$\varepsilon_{sh}$	$E_e$	$\bar{n}^*$	$\rho$	$\varepsilon_{sh,0}$	$P_{cr,sh}$ [kN]
STS12	$-249 \times 10^{-6}$	11344	17.6	0.0114	$-208 \times 10^{-6}$	17.2
STS16	$-249 \times 10^{-6}$	11344	17.6	0.02	$-184 \times 10^{-6}$	17.3



(a)



(b)

Figure 3.5: Comparison between NLFEA results and experimental (Wu and Gilbert, 2008) results in terms of axial load vs average axial strain for (a) STN12 and (b) STN16.

Table 3.9: Comparison between NLFEA results and experimental (Wu and Gilbert, 2008) results for STN specimens.

	STN12		STN16	
	Experimental	PARC_CL 2.1	Experimental	PARC_CL 2.1
$\epsilon_{sh,0}$	$-25 \cdot 10^{-6}$	$-25.4 \cdot 10^{-6}$	$-23 \cdot 10^{-6}$	$-23.7 \cdot 10^{-6}$
$P_{cr,sh}$ [kN]	21.1	20.8	23.0	22.9

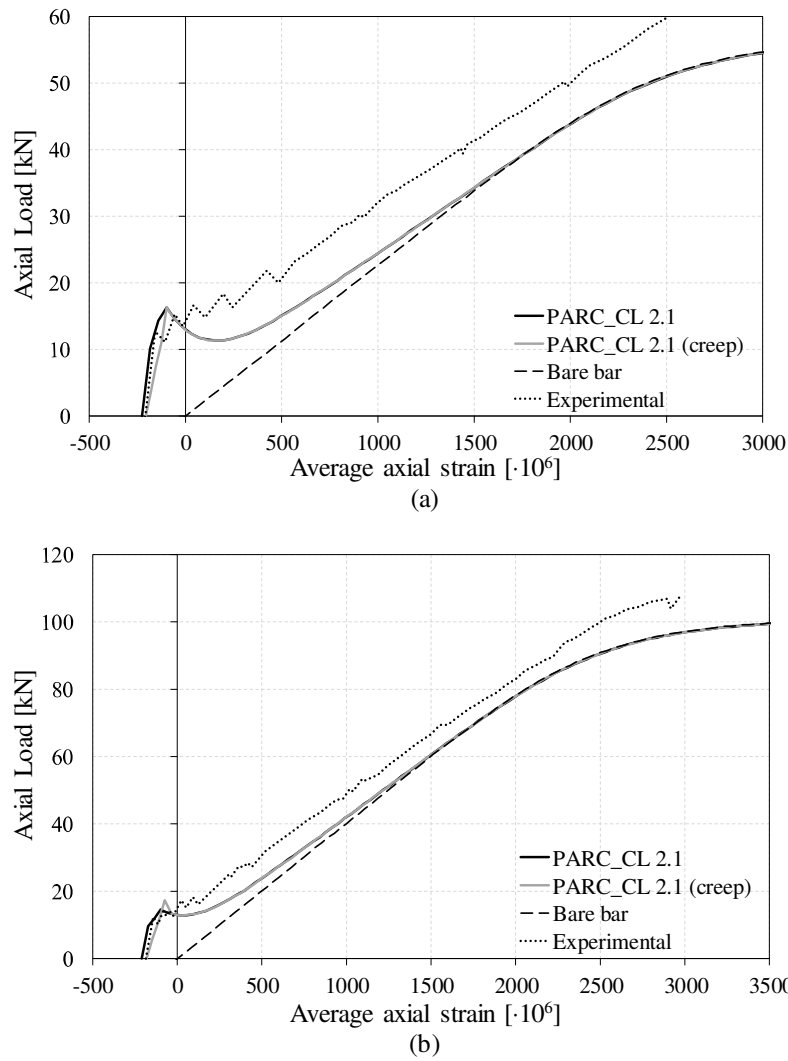


Figure 3.6: Comparison between NLFEA results and experimental (Wu and Gilbert, 2008) results in terms of axial load vs average axial strain for (a) STS12 and (b) STS16.

Table 3.10: Comparison between NLFEA results and experimental (Wu and Gilbert, 2008) results for STS specimens.

	STS12		STS16	
	$\epsilon_{sh,0}$	$P_{cr,sh}$ [kN]	$\epsilon_{sh,0}$	$P_{cr,sh}$ [kN]
<b>Experimental</b>	$-209 \cdot 10^{-6}$	13.0	$-185 \cdot 10^{-6}$	11.6
<b>PARC_CL 2.1</b>	$-225 \cdot 10^{-6}$	16.4	$-210 \cdot 10^{-6}$	15.1
<b>PARC_CL 2.1 (creep)</b>	$-208 \cdot 10^{-6}$	17.2	$-184 \cdot 10^{-6}$	17.3

Two different NLFEA are conducted for STS specimens:

1. ignoring the effects of creep, black curve in Figure 3.6 (“PARC\_CL 2.1”). According to this approach, the initial shrinkage strain is calculated using Eq.(3.1), without considering the age-adjusted effective modulus method proposed by Gilbert (1988);

2. considering the effects of creep, the grey curve in Figure 3.6 (“PARC\_CL 2.1 (creep)”). According to this approach, the initial shrinkage strain is calculated using Eq.(3.30), changing the elastic concrete modulus  $E_c$  with the age-adjusted effective modulus  $E_e$ .

The results obtained from NLFEA are presented in Figure 3.6 and show that, if the effect of the creep is considered, the estimation of  $\varepsilon_{sh,0}$  is more accurate. However, the cracking load  $P_{cr,sh}$  is higher than the value obtained without considering the effect of creep. In addition, the stiffness in the elastic phase underestimates the experimental one.

### 3.4 Concluding Remarks

Shrinkage effects can significantly influence the serviceability performance of RC elements. In fact, the restraint provided by the reinforcement on concrete causes a reduction of the cracking load of the structural element, as well as an increase of its deflection. For this reason, the PARC\_CL 2.1 crack is modified in order to include early-age shrinkage effects.

For validating the model, four tensile members (Wu and Gilbert, 2008) with different reinforcement ratios and initial shrinkage strains are modelled.

The NLFEAs conducted using the PARC\_CL 2.1 demonstrate the capability of the model to return congruent results respect to analytical calculation in terms of  $P_{cr,sh}$  and  $\varepsilon_{sh,0}$ . On the over hand, the NLFEA underestimates the experimental strength and generally is not able to catch the experimental crack pattern. This is due to the simplified adopted modelling in which the reinforcement is smeared along the entire height of the section. This is the reason why the response of the tension member is uniform and the PARC\_CL 2.1 is not able to show the discrete crack propagation.

Future studies will focus on a more realistic modelling, trying, for example, to localize the reinforcement in a smaller number of elements. This procedure will allow to distinguish elements characterized only by concrete and elements with steel and concrete.

Another important remark concerns the underestimation of the results after the reaching of the crack loading. This is due to the fact that the NLFEA do not consider the effect induced by the tension stiffening phenomenon. In order to analyse how the combined effect of shrinkage and tension-stiffening changes the analyses, the same specimens will be analysed in the next paragraph.

### 3.5 References

- Abaqus 6.12* (2012). User's and theory manuals; 2012 <<http://www.3ds.com/>> [1 June 2016].
- Bažant Z.P., Baweja S.* (2000). Creep and shrinkage prediction model for analysis and design of concrete structures: Model B3. As submitted for: Adam Neville Symposium: Creep and Shrinkage - Structural Design Effects, ACI SP-194, A.Al-Manaseer ,ed., Am. Concrete Institute, Farmington Hills, Michigan, pp. 1-83.
- Bernardi P., Michelini E., Cerioni R.*, Numerical simulation of early-age shrinkage effects on RC member deflections and cracking development. *Frattura ed Integrità Strutturale* 10(37):15-21. doi: 10.3221/IGF-ESIS.37.03
- Bischoff P.H.* (2001). Effects of shrinkage on tension stiffening and cracking in reinforced concrete. *Can J Civil Eng*, 28, pp. 363–74. doi: 10.1139/100-117.
- European Committee for Standardization (CEN) (1992). Eurocode 2: Design of concrete structures Part 1-1: General rules for buildings. DD ENV 1992-1-1m European Prestandard,
- fib* – International federation for structural concrete. *fib model code for concrete structures* 2010. 431 Ernst & Sohn; 2013; 434 p.
- Gilbert R.I.* (2001). Shrinkage, cracking and deflection – the serviceability of concrete structures. *EJSE International*, 1:2-14.
- Gilbert R.I.* (1988). Time effects in concrete structures. Elsevier Science Publishers, Amsterdam.
- Gribniak V., Kaklauskas G., Kliukas R., Jakubovskis R.* (2013). Shrinkage effect on short-term deformation behavior of reinforced concrete – when it should not be neglected. *Mater Design*, 51:1060-70. doi:10.1016/j.matdes.2013.05.028
- Holt E, Leivo M.* 2004. Cracking risks associated with early age shrinkage. *Cement and Concrete Composites*. 26:521–530.
- Holt EE.* 2001. Early age autogenous shrinkage of concrete. Ph.D. Thesis, University of Washington, USA. Published by the Technical Research Centre of Finland (VTT).

- Luo Y., Wang M.Y., Zhou M., Deng Z.* (2015). Topology optimization of reinforced concrete structures considering control of shrinkage and strength failure, *Comput Struct*, 157:31-41. doi:10.1016/j.compstruc.2015.05.009
- Maekawa, K., Soltani, M., Ishida, T., Itoyama, Y.* (2006). Time-dependent space-averaged constitutive modeling of cracked reinforced concrete subjected to shrinkage and sustained loads. *J Adv Concr Technol*, 4:193-207. doi:10.3151/jact.4.193
- Scanlon A., Bischoff P.H.* (2008) Shrinkage restraint and loading history effects on deflections of flexural members. *ACI Struct J*, 105: 498–506.
- Tongaroonsri S.* (2009). Prediction of autogenous shrinkage, drying shrinkage and shrinkage cracking in concrete. Ph.D. Thesis, Thammasat University, Pathum Thani, Thailand.
- UNI EN 1992-1-1:2005. Eurocode 2 – Design of concrete structures – Part 1-1: General rules and rules for buildings, 2005.
- Wu H.Q., Gilbert R.I.* (2008). An experimental study of tension stiffening in reinforced concrete members under short-term and long-term loads, UNICIV Report N. R-449, University of NSW.
- Wu H.Q.* (2010). Tension stiffening in reinforced concrete - Instantaneous and time-dependent behaviour, Ph.D. Thesis, University of NSW.

# Tension Stiffening Effect in the PARC\_CL

## 2.1 Crack Model

---

# 4

Concrete between cracks of RC elements carries tensile stress due to the bond between the reinforcing bars and the surrounding concrete. This effect is well known as tension stiffening. Tension stiffening effect depends on several factors, such as member dimensions, reinforcement ratio, rebars diameters and material properties. It occurs until yielding of the longitudinal reinforcement and it tends to increase as the reinforcement ratio of the member decreases.

The description of the tension stiffening effect of RC structures within finite element analysis has led to two fundamentally different approaches: the *microscopic* and the *macroscopic* one. The *macroscopic* one is often associated with a smeared crack approach. Generally, it adjusts the constitutive relationship for concrete in tension to include an unloading branch after cracking (Lin and Scordelis, 1975; Gilbert and Warner, 1978; Gupta and Maestrini, 1990; Prakhya and Morley, 1990; Barros et al., 2001; Ebead and Marzouk, 2005; Nayal and Rasheed, 2006). Alternatively, tension stiffening has been included by adjusting the constitutive relationship for the tensile reinforcement (Gilbert and Warner, 1978; Choi and Cheung, 1994; CEB manual designer, 1985). Instead, the *microscopic approaches* model cracking as discrete discontinuities in the concrete and consider the bond stress on the interface of steel and concrete as a function of slip between them (Floegl and Mang, 1982; Russo and Romano, 1992; Choi and Cheung, 1996; Kwag and Song, 2002). Since tension stiffening is

basically generated from the bond, this approach seems to be a more realistic model of the state of stress and strain between the cracks in the tension zone.

In general, *macroscopic models* are easier to implement. However, most models oversimplify the problem considering only one equation to describe the post-cracking range of the tensile stress-strain curve, independently of the member reinforcement ratio or material properties.

Tension-stiffening effects can influence the deformational behaviour of RC elements in the service range as confirmed by a large number of publications (Bazant and Oh, 1984; Vecchio and Collins, 1986; Hsu, 1996; Kaklauskas, 2009; Gilbert, 2007; Bischoff, 2008). In addition, rheological effects can influence considerably the serviceability range by the introduction of additional deformations (Ghali et al., 2012; Gilbert, 2001). More specifically, the combined effect of shrinkage deformations and tension-stiffening will be treated in this paragraph. In fact, shrinkage causes time-dependent cracking and gradually reduces the beneficial effects of tension stiffening (Bischoff, 2001; Kaklauskas et al., 2009).

A new tension-stiffening model, based on macroscopic hypothesis, is developed. In this thesis, only the monotonic law will be presented, but extensions to cyclic loads are under development.

#### 4.1 Implementation of a Tension Stiffening Model for RC elements

This section presents the modelling tool proposed to solve the bond problem along the distance between two adjacent cracks. The model aims at the calculation of the stress-strain distribution along the crack spacing of a centrically tensioned RC member under monotonic loading, Figure 4.1. The crack pattern is supposed to be fully developed and the crack spacing known.

For any given average rebar strain  $\epsilon_{given}$  and length of reinforcing bar between adjacent cracks,  $l_{s,max}$  as defined in Model Code 2010 (*fib*, 2013), the stress-strain profile along the reinforcement can be computed based on the bond stress distribution. Satisfying the equilibrium conditions on a small segment along the reinforcing bar, Figure 4.1, the equilibrium equation is derived, Eq.(4.1):

$$\frac{d\sigma_x}{dx} = \bar{\tau}_{ts} \frac{U_s}{A_s} \quad (4.1)$$



where  $d\sigma_x/dx$  is the gradient of steel stress along the bar,  $U_s$  is the bar perimeter,  $A_s$  is the area of the rebars, and  $\bar{\tau}_{ts}$  is the average bond stress along the segment.

The half crack spacing ( $l_{s,max}/2$ ) is divided into  $n-1$  segments and  $n$  nodes, Figure 4.2:

$$\Delta x = \frac{l_{s,max}}{2(n-1)} \quad (4.2)$$

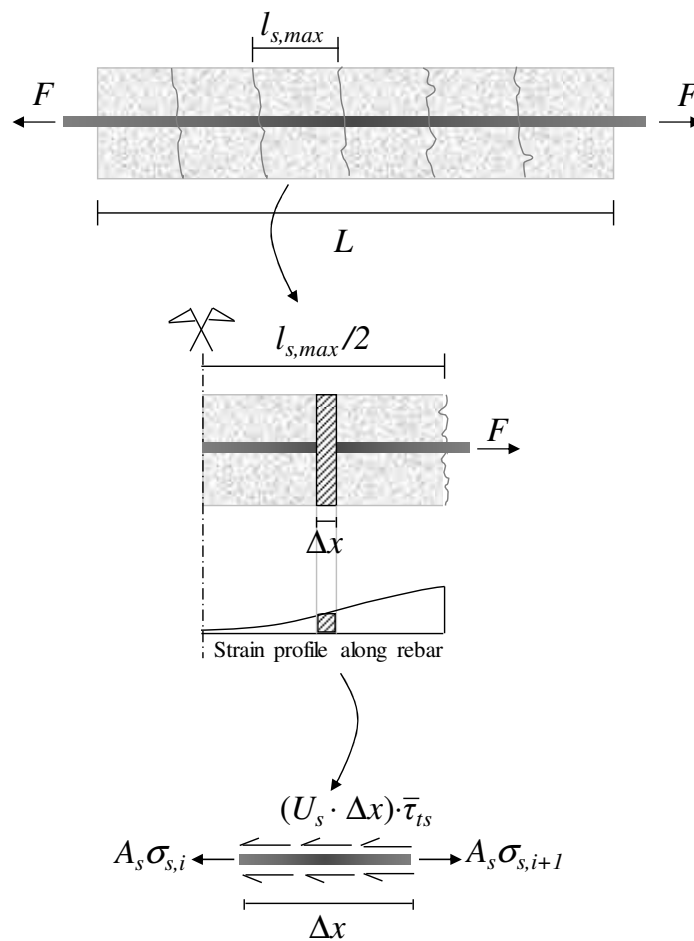


Figure 4.1: Stress transfer mechanism along the small segment  $dx$ .

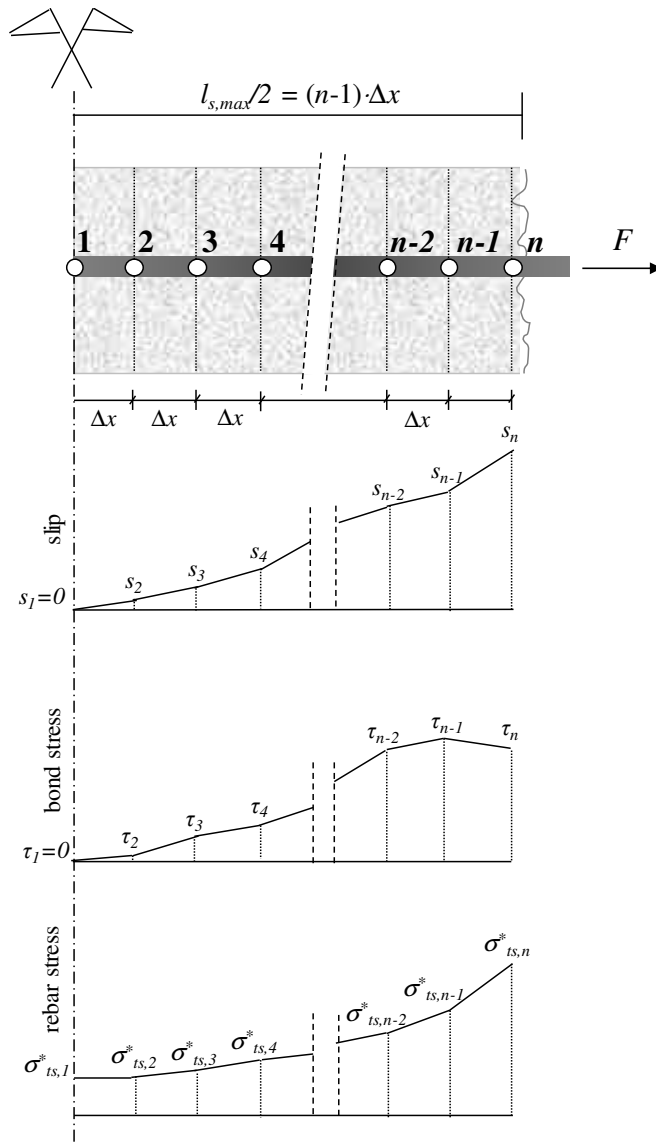


Figure 4.2: Discretization of the section between the cracks and numerical procedure.

The first section ( $i=1, x=0$ ) is located at the midway between two adjacent cracks. The bond stress  $\tau$  and the slip  $s$  associated to the first section are assumed equal to zero. Assuming the strain value at the middle of two cracks as an input data,  $\epsilon_{given}$ , the stress and strain profiles are computed by solving the equilibrium compatibility equations, segment by segment along the rebar, Eq.(4.1).

At this point it is important to underline two fundamental assumptions of the PARC\_CL 2.1 crack model (presented in detail in §2.2):

- The PARC\_CL 2.1 calculates stresses, for each material, starting from the strains in the  $x,y$ -reference system.
- The PARC\_CL 2.1 hypothesizes perfect bond between steel and concrete.

The first assumption implies that strains are a not modifiable input data for the user subroutine. For this reason, the tension stiffening phenomenon is taken into account as an increment of stress and not, as usually, as an increment of strain, applied to steel bars. The second assumption implies that is not possible to calculate the slip,  $s$ , as a difference of concrete strain and steel strain. In order to overcome the problem an iterative procedure is proposed.

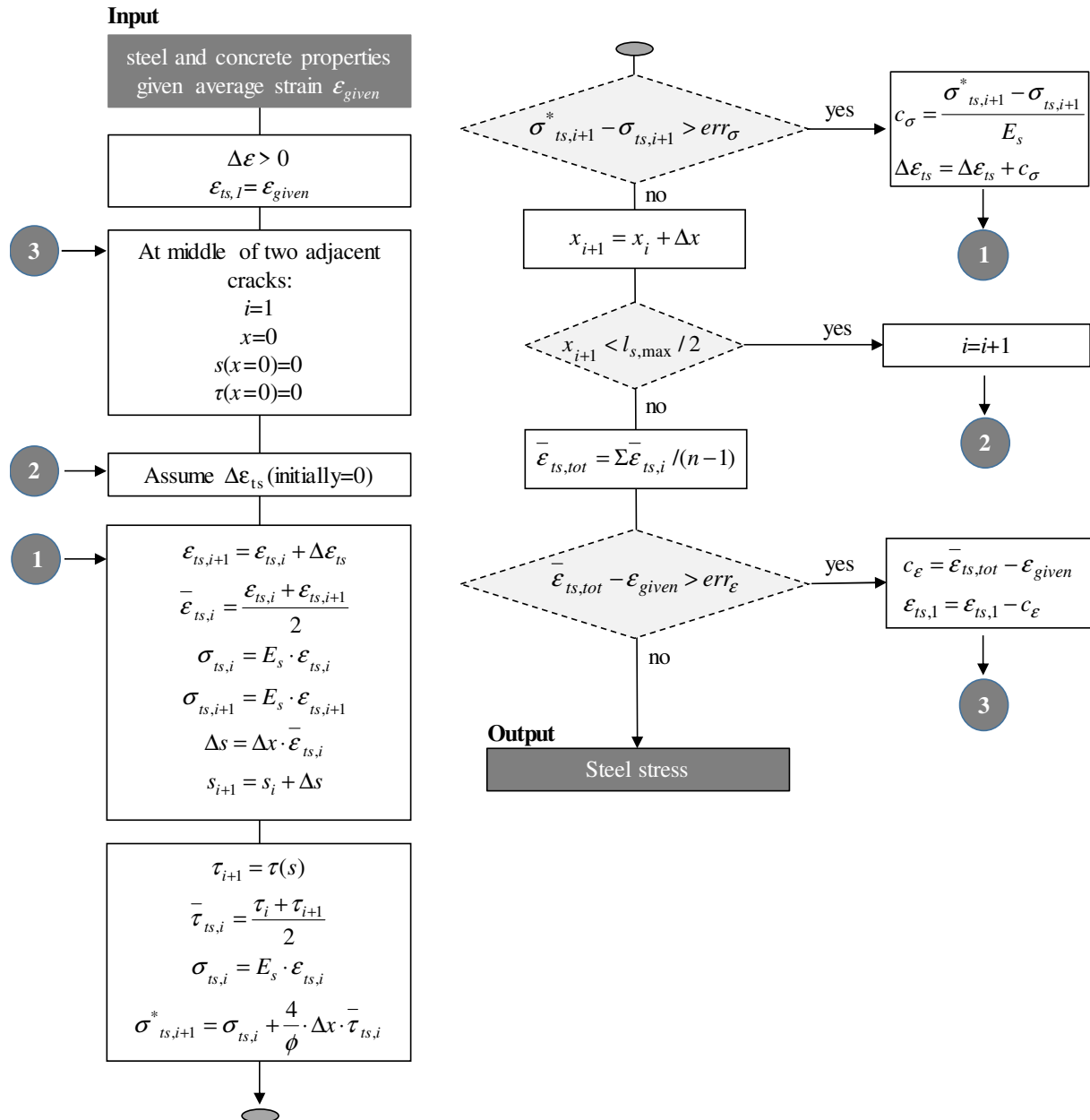


Figure 4.3: Flowchart of computing stress-strain profile along the rebars.

The flow chart for solving bond-governing equations along the reinforcement is shown in Figure 4.3. Starting from the first segment at midway between two adjacent cracks ( $i=1$ ) and

assuming the strain increment  $\Delta\varepsilon_{ts}$  (for the first attempt) equal to the given strain,  $\varepsilon_{given}$ , the stress and the slip value at the other side of the segment ( $i=i+1$ ) and consequently the bond stress, are computed.

Increasing the strain increment  $\Delta\varepsilon_{ts}$  (compared to the previous step), an iterative procedure is used until the obtained stress value satisfies the equilibrium condition (point 1 in Figure 4.3). The computed strain and slip of the first segment are the boundary conditions for the next segment. A similar computation procedure is followed to attain the stress and slip profile along the reinforcing bar, (point 2 in Figure 4.3).

To complete the problem, the bond-slip formulation provided by the Model Code 2010 (*fib*, 2013) is used, Eq.(4.3).

$$\tau = \begin{cases} \tau_u \left( \frac{s}{s_1} \right)^{0.4} & \text{if } s \leq s_1 \\ \tau_u & \text{if } s_1 < s \leq s_2 \\ \tau_u - (\tau_u - \tau_f) \cdot \left( \frac{s - s_2}{s_3 - s_2} \right) & \text{if } s_2 < s \leq s_3 \\ \tau_f & \text{if } s_3 < s \end{cases} \quad (4.3)$$

where the parameters are defined in Table 4.1 (Model Code 2010).

Table 4.1: Parameters defining the mean bond stress-slip relationship of ribbed bars (Model Code 2010).

	Pull-Out (PO)		Splitting (SP)			
	Good bond condition	All other bond condition	Good bond condition		All other bond condition	
			unconfined	stirrups	unconfined	stirrups
$\tau_u$	$2.5\sqrt{f_{cm}}$	$1.25\sqrt{f_{cm}}$	$7 \cdot \left( \frac{f_{cm}}{25} \right)^{0.25}$	$8 \cdot \left( \frac{f_{cm}}{25} \right)^{0.25}$	$5 \cdot \left( \frac{f_{cm}}{25} \right)^{0.25}$	$5.5 \cdot \left( \frac{f_{cm}}{25} \right)^{0.25}$
$s_1$	1.0 mm	1.8 mm	$s(\tau_u)$	$s(\tau_u)$	$s(\tau_u)$	$s(\tau_u)$
$s_2$	2.0 mm	3.6 mm	$s_1$	$s_1$	$s_1$	$s_1$
$s_3$	$c_{clear}^*$	$c_{clear}^*$	$1.2 \cdot s_1$	$0.5 \cdot c_{clear}$	$1.2 \cdot s_1$	$0.5 \cdot c_{clear}$
$\tau_f$	$0.4 \cdot \tau_u$	$0.4 \cdot \tau_u$	0	$0.4 \cdot \tau_u$	0	$0.4 \cdot \tau_u$

\* $c_{clear}$  is the clear distance between ribs.

The Model Code 2010 (*fib*, 2013) formulation is based on Eligehausen et al. (1983) model and it distinguishes the pull-out failure to splitting failure. The pull-out behaviour consists of an initial non-linear relationship, followed by a plateau. After, the bond stress decreases linearly to the value of the ultimate frictional bond resistance  $\tau_f$ . Different values of  $s_1$ ,  $s_2$ ,  $s_3$ ,  $\tau_u$  are proposed for unconfined concrete regions (failing by splitting of concrete cover) and for confined concrete regions (failing by pull-out), Figure 4.4.

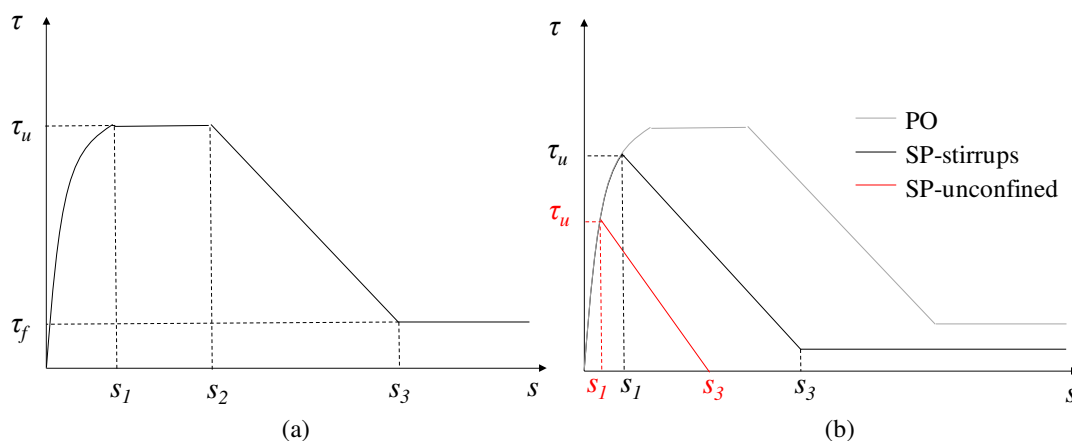


Figure 4.4: Analytical bond stress-slip relationship: (a) Pull-Out failure and (b) splitting failure, Model Code 2010 (*fib*, 2013).

When the stress profile is given for each  $n-1$  segments and  $n$  nodes, the rebar stress  $\sigma_{xi}$  at the integration point is updated (output in Figure 4.3).

Figure 4.5 shows the modified constitutive law of the rebar in terms of stress-strain. For each given strain  $\varepsilon_{given}$  a new stress is defined. The tension stiffening effect is calculated starting from the simplified equation of a bare bar and does not take into account of  $R_0$  (Menegotto and Pinto parameter that influences the shape of the transient curve). When the yielding of the rebar is reached, the tension stiffening effect is not longer considered and the Menegotto and Pinto (1973) formulation is adopted.

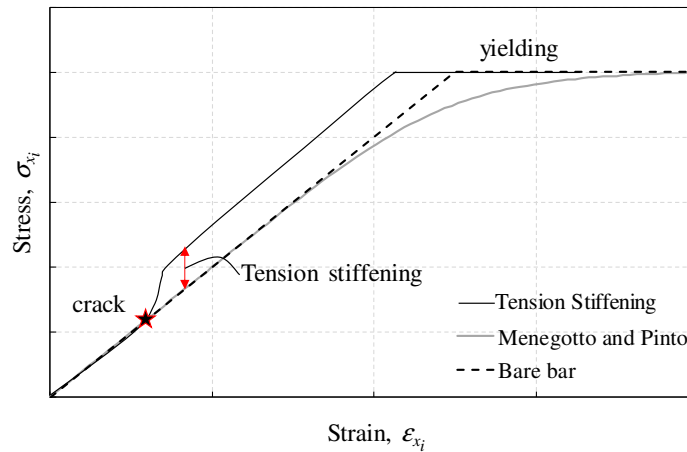


Figure 4.5: Tension stiffening contribution at integration point.

## 4.2 Effects of Shrinkage on Tension Stiffening

As mentioned in §3, shrinkage and tension-stiffening are strictly correlated. To evaluate if the tension-stiffening formulation implemented in the PARC\_CL 2.1 crack model is sufficiently accurate the same tensile members proposed in §3.3.1 are modelled. Furthermore, the effect of shrinkage on tension-stiffening will be pointed out. Subsequently, a more refined case studies will be presented. In particular, the PARC\_CL 2.1 crack model, considering the complementary effect induced by shrinkage and tension-stiffening, has been applied to beams and continuous slabs.

### 4.2.1 Uniaxial Tension Members

In this section, more attention is paid to the tension-stiffening effect on tension members.

Consider the uniaxially loaded tension member shown in §3.3.1. Experimentally, a tension member performs the following step:

- before cracking, the concrete tensile stress increases with load (Figure 4.6a). This corresponds to an elastic part in the load-strain curve, Figure 4.7.
- When the stress in the concrete reaches, for the first time, the tensile strength at the weakest section, cracking occurs in correspondence of the load  $P_{cr}$ , point 1 in Figure 4.7. In the weakest section, the stress in the concrete drops to zero (Figure 4.6b). A new redistribution of stresses develops in the member: due to steel-concrete bond, the concrete stress increases with the increase of the distance from the crack. At distance  $l_{s,max}$  from the crack, the concrete stress is no longer affected by the crack, (Figure 4.6b).

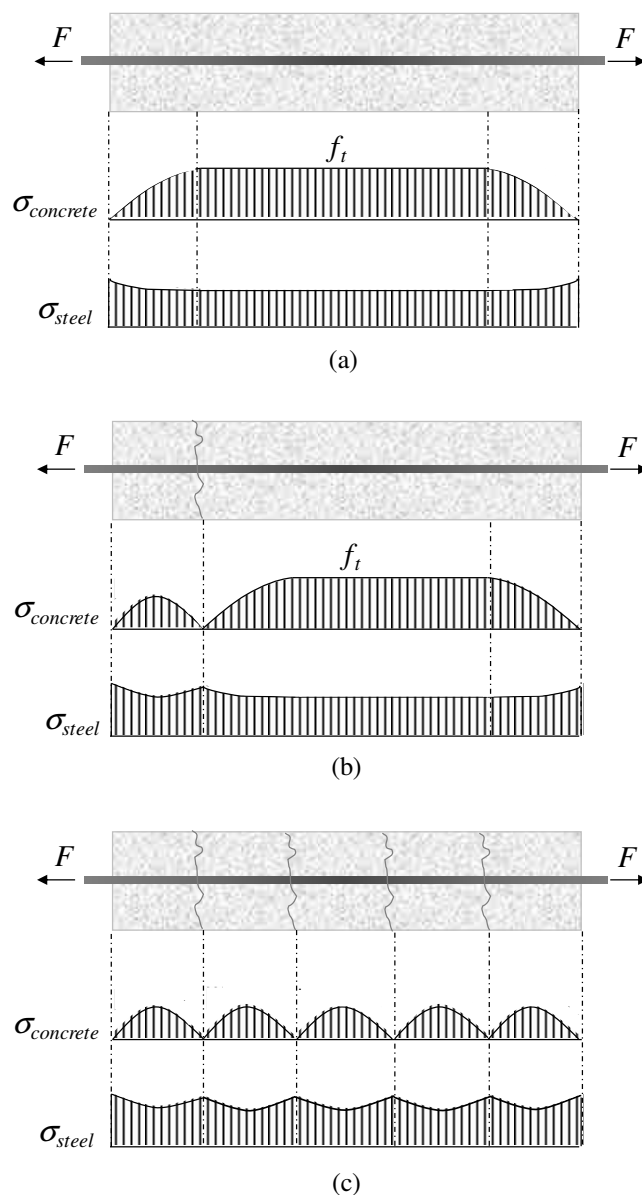


Figure 4.6: Tension stiffening in an axial loaded tension member: (a) before cracking; (b) after the first crack formation; (c) primary crack formation.

- Slip at the concrete-steel interface in the region of significant bond stress ( $l_{s,max}$  on either side of the crack) causes the crack opening. A relatively small increase in load causes the development of a second crack at a distance  $x \geq l_{s,max}$  from the first crack, thereby reducing the concrete stress in the vicinity of that crack.
- Under increasing load, the primary crack pattern is established, (Figure 4.6c). The concrete tensile stress in correspondence of each crack is zero, rising to a maximum value (less than the tensile strength of the concrete) mid-way between adjacent cracks. Consequently, cracking is accompanied by a drop in the average tensile stress carried by the

concrete and, hence, a reduction in tension stiffening, Figure 4.7. After the primary crack pattern is established, further increases in load may result in a further slip at the concrete-steel interface. The slip causes cover-controlled cracks between the primary cracks and a gradual breaking down of the bond between the steel and the concrete, thereby reducing tension stiffening still further, Figure 4.7.

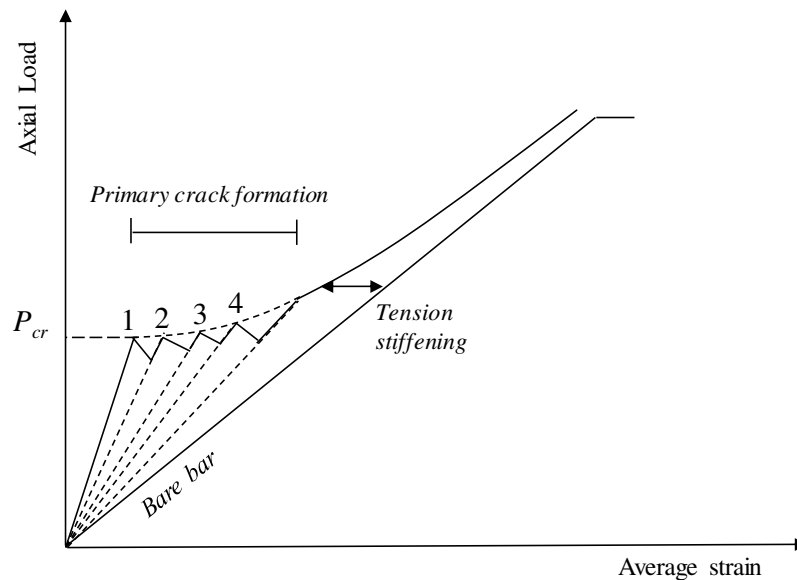


Figure 4.7: Tension stiffening effect in an axially loaded tension member: axial load versus average axial strain response.

Figure 4.7 shows what happens to the experimental tension members proposed by Wu and Gilbert (2008). The experimental tests are modelled as explained in §3.3.1 using membrane elements with smeared reinforcement and the PARC\_CL 2.1 crack model. In this paragraph, also the tension-stiffening contribution is taken into account.

Figure 4.8 and Figure 4.9 show the comparison between NLFEA and experimental results for the tension member with 12mm and 16mm diameter bars respectively. The NLFEA considering at the same time shrinkage (SH) and tension stiffening (TS) are compared with the results obtained in §3.3.1, i.e. considering only shrinkage (SH).

As experimentally demonstrated, the tension stiffening increases as the reinforcement ratio of the member decreases. The tension stiffening model implemented in the PARC\_CL 2.1 is able to reproduce this effect. Indeed, comparing the results of the ST12 member with 12mm diameter bars (Figure 4.8) to the ST16 member with 16 mm diameter bars (Figure 4.9), it is possible to observe that this condition is respected.



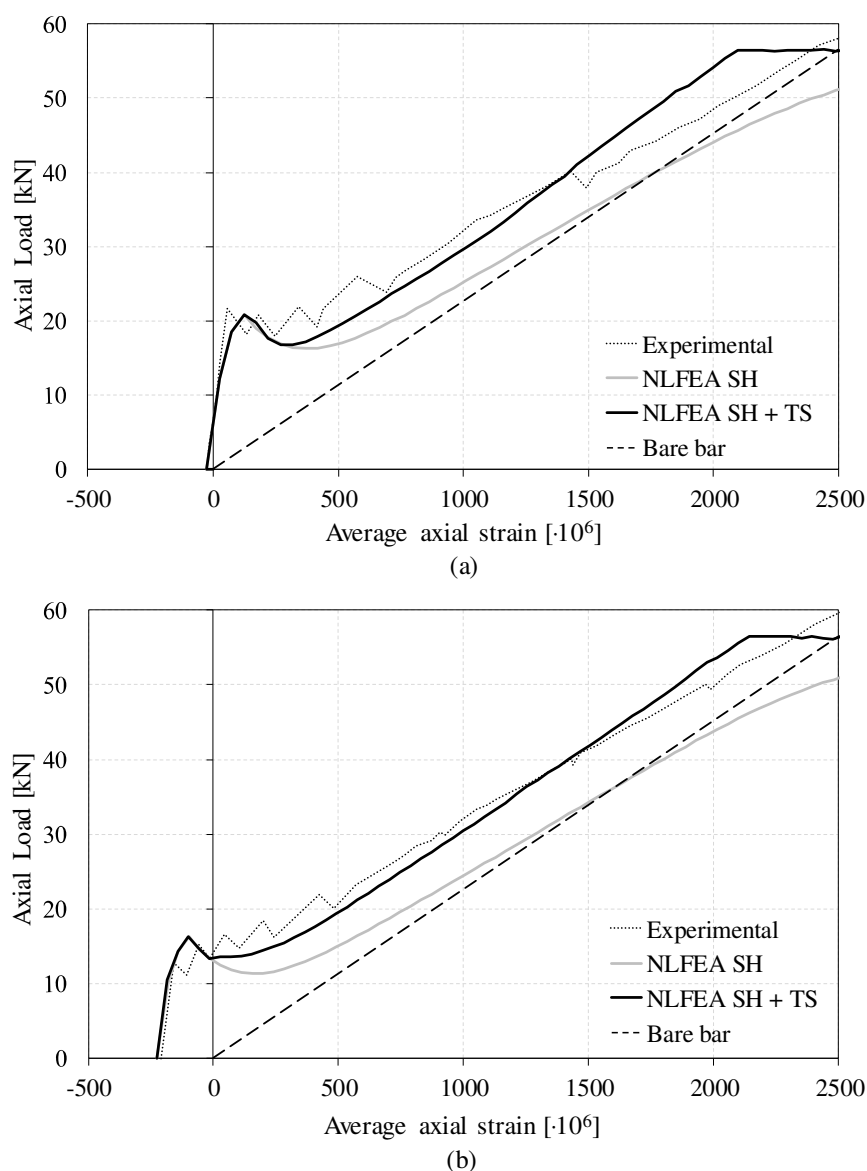


Figure 4.8: Comparison between NLFEA and experimental (Wu and Gilbert, 2008) results in terms of axial load vs average axial strain for (a) STS12 and (b) STN12.

Considering the tension stiffening effect has permitted to obtain better results in terms of load-strain curve; however, the tension stiffening contribution increases with the strain, differently to experimental observation. This is due to the simplified adopted modelling in which the reinforcement is smeared along the entire height of the section. Consequently it was necessary to load the tension member along its entire section, Figure 3.4. This fact caused equal strains in all the non-linear elements and, above all, cracks smeared in all the integration points. Therefore, in this case, the model is not able to show discrete crack propagation as well as the real stress redistribution. Nevertheless, the PARC\_CL 2.1 crack model is able to produce

results, in terms of load-strain, very close to the experimental ones, adopting a simplified modelling that does not require large computational costs.

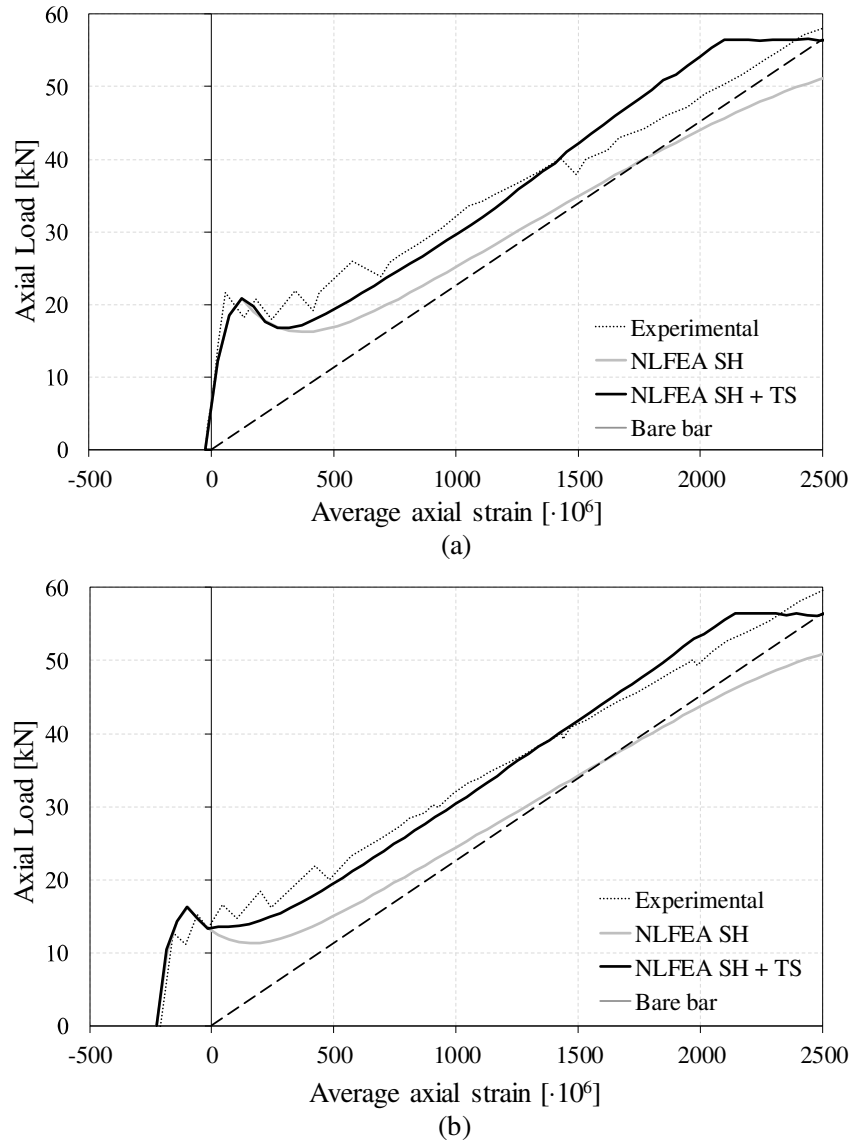


Figure 4.9: Comparison between NLFEA and experimental (Wu and Gilbert, 2008) results in terms of axial load vs average axial strain for (a) STS16 and (b) STN16.

#### 4.2.2 Simulation of RC Beams

An experimental campaign of 12 RC beams subjected to bending tests and short-term loads was carried out at the Structures Laboratory of the Civil Engineering School of the Polytechnic University of Madrid (UPM) during the period between May to October 2009 and May to June 2018 by Caldentey et al (2013), (Parrotta et al., 2014).

All beams were characterized by the same geometry and the same material properties, indicated in Table 4.2. The beams had a rectangular cross-section (450mm deep and 350mm

wide) and a central span of 3420mm, with two cantilever spans of 900mm. The test configuration is presented in Figure 4.10 and corresponds to the well-known “four points test”. Hydraulic jacks located at the end of the cantilever spans loaded a simply supported beam, with a load cell in each support; the jacks applied the load at 750 mm from each support. Thus, due to the fact that the load is applied only at the ends, and dead weight had a small effect, the central span was subjected to a constant bending moment that allowed studying the mean (smeared) behaviour of the beam.

Table 4.2: Material properties.

Property	Value
$f_y$	500 MPa
$f_u$	550 MPa
$E_s$	200000 MPa
Maximum elongation	7.5%
Concrete type	HA-25/B/20/Iia
Cement type	CEM II/AM-VL 42.5 R
Water/cement ratio	0.55
Density	2280 kg/m <sup>3</sup>
$f_{cm,7d}$	21.9 MPa
$f_{cm,28d}$	26.9 MPa

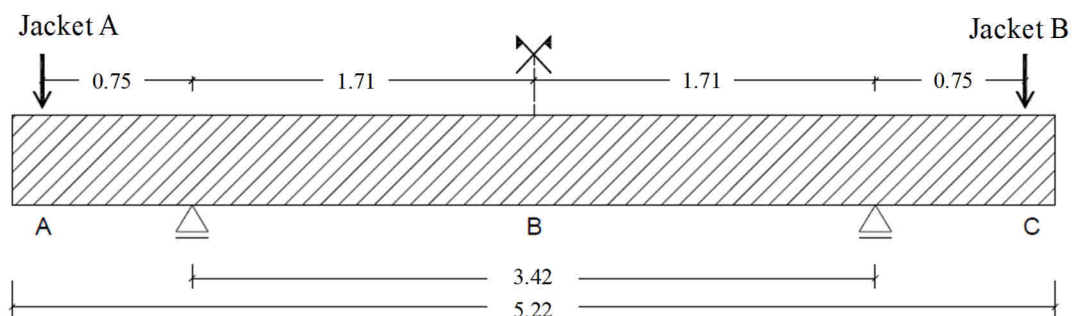


Figure 4.10: Experimental set-up: four points test.

The beams were designed to study the influence of the following parameters on tension-stiffening:

- $\phi/\rho$ : half of the beams were reinforced with  $4\phi 25$  and the other half with  $4\phi 12$ ;
- concrete cover: half of the beams had a concrete cover of 20mm and the other half had 70 mm;
- influence of stirrup spacing: four beams had no stirrups, four had stirrups spaced at 300mm and the remaining four specimens had stirrups spaced at 100mm.

More specifically, the specimens were coded XX-YY-ZZ, where XX is referred to the diameter of the longitudinal reinforcements (12 or 25mm), YY is referred to concrete cover (20 or 70mm) and ZZ is referred to stirrup spacing in the central span (00 for no stirrups).

All beams had the same number and position of the rebars into the cross-section: four rebars in tension (top reinforcement) and two rebars in compression (bottom reinforcement). Other two rebars were added at the middle height of the section for controlling the cracking. The diameter of the central and bottom reinforcement was 12mm, equal for all specimens.

In order to evaluate the efficiency of the PARC\_CL 2.1 model, only two RC beams of the experimental campaign by Caldentey et al (2013) will be analysed in this work. More specifically, two beams with the same geometry and different reinforcing bars diameter will be modelled: beam 12-70-00 and 25-70-00. Table 4.3 summarizes the mean properties of the analysed beams.

An important aspect is referred to the cantilever spans, in which is always present a number of stirrups for preventing the shear failure. Beams 12-70-00 had a double stirrup of 12mm spaces 150mm and the beam 25-70-00 had a double stirrup of 12mm spaces 100mm, Figure 4.11.

Table 4.3: Material properties obtained experimentally for the selected beams.

TEST	$\phi$ (long. reinf.) [mm]	cover [mm]	$E_c$ [MPa]	$f_{cm}$ [MPa]	$f_t$ [MPa]	$G_F$ [N/mm]
12-70-00	12	70	31263	26.9	2.3	0.085
25-70-00	25	70	31192	26.9	2.3	0.085

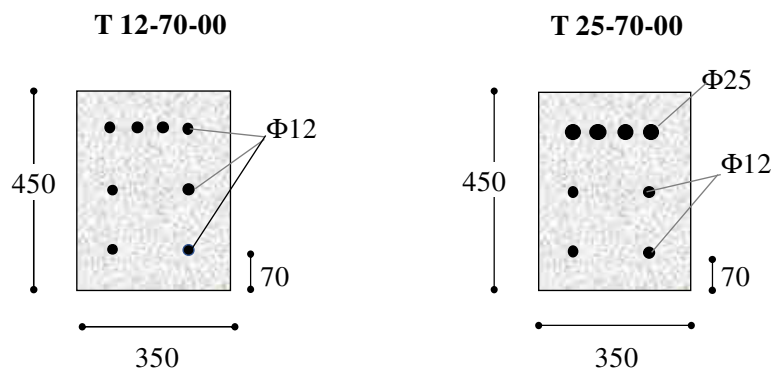


Figure 4.11: Test specimen cross-sections.

Before being tested, the beams have been kept in the laboratory, in order to wait for the concrete maturity, under the same condition of temperature and humidity. The beams were tested in different days implying different values of shrinkage and creep, Table 4.4.

Table 4.4: Rheological characteristic.

TEST	Age [days]	T [°C]	RH [%]	$\varepsilon_{sh}$ [-]	$\phi$
12-70-00	91	22.2	38.2	-5.14e-4	2.75
25-70-00	84	21.6	38.4	-5.02e-4	2.69

Taking advantage by the symmetry of the problem, only one half of each beam is simulated, by adopting an FE mesh constituted by quadratic, isoparametric 8-node membrane elements with reduced integration (4 Gauss integration points), Figure 4.12. The average size of the membrane element is equal to 25x18mm: The standard implicit Abaqus solver is adopted for the resolution of the analysis. The Newton-Raphson method is adopted as convergence criterion.

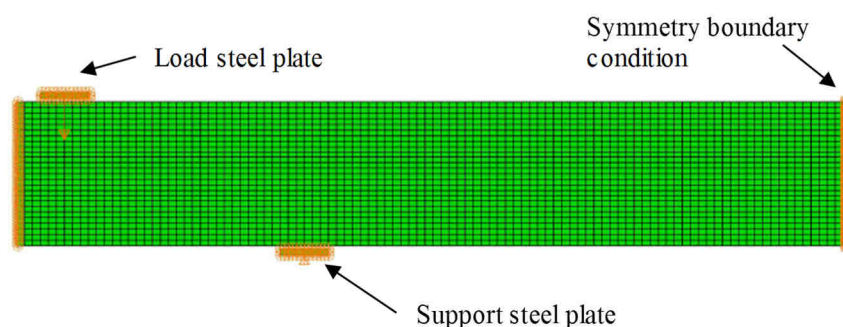


Figure 4.12: Modelling of the beams.

Concentrated loads should be applied to loading plates. Interface elements having “no-tension” behaviour should be inserted between the loading plate and concrete in order to properly reproduce the actual load transfer mechanism. The analyses are conducted in displacement control. For each beam three different case studies are considered to evaluate singularly the effect of tension stiffening and shrinkage on the NLFEA:

- considering only the contribution of tension stiffening (TS) and neglecting shrinkage: PARC\_CL 2.1 TS;
- considering only the contribution of shrinkage (SH) and neglecting tension-stiffening effect: PARC\_CL 2.1 SH;
- considering shrinkage and tension stiffening: PARC\_CL 2.1 TS-SH.

Furthermore, in order to better understand the effect induced by tension stiffening, the theoretical behaviour in state I and state II have been calculated. The analytical values are obtained by using the classical constitutive equations for serviceability. For the analysed beams the static scheme and the deflections are presented in Figure 4.13.

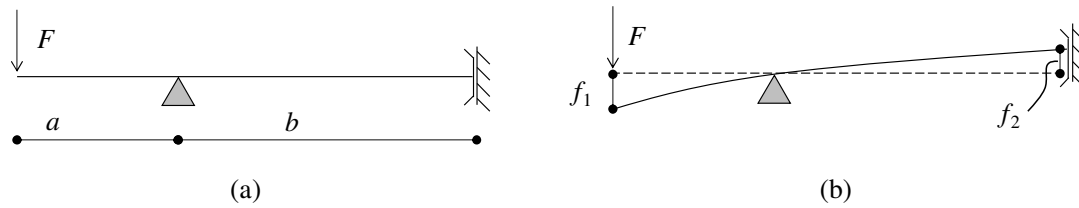


Figure 4.13: (a) Static scheme of the beam and (b) deflections.

The maximum deflection in the cantilever,  $f_1$ , and at the mid-span,  $f_2$ , are obtained by applying the principle of virtual work, Eq.(4.4) and (4.5).

$$f_1 = \frac{F \cdot a^2}{EI} \cdot \left( b + \frac{a}{3} \right) \quad (4.4)$$

$$f_2 = \frac{F \cdot a \cdot b^2}{2EI} \quad (4.5)$$

In order to evaluate deflections of the beam, it is necessary to calculate the inertial properties of the cross section for the uncracked state (State I) and fully cracked state (State II).

It is well known that the displacements are inversely proportional to the flexural rigidity, given by the product of the elasticity modulus of concrete and second moment of area of the uncracked cross-section. The deflection resulting is related to the uncracked state (State I). Conversely, for the fully cracked state (State II) the second moment of the cracked cross-section must be calculated.

In addition, the deflections induced by shrinkage have been evaluated starting from the Eurocode 2 prescription for the calculation of the shrinkage curvature, Eq.(4.6):

$$\left( \frac{1}{r} \right)_{sh} = \frac{E_s}{E_{c,ef}} \epsilon_{sh} \frac{S_S}{I_g} \quad (4.6)$$

where  $E_{c,ef}$  is the concrete effective modulus.  $S_S$  is the first moment of area of the reinforcement about the centroid of the section and  $I_g$  is the second moment of area of the section, calculated for state I and state II.

#### 4.2.2.1 T 12-70-00 Beam

T 12-70-00 beam is characterized by 4 longitudinal reinforcements of 12mm with a concrete cover of 70mm without stirrups, Figure 4.14. The adopted mesh and material sets are reported in Figure 4.14.

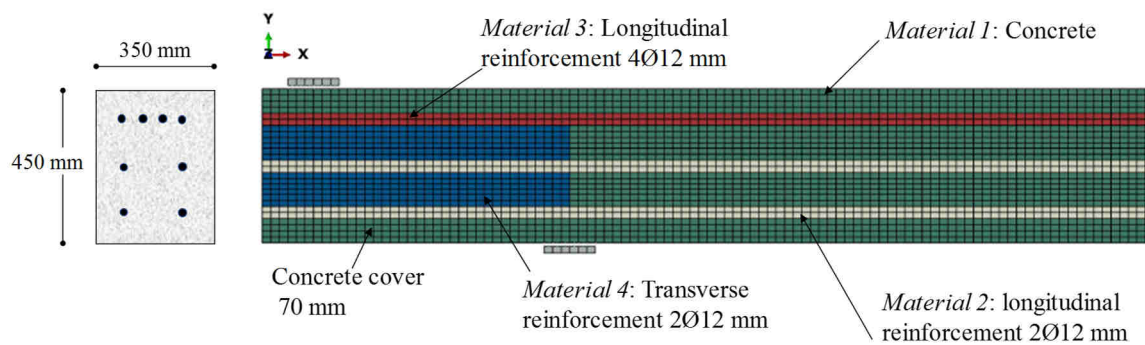


Figure 4.14: T 12-70-00 beam.

The comparison between the NLFEA, conducted using three different versions of PARC\_CL 2.1, and the experimental results is shown in Figure 4.15 in terms of load-deflection curve. In the left side of the graph, the displacement underneath the loading point (point A) is presented whereas in the right side the displacement at mid-span (point B) is shown. Furthermore, the theoretical behaviour in State I and State II, according to §4.2.2, is reported. The NLFEA curve registered in point A is stiffer than the experimental one, whereas, respect to point B, the stiffness is about the same. This difference in stiffness is not registered by theoretical calculation which, instead, is quite similar to NLFEA results.

Figure 4.16 refers only to deflections registered underneath point B. Figure 4.16 evidences that PARC\_CL 2.1 produces closer results when the combined effect of shrinkage and tension stiffening is activated. When the hardening plateau of the rebar is reached the experimental peak load is evaluated with good approximation by the PARC\_CL 2.1 crack model.

In Figure 4.16, three different values of load are remarked corresponding to 60 kN, 100 kN and 150 kN respectively. For these three different loads, the experimental crack pattern is available. Point “2” should represent the stabilized cracking stage, whereas point “3” allows appreciating the behaviour of the beam when it is almost collapsed. For each referred loading points the crack pattern obtained by PARC\_CL 2.1 TS-SH is compared to the experimental one, Figure 4.17. Experimentally, the beam presented only bending cracks at about the same distance and did not show failure.

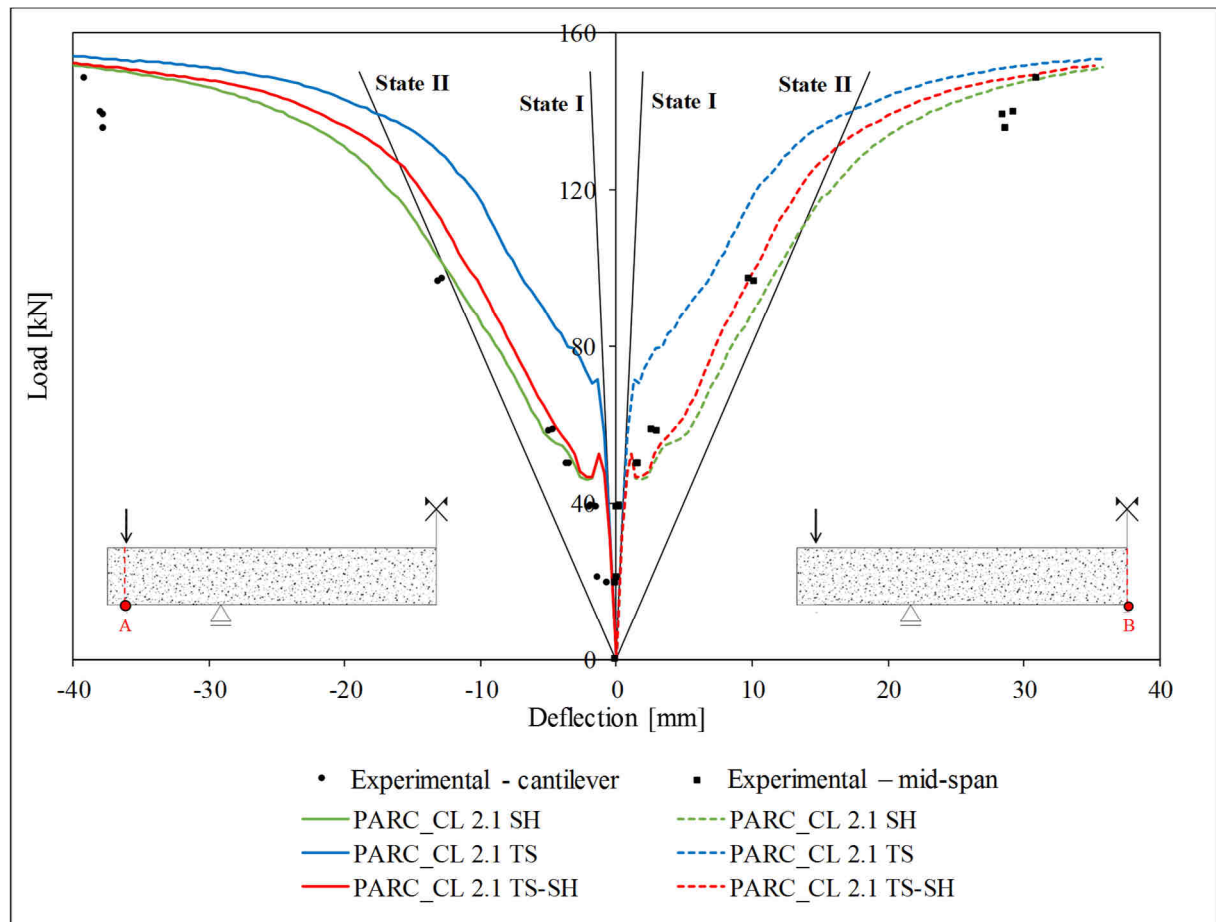


Figure 4.15: Comparison between NLFEA and experimental results for T 12-70-00 beam.



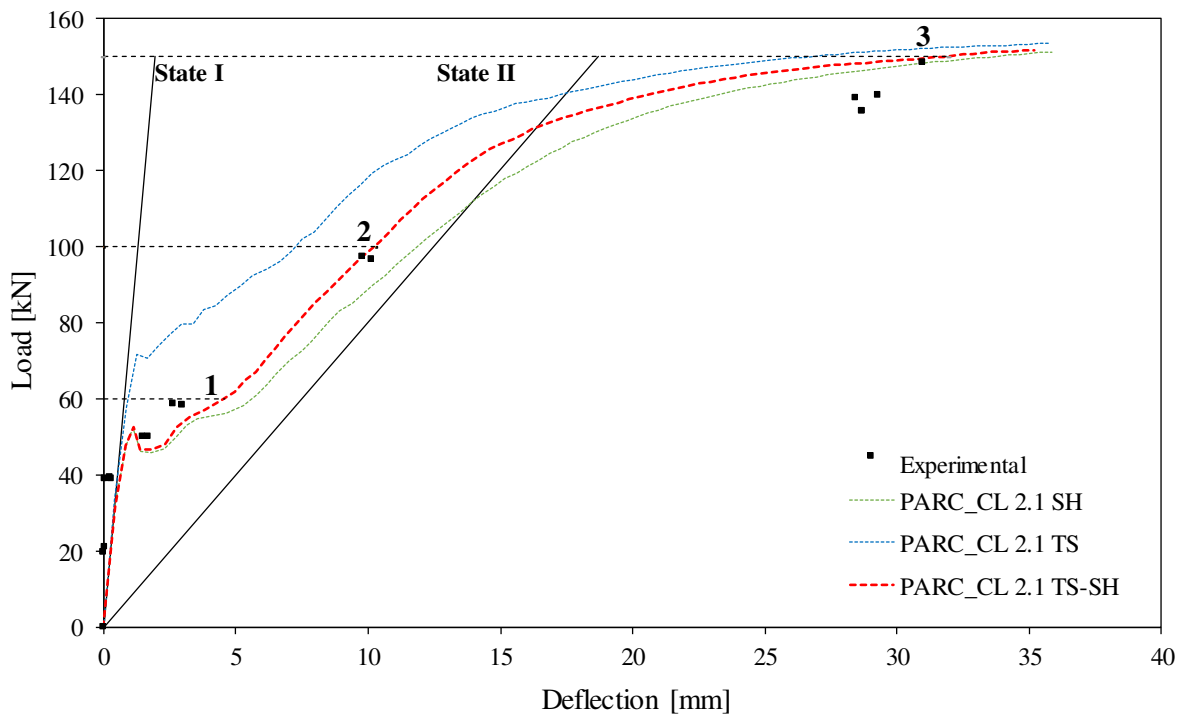


Figure 4.16: Comparison between NLFEA and experimental results in terms of load-deflection at mid-span for T 12-70-00 beam.

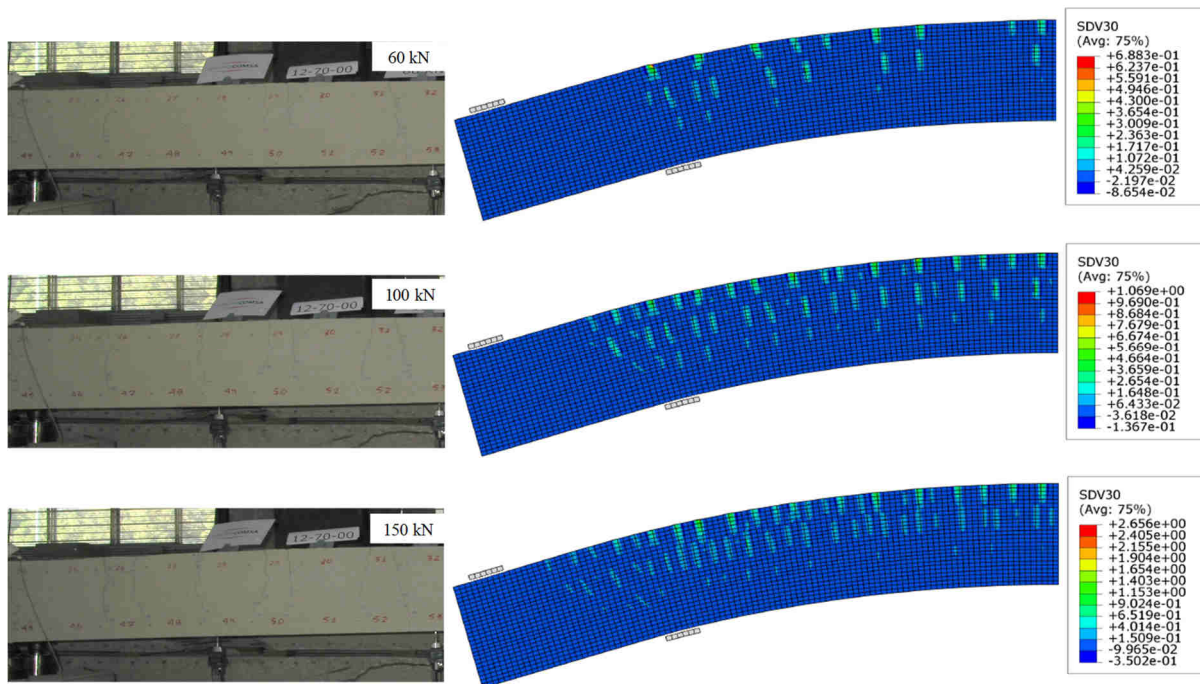


Figure 4.17: Crack pattern evolution: comparison between PARC\_CL 2.1 TS-SH and experimental results for T 12-70-00 beam.

Figure 4.18 shows the strain evolution along the longitudinal rebars for the same values of load. Starting from 100 kN the upper reinforced layer starts to yield in some integration points (yield strain equal to 0.0025). When the load reaches a value of 150 kN, the upper reinforced layer is completely yielded and also a big part of the middle layer is yielded. The maximum value of strain reached by the reinforcement is equal to 0.03967, so there is not integration point that reaches the ultimate strain value equal to 0.075 (as indicated in Table 4.2). For this reason, the NLFEA did not highlight failure, according to the experimental result.

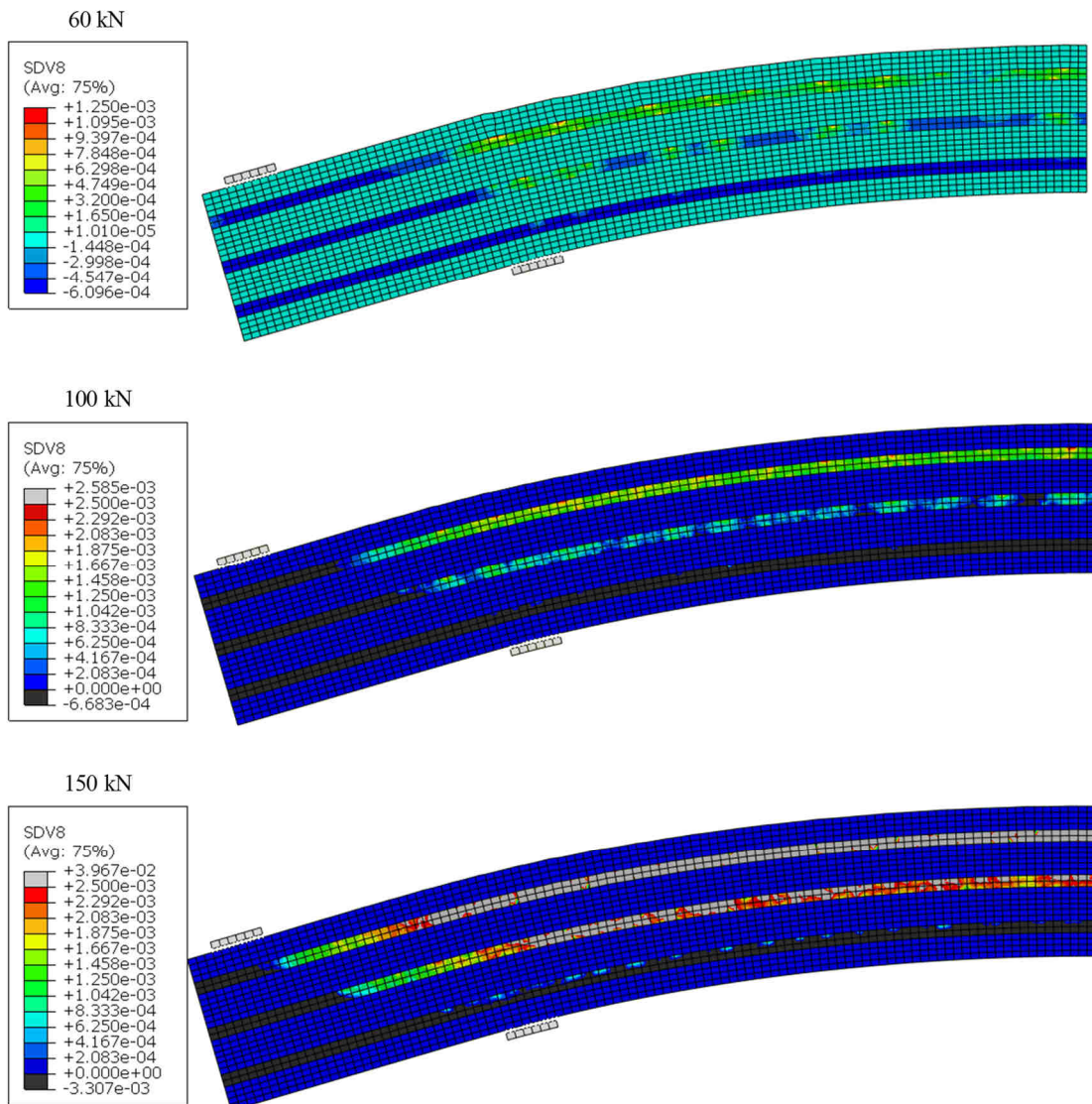


Figure 4.18: Rebar strain evolution obtained by PARC\_CL 2.1 TS-SH for T 12-70-00 beam.

### 4.2.2.2 T 25-70-00 Beam

Finally, the T 25-70-00 beam is shown in Figure 4.19.

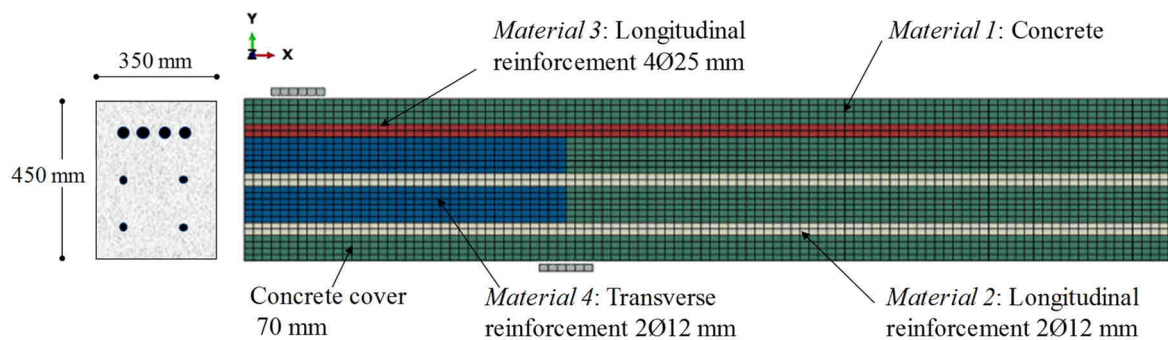


Figure 4.19: T 25-70-00 beam.

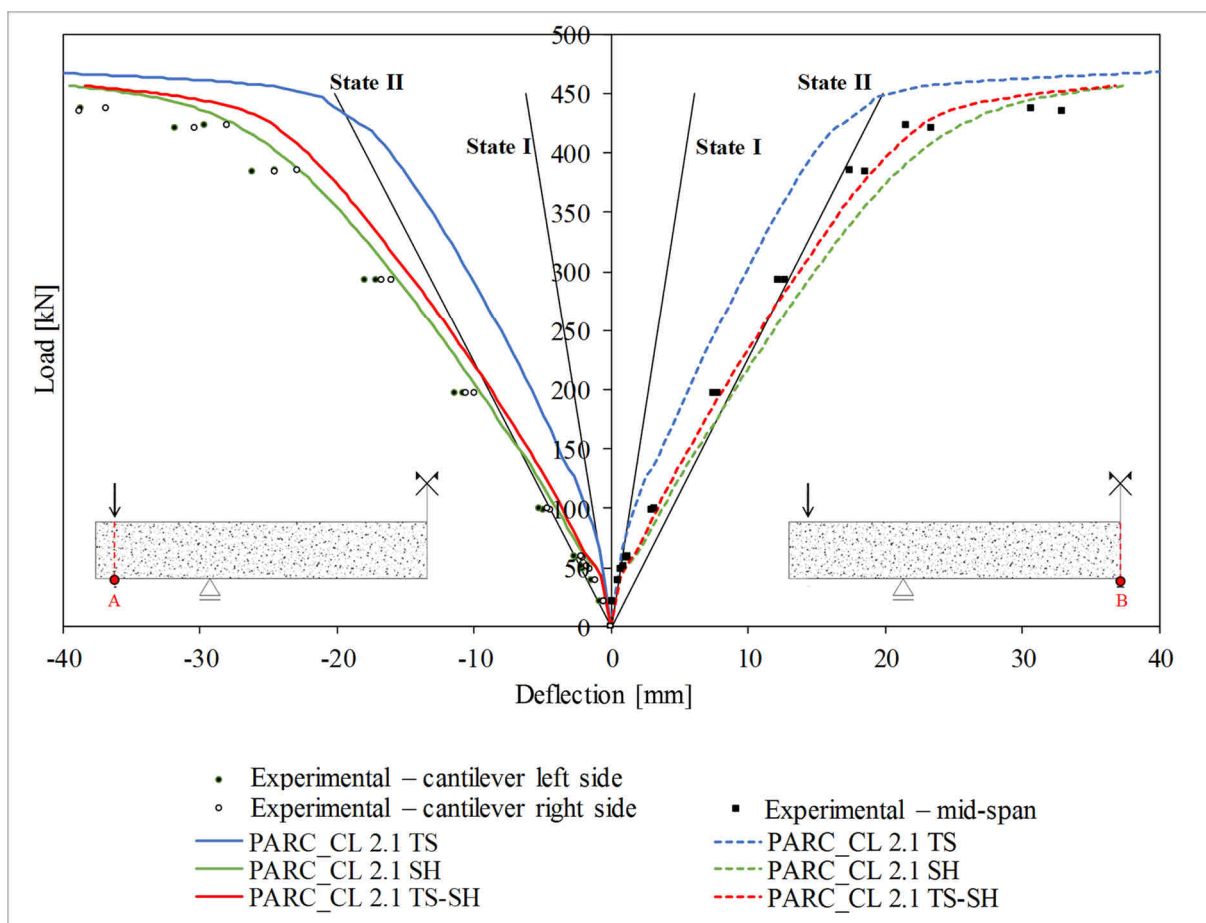


Figure 4.20: Comparison between NLFEA and experimental results for T 25-70-00 beam.

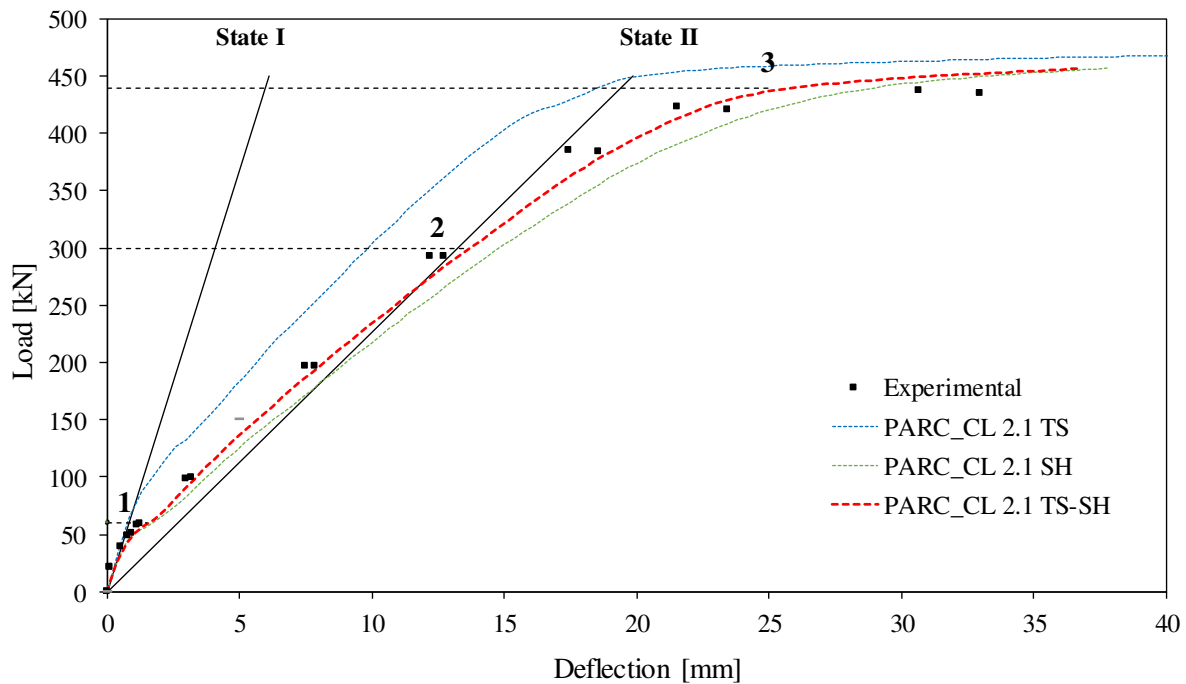


Figure 4.21: Comparison between NLFEA and experimental results in terms of load-deflection at mid-span for T 25-70-00 beam.

The comparison between the NLFEA and the experimental results in terms of load-deflection is shown in Figure 4.20. NLFEA present the same overall behaviour of the previous case study confirming that the combined effect of shrinkage and tension stiffening provides better results both in terms of load-deflection curve, Figure 4.20 and Figure 4.21 and crack pattern, Figure 4.22.

Also for T 25-70-00 beam, three different values of load are indicated in Figure 4.21 in order to compare the crack pattern obtained from the NLFEA, obtained using PARC\_CL 2.1 TS-SH, and the experimental one (Caldentey et al., 2013). Observing Figure 4.21, Point “1” is the point in which the first cracks are formed: it is representative of the passage from State I and State II. Point “3” allows to appreciate the behaviour of the beam in correspondence of the maximum registered load, corresponding to the yielding of the longitudinal bars.

During the experimental test the beam shown only bending cracks, equally spaced, and did not show failure at the end of the test. However, the crack widths are not detected during the test and for this reason detailed comparison are not possible.

Figure 4.23 shows the strain evolution along the longitudinal reinforcement of the beam, confirming that, for a load equal to 440kN, the yielding of the upper layer of the rebars is reached by NLFEA.

Finally, comparing the NLFEA curve obtained for the two beams (Figure 4.16 and Figure 4.21 ) it is possible to observe that the contribute given by the tension stiffening is lower for T 25-70-00 beam respect to T 12-70-00 beam. This is due to the fact that the tension-stiffening effect tends to increase as the reinforcement ratio of the member decreases.

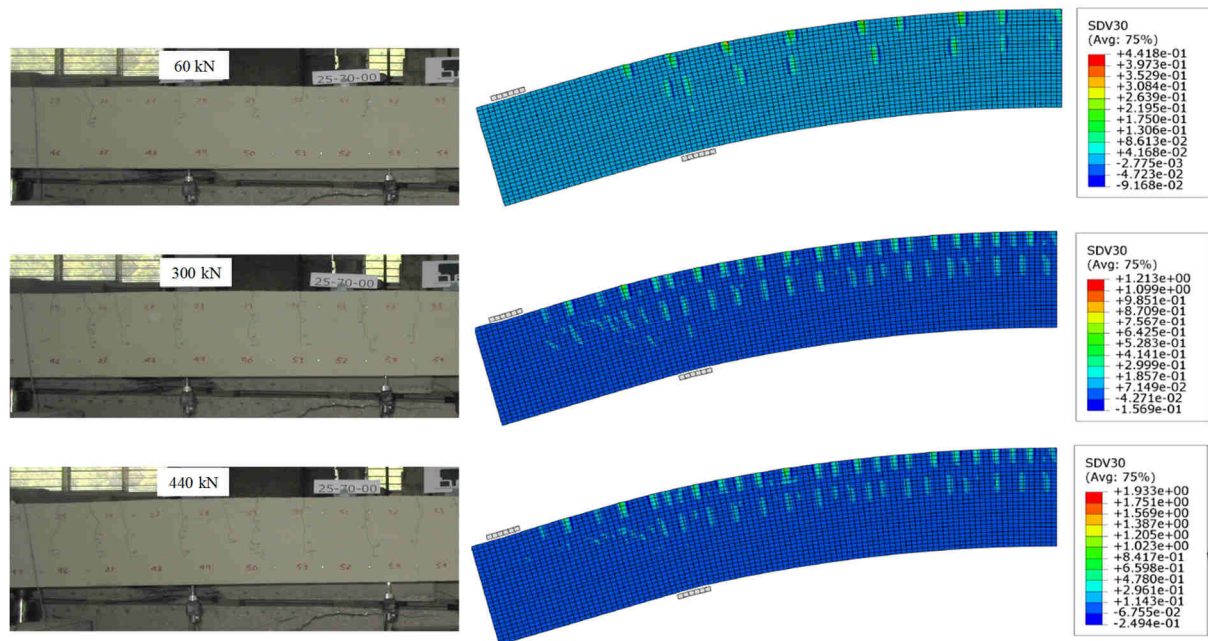


Figure 4.22:Crack pattern evolution: comparison between PARC\_CL 2.1 TS-SH and experimental results for T 25-70-00 beam.

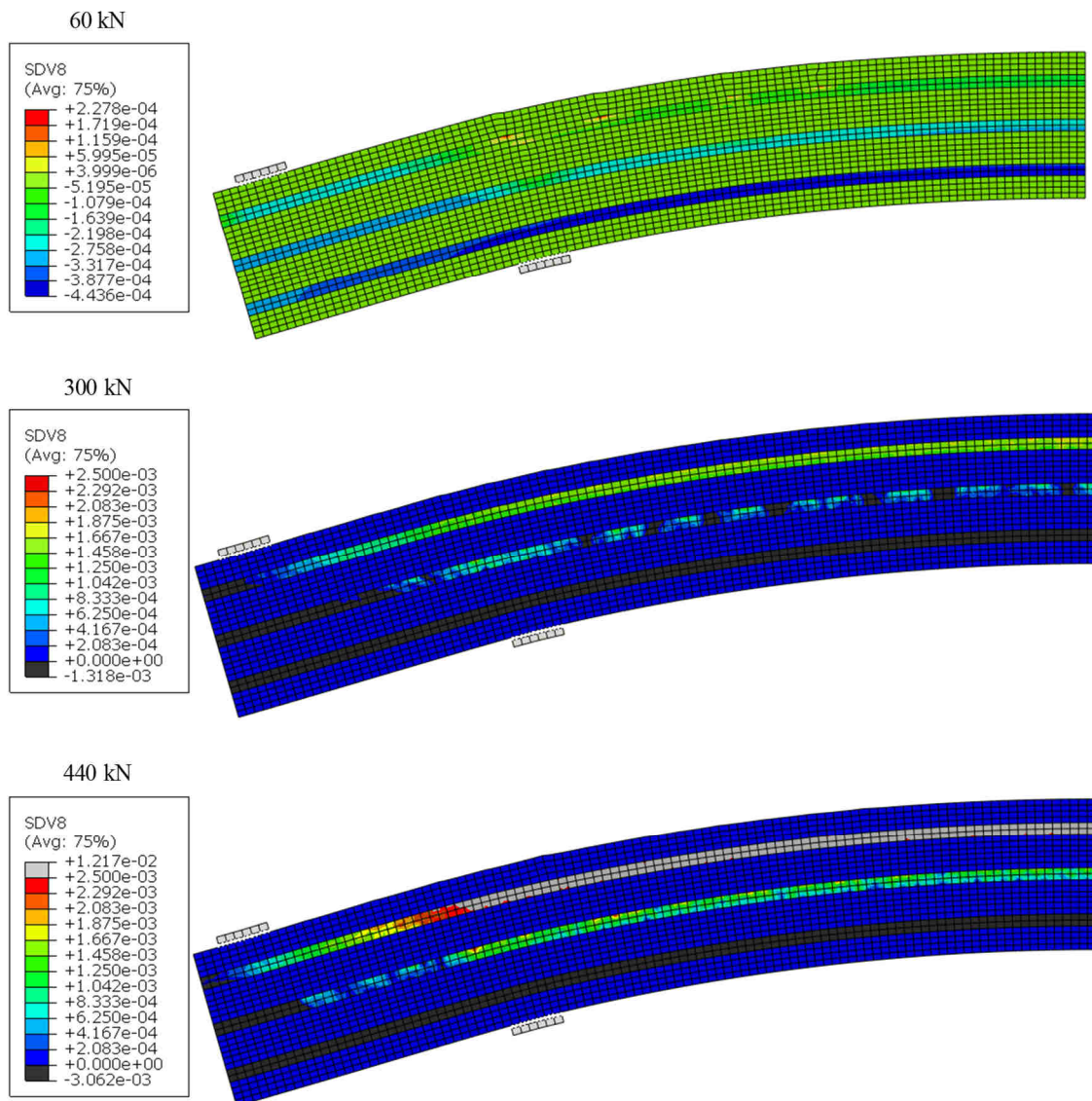


Figure 4.23: Rebar strain evolution obtained by PARC\_CL 2.1 TS-SH for T 25-70-00 beam.

### 4.2.3 Simulation of RC Continuous Slabs

In this paragraph, some results of a wider study published in Belletti et al. 2018 on continuous slabs has been presented. The main objective of this research concerns the dependency between membrane action and punching shear resistance on the reinforcement layout and boundary conditions of continuous slabs.

Reinforced concrete (RC) flat slabs are common structural solutions in residential and multi-storey buildings. The behaviour of reinforced concrete flat slabs can be governed at failure by punching shear close to columns. Most of the code formulations for punching shear strength assessment (*fib*, 2013; Eurocode 2, 1992; ACI, 2014) are based or calibrated on experimental tests usually carried out on isolated specimens. Nevertheless, the bending and the shear resistance of isolated specimens can be lower than the resistance of actual continuous RC flat slabs due to moment redistribution and compressive membrane action (CMA) or tensile membrane action (TMA) effects (Figure 4.24).

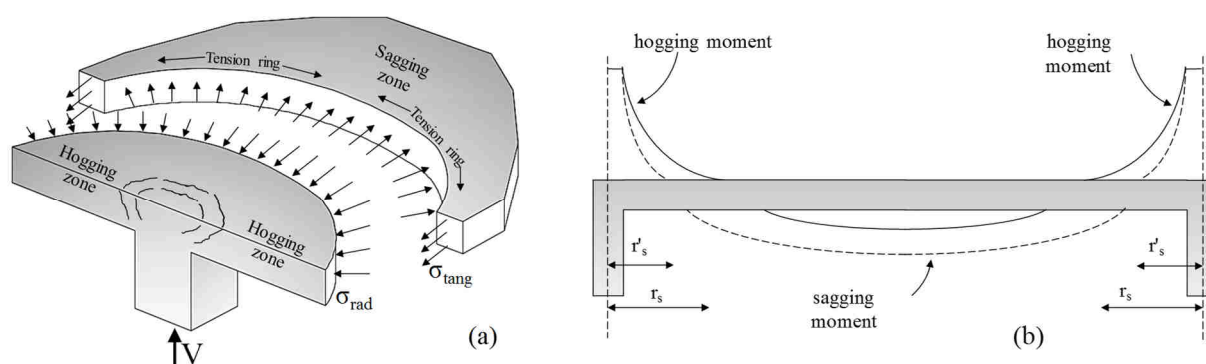


Figure 4.24: (a) Membrane Action – radial and tangential stresses ( $\sigma_{rad}$  and  $\sigma_{tang}$ ) and effect of the tension ring on the hogging area; (b) Moment redistribution between hogging and sagging areas.

The study is of particular interest because NLFEA is conducted applying tension stiffening and observing how considering shrinkage or not influences the results in terms of concrete cracking and punching shear resistance. This aspect could be significant for the structural assessment of existing structures carried out using refined numerical tools, like non-linear finite element methods, which are able to take into account hidden resistance capacities, but are less conservative than analytical approaches (Belletti et al., 2015<sup>b</sup>).

To this aim, a parametric study has been carried out in Belletti et al. (2018) to investigate the dependency of membrane action and moment redistribution on the geometrical features and reinforcement layout of continuous slabs. Different values of base column dimension, slab thickness (with constant value of the effective depth, which means that the influence of

reinforcement cover of the tensile reinforcement is investigated), slab span and ratios of hogging and sagging reinforcement have been considered focusing on the region of the slab supported on internal columns without openings, where the highest influence of compressive membrane action may be expected. In this paragraph, only a case study extracted from Belletti et al. (2018) has been selected to investigate the dependency of the punching resistance of RC continuous slabs on stiffening effects of boundary conditions.

Figure 4.25 shows the Self Confined (SC) analysed slab. The mechanical properties for concrete and steel are indicated in Table 4.5; whereas the geometrical parameters of the slabs (column size  $c$ , thickness  $h$ , effective depth  $d$ , the span between adjacent columns  $L$ ) are reported in Table 4.6. Three cases with three different hogging reinforcement ratios in the column area ( $0.4 L \times 0.4 L$ ) are studied:  $\rho_{hogg} = 1.5\%$ ,  $0.75\%$ ,  $0.375\%$ . The sagging reinforcement is uniformly distributed over the span with a reinforcement ratio  $\rho_{sagg} / \rho_{hogg}$  equal to  $1/3$  in *Zone 1*, to  $2/3$  in *Zone 2 and to  $1$  in *Zone 3*, as indicated in Figure 4.25.*

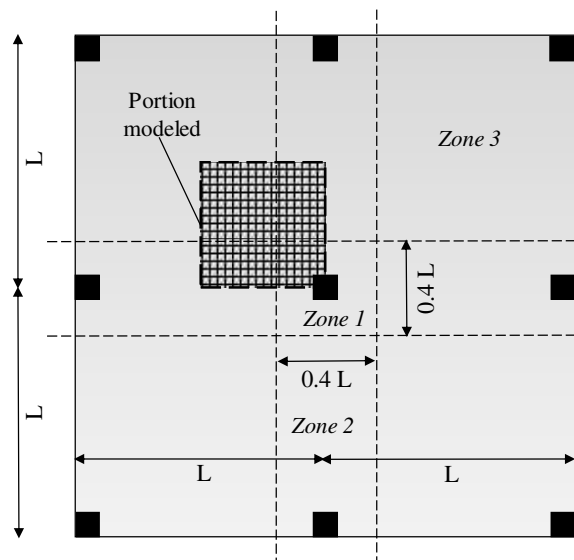


Figure 4.25: Self Confined slab: portion of modelled slab and layout of reinforcements zones.

Table 4.5: Mechanical properties of steel and concrete.

$f_c$ [MPa]	$E_c$ [MPa]	$f_y$ [MPa]	$E_s$ [MPa]
35	32600	520	200000

Table 4.6: Geometrical parameters for the analyses.

$c$ [mm]	$L$ [m]	$h$ [mm]	$d$ [mm]
260	6	250	210



Since membrane actions are strongly dependent on slab boundary conditions, different cases are investigated (Figure 4.25):

- *Isolated slab* reproducing the hogging area of a flat slab having dimensions  $0.22L \times 0.22L$  corresponding to experimental test set-up;
- *Self-confined continuous flat slab* with regular spans  $L$  loaded with a uniform pressure, simulating permanent and variable loads (Figure 4.25);
- *Continuous flat slab restrained with horizontal stiffening springs* having regular spans  $L$  loaded with a uniform pressure. Non-linear springs having no-tension behaviour and compressive stiffness, calculated assuming as vertical members RC wall 3.50 m high and 0.3 m thick, have been used;
- *Fully restrained continuous flat slab* with regular spans  $L$  loaded with a uniform pressure, which lateral displacements set equal to zero.

Since shrinkage may affect the crack pattern in a different way depending on the erection phases of buildings, this last case is divided into two subcases:

- *Fixed restrained continuous slab*: the lateral displacements at boundaries are restrained before the application of shrinkage, self-weight, and pressure load;
- *Post-Fixed restrained continuous slab*: the lateral displacements at boundaries are restrained after the application of shrinkage and self-weight but before the application of pressure load.

In both cases, the membrane action effect is considerable if compared to isolated specimens. Shrinkage effect, in an unsaturated environment, causes an anticipate cracking of concrete specimens, leading to a decrease of bearing capacity. This problem becomes more serious if slab contraction is restrained. A constant shrinkage strain  $\varepsilon_{sh}$  equal to  $3 \cdot 10^{-4}$  is considered (equal to a value which takes place about to 2 years after construction according to Model Code 2010), as an additional tensile strain in PARC\_CL 2.1 crack model.

#### **4.2.3.1 Membrane Action Effects on Punching Shear Resistance**

Since multi-layered shell elements are not able to predict the non-linear behaviour over the thickness of the slab, a post-processing based on the Critical Shear Crack Theory (Muttoni, 2008) is applied.

The CSCT failure criterion is able to predict the punching shear resistance of a slab, subjected to a concentrated load, as a function of the maximum slab rotation  $\Psi$ , Figure 4.26b.

The formula for the failure criterion (Muttoni, 2008; Guidotti, 2010; Muttoni et al., 2017) is given in Eq.(4.7):

$$V_{R(\psi)} = \frac{\frac{3}{4} b_0 d \sqrt{f_c}}{1 + 15 \frac{\psi d}{d_g + d_{g0}}} \quad (4.7)$$

where  $b_0$  is the length of the control perimeter at distance  $0.5d$  from the column edge, Figure 4.26a,  $d$  is the effective depth of the slab,  $f_c$  is the concrete compressive strength in [MPa],  $d_g$  is the maximum aggregate size, and  $d_{g0}$  is the reference aggregate size (16 mm). Punching shear failure occurs at the intersection between the load-rotation curve (obtained from NLFEA) and the CSCT failure criterion, Figure 4.26.

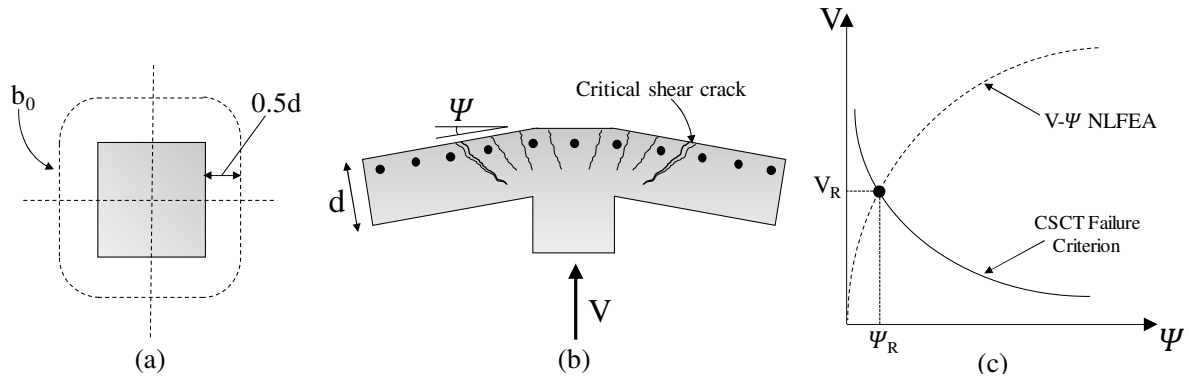


Figure 4.26: (a) Punching shear strength correlated to the crack opening; (b) assumption of control perimeter at  $0.5d$  from the edge of the column; (c) punching shear resistance at the intersection between non-linear load-rotation curve and CSCT failure criterion.

The punching shear resistance corresponds to the intersection of the load-rotation curves with the CSCT failure criterion. It can be observed that the response of continuous slabs is stiffer than the response of isolated specimens, leading to higher punching shear resistances. In addition, the difference between continuous and isolated slab response predictions increases when the hogging reinforcement decreases (Belletti et al., 2018).

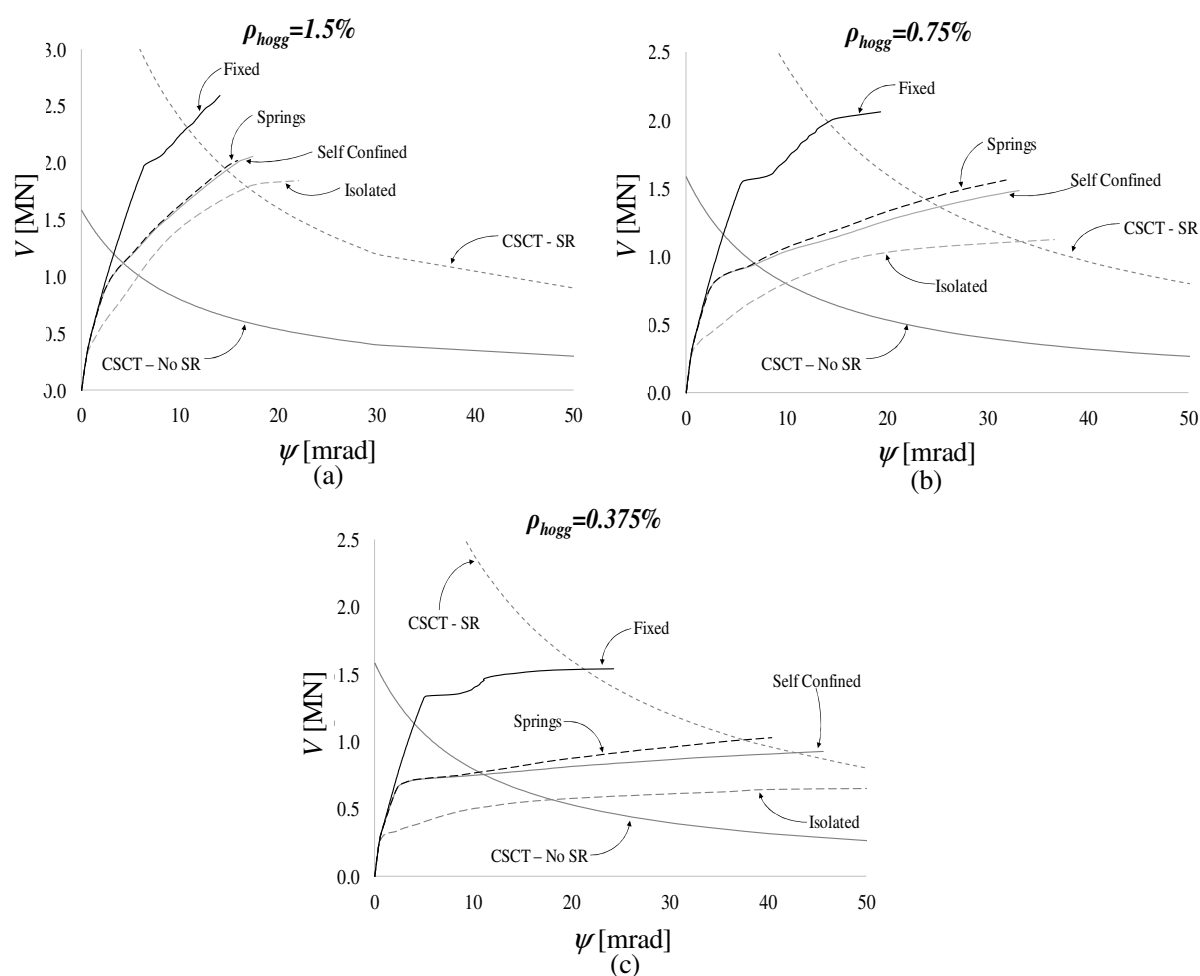


Figure 4.27: Load-Rotation curves vs CSCT Failure Criterion without shrinkage effect for: (a)  $\rho_{hogg} = 1.5\%$ , (b)  $\rho_{hogg} = 0.75\%$ , (c)  $\rho_{hogg} = 0.375\%$ .

In Figure 4.27, the load-rotation curves without shrinkage effect for the isolated specimen, self-confined continuous flat slab and laterally restrained slabs with springs and fixed boundary conditions are shown. To appreciate the difference between the resistance of flat slabs without and with shear reinforcement (SR), the failure criterion associated with shear reinforcement is also considered.

In case of lateral stiffening provided by shear walls, (the so called “Spring” case), the increasing of punching shear resistance with respect to the self-confined slab is very limited and the resistance increases as the hogging reinforcement decreases. There are no differences in the “Fixed” and “Post-Fixed” cases because the shrinkage effect is not considered.

Figure 4.28 shows the influence of concrete shrinkage on the punching shear resistance for all the cases investigated. Shrinkage effects on punching shear resistance are more evident in the “Fixed” case, causing anticipated cracking of the slab and initial loss of stiffness. For “Post-

“Fixed” case the initial loss of stiffness is not observed because the shrinkage is imposed before lateral displacement restraining. “Springs” and “Self-Confined” resistances with shrinkage effects are lower than without shrinkage effects. The shrinkage effect for “Isolated” cases is quite negligible.

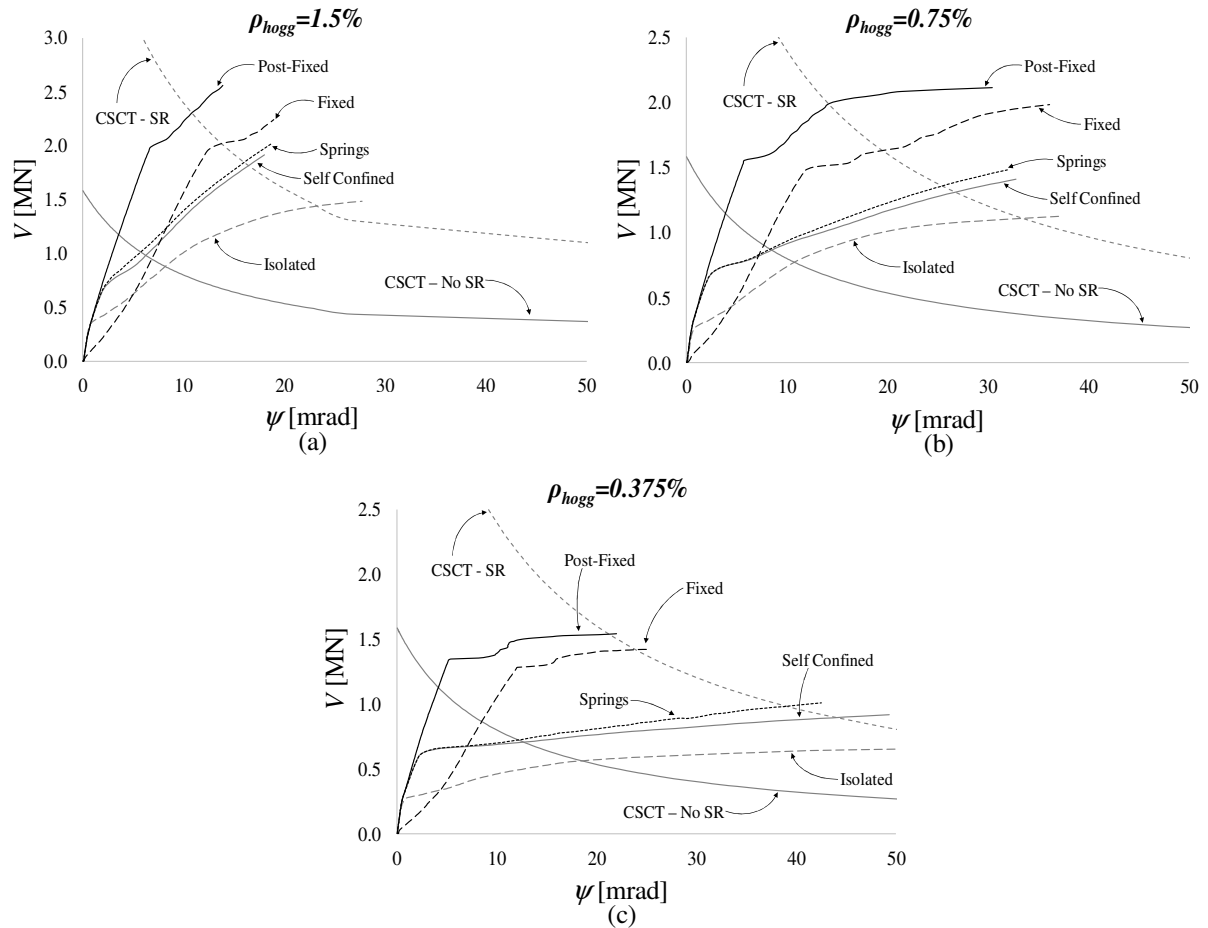


Figure 4.28: Load-Rotation curves vs CSCT Failure Criterion with shrinkage effect for: (a)  $\rho_{hogg} = 1.5\%$ , (b)  $\rho_{hogg} = 0.75\%$ , (c)  $\rho_{hogg} = 0.375\%$ .

#### 4.2.3.2 Membrane Action Dependency on Boundary Conditions

The dilatation of cracked concrete in the hogging area is restrained by the outer part of the slab, leading to the formation of radial and tangential stresses, respectively  $\sigma_{rad}$  and  $\sigma_{tang}$ .

This phenomenon increases stiffness and consequently the strength of slabs (Einpaul et al., 2015; Einpaul et al., 2016; Belletti et al., 2015<sup>a</sup>). The average values of radial stresses  $\sigma_{rad}$ , over the control perimeter  $b_0$  at distance  $0.5d$  from the edge of the column, have been calculated using NLFEA on continuous slabs.

Figure 4.29 shows the graph radial membrane action  $\sigma_{rad}$  vs slab rotation for the cases without shrinkage effect. For “*Springs*” case a negligible increment of  $\sigma_{rad}$  is observed, as expected. No differences between the “*Fixed*” and “*Post-Fixed*” cases can be obtained without shrinkage effects.

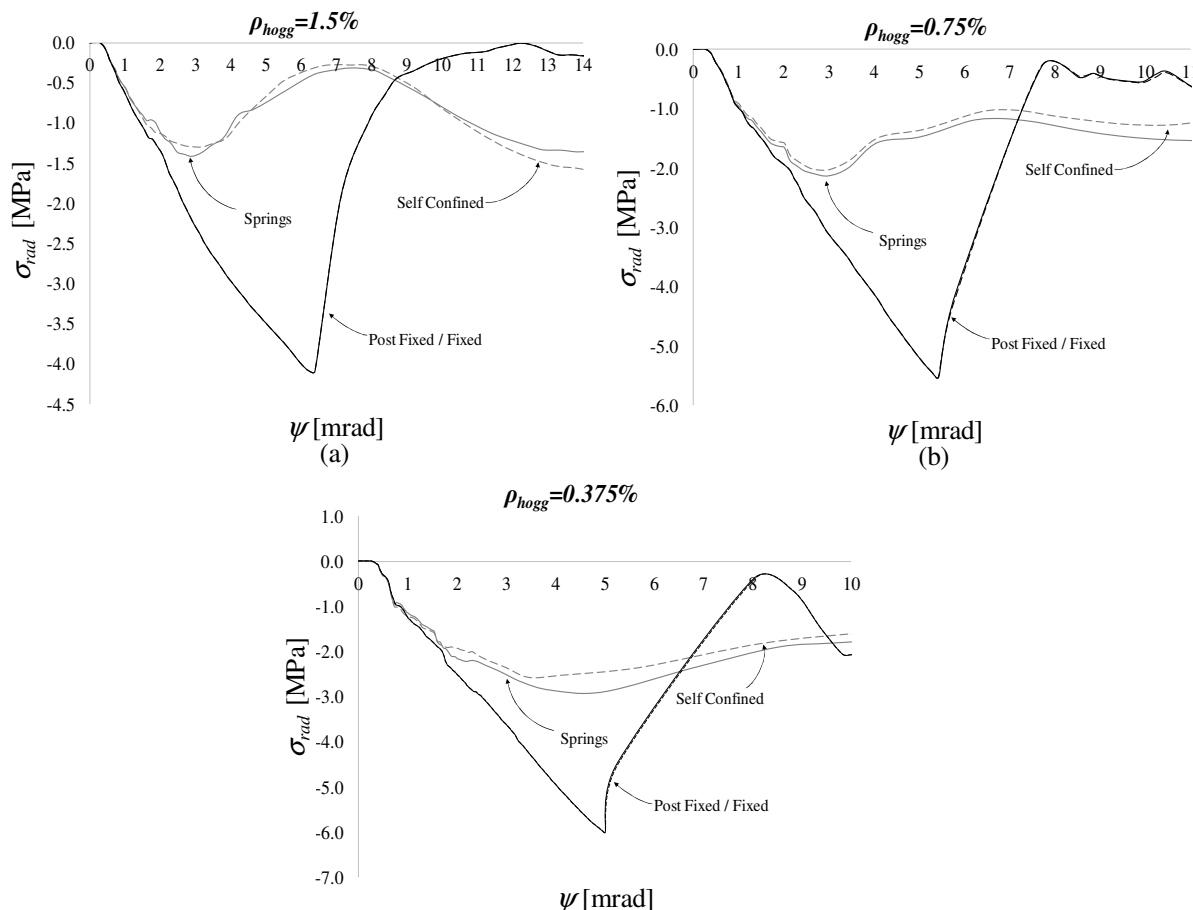


Figure 4.29: Radial stress without shrinkage effect for: (a)  $\rho_{hogg} = 1.5\%$ , (b)  $\rho_{hogg} = 0.75\%$ , (c)  $\rho_{hogg} = 0.375\%$ .

Figure 4.30a-c shows the radial membrane action  $\sigma_{rad}$  vs slab rotation for the cases with shrinkage effect. As expected, the concrete shrinkage leads to a reduction of radial stress  $\sigma_{rad}$ .

For “*Fixed*” case, due to the anticipated cracking of continuous slab, an initial tensile radial stress can be registered in the graph  $\sigma_{rad}$  vs  $\psi$ , causing a reduction of the compressive radial stress  $\sigma_{rad}$  peak and, consequently, a reduction of the punching shear resistance. For “*Springs*” case, applied before the application of shrinkage effects and self-weight, Figure 4.30a-c shows a similar trend than “*Fixed*” case but with lower consequences. For “*Post-Fixed*” case, the confining effects, achieved with fixed restraint of lateral displacement, can provide the maximum values of radial stresses. Figure 4.30d reports the values of initial tensile stress and

the peak values of compressive radial stress as a function of the hogging reinforcement ratio over the column. As expected, the maximum tensile stresses, causing anticipated cracking, is occurring for highest reinforcement ratios; at the contrary, the maximum compressive radial stresses can be encountered for lowest reinforcement ratios.

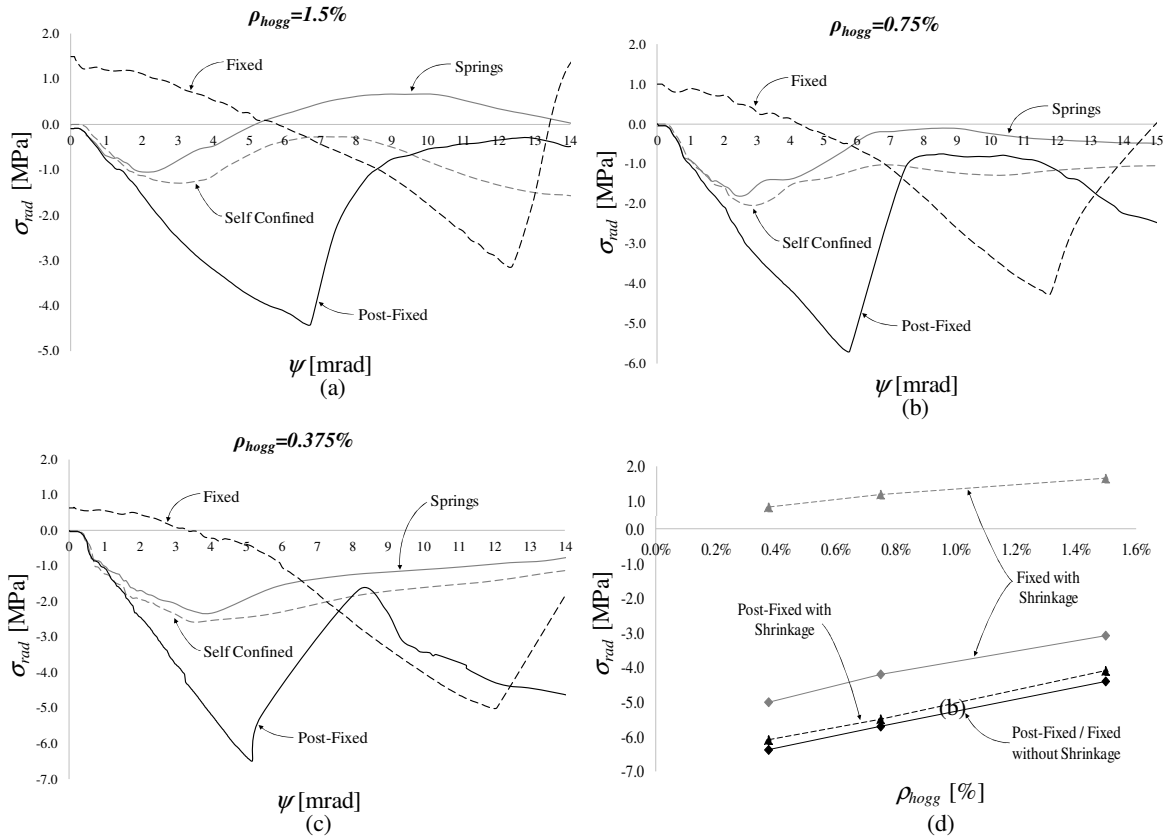


Figure 4.30: Radial stress with shrinkage effect for: (a)  $\rho_{hogg} = 1.5\%$ , (b)  $\rho_{hogg} = 0.75\%$ , (c)  $\rho_{hogg} = 0.375\%$ . (d) Peak tensile and compressive stresses with  $\rho_{hogg}$ .

Higher compressive stresses are observed in case of lower reinforcement ratios due to the higher difference between the stiffness in hogging and sagging zones.

Figure 4.28 and Figure 4.30 demonstrate that, for brittle failure mode (like shear and shear punching failure mode), the shrinkage effects at an early stage and boundary conditions (connected to the erection phases of buildings) can severely affect the serviceability and ultimate limit states. Furthermore, Figure 4.28 and Figure 4.30 show that membrane actions and punching shear resistance are affected by shrinkage effects in different measure depending not only on boundary conditions but also on reinforcement ratios.

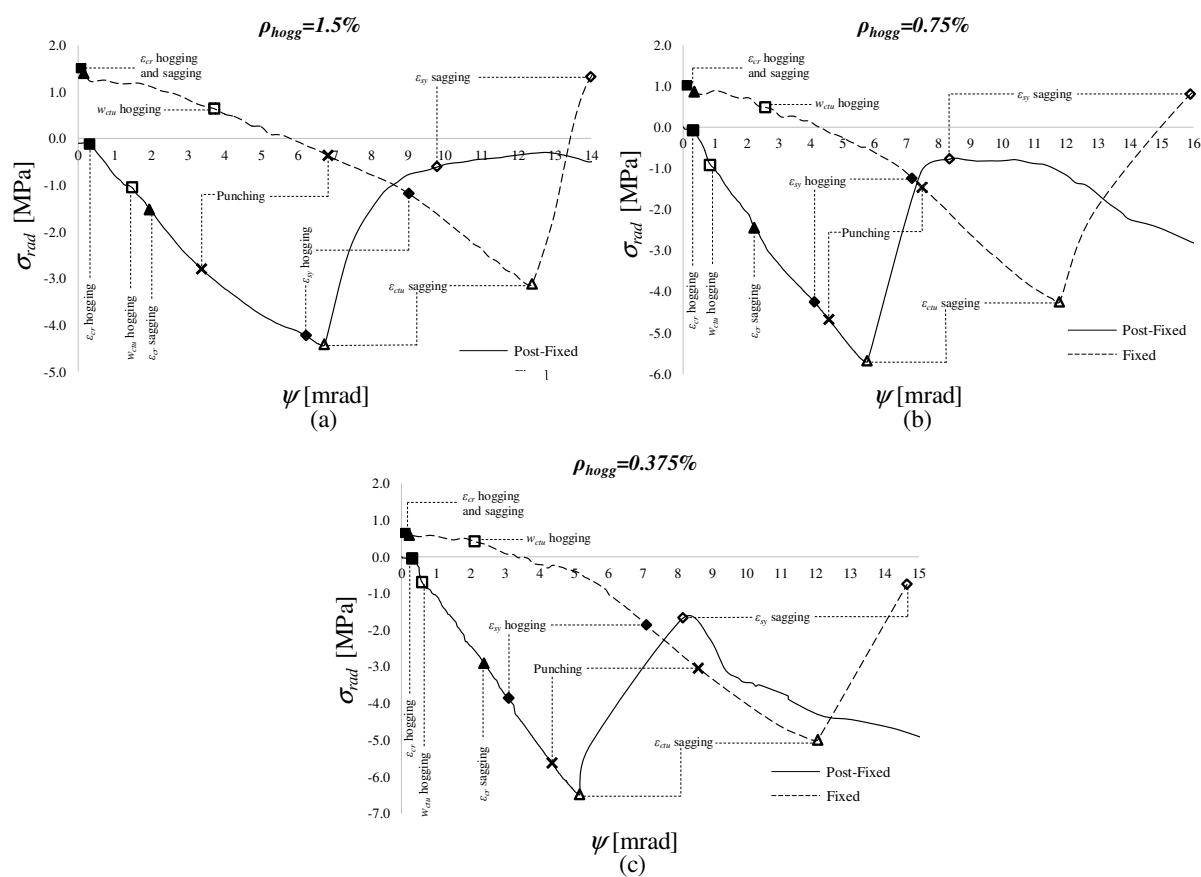


Figure 4.31: Radial stress with shrinkage effect for “Fixed” and “Post-Fixed” cases: (a)  $\rho_{hogg} = 1.5\%$ , (b)  $\rho_{hogg} = 0.75\%$ , (c)  $\rho_{hogg} = 0.375\%$ .

Figure 4.31 shows radial stress  $\sigma_{rad}$  for the “Post-Fixed” and “Fixed” cases considering shrinkage of concrete. The most interesting “events” are marked on radial membrane action  $\sigma_{rad}$  vs slab rotation  $\Psi$ : cracking of concrete (corresponding to  $\epsilon_{t,cr}$ ), maximum crack opening (corresponding to  $w_{ctu}$ , calculated as  $w_{ctu} = \epsilon_{t,u} \cdot a_m$  where  $a_m$  is the distance between cracks, see Belletti et al., 2017), yielding strain of hogging and sagging reinforcement ( $\epsilon_{sy}$ ). It can be noted from Figure 4.31a-c, that the peak value of radial stresses  $\sigma_{rad}$  occurs when the maximum crack opening  $w_{ctu}$  (corresponding to a zero residual tensile stress) is achieved in the sagging area since this circumstance corresponds to the maximum tension ring effect. Depending on the intersection between NLFEA curve and CSCT failure criterion, punching shear failure occurs before yielding of hogging reinforcement for high reinforcement ratio ( $\rho_{hogg} = 1.5\%$ ), after yielding of hogging reinforcement but before yielding of sagging reinforcement for medium and low reinforcement ratio ( $\rho_{hogg} = 0.75\%$  and  $\rho_{hogg} = 0.375\%$ ). Note that for the “Fixed” case, the cracking of hogging and sagging zone are almost simultaneous because of tensile in-

plane stresses. The achievement of  $w_{ctu}$  corresponds to the first plateau observed in load-rotation curves Figure 4.27 and Figure 4.28.

It is important to observe that the sequence of aforesaid events is the same also without considering shrinkage effect.

#### 4.2.3.3 *Moment Redistribution Effect*

The most significant assumption of design methods consists in a constant position of the contraflexure point at  $0.22 L$ , that is valid for isolated elements up to failure. However, for self-confined or fully confined slabs, moment redistribution occurs after the loss of stiffness in the hogging area due to cracking of concrete, triggering to a reduction of  $r_s$ .

Figure 4.32 shows the variation of the point of contraflexure  $r_s$  with the slab rotation  $\Psi$ , neglecting the shrinkage effect. Before cracking in the hogging area, the position of this point remains constant and corresponds approximately to  $0.22 L$ , as expected, then it tends to move closer to the column. Figure 4.32a shows the position of the point of contraflexure  $r_s$  for a “Self-Confined” slab; Figure 4.32b shows the “Post-Fixed” case (equivalent of “Fixed” case if shrinkage effect is neglected), where  $r_s$  tends to decrease more than for self-confined slab, leading to an increment of the punching shear resistance. After a rotation  $\Psi$  about 2 mrad, the point of contraflexure tends to move again to the column, for both cases. It is important to point out that the changing position of  $r_s$  is more pronounced for low reinforcement.

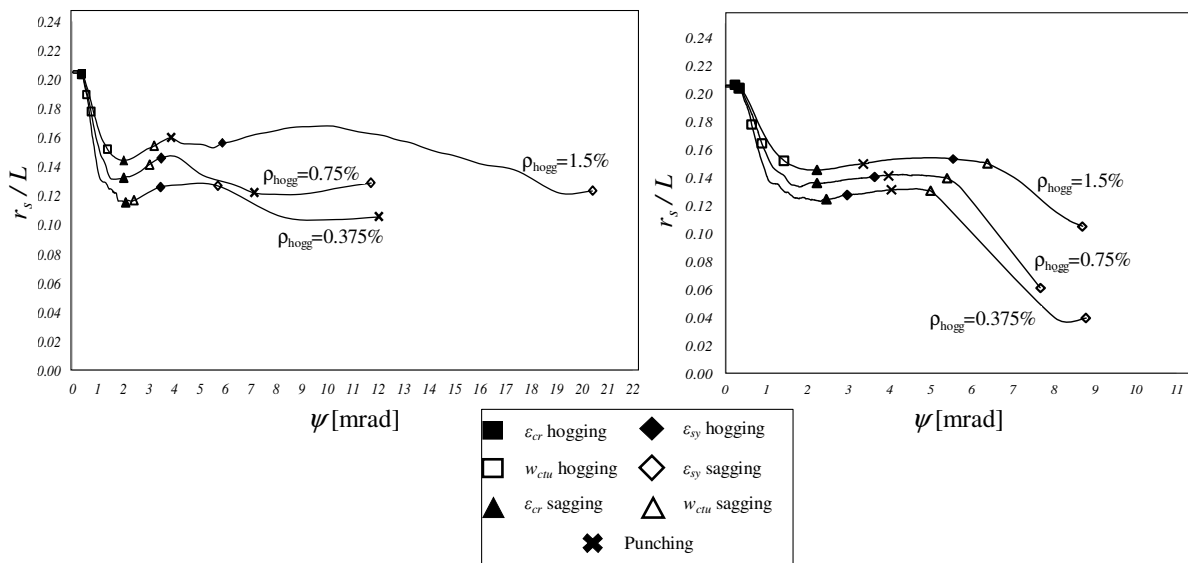


Figure 4.32: Variation of the point of contraflexure  $r_s$  as a function of the rotation  $\Psi$  without shrinkage effect: (a) “Self-Confined” slab, (b) “Post-Fixed” (or “Fixed”) case.



### 4.3 Concluding Remarks

In this chapter, the combined effect of tension stiffening and shrinkage is analysed.

Shrinkage affects significantly tension stiffening causing an underestimation of its value, in function of the amount of shrinkage and the reinforcing percentage. More specifically, neglecting shrinkage leads to a perceived effect on tension stiffening.

Firstly, the tension members analysed in Chapter 3 are modelled in order to validate the implemented formulation. Considering the combined effect of shrinkage and tension stiffening has permitted to obtain better results in terms of load-strain curve respect to consider only the shrinkage contribution; however, the tension stiffening contribution increases with the strain, differently to experimental observation. This is mainly due to the simplified modelling approach adopted in this work, that considers the reinforcement smeared along the entire height of the section. Adopting a simplified modelling means that, when the tension member is loaded equal strains characterize all the non-linear finite elements. Consequently, all elements and all integration points are cracked.

Afterwards the updated version of the PARC\_CL 2.1 formulation was applied to RC beams tested by Caldentey et al (2013). The beams were designed to study the influence of different mechanical parameters on tension-stiffening. In this case, a more refined modelling technique is used: this aspect has permitted to obtain a more realistic crack pattern and stress-strain profiles along rebars length. Comparison with experimental results has been demonstrated the reliability of the model and the importance to consider the combined effect of shrinkage and tension-stiffening in order to obtain more realistic results by means NLFEA.

Finally, tension stiffening and shrinkage formulations are applied to the study of continuous slabs. The dependency between membrane action and punching shear resistance on the reinforcement layout and boundary conditions are analysed. Very interesting conclusions about shrinkage are emerged:

- shrinkage of concrete leads to a reduction of membrane action and, consequently, of punching shear resistance. This effect is more pronounced for slabs with high reinforcement ratios (where restrained deformations cause higher tensile membrane stresses with anticipated cracking).
- shrinkage effect is strongly depending on boundary conditions and erection phases of buildings.

## 4.4 References

- ACI Committee 318 (2014). Building Code Requirements for Structural Concrete (ACI 318-14) and Commentary.
- Barros M.H.F.M., Martins R.A.F., Ferreira C.C.* (2001). Tension stiffening model with increasing damage for reinforced concrete. *Engineering Computations (Swansea, Wales)*, 18(5-6): 759-785.
- Bazant Z.P., and Oh B.H.* (1984). Deformations of progressively cracking reinforced concrete beams, *American Concrete Institute Journal*, Vol. 81:268-278.
- Belletti B., Walraven J.C., Trapani F.* (2015a). Evaluation of compressive membrane action effects on punching shear resistance of reinforced concrete slabs. *Engineering Structures*, 95(7):25-39
- Belletti B., Pimentel M., Scolari M., Walraven J.C.* (2015<sup>b</sup>). Safety assessment of punching shear failure according to level of approximation approach. *Structural Concrete*, 16(3):366-380.
- Belletti B., Damoni C., Cervenka V., Hendriks M.A.N.* (2016). Catenary action effects on the structural robustness assessment of RC slab strips subjected to shear and tensile forces. *Structural Concrete*, 17(6):1003-1016.
- Belletti B., Scolari M., Vecchi F.* (2017). PARC\_CL 2.0 crack model for NLFEA of reinforced concrete structures under cyclic loadings. *Computers and Structures* 191: 165-179.
- Belletti, B., Muttoni, A., Ravasini, S., Vecchi, F.* (2018). Parametric analysis on punching shear resistance of reinforced concrete continuous slabs. *Magazine of Concrete Research*, <https://doi.org/10.1680/jmacr.18.00123>.
- Bischoff P.H.* (2001). Effects of shrinkage on tension stiffening and cracking in reinforced concrete; *Canadian Journal of Civil Engineering*, 28: 363-374.
- Bischoff P.H.* (2008). Discussion of Tension Stiffening in Lightly Reinforced Concrete Slabs. By Gilbert R.I., *J Struct Eng*, 133(6):1259-1260.

- Caldentey A.P., Peiretti H.C., Iribarren J.P., Soto A.G.* (2013). Cracking of RC members revisited: influence of cover,  $\Phi/\rho_{s,ef}$  and stirrup spacing –an experimental and theoretical study. *Struct. Concr.*, 14(1): 69–78.
- CEB (1985). Cracking and deformation. Bulletin d’information N158. Paris, France.
- Choi C.K., Cheung S.H.* (1996). Tension stiffening model for planar reinforced concrete members. *Computer and Structures*, 59(1):179-90.
- Choi C.K., Cheung S.H.* (1994). A simplified model for predicting the shear response of reinforced concrete membranes. *Thin-Walled Structures*, 19:37-60.
- Ebead U.A., Marzouk H. (2005). Tension-stiffening model for FRP-strengthened RC concrete two-way slabs. *Materials and Structures*, 38, 193-200.
- Einpaul J., Ruiz M. F., Muttoni A.* (2015). Influence of moment redistribution and compressive membrane action on punching strength of flat slabs. *Engineering Structures* 86: 43–57.
- Einpaul J., Ospina C.E., Ruiz M.F., Muttoni A.* (2016). Punching Shear Capacity of Continuous Slabs. *ACI Structural Journal*, 113(4):861-872.
- Eligehausen R., Popov E.P., Bertero V.V.* (1983). Local Bond Stress-Slip Relationship of Deformed Bars Under Generalized Excitations, Report no. UCB/EERC-83/23, Earthquake Engineering Research Center, University of California, Berkeley, CA, USA.
- Eurocode 2 (2004). Design of Concrete Structures—General Rules and Rules for Buildings, EN 1992-1-1. Brussels, Belgium: CEN European Committee for Standardization; 225 p.
- fib* – International federation for structural concrete. *fib model code for concrete structures* 2010. Ernst & Sohn; 2013; 434 p.
- Floegl H., Mang H.A.* (1982). Tension stiffening concept based on bond slip. *Journal of the Structural Division ASCE*, 108(12):2681-701.
- Ghali A., Favre R., Elbadry M.* (2012). Concrete structures. Stresses and Deformations: Analysis and Design for serviceability, Spon. Press. London, UK.

- Gilbert R.I., Warner R. F.* (1978). Tension stiffening in reinforced concrete slabs. *Journal of the Structural Division, ASCE*, 104(12):1885-1900.
- Gilbert R.I.* (2001). Shrinkage, cracking and deflections – the serviceability of concrete structures. *Electronic Journal of Structural Engineering*, 1:15-37.
- Gilbert R.I.* (2007). Tension Stiffening in Lightly Reinforced Concrete Slabs. *J Struct Eng*, 133(6):899-903.
- Guidotti R.* (2010). Poinçonnement des planchers-dalles avec colonnes superposées fortement sollicitées (Doctoral thesis, in French), EPFL, Lausanne, Switzerland, p. 230.
- Guptam, A.K., Maestrini, S.R.* (1990). Tension-stiffness model for reinforced concrete bars. *Journal of the Structural Division, ASCE*, 116(3): 769-791.
- Hsu T.T.C.* (1996). Toward a unified nomenclature for reinforced concrete theory. *J. Struct. Eng.*, 122(3):275–283.
- Kaklauskas G., Gribniak V., Bacinskas D., Vainiunas P.* (2009). Shrinkage influence on tension stiffening in concrete members. *Eng Struct*, 31:1305-12.
- Kwag H.G., Song J.Y.* (2002). Cracking analysis of RC members using polynomial strain distribution function. *Engineering Structures*, 24:455-68.
- Lin C.S., Scordelis A.C.* (1975). Nonlinear analysis of RC shells of general form. *J Struct Div ASCE*, 101(3): 523-538.
- Muttoni A.*, (2008). Punching shear strength of reinforced concrete slabs without transverse reinforcement. *ACI Structural Journal*, 105:440–50.
- Muttoni A., Fernández Ruiz M., Simões J.T.* (2017). The theoretical principles of the critical shear crack theory for punching shear failures and derivation of consistent closed-form design expressions. *Structural Concrete*: 1–17.
- Nayal R., Rasheed H.A.* (2006). Tension stiffening model for concrete beams reinforced with steel and FRP bars. *ASCE Journal of Materials in Civil Engineering*, 18(6):831-841.

- 
- Parrotta J.E., Peiretti H.C., Gribniak V., Caldentey A.P.* (2014). Investigating deformations of RC beams: experimental and analytical study. *Computers and Concrete*, 13(6): 799-827.
- Prakhya G.K.V., and Morley C.T.* (1990). Tension-stiffening and moment-curvature relations of reinforced concrete elements. *ACI Structural Journal*, 87(5):597-605.
- Russo G., Romano F.* (1992). Cracking response of RC members subjected to uniaxial tension. *ASCE Journal of Structural Engineering*, 118(5):1172-90.
- Vecchio F.J., Collins M.P.* (1986). The modified compression-field theory for reinforced concrete elements subjected to shear, *J. Am. Concrete Inst.* 83(2): 219-231.
- Wu H.Q., Gilbert R.I.* (2008). An experimental study of tension stiffening in reinforced concrete members under short-term and long-term loads, UNICIV Report N. R-449, University of NSW.



# PARC\_CL 2.1 Crack Model for Existing RC Members

---

# 5

RC structures designed and built before the entry into force of seismic codes are characterized by lacking details and/or poor material characteristics. As consequence, they constitute a source of seismic risk worldwide, due to their vulnerability. The crisis of these structures can determine the global collapse with serious economic damage and possible loss of lives.

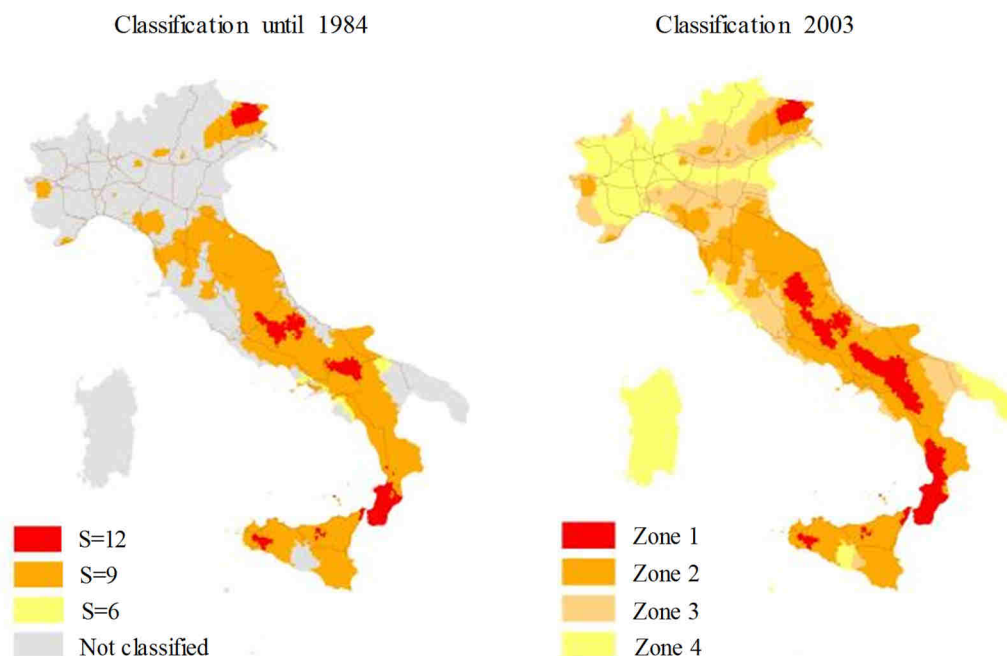


Figure 5.1: Seismic mapping of Italy: (a) classification according to the decrees issued until 1984; (b) classification according to OPCM n.3274 20.03.2003.

The Italian building heritage is characterized by an important component of RC structures built before the seismic classification of the site. Currently, in Italy, it is estimated that 60% of the existing buildings were built in areas classified, at the time of the construction, as non-seismic. Moreover, a large part of these buildings mostly dates back to the post-war period, in particular the 60s, and have therefore reached and overcome their conventional service life. This could lead to deterioration and material deterioration problems even of the mechanical properties of the structural elements.

Despite the first Italian seismic regulations dates back to the beginning of the twentieth century, only in 1984 there was a first seismic classification of the Italian territory, which considered a large part of northern Italy "no seismic risk". In 2003 with the PCM Ordinance no. 3274 of 20.03.2003 the classification of the territory has been refined and extended also to the not yet categorized areas, Figure 5.1.

From a study conducted by Parisi et al. (2013) it emerged that, using the seismic zoning established in 2003 by Italian code, almost 60% of the structures (about three million) have been built without reference to seismic criteria, Figure 5.2.

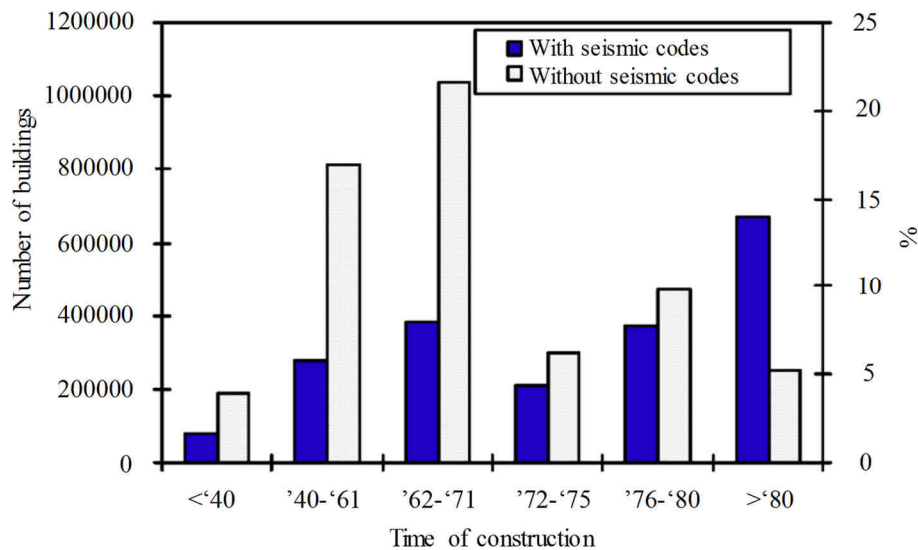


Figure 5.2: Distribution of RC buildings in seismic area, with reference to regulatory requirements at the time of construction, Parisi et al. (2013).

Furthermore, it must be considered that the previous seismic regulations imposed the problem of security in different terms, with less explicit objectives than the current situation, which is characterized by a clear reference to the limit states of damage and collapse and an



explicit treatment of post-elastic behavior. In general terms the previous seismic regulations follow a lower level of protection.

The analysis of the damage caused by the 2009 L'Aquila earthquake has shown (Oliveto et al., 2011) the main deficiencies that most influence the seismic response of buildings:

- “soft/weak” storey;
- frame designed only for gravity loading characterized by a weak and a strong direction of column;
- presence of squat columns;
- risk of collapse of non-structural elements;
- lack of details: bracketing of columns and nodes, anchoring length and reinforcement overlap;
- insufficient quality of concrete;
- smooth bars.

As consequence, existing RC structures are often subject to unexpected collapses typically not present in new buildings, linked to brittle failure on the concrete side or to the instability of longitudinal rebars. The need to develop numerical tools for the reliable prediction of failure mechanisms and of the performance of existing structures (also subject to corrosive phenomena) has emerged (Cosenza et al., 2002; Del Gaudio et al., 2018).

## 5.1 The Buckling Phenomenon

One of the main characteristic of existing structures is the presence of columns with sub-dimensioned cross-section. When subjected to large transverse and/or cyclic deformations, these elements typically fail for spalling of concrete cover (typically for strain values between 0.003 and 0.004, Papia et al., 1988) with consequent buckling of the longitudinal reinforcement (Wallace et al., 2012; Massone, 2013). In fact, during loading inversions, the concrete prevents the development of high compressive deformations in steel bars, but, when the concrete fails, the compressive steel strains increase with buckling of bars, Figure 5.3.

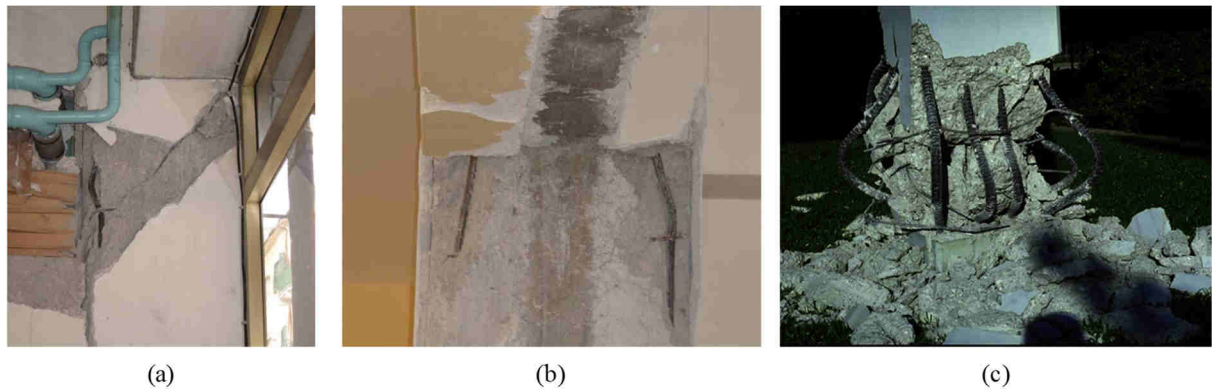


Figure 5.3: RC columns subjected to buckling: (a) shear crack and (b) absence of adequate stirrups at Scuola Media Statale Craducci, Aquila, Italy (Salvatore et al., 2009); (c) failure at the bottom of a column of the Imperial County Services building due to not adequate confinement (Comartin et al., 2004).

The cyclical damage and post-elastic buckling are also significant in the beam-column nodes, since the construction practice before the seismic regulations did not include brackets or prescribed too high spacing between them. Furthermore, the typical failure mechanism of RC bridges subjected to seismic loading is associated with flexural yielding of the columns or piers characterized by buckling and followed by fracture of longitudinal reinforcing bars.

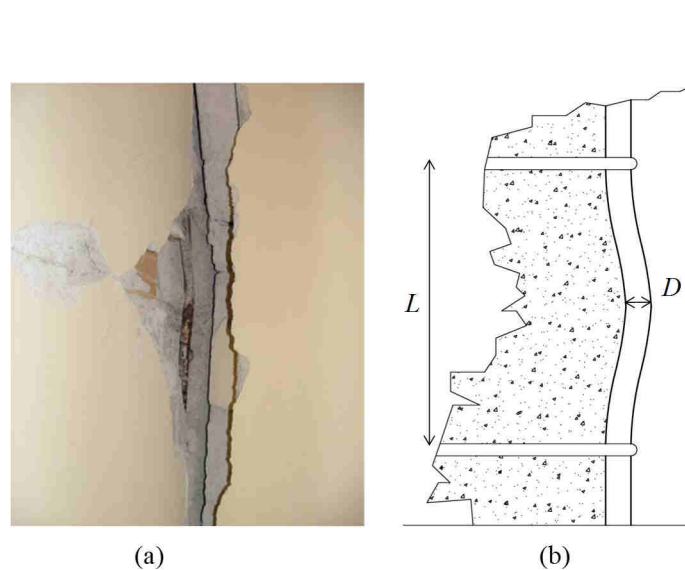


Figure 5.4: Buckling of longitudinal rebars: (a) a real case by Salvatore et al. (2009) and (b) local buckling.

The buckling of longitudinal reinforcement is avoided or limited by the stabilising effect provided by stirrups if they are not too distant. The typically observed failure modes associated with this phenomenon are primarily the bending of the longitudinal reinforcement between two consecutive stirrups, Figure 5.4, and, less commonly, an increase in slenderness due to the breaking of a stirrup, (Massone and López, 2014).

Since after cracking, the behaviour of the reinforced concrete section is controlled mainly by the steel, the accurate prediction depends on the precision of the steel constitutive law. It is, therefore, necessary to use a model able to consider the buckling effect of the longitudinal reinforcements. However, if the modelling of the monotonic behaviour has been carefully studied, the modelling of the cyclic behaviour is still under investigation (Monti and Nuti, 1992; Dodd and Restrepo-Posada, 1995; Gomes and Appleton, 1997; Albanesi et al., 2001; Dhakal and Maekawa, 2002<sup>a</sup>) both for ribbed and plain bars (Cosenza and Prota, 2005), Figure 5.5.

The monotonic compressive behaviour of steel subjected to buckling changes with the slenderness ratio  $\lambda$ , i.e. the ratio between the stirrups distance  $L$  and the longitudinal bar diameter  $D$ , Figure 5.4b. Mau and El-Mabsout (1989) through observation of the compressive behaviour of steel bars with different slenderness ratio founding that higher  $\lambda$  was, lower the yielding strength was. They identified a limit value of  $\lambda$ , equal to 5: if  $\lambda$  is lower than 5, the behaviour in tension and in compression is similar; otherwise, the buckling effect occurs.

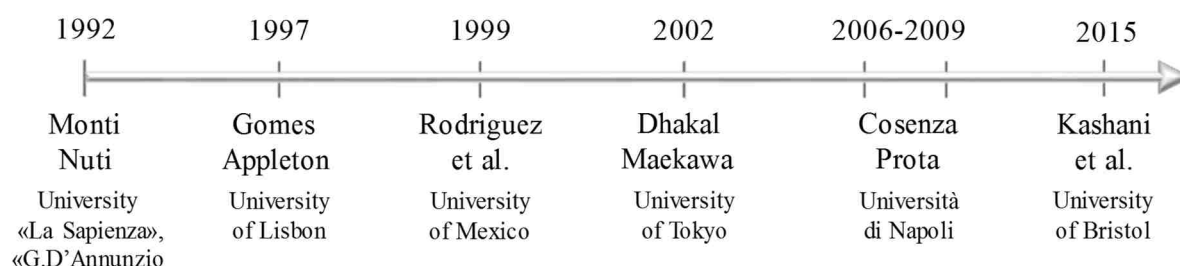


Figure 5.5: Authors who have proposed steel constitutive law including buckling in case of cyclic loading.

Monti and Nuti (1992) proposed the first model able to consider the effect of buckling in the cyclic behaviour of steel reinforcing bars. The model takes into account the effects of strain hardening on the yield stress and hardening ratio in compression by means a series of “hardening rules”.

The formulation was based on the experimental observation of carbon steel rebar Feb44 with yield stress 450 MPa. For this reason, the model is not able to properly catch the effect of buckling in case of bars with different yield stresses. Furthermore, the formulation is valid only for a limited range of slenderness values, i.e. less than 11.

Gomes and Appleton (1997) proposed a simplified model in which the monotonic compressive skeleton curve was based on the equilibrium of plastic mechanism of a buckled rebar. The authors described the buckled compressive branch with the proposed model and simulated the tensile branch and the unbuckled compressive branch by means the Menegotto

and Pinto (1973) model. The Gomes and Appleton model was set up based on the equilibrium equation of fix-ended column and hypothesized the plastic hinge occurring in the mid-span of the column. Furthermore, the model was not able to consider the effect of cyclic loading and unloading on the yield stress variation.

Rodriguez et al. (1999) conducted an experimental campaign on steel bars typically used in the construction industry in Mexico ( $f_y = 410$  MPa and  $f_u 550$ MPa) with slenderness values of 2.5, 4, 6, 8 as prescribed by Mexican seismic regulations. From these results derived a tension-strain model for steel with buckling. However, the model was not innovative because of the limited values of slenderness.

Dhakal and Maekawa (2002<sup>a</sup>), starting from Monti and Nuti (1992) experimental tests, elaborated the monotonic skeleton curves of reinforcement both in tension and compression. The formulation was based on the Menegotto and Pinto one but also took into account the update of the tangent modulus at the reversal points in tension and compression, respectively. However, this model too did not consider the yield stress variation at the reversal. Furthermore, the authors demonstrated (Dhakal and Maekawa, 2002<sup>b</sup>) that the compressive behaviour of reinforcing bar subjected to buckling depended both on the yield stress and the slenderness. In fact, through a series of experimental tests, they showed that reinforcements with different slenderness ratios and different yield stresses could generate an identical stress-strain curve if the combined parameter was the same.

Since in early 1970s smooth steel bars were widely used in Italy, Cosenza and Prota (2006) started a study on the cyclic behaviour of this type of reinforcement. The aim of the study was the calibration of a new constitutive model for smooth bars able to consider buckling. They proposed a new monotonic curve for smooth bars with a slenderness ratio between 5 and 70. They also extended this study to the cyclic case (Cosenza and Prota, 2009) but they did not propose analytical formulations. However, they highlighted that for the very high value of slenderness, the compression to tension reloading curve was characterized by an accentuated pinching effect.

More recently, Kashani et al. (2015) conducted a parametric study of the non-linear cyclic behaviour of ribbed reinforcing bars with and without corrosion. The behaviour of rebars with slenderness ratio higher than 8 is characterized by complex pinching. This effect is not included in existing constitutive models but it has a significant influence on the cycle degradation of RC elements subjected to seismic loading.

In this sense, a proper steel material model for rebar incorporating buckling is crucial for the seismic analysis of reinforced concrete structures. As a result, behaviour at large inelastic deformations may be over predicted with respect to strength and ductility.

Recently steel formulations including buckling were implemented in NLFE programs, specifically in fiber models. For example, the uniaxial steel model incorporating the combined material laws proposed by Gomes-Appleton (1997) and Dhakal-Maekawa (2002<sup>a</sup>) was implemented in Opensees (2011) (“ReinforcingSteel”) as well as the Kashani et al. (2014) model including buckling of corroded rebars. However, even if the fibre models are widely diffused in engineering practice, it is important to observe that this ‘type’ of model is able to consider only flexural failure and not shear or torsional effects. Nevertheless, buckling failure is associated also to shear failure, Figure 5.6. In order to fill this gap, formulations for steel including buckling have been implemented in the PARC\_CL 2.1 crack model.

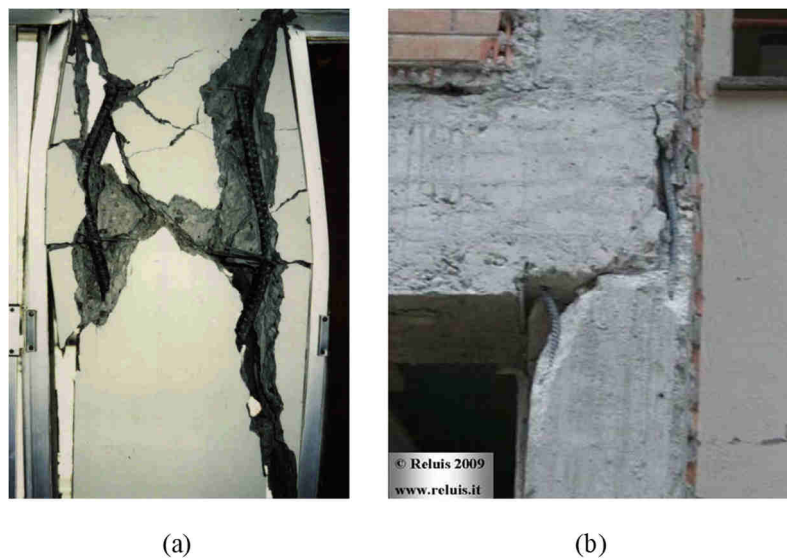


Figure 5.6: (a) Shear failure of columns and subsequent buckling of vertical reinforcement between the ties, (Comartin et al., 2004); (b) shear failure in beam-column joint (Verderame et al., 2009).

## 5.2 Implementation of Steel Constitutive Laws Including Buckling

In order to extend the PARC\_CL 2.1 crack model to the analyses of existing RC structures, two different constitutive laws for steel accounting for buckling have been implemented. More specifically, the Monti and Nuti model (1992) and Kashani et al. (2015) are first deeply studied and then added to the user subroutine.

The first constitutive law that will be presented (§5.2.1) is the Monti and Nuti (1992) one in its updated version by Zhou (2015), Zhou et al. (2014) and Zhou et al. (2015). The model

has been chosen because the basic formulation is based on the Menegotto and Pinto (1973) one already introduced in PARC\_CL 2.1. This allowed exploiting already existing variables without overloading the user subroutine with new variables to be memorized.

However, during the numerical simulations performed on experimental tests, which will be presented in detail in (§5.3), some shortcomings and limitations have been observed. For this reason, it was decided to introduce also the formulation proposed by Kashani et al. (2015) (§5.2.2). The results obtained by the two models are compared in terms of reliability respect to experimental results.

Both the constitutive laws are extensible to the case of corroded reinforcement. This feature is essential for future developments of the PARC\_CL 2.1 model.

## 5.2.1 Implementation of Monti and Nuti (1992) Model

### 5.2.1.1 *Monotonic Behaviour*

The Monti and Nuti (1992) formulation is based on the behaviour of bare bars characterized by different lengths  $L$  and diameters  $D$ . The  $L/D$  ratio is defined as slenderness ratio  $\lambda$ .

Experimental tests on bare bars subjected to monotonic load show that the buckling occurs when the slenderness ratio exceeds the critical slenderness ratio,  $\lambda_{cr}$ , equal to 5. Indeed, when  $\lambda \leq 5$ , the monotonic curve in compression coincides with the tensile one. In this case, the first branch in compression is defined by a straight-line asymptote with slope  $E_{si}$  until the yielding point **A**, followed by the asymptote (1) with slope equal to  $b_0^+ E_{si}$ , where  $b_0^+$  is the hardening coefficient in tension, defined as the ratio between the elastic modulus  $E_{si}$  and the hardening modulus  $E_{hi}$ , Figure 5.7. Instead, when  $\lambda$  exceeds the critical value, two different behaviours can be defined:

- $5 < \lambda < 11$ : the monotonic response is affected by buckling after the overcoming of  $\gamma_s$ . For a length equal to  $\gamma_s$ , defined in Eq.(5.1), an asymptote with positive slope  $b_0^+ E_{si}$  defines the rebar behaviour. Then, from the point **B**, an asymptote with negative slope equal to  $b_0^- E_{si}$  (3) is followed.  $b_0^-$  decreases with the increasing of the slenderness ratio and it does not depend to material properties.

$$\gamma_s = \frac{11 - \lambda}{e^{c \cdot \lambda} - 1} \geq 0 \quad (5.1)$$

where  $c$  is a parameter related to the type of rebar, equal to 0.5 in Monti and Nuti's test.

- $\lambda \geq 11$ : once the point A is reached the curve presents a negative slope  $b_0^- E_{si}$ , line (2).

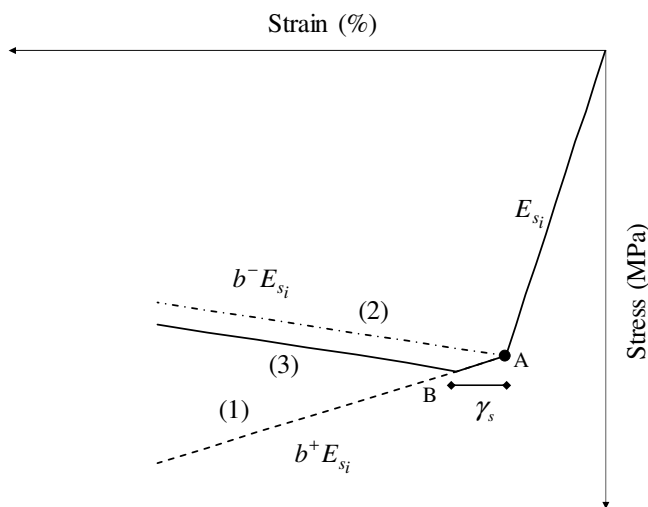


Figure 5.7: Monotonic compressive behaviour of steel, Monti and Nuti (1992).

The limit of the compressive stress, in presence of buckling, is defined by the asymptotic value  $\sigma_\infty$ , defined by Eq.(5.2), Figure 5.8.

$$\sigma_\infty = 6 \cdot f_{yi} / \lambda \tag{5.2}$$

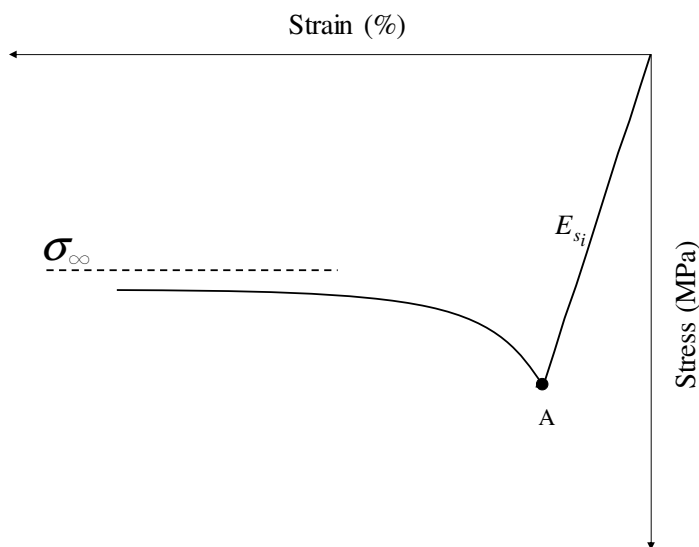


Figure 5.8: Asymptotic limit value in compression, Monti and Nuti (1992).

### 5.2.1.2 *Cyclic Behaviour*

The Monti and Nuti (1992) model updates the yield stress and the hardening coefficient  $b$  at each half-cycle. The stress variation is calculated using equations that incorporate the effects of hardening, generated by the plastic deformation of the bars caused by the achievement of the yield stress. If an isotropic sample subjected to tensile or compressive stresses undergoes, in the process, a load which exceeds the yield stress, a discharge and again a reload with respect to the opposite direction, the yield stress becomes smaller or greater depending on the plastic deformation to the previous half-cycle. This effect is characterized by a kinematic component and an isotropic component.

Due to buckling, the absolute value of the compressive stress decreases with increasing deformations after the yield stress. The yield stress referred to the  $n+1$  half-cycle,  $\sigma_0^{n+1}$ , is therefore defined in Eq.(5.3):

$$\sigma_0^{n+1} = f_{y_i} \cdot \text{sign}(-\xi_p^n) + \Delta\sigma_{KIM}^{n+1} \quad (5.3)$$

where  $f_{y_i}$  is the initial value of the yield stress for the  $i$ th order of bars. In this sense, it is necessary to underline that in case of not isotropic stainless steel rebar, i.e. rebars in which the yield strengths in tension and in compression are different, to distinguish two different values of yield stress are defined:  $f_{y_i}^t$  in tension and  $f_{y_i}^c$  in compression.  $\xi_p^n$  is the plastic excursion and  $\Delta\sigma_{KIM}^{n+1}$  is the additional contribution due to the kinematic and isotropic hardening, defined as in Eq.(5.4):

$$\Delta\sigma_{KIM}^{n+1} = P\Delta\sigma_{KM}^n + (1-P)\Delta\sigma_I^n \cdot \text{sign}(-\xi_p^n) \quad (5.4)$$

where  $P$  is the weight attributed to each rule (isotropic and kinematic) and can be calibrated on the basis of the experimental results as reported in Monti and Nuti (1992).  $P$  can range between 0 and 1.  $\Delta\sigma_{KM}^n$  and  $\Delta\sigma_I^n$  represent the stress contributions due to the kinematic and isotropic hardening respectively.

#### 5.2.1.2.1 *Kinematic and Memory rules*

As shown in Figure 5.9, the kinematic hardening effect in tension differs from compression. In fact, tensile strain (point **B**) can cause a reduction of the absolute value of the yield stress in



compression (point **C**); whereas the compressive strain (point **D**) can cause an increment of the yield stress in tension (point **E2**). Observing the half-cycles in Figure 5.9, it can be noticed that:

- $n=1$  half-cycle: the hardening branch **AB** is characterized by a positive slope that generates a positive stress increment ( $\Delta\sigma_1$ );
- $n=2$  half-cycle: the absolute value of the stress at the point **C** is less than the yield stress in compression (point **A1**). The stress decrease ( $\Delta\sigma_1$ ) is due to the kinematic rule. The negative value of the hardening branch causes a further decrease of the absolute value of the compressive stress in correspondence of the point **D**;
- $n=3$  half-cycle: the increase of the absolute value of the yield stress, from point **E1** to point **E2**, is due to the effect of the kinematic contributions deriving from the previous half-cycles  $n=1$  and  $n=2$ .

The stress variation due to the kinematic contribution,  $\Delta\sigma_{KM}^n$ , is evaluated in Eq.(5.5):

$$\Delta\sigma_{KM}^n = \sum_{i=1}^n b^i E^i \gamma_p^i \quad (5.5)$$

The memory rule is introduced by an additional plastic excursion,  $\gamma_p^n$ , Eq.(5.6):

$$\gamma_p^n = \left\langle \left| \xi_p^n - \xi_{\max}^n \right| \right\rangle \cdot \text{sign}(\xi_p^n) \quad (5.6)$$

where  $\langle u \rangle = uH(u)$  is the step function. If  $u > 0$ ,  $H(u) = 1$  otherwise  $H(u) = 0$ .  $\xi_{\max}^n$  is the maximum plastic excursion of the  $n$ th half-cycle and is defined in Eq.(5.7):

$$\xi_{\max}^n = \left| \xi_p^n \right| \quad (5.7)$$

The plastic excursion at the  $n$ th half-cycle,  $\xi_p^n$ , is defined in Eq.(5.8) and shown in Figure 5.9:

$$\xi_p^n = \varepsilon_r^n - \varepsilon_0^n \quad (5.8)$$

where  $\varepsilon_r^n$  is the strain corresponding to last strain reversal at the end of the  $n$ th half-cycle (in Figure 5.9 point **B** for  $n=1$  and point **D** for the  $n=2$ );  $\varepsilon_0^n$  defines the intersection point of the two asymptotes of the  $n$ th half-cycle (in Figure 5.9 point **C** for  $n=2$  and point **E2** for the cycle  $n=3$ ), Eq.(5.9).

$$\varepsilon_0^n = \varepsilon_r^{n-1} + \frac{\sigma_0^n - \sigma_r^{n-1}}{E_{s_i}^n} \tag{5.9}$$

where  $\sigma_0^n$  is the yield stress at the  $n$ th half cycle, Eq.(5.3), and  $\sigma_r^{n-1}$  is the last stress reversal of  $(n-1)$ th half-cycle.

In summary, the kinematic hardening rule results in a shift upwards. Moreover, the kinematic hardening has not effect if the absolute value of the plastic hardening of the current half-cycle,  $\xi_p^n$ , does not exceed the maximum plastic deformation of the previous half-cycle,  $\xi_{\max}^{(n-1)}$  (for example, if  $|\xi_p^2| \leq \xi_{\max}^1$  the variation of the tension is  $\Delta\sigma_2 = 0$ ): this means that, in presence of buckling, the kinematic hardening  $\Delta\sigma_{KM}^n$  is characterized by a memory component.

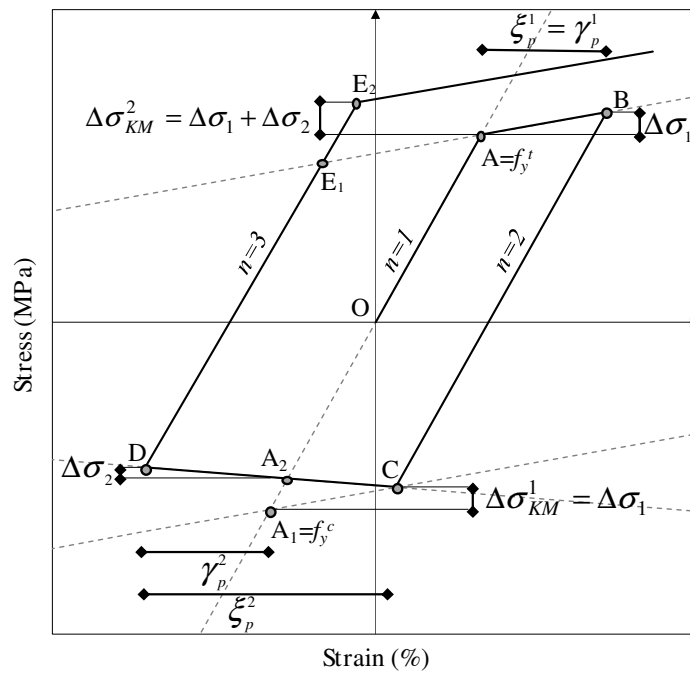


Figure 5.9: Kinematic and memory rule, Monti and Nuti (1992).

### 5.2.1.2.2 Isotropic Rule

The effect of isotropic hardening generates an expansion of the cyclic curve. In fact, analysing Figure 5.10, it is possible to observe:

- $n=1$  half-cycle: the hardening branch **AB** is characterized by a positive slope  $b^+$  generating an upward displacement of the curve;

- $n=2$  half-cycle: the yielding point **C** undergoes a downward displacement due to the isotropic rule applied to the previous half-cycle;
- $n=3$  half-cycle: the yielding point passes from **E<sub>1</sub>** to **E<sub>2</sub>**. The updated yield stress is translated by a quantity equal to the sum of the contributions of the two previous half-cycles.

The stress contribution associated with the isotropic rule is expressed in Eq.(5.10):

$$\Delta\sigma_I^n = \sum_{i=1}^n \left| b^i E_{s_i}^i \xi_p^i \right| \cdot \text{sign}(\Phi_p^n) \tag{5.10}$$

where  $\Phi_p^n$  is the plastic work, defined in Eq.(5.11).

$$\Phi_p^n = \frac{1}{2} (\sigma_r^n - \sigma_0^n) \xi_p^n \tag{5.11}$$

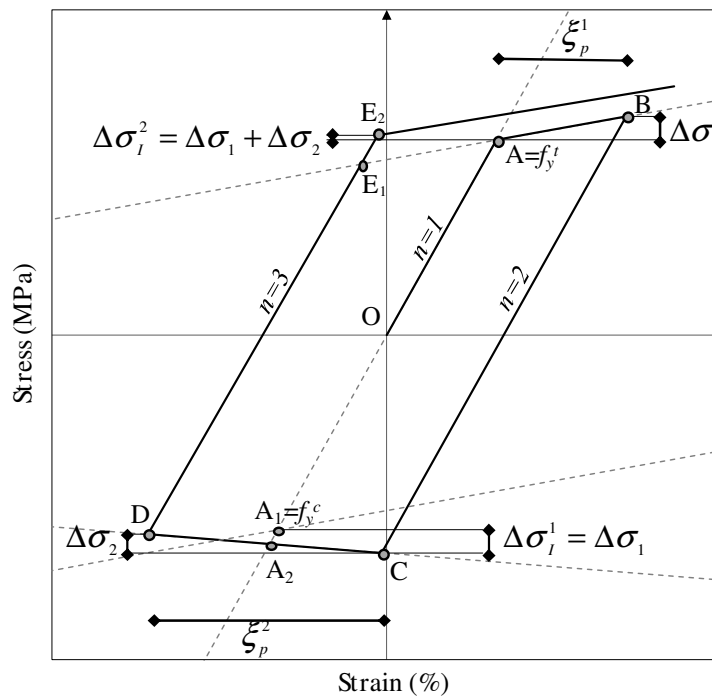


Figure 5.10: Isotropic rule, Monti and Nuti (1992).

The hardening factor  $b$  is always positive when the bar is subjected to tensile load but becomes negative in compression. This means that the plastic work  $\Phi_p^n$  assumes positive signs in case of tension and negative sign in compression. In fact, in tension the stress variation  $(\sigma_r^n - \sigma_0^n)$  and the plastic excursion  $\xi_p^n$  have concordant signs, consequently, the absolute value

of the compressive yield stress increases; whereas in compression the stress variation  $(\sigma_r^n - \sigma_0^n)$  is positive whereas the plastic excursion  $\xi_p^n$  is negative, consequently, the yield stress decreases.

### 5.2.1.2.3 The curvature parameter $R$

$R$  is the parameter that influences the shape of the transient curve from the first to the second asymptote: its value decreases with the half-cycles. So,  $R_1 > R_2 > R_3$ , Figure 5.11.

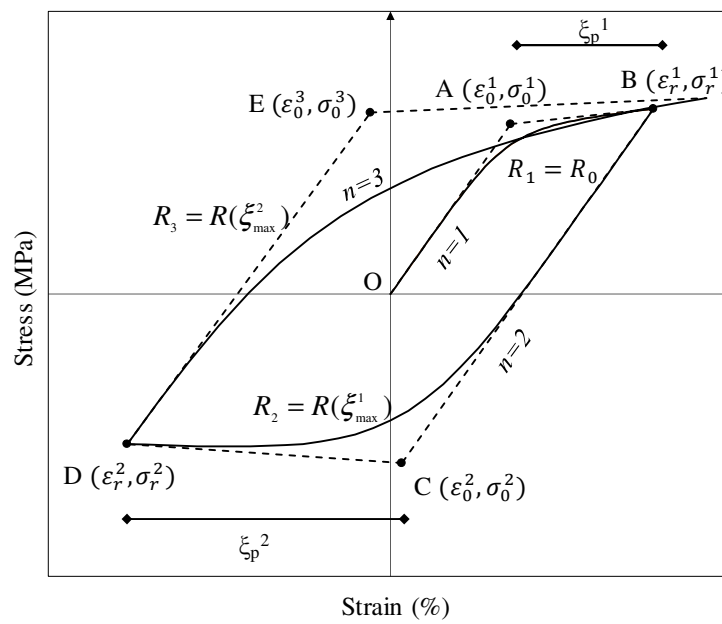


Figure 5.11: Degradation of curve transition.

In tension,  $\Delta\varepsilon > 0$ ,  $R$  is defined in Eq.(5.12):

$$R_{n+1} = R_0^t - \frac{A_1^t \cdot \xi_{\max}^n}{A_2^t + \xi_{\max}^n} \quad (5.12)$$

where to consider the possibility of anisotropic rebars (characterized by different behaviour in compression and tension), the following parameters are defined in Eq.(5.13)-(5.18).

$$R_0^t = \frac{\alpha\beta}{2} \cdot R_0 \quad (5.13)$$

where  $R_0$  is the first value assumed by the curvature. In general, it is imposed equal to 20 as indicated in §2.2.7.

$$A_1^t = \frac{1}{100} \cdot [\lambda_{cr} \cdot (\alpha\beta)^2 \cdot (\lambda - \lambda_{cr})] + \alpha \quad (5.14)$$

$$A_2^t = -\frac{8\alpha\beta}{10000} \cdot (\lambda - 4\lambda_{cr}) \quad (5.15)$$

$$\alpha = \frac{f_{yi}^t}{f_{yi}^c} \quad (5.16)$$

$$\beta = \frac{f_{yi}^c}{450} \quad (5.17)$$

$$\lambda_{cr} = \frac{5}{\sqrt{\beta}} \quad (5.18)$$

In compression, the value of  $R$  is expressed by means Eq.(5.19):

$$R_{n+1} = \max(R_1; R_2) \quad (5.19)$$

where:

$$R_1 = R_0^c - \frac{A_1^c \cdot \xi_{\max}^n}{A_2^c + \xi_{\max}^n} \quad (5.20)$$

$$R_2 = 10 \cdot (\lambda - \lambda_{cr}) \cdot b_0^+ \quad (5.21)$$

$$R_0^c = \frac{\beta}{2} \cdot R_0 \quad (5.22)$$

$$A_1^c = \alpha A_1^t \quad (5.23)$$

$$A_2^c = \frac{6\beta}{1000} \cdot (\lambda - 2\beta) \quad (5.24)$$

#### 5.2.1.2.4 The hardening ratio $b$

In Figure 5.7, the effect of the hardening ratio  $b$  on the monotonic compressive curve is presented:

- $b=b^+ > 0$ , both stress and strain increase after reaching the yield stress;
- $b=b^- < 0$ , the absolute value of the stress decreases whereas the deformation increases after reaching the yield stress.

Subsequently, the value of  $b$  varies according to the plastic deformation,  $\xi_p^n$ .

In tension, the value of  $b$  is formulated by Eq.(5.25).

$$b_{n+1} = b_0 \exp\left(\frac{b_0 E_{s_i} \sum_{i=1}^n \gamma_p^i}{-0,5 f_{y_i}^t}\right) \quad (5.25)$$

where  $b_0$  is the ratio between the initial hardening, defined as in §2.2.7.

In compression, the value of  $b$  is formulated by Eq.(5.26).

$$b_{n+1}^- = b_0^- \exp\left(\frac{b_0^- E_{s_i} \sum_{i=1}^n \gamma_p^i}{f_{y_i}^t \cdot (1 - \lambda_{cr} / \lambda)}\right) \quad (5.26)$$

where:

$$b_0^- = a \cdot (\lambda_{cr} - \lambda) \quad (5.27)$$

with the experimental parameter  $a=0.0025$ .

#### 5.2.1.2.5 Elastic modulus $E_s$

According to experimental analyses, the elastic modulus at the reversal from compression to tension could be different from the original elastic modulus  $E_{s_i}$  of the rebar. So, two different formulations in tension and in compression are proposed, Figure 5.12:

- in tension the elastic modulus does not degrade, remaining equal to the initial one  $E_{s_i}$ ;
- in compression the elastic modulus is degraded, and it is calculated as in Eq.(5.28):

$$E_{s_i}^n = E_{s_i} \left[ a_5 + (1 - a_5) \cdot \exp\left(-a_6 \left(\xi_p^{n-1}\right)^2\right) \right] \quad (5.28)$$

with  $a_6=1500$  and:

$$a_5 = 1 + \frac{(\lambda_{cr} - \lambda)}{7.5} \quad (5.29)$$

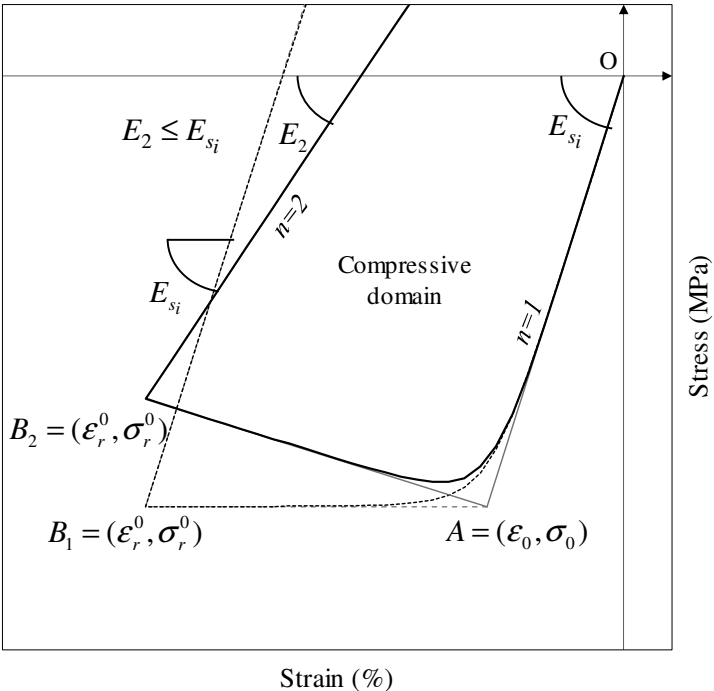


Figure 5.12: Elastic modulus degradation in compression.

One of the main limitations of the model is that formulations have been calibrated according to the results obtained on a limited set of reinforcements. Taking as reference the parameter  $a_5$  presented in Eq.(5.29) and used for the calculation of the degraded elastic modulus, it is shown in Figure 5.13a that, when  $\lambda$  exceeds the value of 12.5,  $a_5$  becomes negative. These values do not negatively influence the analysis until  $\xi_p^{n-1}$  does not reach high values (typical of buckling failure). When it becomes large (this value can change according to  $\lambda$ , Figure 5.13b), the square bracket in Eq.(5.28) becomes negative and consequently the reduced elastic modulus becomes negative. This involves non-physical values.

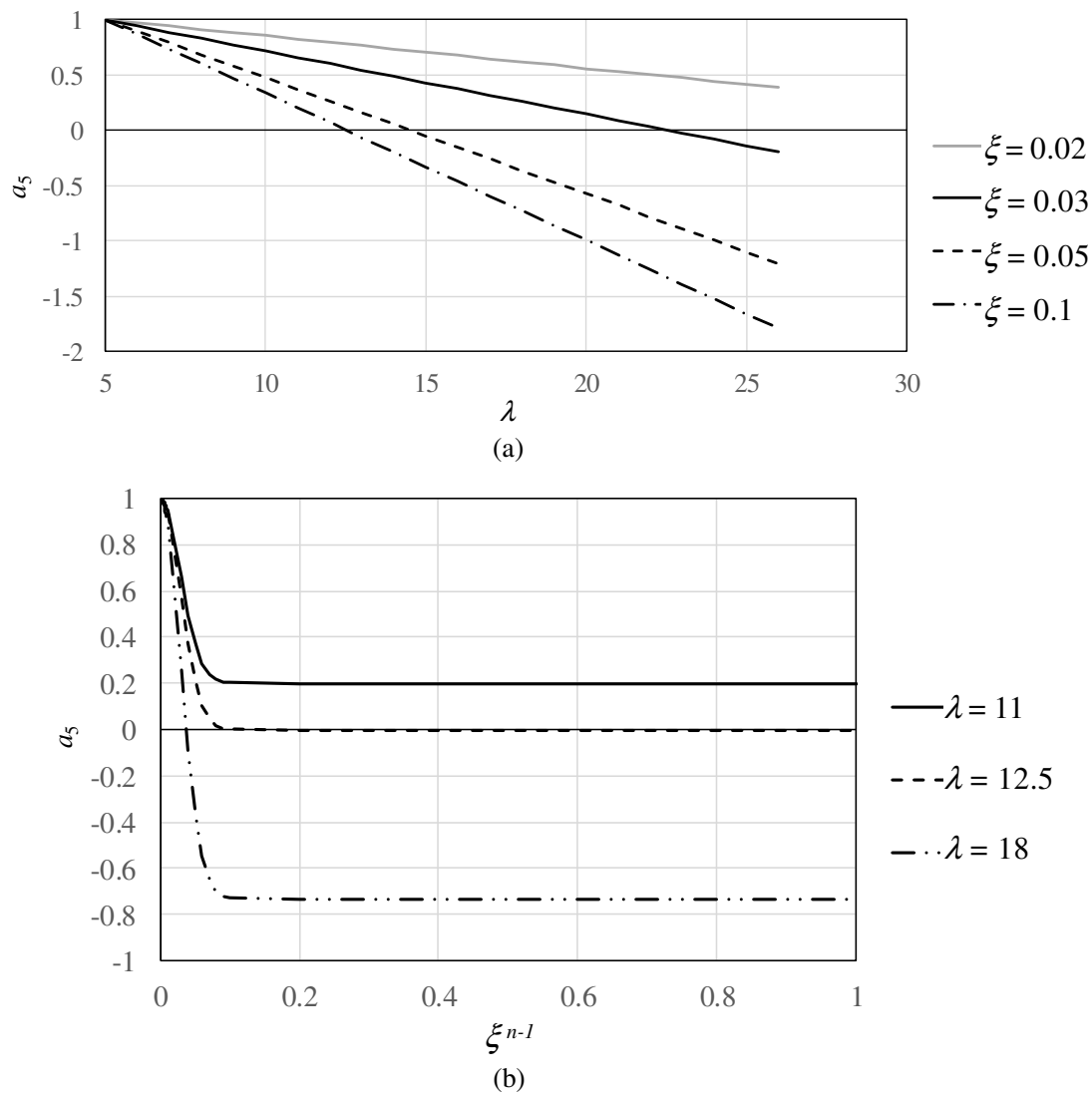


Figure 5.13: Value of  $a_s$  in function of (a)  $\lambda$  for assigned values of  $\xi^{n-1}$  and (b)  $\xi^{n-1}$  for assigned values of  $\lambda$ .

### 5.2.2 Implementation of Kashani et al. (2015) Model

Kashani et al. (2013<sup>a</sup>) conducted a parametric study on the behaviour of corroded and non-corroded bars subjected to monotonic and cyclic loading. The results on bare bars with yield strength between 400 and 500 MPa showed that, when the slenderness ratio  $\lambda$  exceeded the value of 8, the reinforcements present a complex pinching effect in the hysteretic cycles. Furthermore, it becomes more severe increasing the slenderness ratio  $\lambda$ . Also, Nakamura et al. (2002) and Prota et al. (2009) came up to the same conclusions. Despite the pinching effect has a significant influence on the cyclical degradation of elements subjected to cyclic loads, it is not considered by the Monti and Nuti (1992) model. For this reason, the model proposed by



Kashani et al. (2015) has been implemented in the new version of the PARC\_CL 2.1 crack model.

The experimental campaigns, conducted on reinforcement bars with yield stresses between 400 and 500 MPa and subjected to compressive loads, have highlighted that buckling does not manifest itself for  $\lambda < 6$ . In this case, the compressive behaviour can be assumed to be equal to their tensile behaviour. For  $6 < \lambda < 8$  the samples buckle but, since the length is relatively small, the buckling effect does not influence the post-yield softening in compression. Also in this case the compressive behaviour can be assumed as elastic perfectly plastic. When  $\lambda \geq 8$ , the effect of buckling results in a compression softening curve, Figure 5.15.

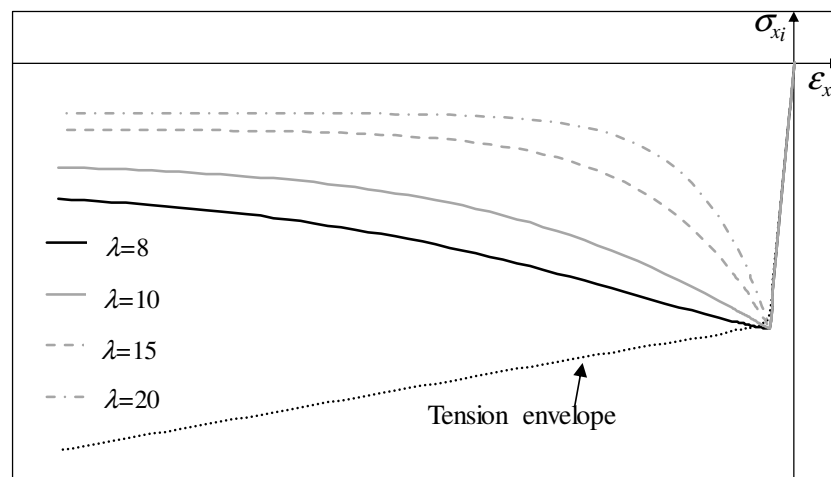


Figure 5.14: Compressive envelope curve for different slenderness ratio.

Therefore, starting from the observation of bare bars with  $8 \leq \lambda \leq 30$ , Kashani et al. (2015) proposed a stress-strain model able to consider the cyclical and fatigue degradation in compression and the pinching effect.

The model is composed of the following main states: tensile envelope *TE*; compression envelope *CE*; unload-reload response for tension to compression *URTC*; unload-reload response for compression to tension *URCT*. These represent the main curve as shown in Figure 5.15. In addition, three more branches are proposed: incomplete unload-reload cycle *IURC*; degradation in buckling strength due to cyclic loading *BUCKDEG*; degradation in tension strength due to low-cycle fatigue/cyclic loading *FATDEG*. In the PARC\_CL 2.1 crack model, for now, *FATDEG* rule is not taken into account.

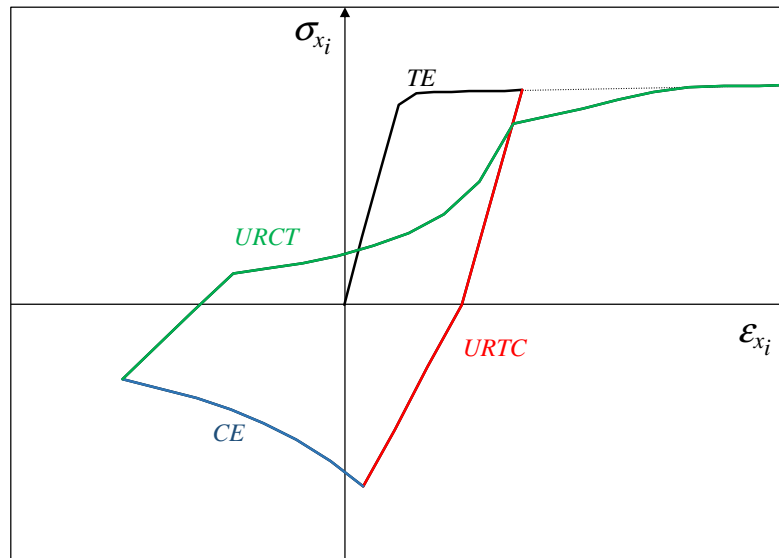


Figure 5.15: The main curve of the phenomenological hysteretic model proposed by Kashani et al. (2014).

### 5.2.2.1 Tensile Envelope TE

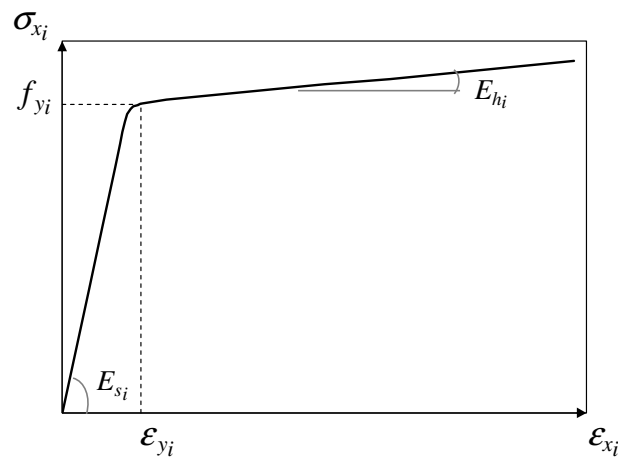


Figure 5.16: Tensile envelope curve of steel, Balan et al. (1998).

A continuous hyperbolic function between the two asymptotes of slope  $E_{si}$  and  $E_{hi}$  (Balan et al., 1998), Eq.(5.30), is used to simulate the monotonic tensile curve of the steel bar, Figure 5.16.

$$\sigma_{x_i} = f_{y_i} \frac{(1-\mu)}{2} \left[ 1 + \frac{(1+\mu)}{(1-\mu)} \frac{\epsilon}{\epsilon_{y_i}} - \sqrt{\left( \frac{\epsilon}{\epsilon_{y_i}} - 1 \right)^2 + \delta} \right] \quad (5.30)$$

where  $\mu$  is equal to  $Eh_i/E_{si}$ , whereas  $\delta$  is a shape parameter that defines the curvature radius of the transition between linear elastic and hardening region of the curve, according to Balan et al. (1998).

### 5.2.2.2 Compressive Envelope CE

The expression used to define the compressive envelope curve is a function of the so called non-dimensional slenderness ratio  $\lambda_p$  (Dhakal and Maekawa, 2002<sup>c</sup>) defined in Eq. (5.31):

$$\lambda_p = \sqrt{\frac{f_{yi}}{100}} \frac{L}{D} \quad (5.31)$$

The compressive envelope is defined by a first elastic part until the yielding, followed by an exponential law (Hill et al., 1989; Thai et al., 2011), Eq.(5.32):

$$\sigma_{xi} = \begin{cases} E_{si} \varepsilon & \text{if } \varepsilon \geq \varepsilon_{yi} \\ \sigma^* + (f_{yi} - \sigma^*) \cdot \exp(-\varepsilon_p \cdot (\rho_1 + \rho_2 \sqrt{\varepsilon_p})) & \text{if } \varepsilon < \varepsilon_{yi} \end{cases} \quad (5.32)$$

where  $\rho_1$  is the initial tangent of the post-buckling response curve,  $\rho_2$  is the rate of change of the tangent,  $\varepsilon_p = |\varepsilon - \varepsilon_y|$  is the plastic strain and  $\sigma^*$  is the asymptotic lower stress limit, Figure 5.17.

$$\rho_1 = 4.572\lambda_p - 74.43 \quad (5.33)$$

$$\rho_2 = 318.4 \exp(-0.071\lambda_p) \quad (5.34)$$

$$\sigma^* = 3.75 \frac{f_{yi}}{L/D} \quad (5.35)$$

The parameters defined in Eq.(5.33)-(5.35) were obtained through post-processing of experimental results by means Matlab tools, as explained in Kashani et al. (2015). A large database consisting of 50 bare bars samples with different yield stress values and slenderness ratios was used.

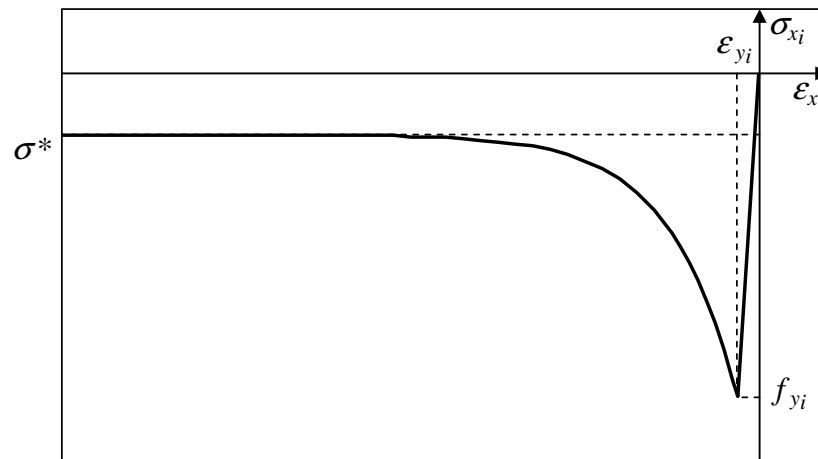


Figure 5.17: Buckling effect on the compressive envelope curve, Kashani et al. (2014).

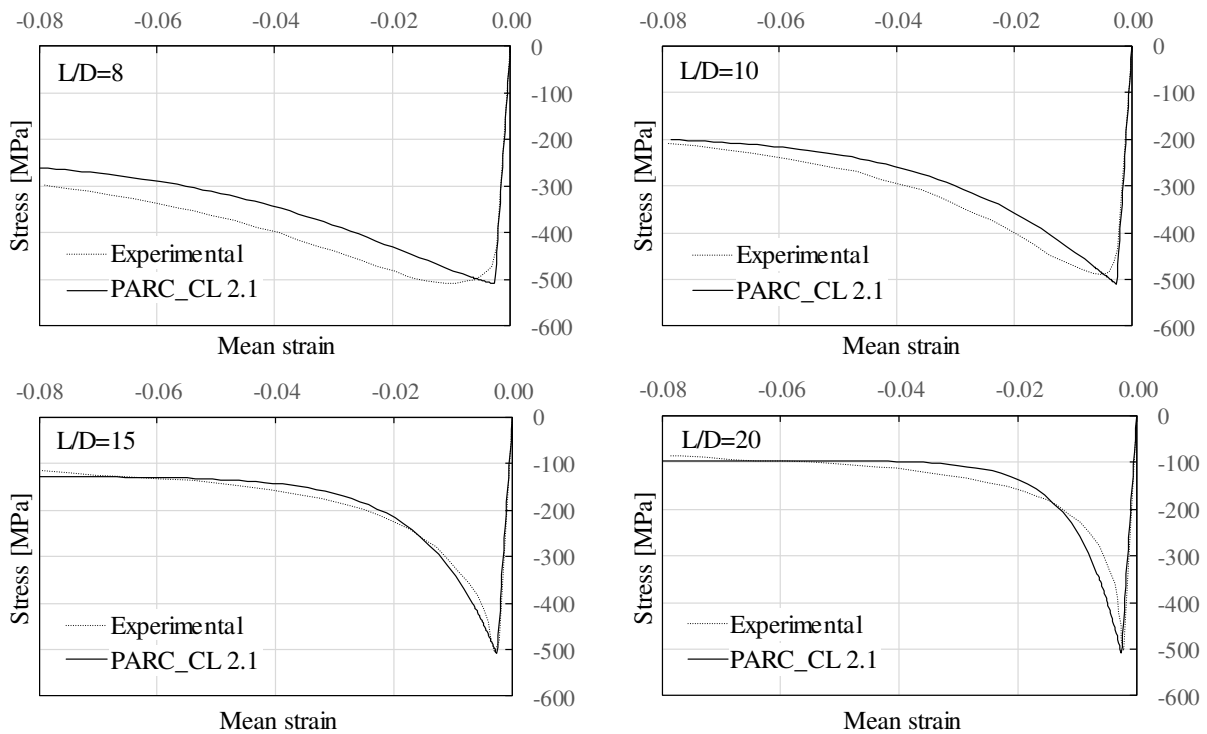


Figure 5.18: Comparison of experimental results obtained on bare bars with different values of slenderness ratio (Kashani et al., 2014) and PARC\_CL 2.1 ones.

These formulations have been included in the PARC\_CL 2.1 model and used to perform non-linear finite element analyses on bare bars, tested monotonically by Kashani et al. (2014), with the aim to validate the model. The samples have been modeled with simple M3D4R membrane elements characterized by a single integration point. In Figure 5.18, the PARC\_CL 2.1 results are compared with the experimental results (Kashani et al., 2014) providing good results in terms of stress-strain behaviour and minimum stress limit asymptote  $\sigma^*$ .

The experimental results have shown that the cyclic behaviour of bare bars or reinforcement of RC columns (Moyer and Kowalsky, 2003) depends on the applied strain history and the slenderness ratio (Cosenza and Prota, 2009). The results obtained from tests on bare bars with different values of  $\lambda_p$  and different load history were used by Kashani et al. (2014) to develop a constitutive model capable of predicting the stress and stiffness degradation during the unloading-reloading cycles induced by buckling phenomenon.

### 5.2.2.3 Unloading Reloading from Tension to Compression URTC

The unloading branch from tension to compression is defined by means of two linear branches defining the URTC branch. The first branch ends when the stress reaches a zero value and is characterized by the unloading stiffness  $E_{un}$ , calculated as proposed by Dodd et al. (1995), Eq.(5.36).

$$E_{un} = E_{si} \left( 0.82 + \frac{1}{5.55 + 1000\varepsilon_p} \right) \quad (5.36)$$

where  $\varepsilon_p$  is the plastic strain and it is defined as  $\varepsilon_p = \varepsilon_{un} - \varepsilon_y$ .

The second branch is defined by the reloading stiffness  $E_{sec}$ , obtained by Kashani et al. (2015) from numerical simulations of bare bars, Eq.(5.37).

$$E_{sec} = \frac{E_{si}}{1 + \left( \frac{\varepsilon_p}{0.005} \right)^{0.5}} \geq 0.2E_{si} \quad (5.37)$$

Finally, to consider the degradation of the compressive stress, the value of the buckling stress  $\sigma_{yc}$  is updated at each cycle in function of the plastic strain  $\varepsilon_p$ , Eq.(5.38).

$$\sigma_{yc} = \frac{f_{yi}}{1 + 0.7\varepsilon_p\lambda_p} \geq 0.25f_{yi} \quad (5.38)$$

Figure 5.19 shows the effects of Eq.(5.36)-(5.38) on the unloading URTC curve.

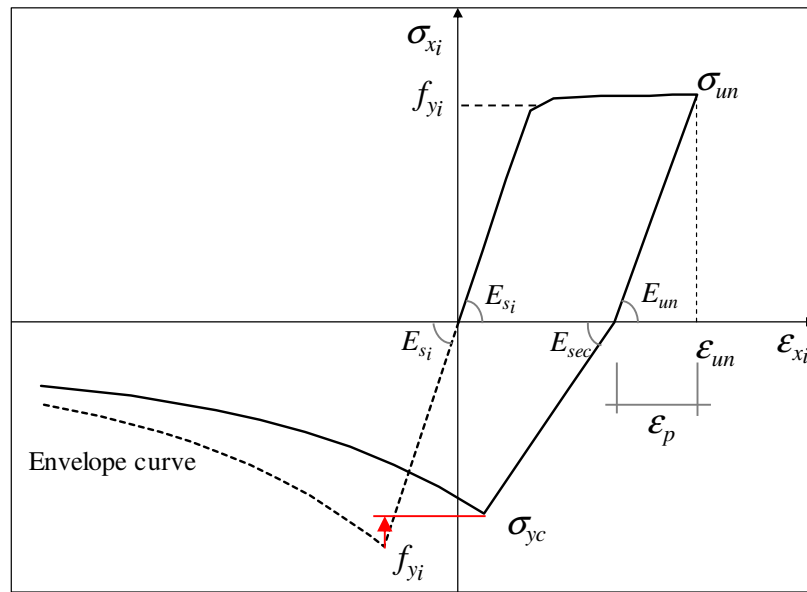


Figure 5.19: Unloading from tension to compression.

#### 5.2.2.4 Unloading Reloading from Compression to Tension URCT

Kashani et al. (2014) and Cosenza and Prota (2009) observed that the unloading-reloading branch from compression to tension of bare bars with slenderness ratio greater than 8 is strictly dependent on the cycle's amplitude. When cycles develop at small strain demands, this branch is convex in shape, whereas, if the strain demand increases, the unloading-reloading response becomes concave and pinched. For this reason, in the Kashani et al. (2014) model two different equations are proposed:

- $\varepsilon \leq 9\varepsilon_{yi}$ , trilinear curve, Figure 5.20a;
- $\varepsilon > 9\varepsilon_{yi}$ , linear-hyperbolic curve, Figure 5.20b;

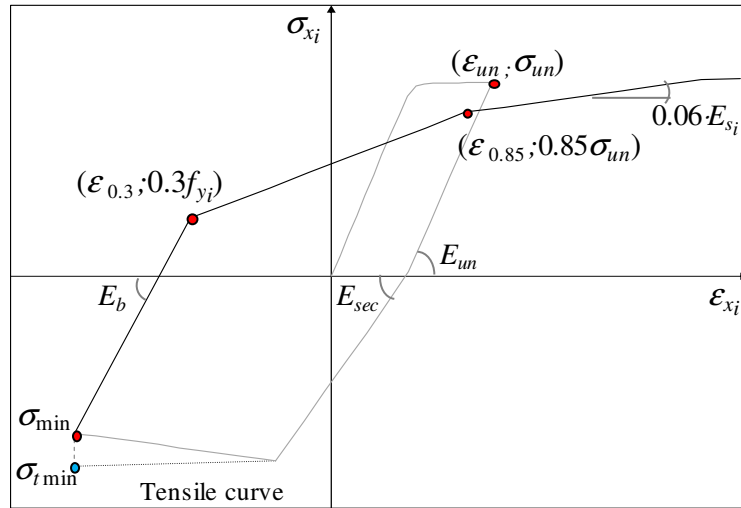
As shown in Figure 5.20, the initial unloading stiffness  $E_b$  is defined in Eq.(5.39).

$$E_b = E_{si} \left( \frac{\sigma_{\min}}{\sigma_{t\min}} \right)^{1.5} \quad (5.39)$$

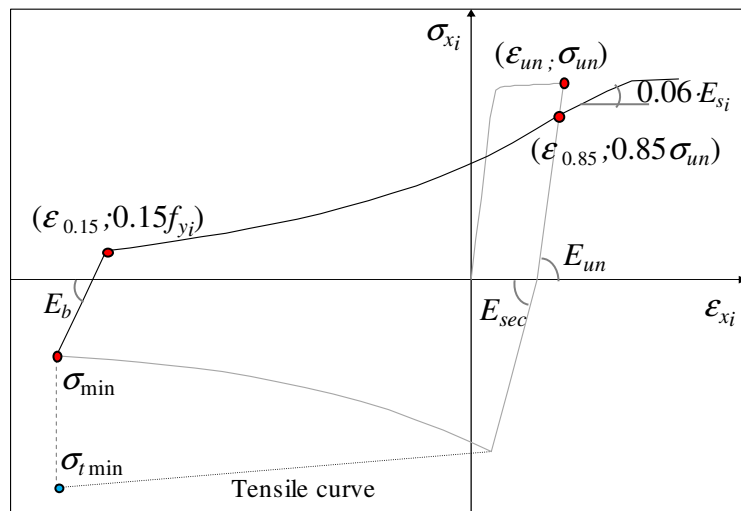
where  $\sigma_{\min}$  is the minimum stress value reached by steel in compression in case of buckling and  $\sigma_{t\min}$  minimum stress value reached by steel in compression in case of absence of buckling.

In case of small strains, Figure 5.20a, the first linear branch develops until the reaching of  $\varepsilon_{0.3}$  (corresponding to the achievement of  $0.3f_{yi}$ ). Then it follows a second linear branch up to

$\epsilon_{0.85}$  (which corresponds to a stress equal to  $0.85f_{y_i}$ ). Finally, the third section is characterized by a slope equal to  $0.06E_{s_i}$  up to the intersection with the tensile envelope.



(a)



(b)

Figure 5.20: Modelling of compression unloading branch according to Kashani et al. (2014): (a) at small strain demand ( $\epsilon \leq 9\epsilon_y$ ); (b) at large strain demand ( $\epsilon > 9\epsilon_y$ ).

In case of large strain demand, Figure 5.20b, the linear branch with slope  $E_b$  develops up to  $\epsilon_{0.15}$  (that corresponds to the achievement of  $0.15f_{y_i}$ ). Then a hyperbolic branch is defined until reaching  $\epsilon_{0.85}$  (corresponding to  $0.85f_{y_i}$ ). The hyperbolic curve is defined in Eq.(5.40):

$$\sigma_h = \frac{\epsilon_h}{\eta_1 + \eta_2 \epsilon_h} \tag{5.40}$$

where  $\sigma_h$  and  $\varepsilon_h$  are the coordinates of the hyperbolic curve referred to its reference system. Instead, the hyperbolic curve coordinates in the  $x_i, y_i$ -system of the rebar are defined in Eq.(5.41) and Eq.(5.42).

$$\varepsilon = \varepsilon_h + \varepsilon_{0.15} \quad (5.41)$$

$$\sigma = \sigma_h + 0.15 f_{y_i} \quad (5.42)$$

where:

$$\eta_1 = \begin{cases} \frac{1}{0.03E_{s_i}} & \lambda_p \leq 45 \\ \frac{1}{0.015E_{s_i}} & \lambda_p > 45 \end{cases} \quad (5.43)$$

$$\eta_2 = \frac{1}{0.85 \cdot f_{y_i} - 0.15 \cdot f_{y_i}} - \frac{\eta_1}{\varepsilon_{0.85} - \varepsilon_{0.15}} \quad (5.44)$$

Finally, the third branch is characterized by a slope of  $0.06E_s$  until the intersection with the tensile envelope.

### 5.2.2.5 Incomplete Unload-Reload Cycles IURC

In order to simulate a generic load history, partial loading-unloading cycles formulations have been included. In fact, generally, it is possible that unloads or reloads occur before the reaching of the compressive or tensile envelope curve. In case of the partial reload occurs in the tensile domain, Figure 5.21, an elastic line with slope  $E_{un}$  (equal to the unloading one) is expected, Eq.(5.36). If the partial reload occurs in the compressive domain, Figure 5.22, the reload line has a slope equal to  $E_{sec}$ , Eq.(5.37).

Figure 5.23 shows an example of the result obtained for a cyclic load history applied to a bare bar with a slenderness ratio equal to  $L/D = 20$  and yield stress  $\sigma_y = 500$  MPa. As shown, the cyclic degradation due to buckling leads to a reduction of the compressive stress and degradation of the elastic modulus. Furthermore, the *URCT* law changes from a linear to an hyperbolic law with increasing strain demand.



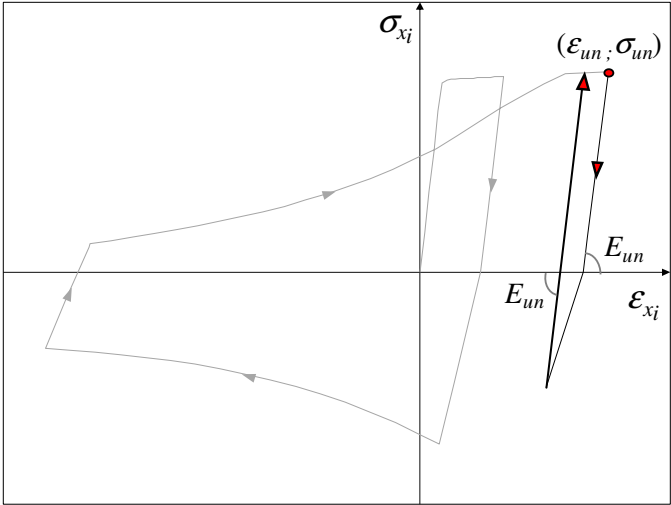


Figure 5.21: Incomplete unloading reloading cycle IURC in the tensile domain, Kashani et al. (2014).

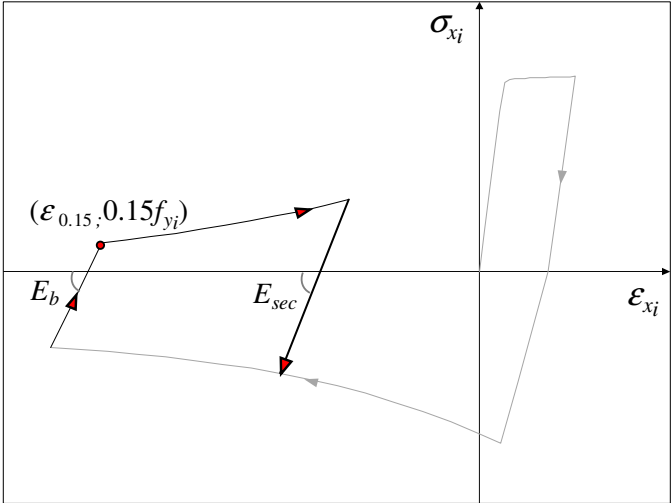


Figure 5.22: Incomplete unloading reloading cycle IURC in the compressive domain, Kashani et al. (2014).

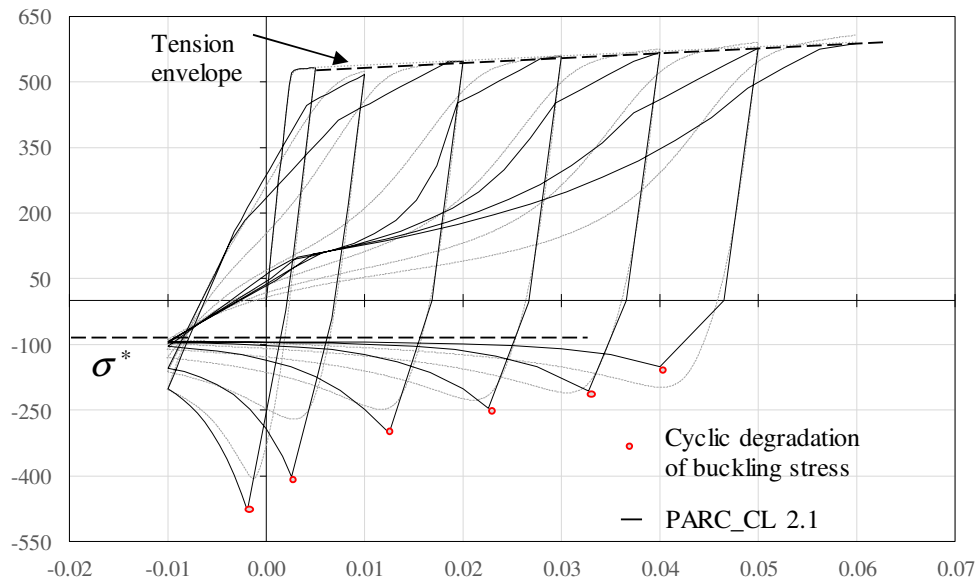


Figure 5.23: Comparison between NLFEA with PARC\_CL 2.1 and numerical simulation by Kashani et al. 2015 for a bare bar with  $L/D=20$ .

### 5.3 Validation of the Implemented Formulations

The objective of this work is to use existing models for steel (Monti and Nuti, 1992; Kashani et al., 2015), which have shown good performance in representing the local buckling, to simulate existing RC structures. Typically, the inelastic behaviour of RC structures subjected to seismic loading is analysed by using fiber-based discretization of the member cross section (Mullapudi, 2010). Indeed, both the Monti and Nuti (1992) and the Kashani et al. (2015) formulations are implemented in a fibre model. For the first time, two constitutive laws for steel including buckling are implemented in a smeared crack model, the PARC\_CL 2.1 one.

Firstly, the effectiveness of the proposed model is tested through the comparison of NLFEA results with the experimental measurements of bare bars. Subsequently, a non-conforming column tested at the University of Bergamo (Meda et al., 2014) is analysed.

#### 5.3.1 Simulation of Bare Bars

The effectiveness of the presented model has been verified by simulating the cyclic behaviour of bare bars by means of the PARC\_CL 2.1 crack model. 3 specimens are selected: XC1, XC2 and XC3 by Zhou (2015). The specimens are characterised by different values of tensile and compressive yield stress, respectively  $f_y^t$  and  $f_y^c$ . NLFEA has been carried out using a single 4-node membrane element with reduced integration scheme (defined M3D4R in Abaqus), Figure 5.24. The properties of the reinforcements are reported in Table 5.1.

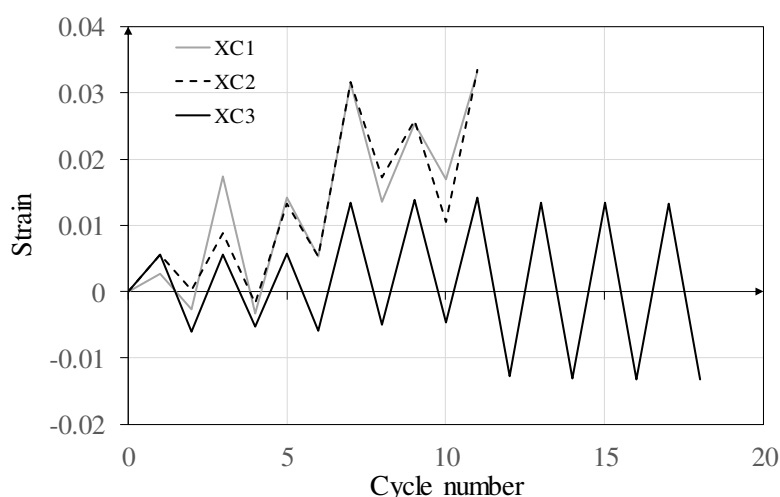


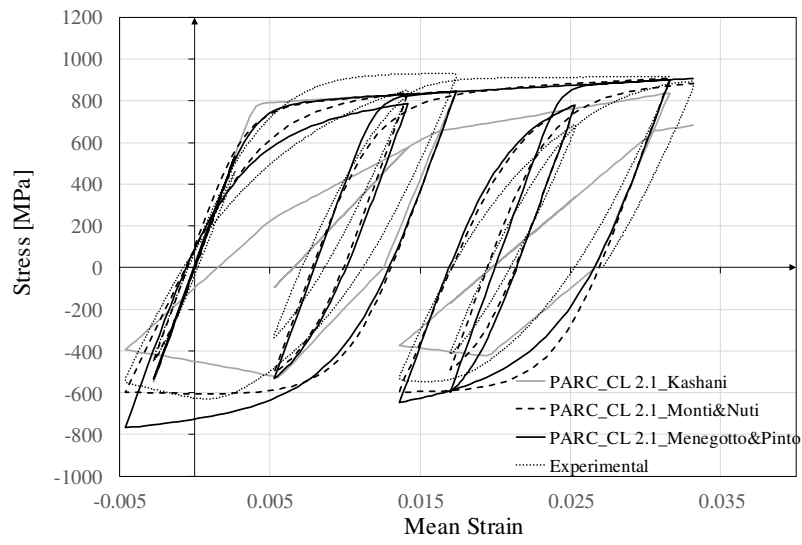
Figure 5.24: Strain histories for XC1, XC2, XC3 bare bars (Zhou, 2015).

NLFEA has been conducted with PARC\_CL 2.1 model using the three constitutive laws implemented for steel: Menegotto and Pinto (1973), Monti and Nuti (1992) and Kashani et al. (2015).

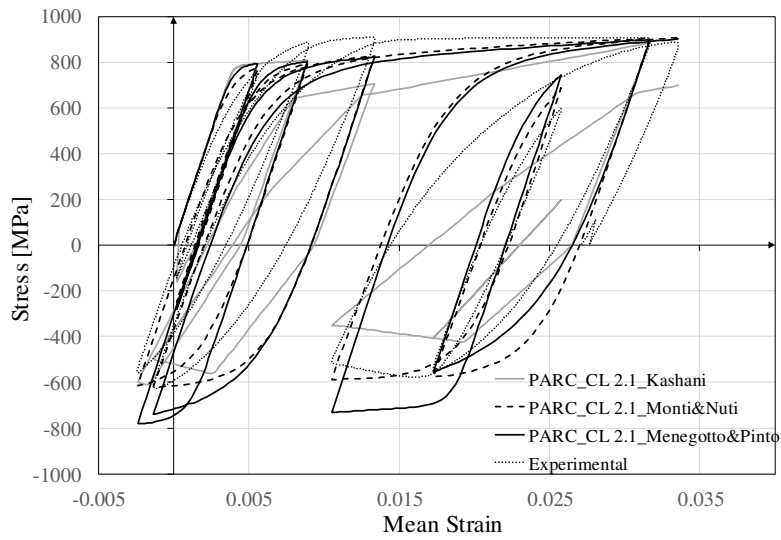
Table 5.1: Mechanical properties of the bare bars proposed by Zhou (2015).

Test	$\lambda$	$f_y^t$ [MPa]	$f_y^c$ [MPa]	$E_s$ [MPa]	$b$
XC1	11	790	680	200000	0.02
XC2	11	790	680	200000	0.02
XC3	11	790	680	200000	0.02

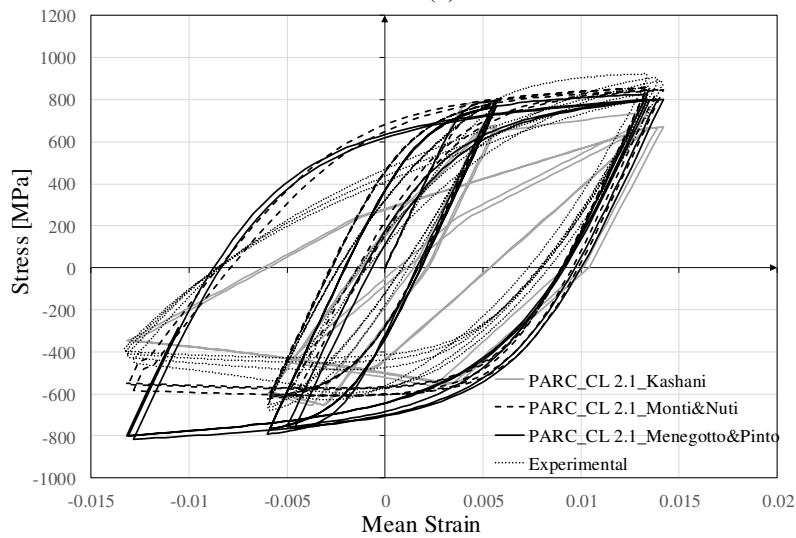
The obtained results are shown in Figure 5.25: the Menegotto&Pinto model is able to estimate with good approximation the tensile stress value but, due to its formulation, it is not able to simulate the softening in compression caused by buckling. Instead, the Monti&Nuti as well as the Kashani model is able to catch both the tensile and compressive response in terms of achieved stress. However, the Kashani et al. (2015) model shows a markedly underestimation of the unload-reload from compression to compression (URCT) branches when strains occur in small ranges, Figure 5.25a,b. This does not happen when strains increase as in the case of the XC3 specimen, Figure 5.25c. The experimental curve of the XC3 specimen presents an average behaviour between the curves obtained with the Monti&Nuti model and the Kashani et al. (2015) model.



(a)



(b)



(c)

Figure 5.25: Comparison between experimental results and NLFEA conducted by means PARC\_CL 2.1 crack model for (a) XC1, (b) XC2 and (c) XC3 bare bars, Zhou (2015).

Other two samples proposed by Kashani et al. (2013<sup>b</sup>) and subjected to symmetrical strain history have been modelled. The mechanical properties are reported in Table 5.2 and the applied strain history is shown in Figure 5.26.

Table 5.2: Bare bars mechanical properties by Kashani et al., 2013<sup>b</sup>.

Test number	$\lambda$	$f_y^t$ [MPa]	$E_s$ [MPa]	$E_h$ [MPa]
1	10	540	210000	2000
2	15	540	210000	2000

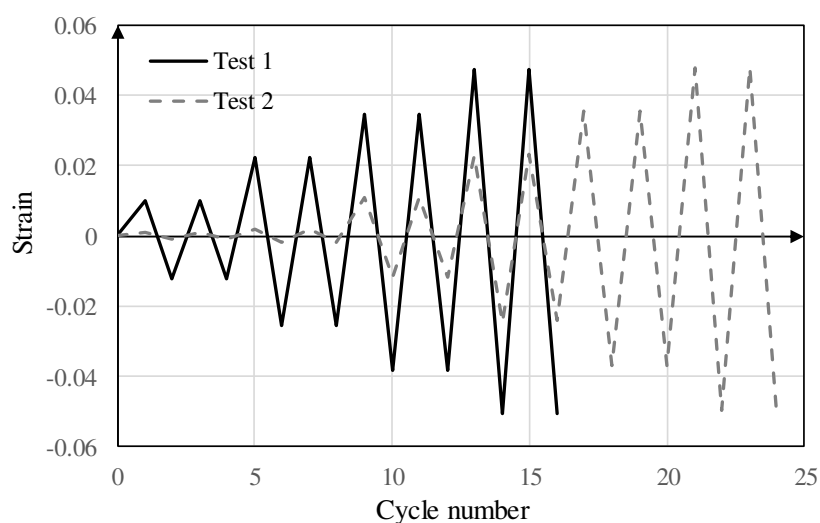


Figure 5.26: Strain histories for Test 1 and 2 (Kashani et al. 2013<sup>b</sup>).

Figure 5.27 shows the results obtained by means of the PARC\_CL 2.1 using the three implemented models for steel. In this case, the strain history load is symmetrical in tension and compression, and only the Kashani et al. (2015) model is able to catch with good approximation the experimental results. In general, the Monti&Nuti model overestimates the results both in reloading from compression to tension and in the compression branch. As shown in Figure 5.27b, the Monti&Nuti model is highly limited in the buckling branch due to the asymptotic limit of the compressive stress,  $\sigma_\infty$ , Eq.(5.2). Indeed, when  $\sigma_\infty$  is reached, the curve can no longer diminish, and, as consequence, the stress-strain curve underestimates the buckling effect.

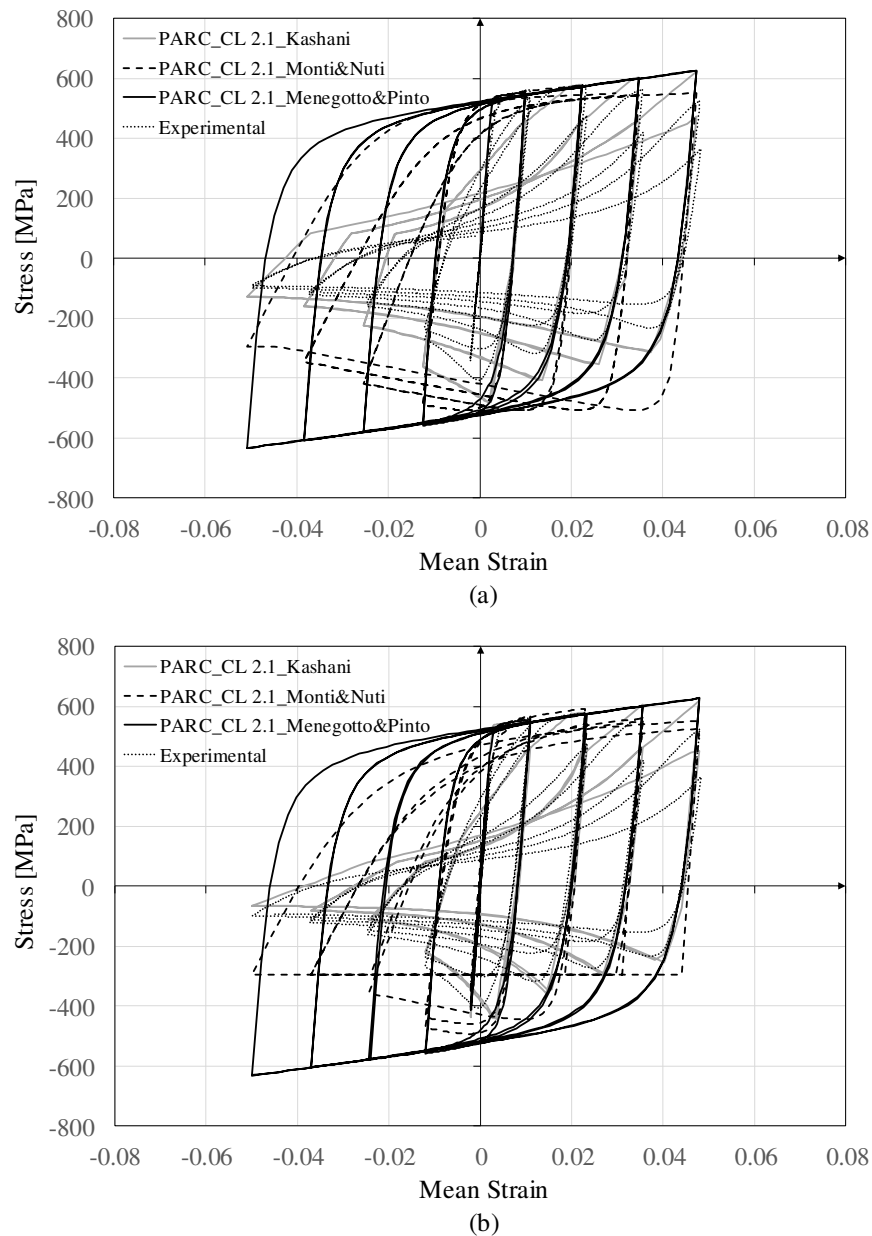


Figure 5.27: Comparison between NLFEA obtained using the PARC\_CL 2.1 crack model and experimental results for (a) Test 1 and (b) Test 2 Kashani et al. (2013<sup>b</sup>).

### 5.3.2 Simulation of RC Elements

The constitutive laws for steel, presented in the previous paragraphs, have been calibrated on the basis of the average behavior of a bare bar cyclically stressed, Figure 5.28a. It remains to be seen whether these laws are suitable for simulating the behaviour of reinforcement in RC elements and not only the behavior of bare bars. However, in literature, there are not cyclic tests on RC elements (with high slenderness ratios) to compare with the results of numerical simulation.

So, before proceeding to analyze complex structural elements, it was necessary to validate the model by means the simulation of a simple RC element, Figure 5.28b. This element, characterized by a length of  $L$  and the presence of a longitudinal bar, can be thought as an element extracted from a column between two consecutive stirrups, Figure 5.28c.

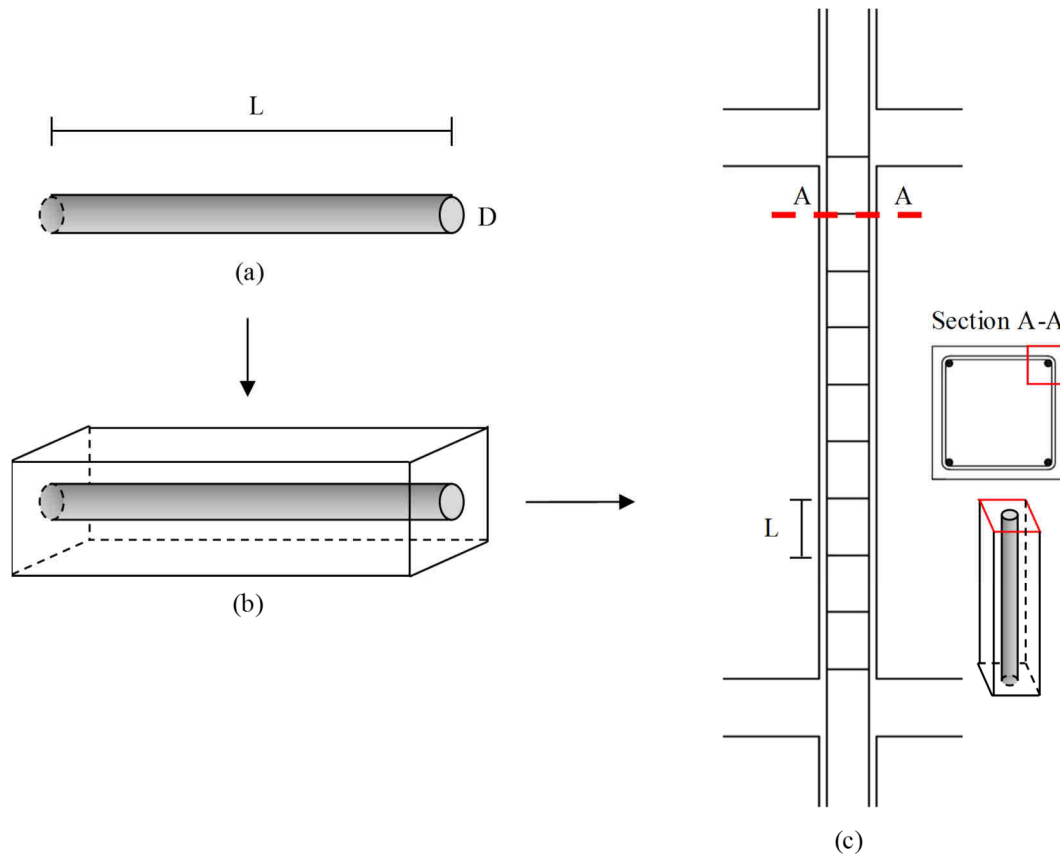


Figure 5.28: From the bare bars behaviour to RC elements: (a) bare bar, (b) bar in a simple RC element and (c) RC column.

Consider, for example, a RC element, Figure 5.28b, with a square cross-section of 120x120mm and 300mm long, characterized by the presence of a reinforcing bar with a diameter of 16mm. The obtained slenderness ratio is equal to 18.75. The hypothesized mechanical properties are presented in Table 5.3.

Three different modellings are used, Figure 5.29. The first modeling was made using a single 4-node membrane element with reduced integration scheme (M3D4R), Figure 5.29a. The result of this model is presented in Figure 5.30 and it was used as a reference for comparison with the other two approaches. The analyses are conducted in displacement control and using the three constitutive laws for steel. Obviously, the slenderness ratio is irrelevant for the Menegotto&Pinto model, whereas the Monti&Nuti model is not able to reach slenderness ratio

higher than 11. For this reason, the slenderness ratio for the Monti&Nuti NLFEA was fixed equal to 11.

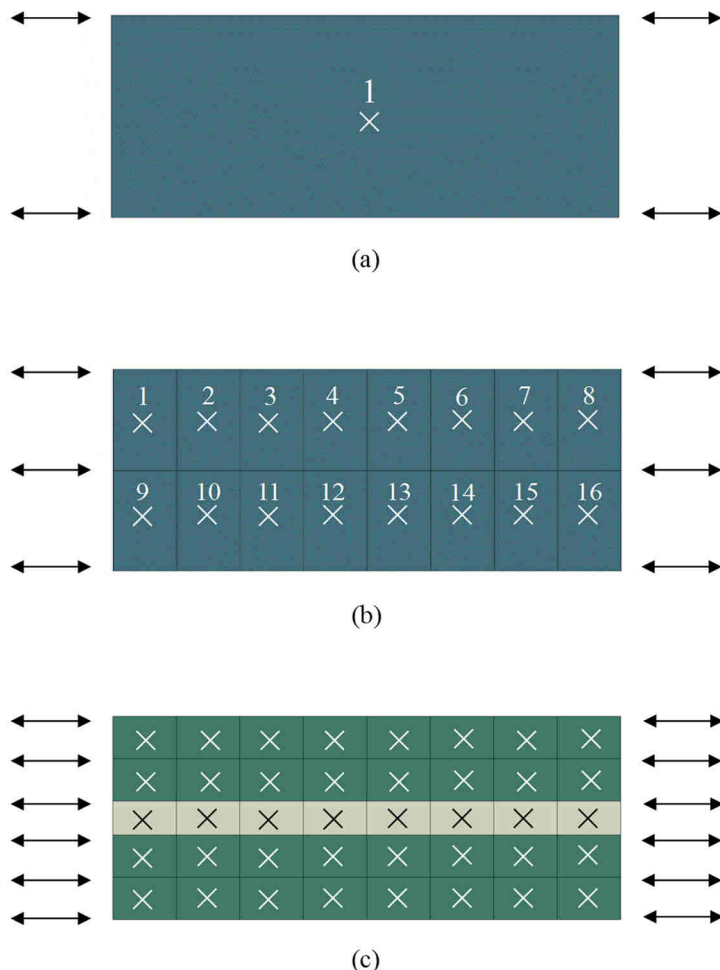


Figure 5.29: Different modelling approaches for the validation of the buckling effect in RC elements: (a) membrane element with a single integration point, (b) discretization of the problem with 16 elements, (c) typically adopted mesh for RC elements.

The second configuration, shown in Figure 5.29b, is characterized by 16 M3D4R elements and has the purpose of analyzing if the average global behavior changes when the mesh used changes. Finally, the last approach proposed is the one closest to the type of modeling that is usually adopted for the simulation of columns and beams, Figure 5.29c. This approach involves placing the reinforcing bar in its exact position (in this case, in the center) and concentrating its presence in a row of elements. In this way, it is possible to distinguish two materials: the first consisting of concrete (the green one in Figure 5.29c) and the second of reinforced concrete (the grey one in Figure 5.29c). The results obtained for both the proposed meshes are identical to the results shown in Figure 5.30. This is due to the fact that all the integration points respond



in the same way to the cyclic imposed history, by returning an average behaviour identical to that obtained by the model with only one integration point. This means that different meshes do not influence the result of the non-linear analysis. In fact, it could happen that the strong non-linearity associated with the softening branch (induced by buckling) could cause convergence problems and consequently difference deformations between the elements of the mesh, preventing the desired average behaviour from being obtained.

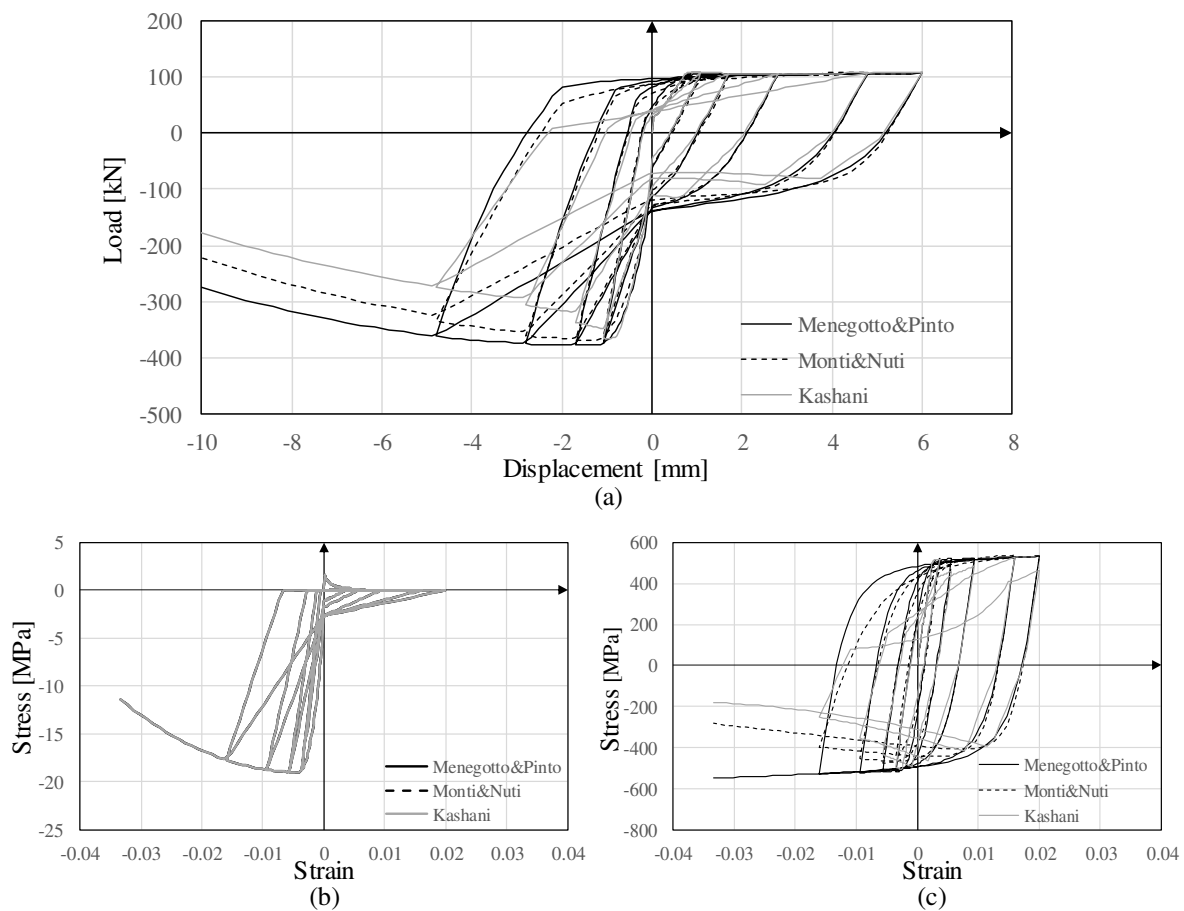


Figure 5.30: Results of NLFEA obtained for the RC element shown in Figure 5.29: (a) load-displacement result, (b) concrete cyclic behaviour and (c) steel cyclic behaviour.

### 5.3.3 Simulation of an Existing RC Column

In framed structures, columns are generally the most important structural members. Understanding their seismic behavior is very helpful for the evaluation of the structural response of entire buildings in terms of deformations, forces, and energy dissipation capacities. Furthermore, in most old-framed building, beams have much more flexural stiffness and strength than columns.

For these reasons, to evaluate the efficiency of the two implemented models for steel including buckling, a RC column tested at the University of Bergamo by Meda et al. (2014) has been analysed. More specifically, two 1800mm height columns were tested, one corroded and one not corroded. This aspect is certainly of interest because the corrosion phenomenon is a contribution in phase of implementation in the PARC\_CL 2.1 crack model; however, in the present work, only the results obtained for the uncorroded column will be presented. The columns were characterized by the same geometry: a square section of 300mm x 300mm reinforced with four longitudinal bars  $\phi 16$ mm, with concrete cover equal to 30mm. The transverse reinforcement consisted in  $\phi 8$ mm stirrups, 300mm spaced, except near to the load application, placed at 1.50m from foundation extrados, where the spacing between the stirrups became 100mm, Figure 5.31. The non-seismic resistant details are typical of structures built in Italy in the 60s and 70s. Considering the slenderness ratio as the ratio between the distance between stirrups and the longitudinal rebar diameter, for this case study, a slenderness ratio equal to 19 has been obtained except for the higher part of the column where the stirrups were closer. The element was cast on a 500mm thick foundation, as shown in Figure 5.31. The foundation was 1300mm x 600mm x 500mm, symmetrically reinforced with 4 $\phi 20$  rebars.

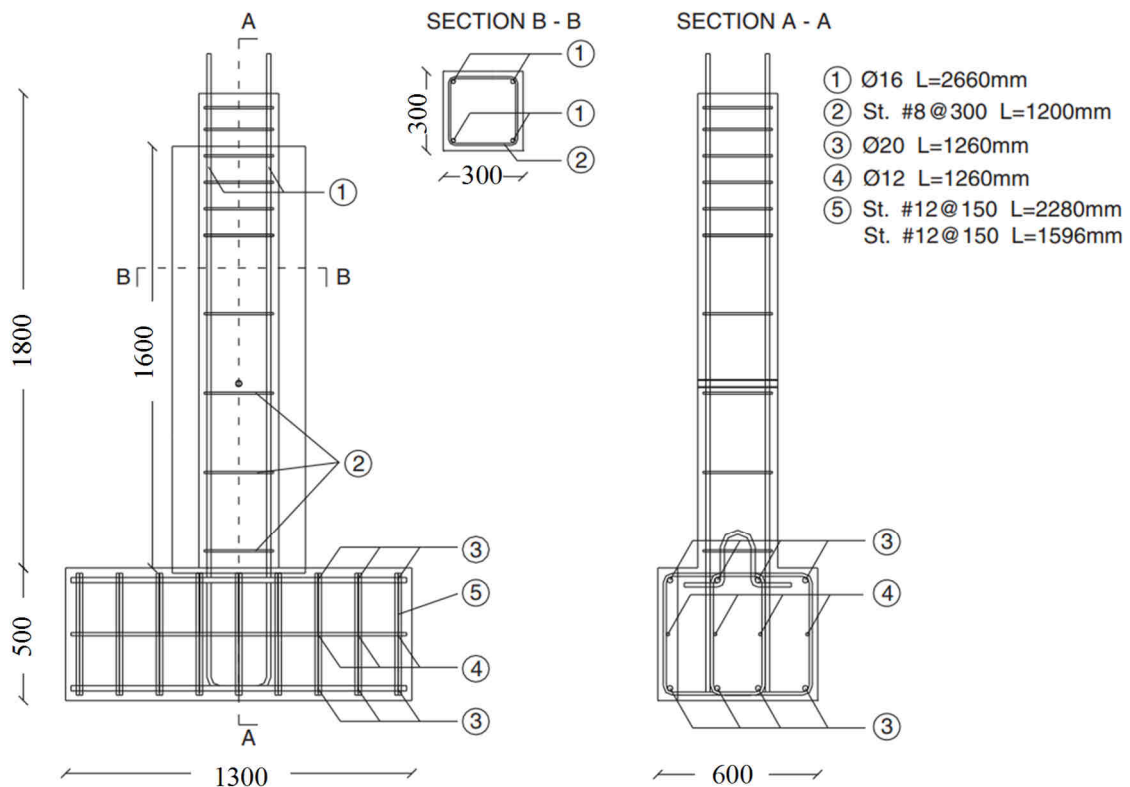


Figure 5.31: Column geometry (Meda et al., 2014).

The adopted materials were typical of the '70s buildings in Italy, Table 5.3. An axial load of 400kN was applied with two hydraulic jacks and monitored by a pressure transducer. Then the horizontal cyclic load (Figure 5.32) was applied by means of an electro-mechanical jack at a height of 1500m from the column foundation connection.

Table 5.3: Mechanical properties of materials for RC column (Meda et al., 2014).

Concrete			Steel		
$f_c$ [MPa]	$f_t$ [MPa]	$E_c$ [MPa]	$f_y$ [MPa]	$E_s$ [MPa]	$E_h$ [MPa]
19	1.5	25000	521	210000	1050

### 5.3.3.1 *NLFEA by means of PARC\_CL 2.1 crack model*

Two different modelling techniques are proposed in this PhD thesis, for the RC column tested by Meda et al. (2014). The first modelling approach has been characterized by large size elements. Thanks to the small number of the elements, the analyses was quick. The concrete cover has not been modelled in the shell plane because the first row of elements is characterized by the co-presence of reinforcement and concrete. For this reason, the concrete is helped by the reinforcement and the real spalling of concrete cover has not been considered. However, for taking this into account, a modified constitutive law for concrete has been adopted.

For the second modelling technique a more refined mesh has been used. In this case it has not been necessary to induce the spalling of concrete cover because the external row of elements has been characterized by concrete material without reinforcement.

In both cases, the column has been modelled with 4 nodes multi-layered shell elements (S4, Abaqus 2016). A complete Gaussian integration scheme has been adopted in the plane of the elements, whereas 3 Simpson integration points have been adopted for each layer along the thickness. The foundation has been modelled with an elastic material, whereas the column has been divided into sections with different material properties to distinguish the slenderness ratios of longitudinal rebars and reinforcement ratios of stirrups. The thickness of the element has been subdivided into 7 layers to properly describe the reinforcement layout, Figure 5.34 (coarse mesh) and Figure 5.40 (fine mesh).

The NLFEA has been performed in displacement control by imposing horizontal displacements and using the Newton-Raphson incremental iterative method.

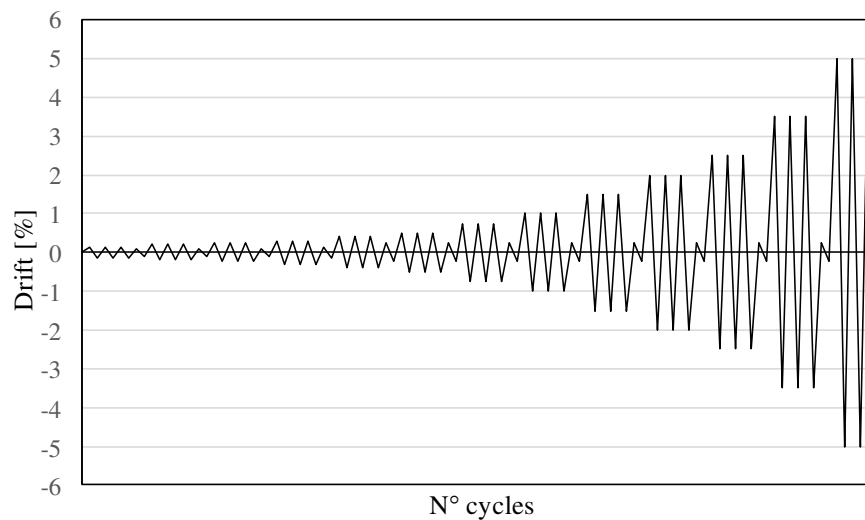


Figure 5.32: Experimental cyclic load history applied to the RC column (Meda et al., 2014).

All nodes have been constrained to displacement in  $z$  direction at the base section. Furthermore, the extreme nodes of the foundation have been constrained in the  $x$  direction and finally, all the nodes have been constrained in the  $y$  direction (Figure 5.34a).

The NLFEA have been conducted with the software Abaqus and the PARC\_CL 2.1 user subroutine using three different implemented laws for modelling the cyclic response of the longitudinal reinforcement.

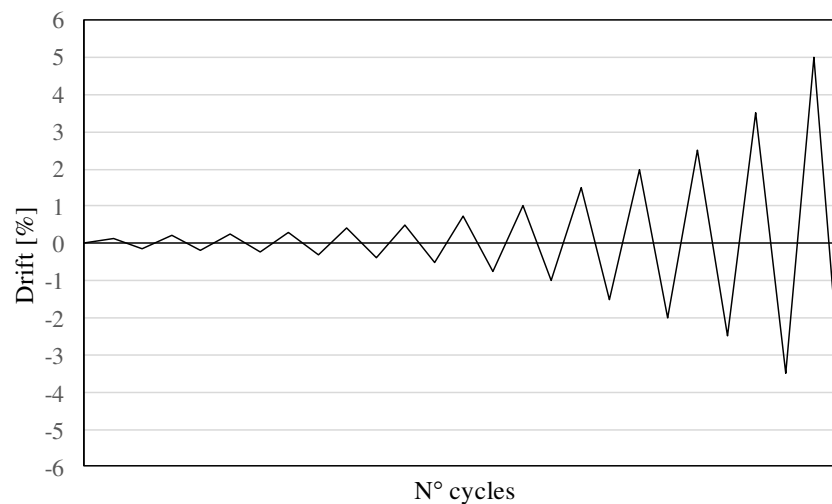


Figure 5.33: NLFEA cyclic history.

As explained in §5.2.2, the *FATDEG* branch (degradation in tension strength due to low-cycle fatigue/cyclic loading) of the original Kashani et al. (2015) model is not yet implemented in PARC\_CL 2.1. Furthermore, the formulation proposed by Monti and Nuti (1992) does not

take into account degradation. For this reason, when cycles have the same amplitude, i.e. the maximum reached strain does not increase from cycle to cycle, the hysteretic curve remains the same. This aspect together with the need to reduce time calculation, induced the author of this thesis to apply a reduced loading history. The maximum applied drift was applied once as shown in Figure 5.33.

5.3.3.1.1 Simplified modelling approach

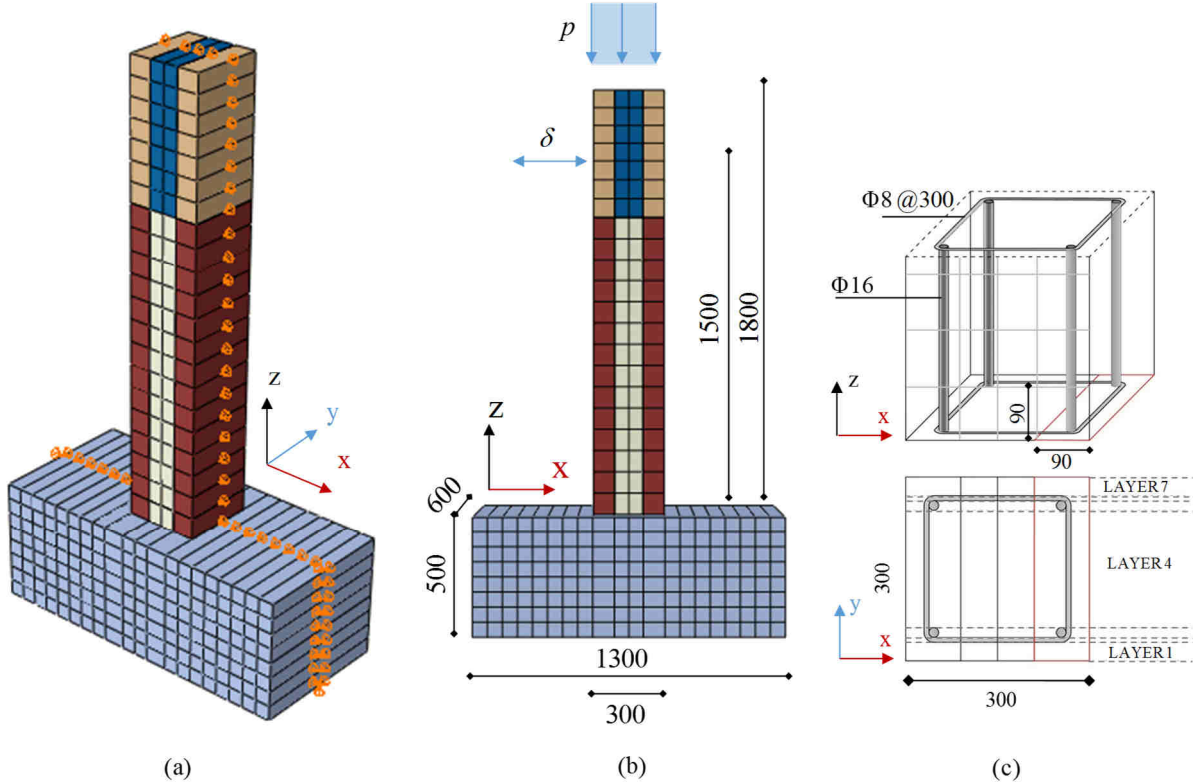


Figure 5.34: Coarse mesh adopted for the RC column: (a) orientation and boundary condition; (b) geometry and applied loads; (c) shell elements.

The first adopted modelling approach consists of a coarse mesh, Figure 5.34, in which the average size of the elements is about 90x90mm. In this way, longitudinal rebars are positioned in the middle of the first elements, Figure 5.34c.

In Figure 5.34a-b different colors are adopted to highlight the assigned materials, in order to distinguish the zone in which the slenderness ratio is equal to 19 (red) and 6 (ochres).

Since this type of modelling does not permit to consider properly the concrete cover, because the longitudinal rebars are smeared in the element, the spalling of concrete cover is added. The constitutive law for concrete is modified in order to consider this contribute. Specifically, when a compressive strain equal to 0.025 is reached by the concrete, it is assumed

that the integration points of the cover elements do not contribute anymore to the global resistance and stiffness, Figure 5.35.

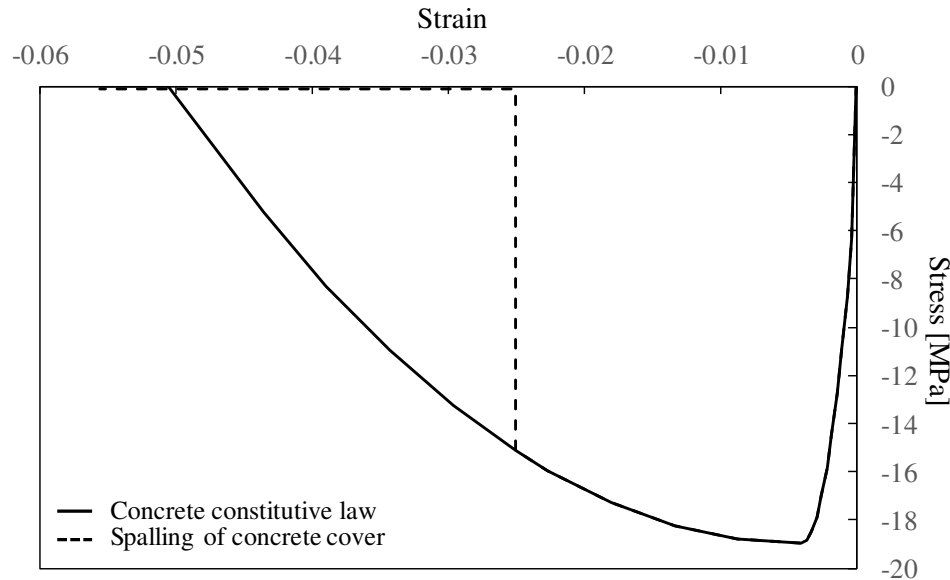


Figure 5.35: Constitutive law for concrete in PARC\_CL 2.1: spalling of concrete cover.

Figure 5.36 shows the load-drift curve obtained from NLFEA carried out with the PARC\_CL 2.1 model using three different laws (Menegotto et al., 1973, Monti et al., 1992 and Kashani et al., 2015). The pinching in the experimental curve starts when the buckling of longitudinal bars occurs for drifts greater than 2%, (Meda et al., 2014).

The first cycles for the three load-drift curves are very similar. Indeed, until 2.5% drift, the concrete controls the global behavior of the column and does not permit to the bars to exhibit large deformations in compression, Figure 5.37c-d. When the spalling of the concrete occurs, the compressive stresses in bars are suddenly increasing, leading to buckling phenomena, Figure 5.37a-b. As shown in Figure 5.37a, the only model that really catch the buckling failure is the Kashani model, (Kashani et al. 2015). Due to the large displacements involved, the analysis finishes before completing the last reloading, Figure 5.36.

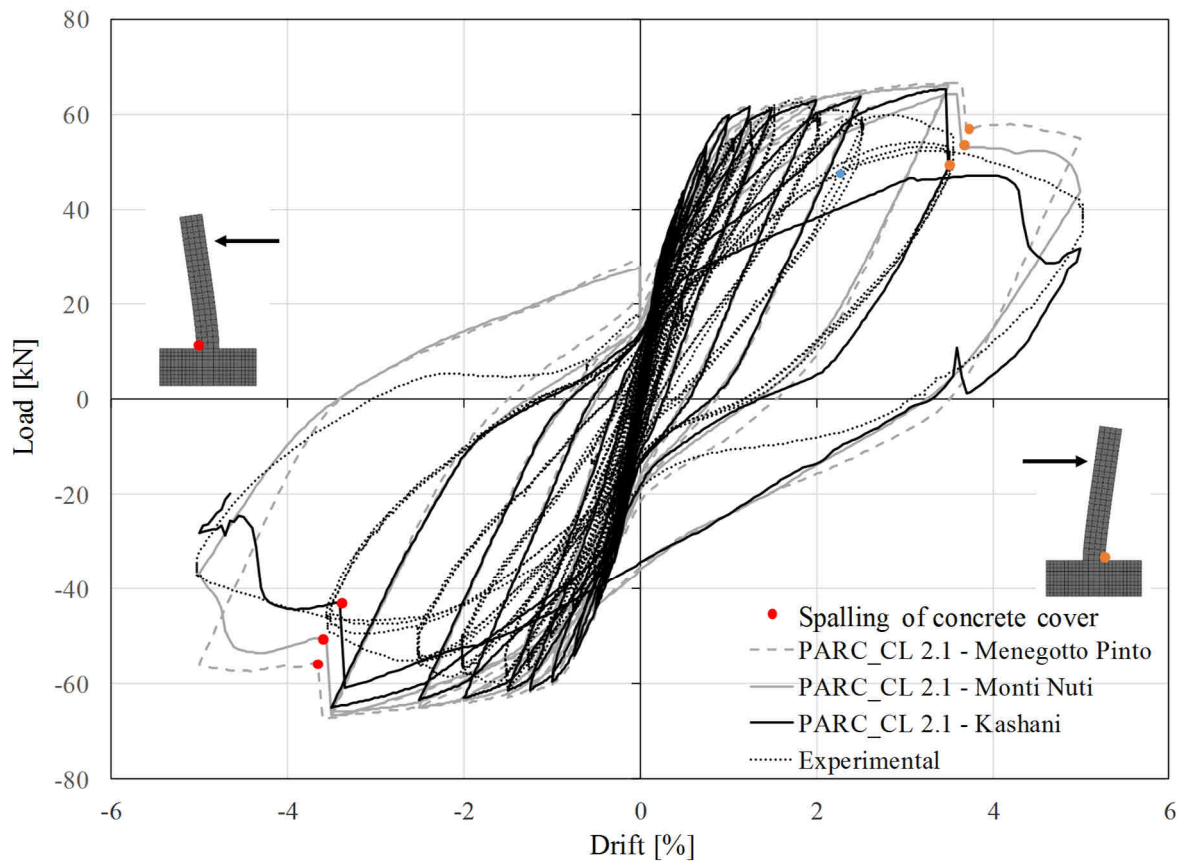


Figure 5.36: Comparison between the experimental result and the NLFEA with PARC\_CL 2.1 crack model using different steel laws in terms of load-drift curve.

Figure 5.38 shows the influence of the steel constitutive law on the global behaviour of the column for a drift equal to 3.5%. In this case, the compressive behaviour of the steel rebars, Figure 5.38b-c for the three different laws (Menegotto and Pinto, 1973; Monti and Nuti, 1992; Kashani et al., 2015) is similar. This is due to the fact that the compressive strains are not large and the buckling is not so evident. When the column is loaded in the positive  $x$  direction (from point 1 to 2, Figure 5.38a) the rebars on the left side of the column pass from compression to tension and this influences the global shape of the load-drift curve, Figure 5.38b. At the same time, the rebars on the right side of the column pass from tension to compression, Figure 5.38c. When the load is inverted (from point 2 to 3 in Figure 5.38), until the drift is in the positive domain, the unloading constitutive law of the rebars on the right side controls the load-drift curve, but, when the drift becomes negative the behaviour is inverted and the stress-strain law of the rebars at the right side controls the global response. Instead, the unloading phase is controlled by rebars in tension, explaining the few differences between the Kashani model, the

Monti-Nuti model (Monti et al., 1992) and the Menegotto-Pinto model (Menegotto et al., 1973). Indeed, as illustrated in Figure 5.38b, the unloading phase (from point 2 to 3) is similar in the three models. This is probably due to the fact that this modelling approach is too simplified.

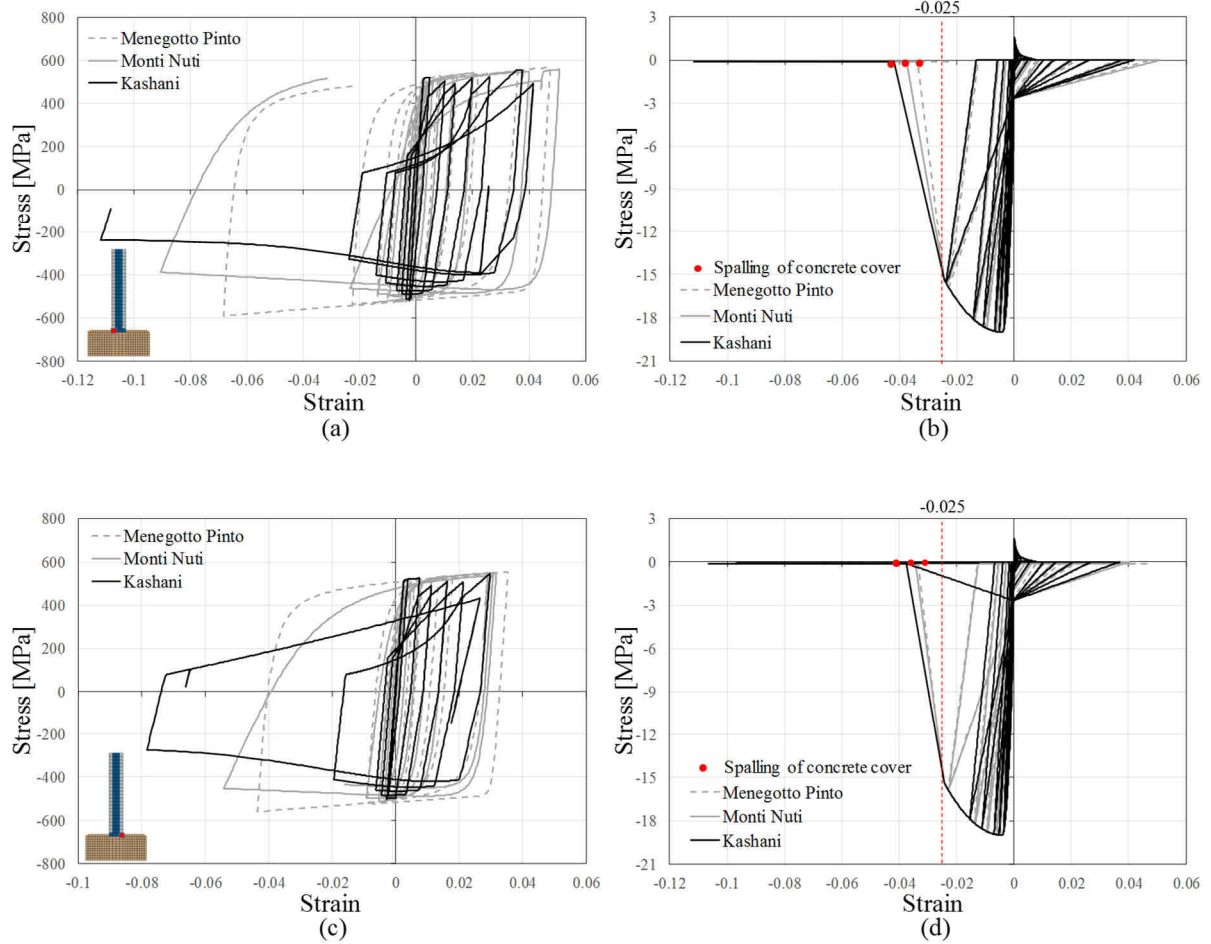


Figure 5.37: Stress-strain behaviour of the corner element at the left side: (a) concrete and (b) steel; behaviour of the corner element at the right side: (c) concrete and (d) steel.



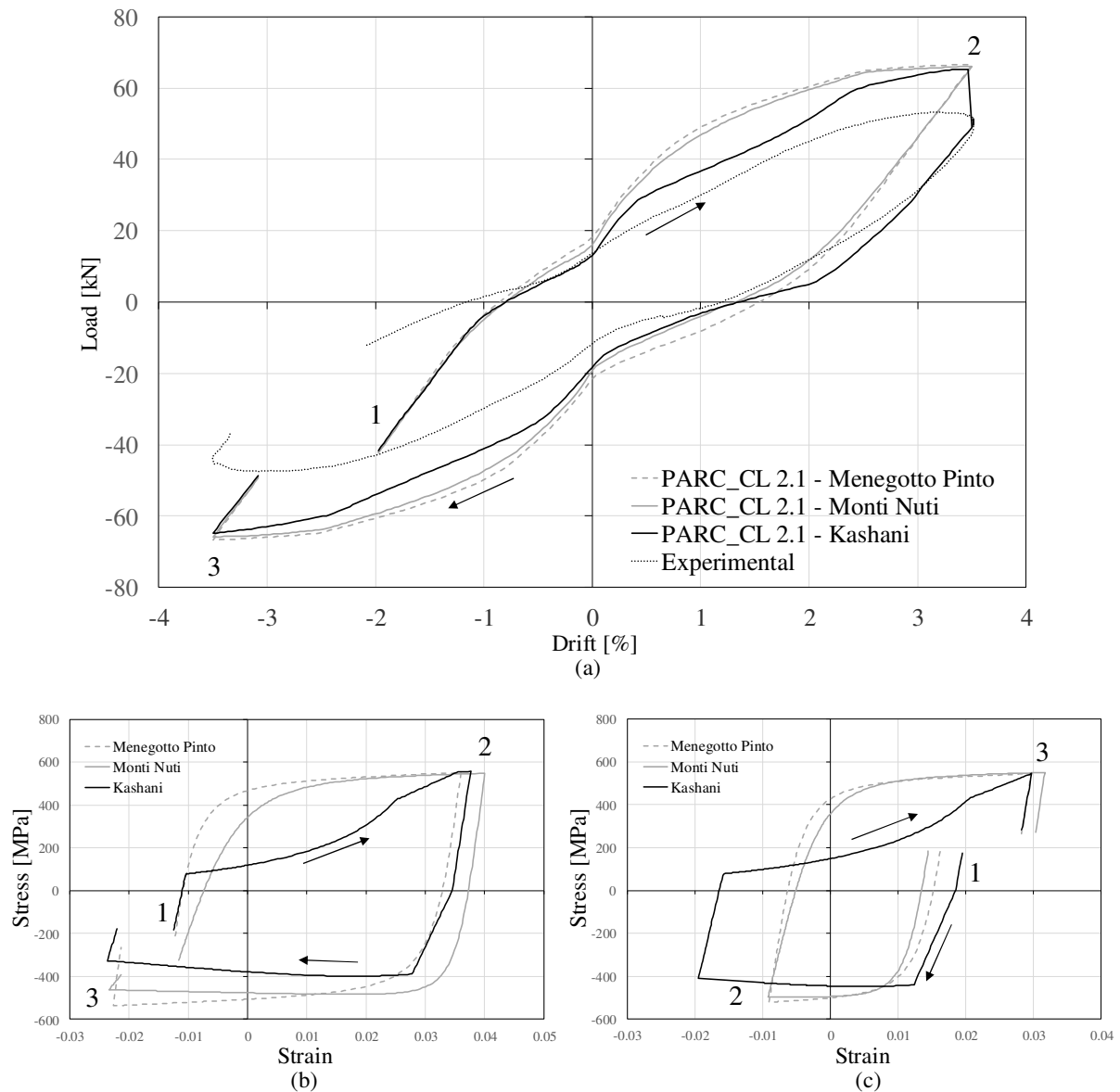


Figure 5.38: Comparison between PARC\_CL 2.1 and experimental results for drift equal to 3.5%: (a) load-drift curve, (b) steel cycle for the element at the left side and (c) steel cycle for the element at the right side.

Figure 5.39 shows the crack pattern for different values of drift, obtained using the PARC\_CL 2.1 crack model and the Kashani model for steel, (Kashani et al. 2015). The crack pattern obtained by the NLFEA shows that the higher cracks localize at the base of the column as shown in the experimental results (Meda et al. 2014). Flexural cracks affect a zone of about 200mm in NLFEA.

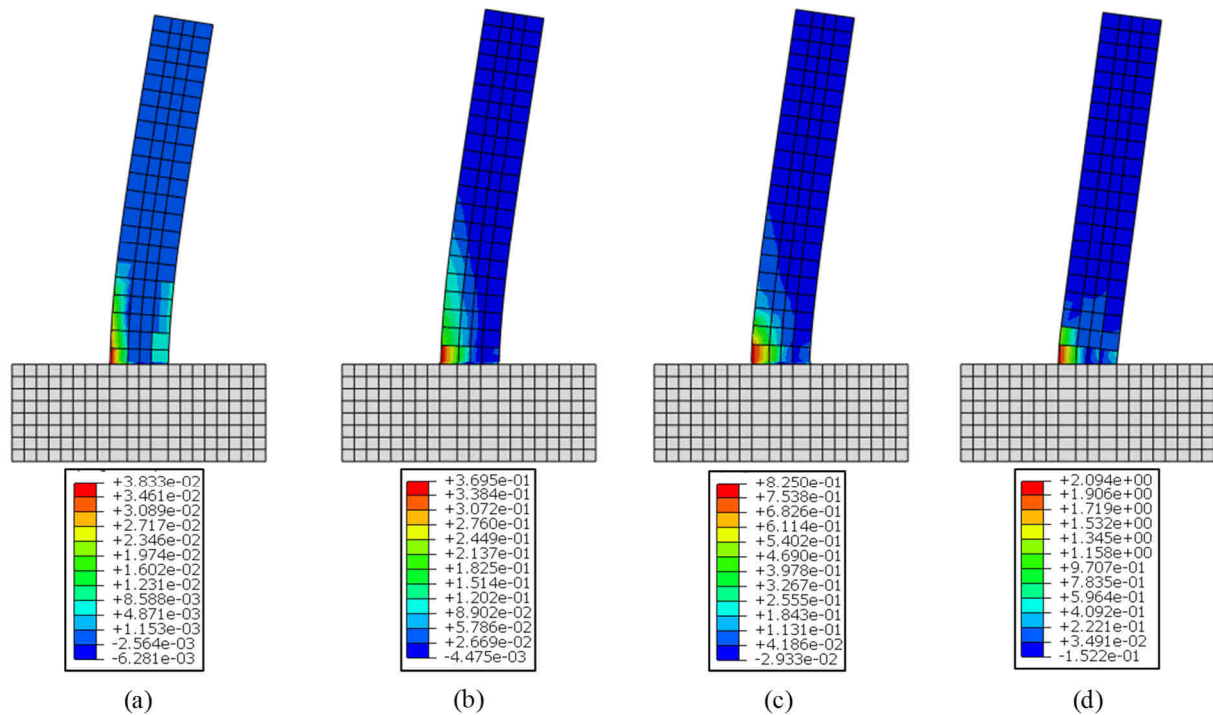


Figure 5.39: Crack pattern obtained using coarse mesh and PARC\_CL 2.1 with Kashani et al. (2015) law for drift equal to: (a) 0.3%, (b) 1.25%, (c) 2%, (d) 5%.

Thanks to the modification applied to the concrete constitutive law in compression, the spalling of concrete cover is taken into account; as consequence, the peak curve in the last cycles is reduced. However, it is an approximation due to the simplification of the problem. Indeed, the presence of longitudinal rebars in the external elements of the column does not permit to the concrete to reach high value of strains and to follow the softening branch in compression. For this reason, a more refined modelling technique is proposed in the next paragraph.

5.3.3.1.2 Detailed modelling

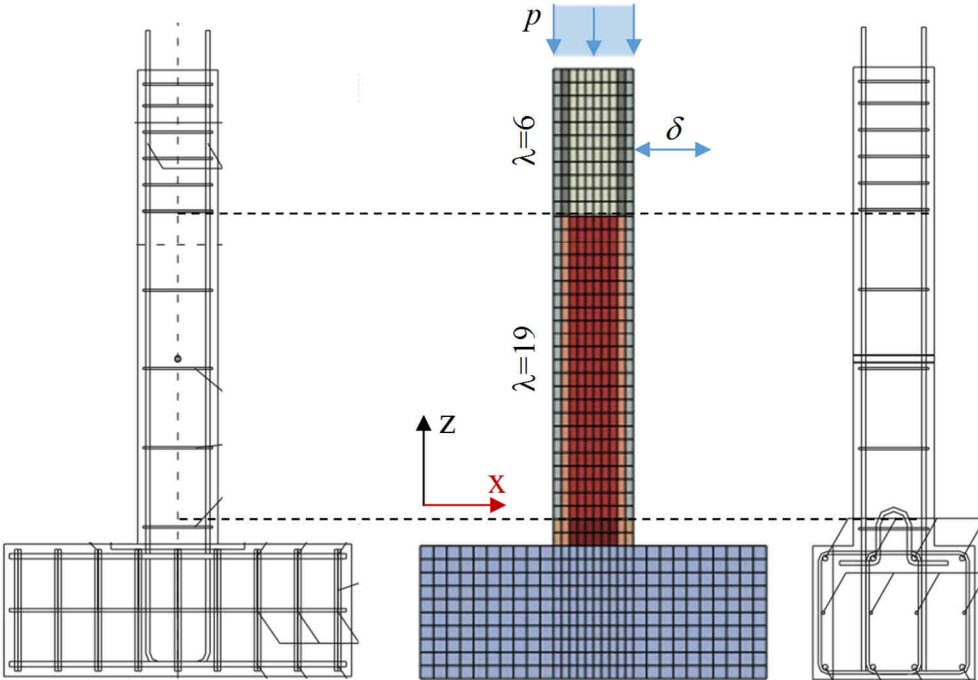


Figure 5.40: Fine mesh adopted for the RC column.

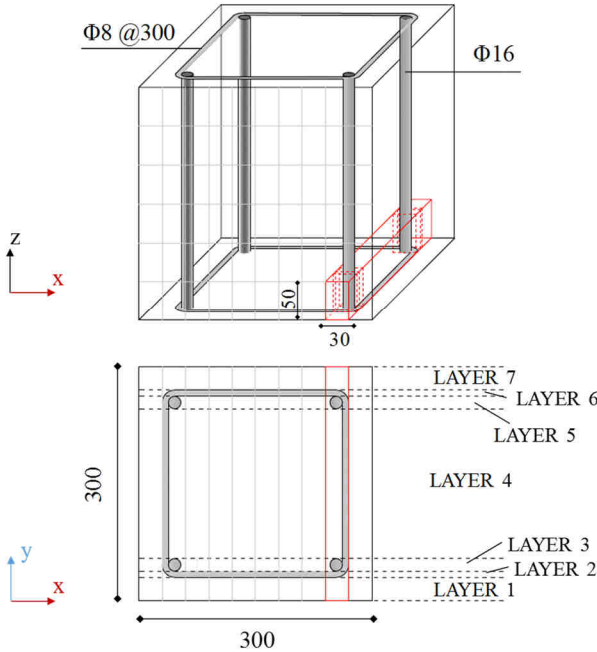


Figure 5.41: Mesh discretization: shell elements in plane and out of plane layers.

A more refined modelling technique is proposed in this paragraph, Figure 5.40. For this case study, the average size of the elements is about 30x30mm, Figure 5.41.

According to a study presented in Kashani et al. (2016) on the influence of pinching parameters on the non-linear cyclic response of RC column, a modification on the constitutive law for steel is proposed. Kashani et al. (2016) used the hysteretic energy dissipation during the cycles as a parameter to measure the accuracy of the prediction. They demonstrated that, for RC columns, better results can be obtained by reducing the pinching effect. In other terms for RC elements it is not properly correct to take into account the high value of pinching mechanisms. Indeed, the pinching effect is related to the geometrical non-linearity on stress–strain behaviour of isolated bars. However, when reinforcing bars are inside the concrete the cyclic response of longitudinal bars is influenced by tie stiffness. Therefore, the pinching effect in cyclic response of reinforcing bars inside the concrete is not as severe as in the isolated bars. For this reason, according to this remark, the Kashani et al. (2015) model implemented in PARC\_CL 2.1 has been modified, Figure 5.42.

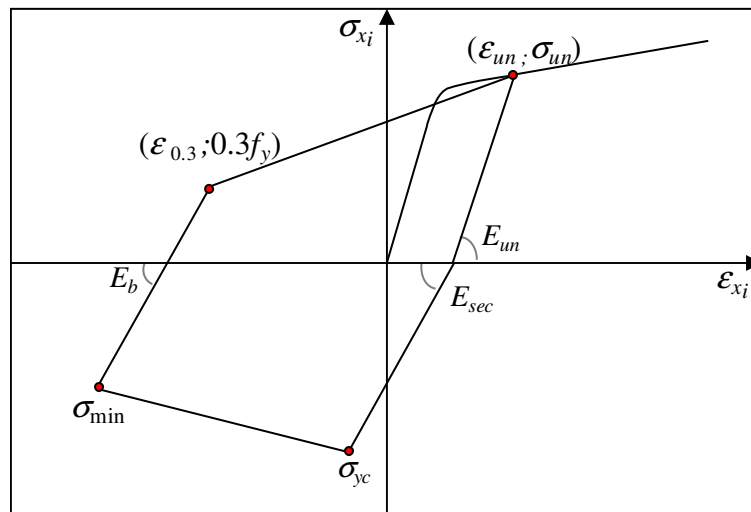


Figure 5.42: Modification of the *URCT* branch according to Kashani et al. (2016).

In Figure 5.43 the comparison between the original law for steel proposed by Kashani et al. (2015) and the modified law according to Kashani et al. (2016) for the RC element presented in §5.3.2 is shown. The reduction of the pinching effect in the steel law, Figure 5.43c, produces a different global response not only in the reloading from compression to tension branch but also into the unloading from tension to compression branches, Figure 5.43a.

According to this important remark, the NLFEMs of the RC column have been conducted using the modified law.

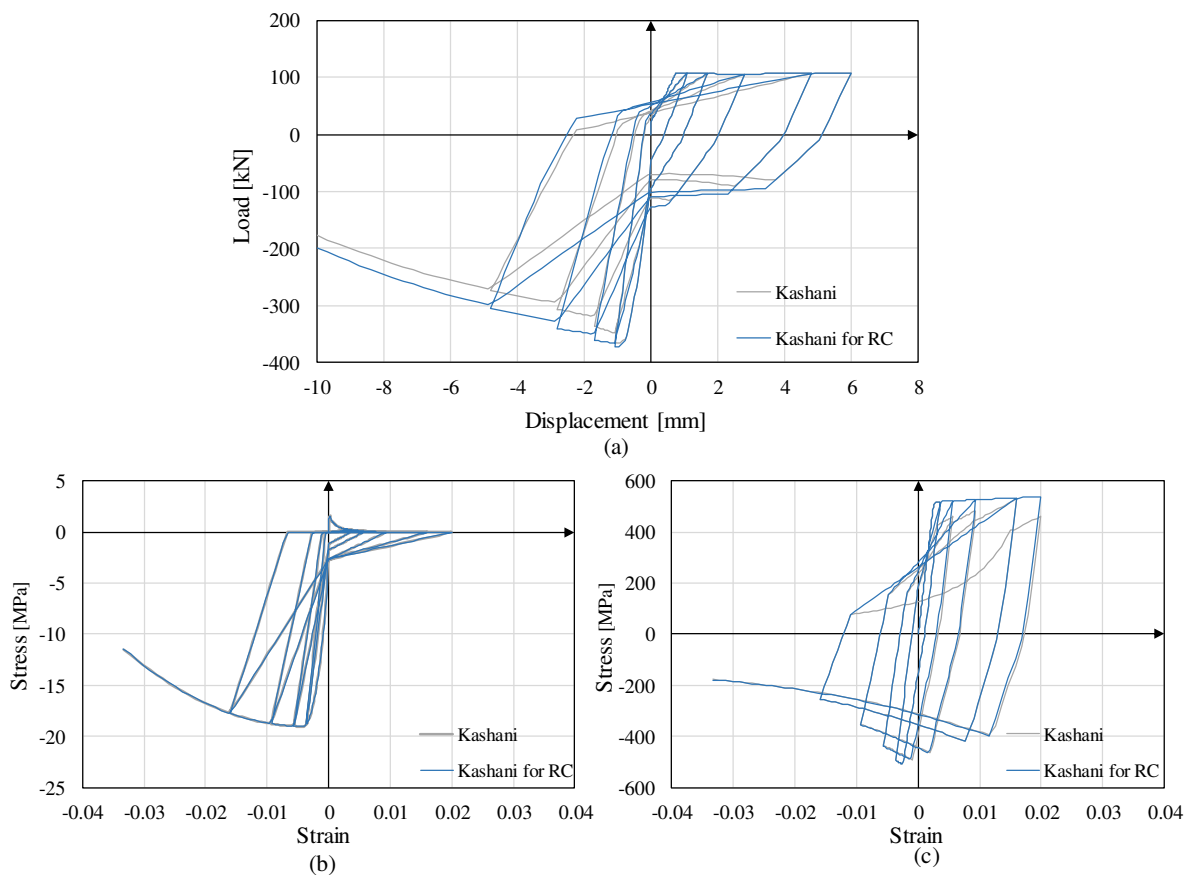


Figure 5.43: Comparison between the Kashani et al. (2015) law and the modification proposed in Kashani et al. (2016) for the RC element of §5.3.2.

Figure 5.44 shows the load-drift curve obtained from NLFEAs carried out with the PARC\_CL 2.1 model using three different laws (Menegotto and Pinto, 1973, Monti and Nuti, 1992 and Kashani et al., 2015). However, it is important to underline that only with the Kashani model it has been possible to use the real slenderness ratio of the column, equal to 18.75, for the analysis. The slenderness ratio used for the NLFEA conducted with the Monti&Nuti model has been equal to 11. As a consequence of this, the model has not been able to catch the real softening behaviour caused by buckling. The softening trend of the experimental curve started due to buckling of longitudinal bars for drifts greater than 2%, (Meda et al., 2014). As shown in Figure 5.44 the best fitting of the experimental curve is obtained by Kashani et al. (2015) model both in terms of load-drift curve and stiffness during the unloading reloading branches.

On the other hand, the Monti&Nuti model better reproduces the first cycles. Observing Figure 5.45 is possible to highlight that the Kashani model (Figure 5.45a), with respect to the Monti&Nuti one (Figure 5.45b), overestimates the load until a drift equal to 1.25%. This is due to the formulation of the *TE* branch. Indeed, observing Figure 5.45c it is possible to see the

differences between the two monotonic laws. The Monti&Nuti law is based on the Menegotto&Pinto one and depends only on the  $R$  parameter (described at §5.2.1.2.3), whereas the Kashani model uses the formulation proposed by Balan et al. (1998). This formulation depends basically to  $\delta$ , called shape parameter. The first adopted value used for the analyses was 0.005 as proposed by Balan et al. (1998). Using the results obtained by Monti&Nuti as reference, it was possible to calibrate this parameter to improve the prediction, Figure 5.46a.

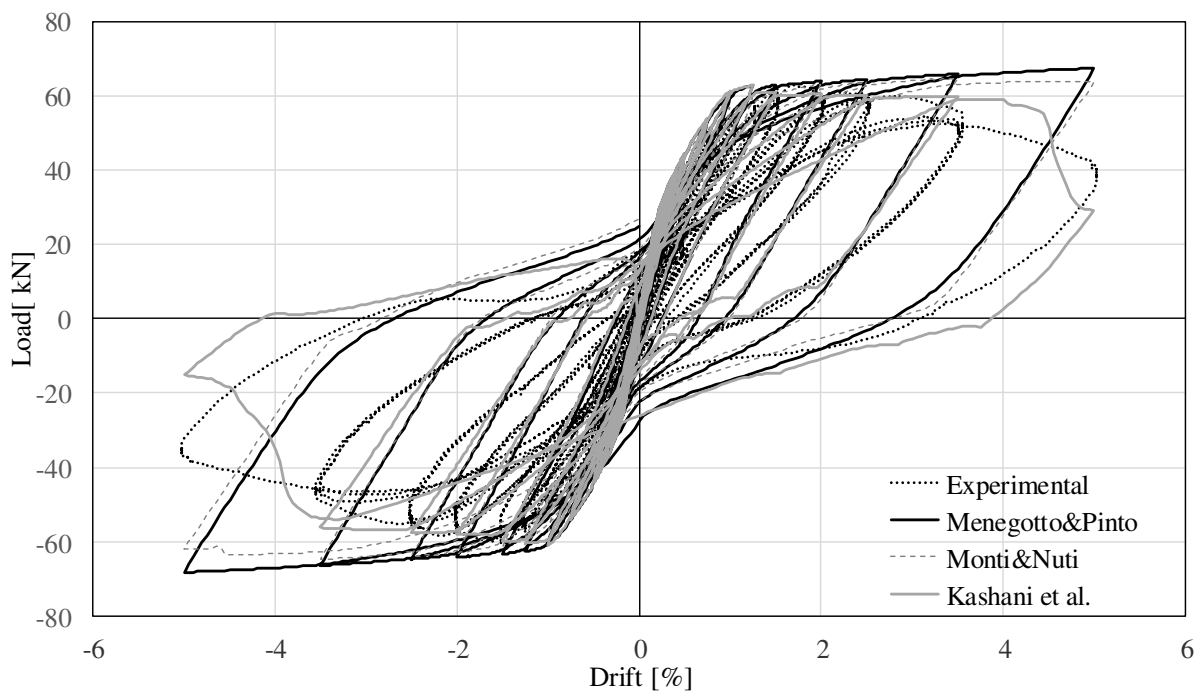


Figure 5.44: Comparison between the experimental result and the NLFEA with PARC\_CL 2.1 crack model using different steel laws in terms of load-drift curve.

After the calibration of the shape parameter, the NLFEA obtained with the Kashani et al. (2015) formulation shows better results both in terms of strength and stiffness respect to the Monti&Nuti one. For this reason, more details will be detected for this model.

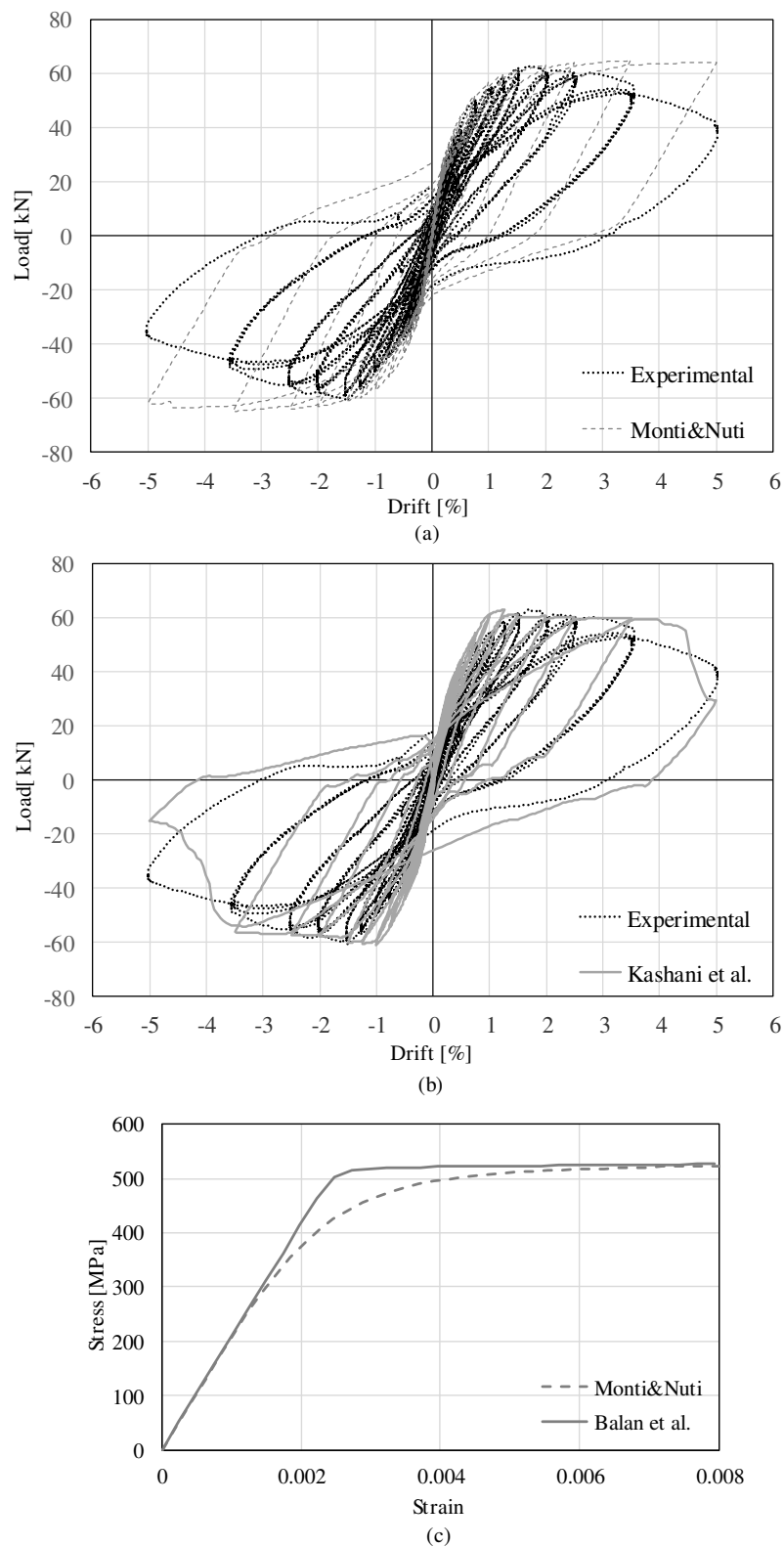


Figure 5.45: Load-drift curve obtained with: (a) Monti and Nuti (1992) model and (b) Kashani et al. (2015) model. (c) Differences between the tensile envelope in the two models.

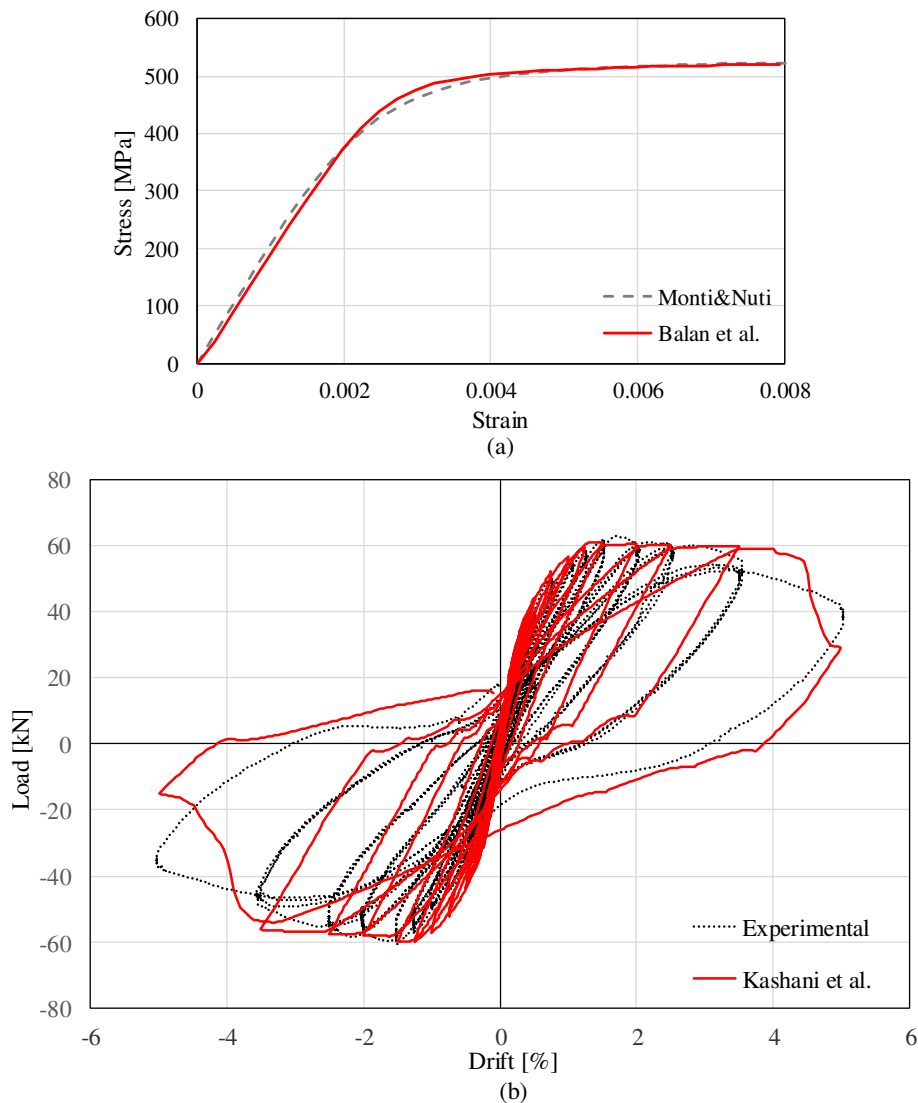


Figure 5.46: (a) Modified tensile envelope and (b) comparison between the modified Kashani et al. (2015) model and Monti and Nuti (1992) model.

In Figure 5.47 the load-drift curves obtained by using the Kashani et al. formulation, are reported and compared with the experimental results for different values of drift. By means of these comparisons it is possible to highlight the effectiveness of the model during cycles. Indeed PARC\_CL 2.1 is able to predict with good accuracy the hysteretic behavior of the cycles, both for low (Figure 5.47a-b) and high levels of drift (Figure 5.47c-d). The NLFEA results are able to simulate the response in terms of strength and stiffness.

Finally, the crack patterns during the loading history are shown in Figure 5.48. The experimental results reported that the first crack was formed for a drift equal to 0.3%. A stress localization at the column base connection led to concrete cover spalling and buckling of longitudinal rebars, (Meda et al., 2014). These observations can be deduced also by the NLFEA,



Figure 5.48. Until a drift equal to 2%, PARC\_CL 2.1 produces horizontal cracks localized at the base of the column, Figure 5.48a-b; in the last cycles, the crack propagation along the height of the column and related to concrete spalling is observed, Figure 5.48c-d.

Figure 5.49 shows the evolution of the stresses along the longitudinal rebars. It is interesting to observe that, when the drift increases and the concrete cover spalls, the buckling localizes at the base of the column causing deformations of finite elements. As consequence, when the buckling effect increases the strength reduction becomes more evident.

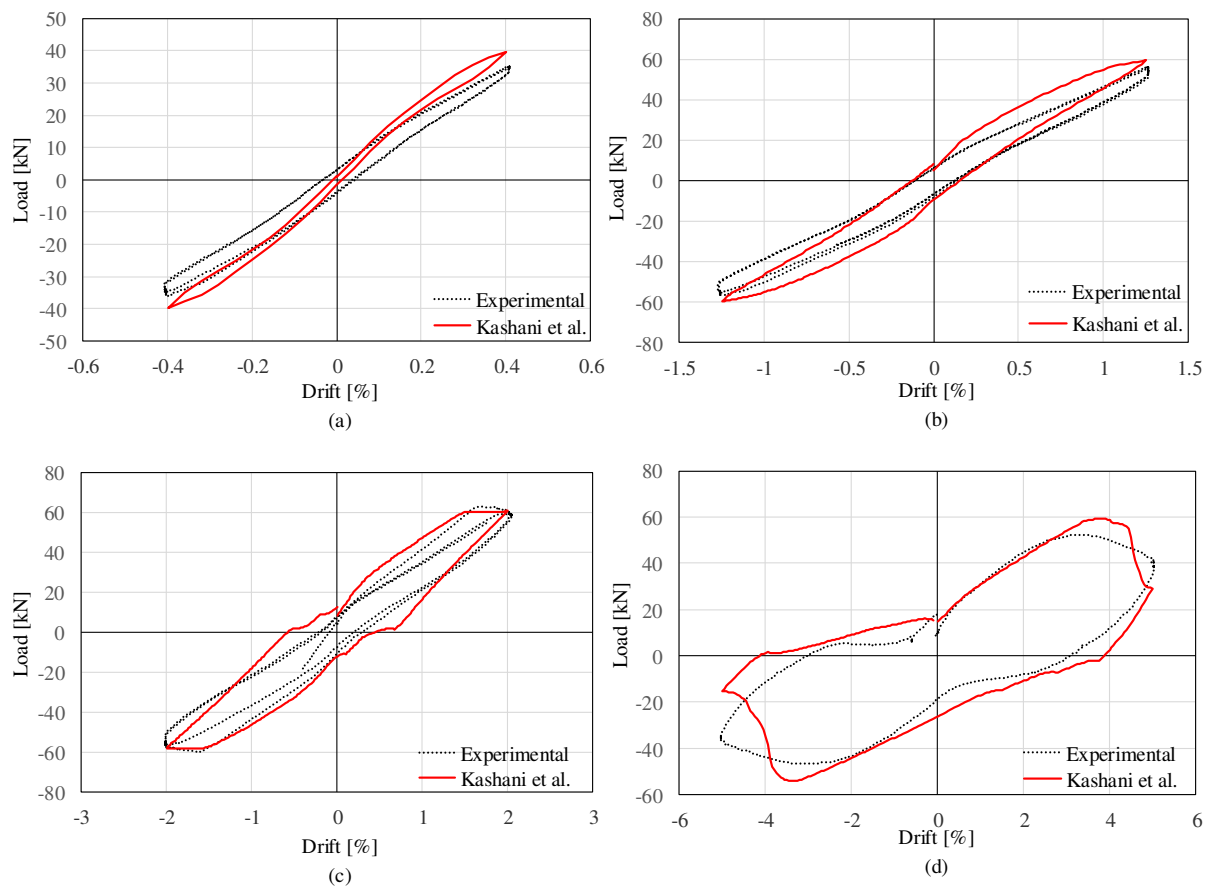


Figure 5.47: Comparison between experimental and numerical results for drifts equal to: (a) 0.4%, (b) 1.25%, (c) 2% and (d) 5%.

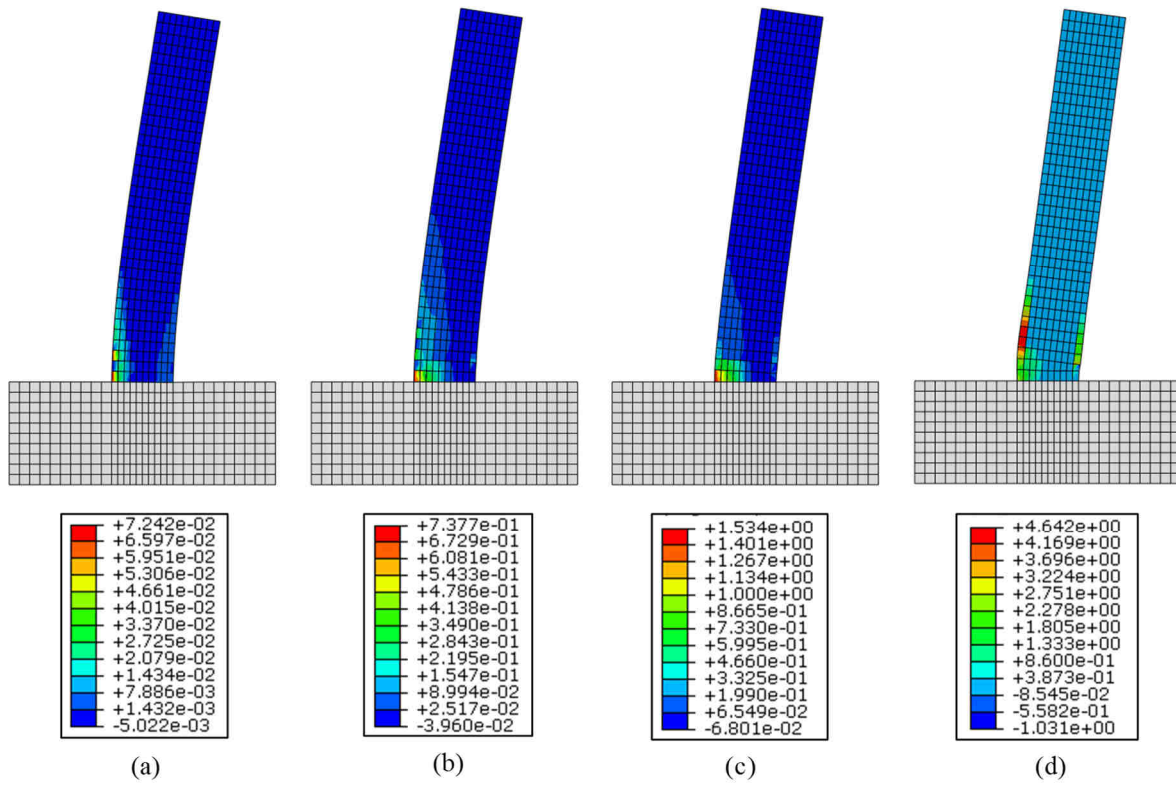


Figure 5.48: Crack pattern obtained with PARC\_CL 2.1 using the Kashani et al. (2015) law for drift equal to: (a) 0.3%, (b) 1.25%, (c) 2%, (d) 5%.

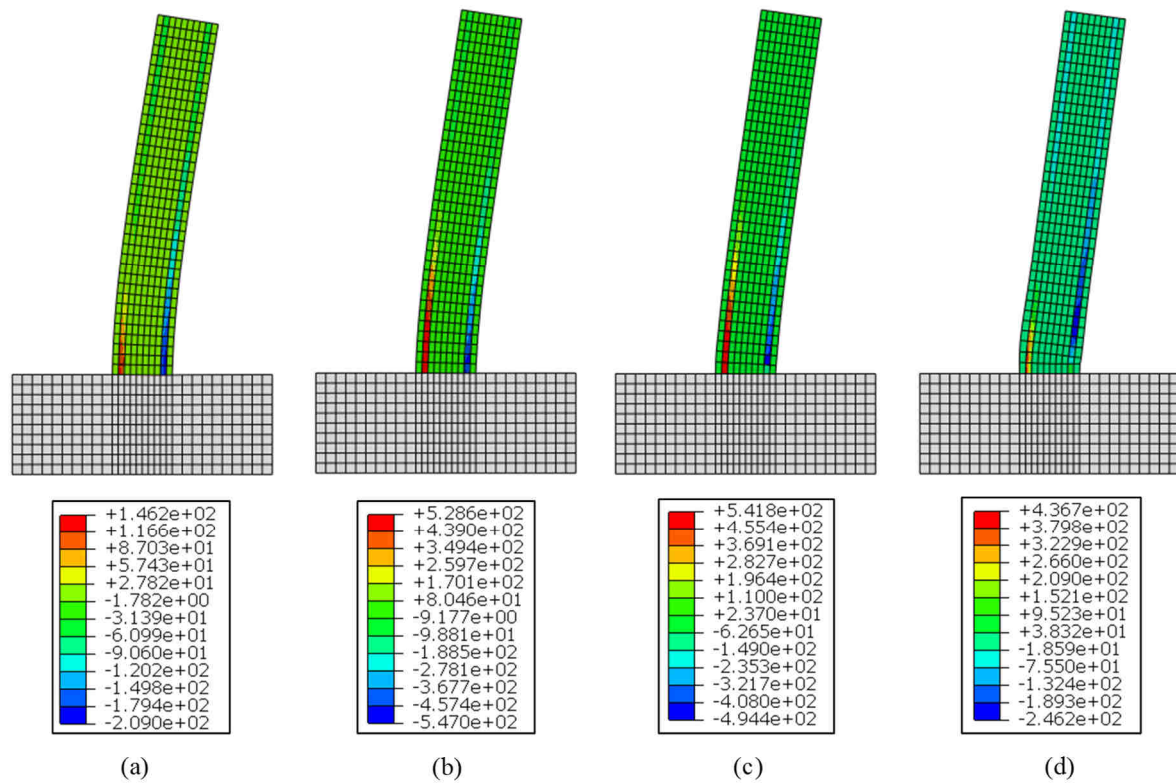


Figure 5.49: Longitudinal rebars stresses obtained with PARC\_CL 2.1 using the Kashani et al. (2015) law for drift equal to: (a) 0.3%, (b) 1.25%, (c) 2%, (d) 5%.

## 5.4 Concluding Remarks

The buckling of longitudinal reinforcement can substantially influence the response of RC existing structural elements. For this reason, a numerical model able to reproduce the buckling failure is developed and applied to a RC column experimentally tested.

Three different models for steel are implemented in the PARC\_CL 2.1 crack model which assumes reinforcement smeared in the hosting concrete element. The first one is the widely known Menegotto&Pinto (Menegotto et al., 1973), the second one is the Monti&Nuti (Monti et al., 1992) and the third one is the Kashani (Kashani et al., 2015). The Monti&Nuti and the Kashani models are able to consider the buckling effect, differently to the Menegotto&Pinto formulation. For evaluating the efficiency of the models, the cyclic response of a RC column is compared with the NLFEA conducted with PARC\_CL 2.1 model.

Two different modeling strategies are proposed: coarse mesh with high mesh size and a more refined version with smaller element size. The second approach has shown more accurate results both in terms of load-drift curve and crack pattern. This is mainly due to the presence of the concrete cover, i.e. elements in which only concrete is modeled without reinforcement.

The main outcomes are briefly reported:

- the Monti&Nuti (1992) model and the Kashani et al. (2015) model are able to catch the buckling localization at the base of the column with respect to the Menegotto&Pinto (1973).
- Even if the three NLFEA load-drift curves are similar in terms of global response mostly in the first cycles, the stress-strain relationship of the steel is very different.
- Each model adopted for steel is calibrated on the basis of bare bars behaviour and without taking into account the interaction with the surrounding concrete. For this reason, the modification proposed in Kashani et al. (2016) is introduced in the PARC\_CL 2.1 model. Thanks to this improvement it was possible to obtain effective results.

The Menegotto&Pinto model is the most widespread used for modeling the cyclic behavior of steel in RC elements. However, it has been demonstrated that this model is not able to capture the resistance reduction induced by the buckling of longitudinal reinforcements. This lead to an overestimation of the resistance of about 60% in case of drift equal to 5%, corresponding to the last drift reached by the column before failure. Furthermore, also the stiffness in the unloading and reloading branches is overestimated and the model is not able to accurately simulate the hysteretic cycles. However, the most important aspect to be underlined is the impossibility of the model to predict the ultimate ductility recorded during the experimental test. Indeed,

Figure 5.50 shows the behaviour of the column until failure using the Menegotto&Pinto law. The NLFEA demonstrates that the failure would occur because of the achievement of the ultimate stress of the reinforcements, corresponding to a drift equal to 12% (more than double that recorded experimentally).

This analysis highlights the need for an efficient model capable of grasping a more realistic behavior of the materials as well as the failure mode. A model for steel including buckling, therefore, avoids overestimation of the strength and ultimate capacity of the structure.

Future improvement will focus on the modelling of degradation of tensile strength, due to low-cycle fatigue loading. By means of this contribution it will be possible to predict the loss of strength due to a high number of cycles.

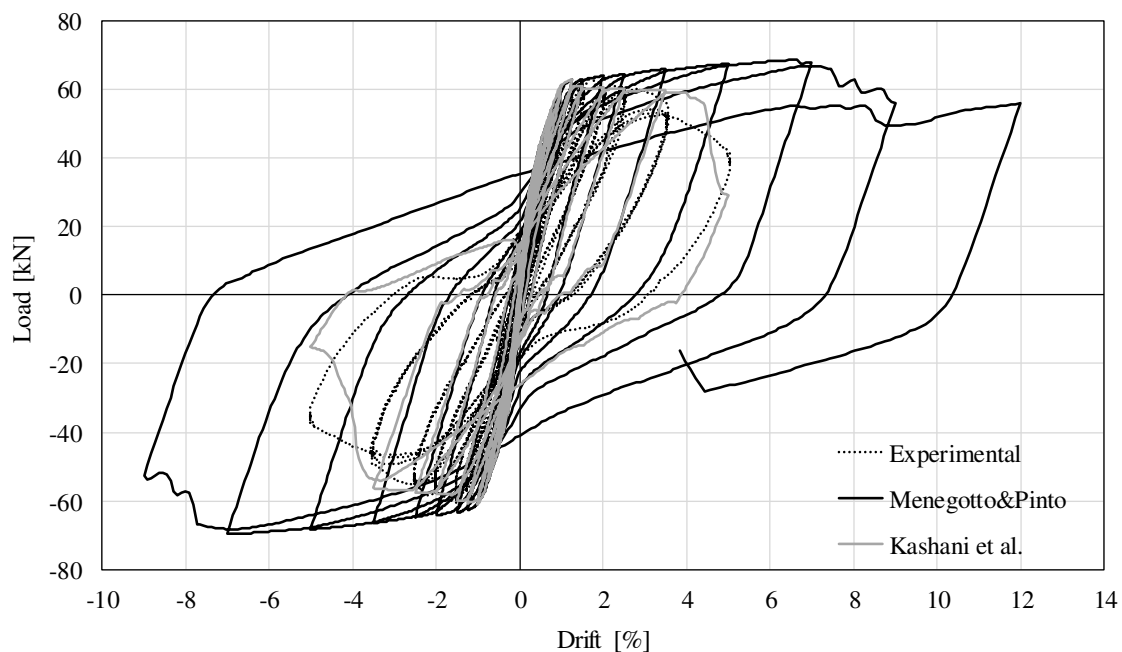


Figure 5.50: NLFEA using Menegotto&Pinto model until failure.

Further validation will be necessary to assess the efficiency of the proposed model for the prevision of existing RC elements typically characterized by poor structural details, as beam-column joints (Verderame et al., 2018). Even if conventional modelling approach considers only beam and column flexibility, the seismic performance of existing buildings is typically influenced by the non-linear behavior of joints (characterized by lack of an adequate transverse reinforcement, deficiencies or absence in the anchorage), De Risi et al. (2015).

Another important aspect will concern the modelling of corrosion effects. Indeed, one of the most interesting characteristics of the Kashani law is the extensibility of the formulation to

corroded rebars. In this way, it may be possible to analyze the corroded column tested by Meda et al. (2014). Starting from this validation further corroded RC elements will be modeled.

## 5.5 References

- Albanesi T., Biondi S., Nuti C.* (2001). Influenza dell'instabilità delle armature longitudinali sulla risposta d'elementi in c.a. Proc. of the 10th Italian Conference on Earthquake Engineering.
- Bae S., Miseses A.M., Bayrak O.* (2005). Inelastic buckling of reinforcing bars. *Journal of Structural Engineering*, 131(2):314-321.
- Balan T.A., Filippou F.C., Popov E.P.* (1998). Hysteretic model of ordinary and high-strength reinforcing steel. *Journal of Structural Engineering*, 124(3):288–297.
- Belletti B., Scolari M., Vecchi F.* (2017a). PARC\_CL 2.0 crack model for NLFEA of reinforced concrete structures under cyclic loadings. *Computers and Structures*, 191(2017):165–179.
- Belletti B., Vecchi F.* (2017b). Implementazione del fenomeno del buckling delle armature soggette a carichi ciclici nel modello fessurativo PARC\_CL 2.1. Convegno Anidis, Pistoia (Italy).
- Cosenza E., Manfredi G., Verderame G.* (2002). Seismic assessment of gravity load designed RC frames: Critical issues in structural modelling. *Journal of Earthquake Engineering* 6:101-122.
- Cosenza E., Prota A.* (2006). Experimental Behaviour and Numerical Modelling of Smooth Steel Bars Under Compression. *Journal of Earthquake Engineering*, 10(3):313-329.
- Cosenza E., Prota A.* (2009). Cyclic Behavior of Smooth Steel Reinforcing Bars: Experimental Analysis and Modeling Issues. *Journal of Earthquake Engineering*, 13(4):500-519.
- Comartin C., Elwood K., Faison H.* (2004). Housing report: Reinforced Concrete Moment Frame Building without Seismic Details. *World Housing Encyclopedia*.

- Del Gaudio C., Ricci P., Verderame G.M.* (2018). A class-oriented mechanical approach for seismic damage assessment of RC buildings subjected to the 2009 L'Aquila earthquake. *Bulletin of Earthquake Engineering*, 16(10):4581-4605.
- De Risi M.T., Ricci P., Verderame G.M.* (2015). Influence of joint response in the assessment of seismic performance of existing reinforced concrete frames. *COMPdyn 2015 - 5th ECCOMAS Thematic Conference on Computational Methods in Structural Dynamics and Earthquake Engineering 2015*, Pages 1560-1579
- Dhakal R.P., Maekawa K.* (2002<sup>a</sup>). Path-dependent cyclic stress–strain relationship of reinforcing bar including buckling. *Engineering Structures*, 24(11):1383-1396.
- Dhakal R.P., Maekawa K.* (2002<sup>b</sup>). Modeling for postyield buckling of reinforcement. *Journal of Structural Engineering*, 128(9):1139-1147.
- Dhakal R.P., Maekawa K.* (2002<sup>c</sup>). Reinforcement stability and fracture of cover concrete in reinforced concrete members. *Journal of Structural Engineering*, 128(10):1253-62.
- Dodd L.L., Restrepo-Posada J.I.* (1995). Model for Predicting Cyclic Behavior of Reinforcing Steel. *Journal of Structural Engineering*, 121(3):433-45.
- Gomes A., Appleton J.* (1997). Nonlinear cyclic stress-strain relationship of reinforcing bars including buckling. *Engineering Structures*, 10(19):822-826.
- Hill C.D., Blandford G.E., Wang S.T.* (1989). Post-buckling analysis of steel space trusses. *Journal of Structural Engineering*, 115(4):900-19.
- Kashani M.M., Crewe A.J., Alexander N.A.* (2013<sup>a</sup>). Nonlinear stress-strain behaviour of corrosion-damaged reinforcing bars including inelastic buckling. *Eng Struct*, 48:417-29.
- Kashani M.M., Crewe A.J., Alexander N.A.* (2013<sup>b</sup>). Nonlinear cyclic response of corrosion-damaged reinforcing bar with the effect of buckling. *Constr Build Mater*, 41:388–400.
- Kashani M.M., Lowes L.N., Crewe A.J., Alexander N.A.* (2014). Finite element investigation of the influence of corrosion pattern on inelastic buckling and cyclic response of corroded reinforcing bars. *Engineering Structures*, 75:113-25.

- Kashani M.M., Lowes L.N., Crewe A.J., Alexander N.A.* (2015). Phenomenological hysteretic model for corroded reinforcing bars including inelastic buckling and low-cycle fatigue degradation. *Computers and Structures*, 156:58–71.
- Kashani M.M., Lowes L.N., Crewe A.J., Alexander N.A.* (2016). Nonlinear fibre element modelling of RC bridge piers considering inelastic buckling of reinforcement. *Engineering Structures*, 116:163–177.
- Massone L.M.* (2013). Fundamental principles of the reinforced concrete design code changes in Chile following the Mw 8.8 earthquake in 2010. *Engineering Structures* 56:1335-1345.
- Massone L.M. and López E.E.* (2014). Modeling of reinforcement global buckling in RC elements. *Engineering Structures*, 59:484–94.
- Mau S.T., El-Mabsout M.* (1989). Inelastic buckling of reinforcing bars. *Journal of Engineering Mechanics*, 115(1):1-17.
- Meda A., Mostosi S., Rinaldi Z., Riva P.* (2014). Experimental evaluation of the corrosion influence on the cyclic behaviour of RC columns. *Engineering Structures*, 76:112-123.
- Menegotto M., Pinto P.E.* (1973). Method of analysis for cyclically loaded R.C. plane frames including changes in geometry and non-elastic behaviour of elements under combined normal force and bending, Symposium on the Resistance and Ultimate Deformability of Structures Acted on by Well Defined Repeated Loads. IABSE, Lisbon (Portugal).
- Moyer M.J., Kowalsky M.J.* (2003). Influence of tension strain on buckling of reinforcement in concrete columns. *ACI Struct J* 100, 1:75-85.
- Monti G., Nuti C.* (1992). Nonlinear cyclic behavior of reinforcing bars including buckling. *Journal of Structural Engineering*, 118(12):3268-3284.
- Mullapudi T.R.S.* (2010). Seismic analysis of reinforced concrete structures subjected to combined axial, flexure, shear and torsional loads. Ph.D. Dissertation, University of Houston.
- OpenSees (2011). The open system for earthquake engineering simulation. Pacific Earthquake Engineering Research centre, University of California, Berkeley.

- Oliveto G., Liberatore L., Decanin L.D.* (2011). Evoluzione storica della normativa sismica italiana alla luce degli effetti causati dal terremoto dell'Aquila del 2009. (in Italian) XIV Convegno ANIDIS L'Ingegneria Sismica in Italia, Bari, Italy.
- Papia M., Russo G., Zingone G.* (1988). Instability of longitudinal bars in RC columns. *J Struct Eng*; 114(2):445–61.
- Parisi M.A., Maggio E., Marini C., Sumini V.* (2013). Edifici storici in calcestruzzo armato in zona sismica: valutazione delle risorse. (in Italian) XV Convegno ANIDIS L'Ingegneria Sismica in Italia, Padova, Italy.
- Rodriguez M., Botero J., Villa J.* (1999). Cyclic Stress-Strain Behavior of Reinforcing Steel Including Effect of Buckling. *Journal of Structural Engineering*, 125(6):605-612.
- Salvatore W., Caprili S., Barberi V.* (2009). Rapporto dei danni provocati dall'evento sismico del 6 aprile sugli edifici scolastici del centro storico de L'Aquila. Available on-line from [www.reluis.it](http://www.reluis.it)
- Thai H.T., Kim S.E.* (2011). Nonlinear inelastic time-history analysis of truss structures. *J Constr Steel Res*, 67:1966-72.
- Verderame G.M., Iervolino I., Ricci P.* (2009). Report on the damages on buildings following the seismic event of 6th of April 2009, V1.20. <http://www.reluis.it>
- Verderame G.M., De Risi M.T., Ricci P.* (2018). Experimental Investigation of Exterior Unreinforced Beam-Column Joints with Plain and Deformed Bars. *Journal of Earthquake Engineering*, 22(3):404-434
- Wallace J.W., Massone L.M., Bonelli P., Dragovich J., Lagos R., Lüders C., Moehle J.* (2012). Damage and implications for seismic design of RC structural wall buildings. *Earthquake Spectra* 28(S1):281-299.
- Zhou Z., Nuti C., Lavorato D.* (2014). Modeling of the mechanical behavior of stainless reinforcing steel. Proceedings of the 10th fib International Ph.D. Symposium in Civil Engineering, pp. 515-520.



*Zhou Z.*, (2015). Uniaxial Material Model for Reinforcing Bar Including Buckling in RC Structures. Ph.D. Dissertation, Università degli studi Roma Tre.

*Zhou Z., Lavorato D., Nuti C., Marano G.C.* (2015). A model for carbon and stainless-steel reinforcing bars including inelastic buckling for evaluation of capacity of existing structures COMPDYN 2015 - 5th ECCOMAS Thematic Conference on Computational Methods in Structural Dynamics and Earthquake Engineering, pp. 876-886.



# General Conclusions and Recommendations

---

# 6

This research aims to provide a contribution to a correct methodological and engineering approach to the problem of predictive evaluation of the collapse mechanisms typical of new and existing structures.

The proposed theoretical model, suitable for the analysis of multi-layer shell elements, is implemented as a user subroutine UMAT.for in Fortran code within the software Abaqus.

The basic assumptions of PARC\_CL 2.1 refer to the first version of the PARC model proposed by Belletti et al. (2001): the cracking is assumed as being uniform, the orientation of the cracks remains fixed upon further loading, the crack spacing is assumed to be constant and the reinforcement is smeared in the element. However, the limitation of the PARC model was the impossibility of being applied to structures subjected to cyclic and dynamic loading. For this reason, the model has been extended to be generalized to any loading case.

Reliable constitutive models are necessary, most of all in case of seismic analyses, in order to represent the significant aspect during cycles, as for example, irrecoverable strains, energy dissipation, stiffness, and strength deterioration. In the PARC\_CL 2.1 crack model, constitutive laws for concrete and steel enable to consider plastic and irreversible deformation in the unloading phase and to take into account the hysteretic cycles are implemented.

Another fundamental aspect refers to the aggregate interlock phenomenon. In fact, being a fixed crack model, the prediction of shear stresses generated along the cracks becomes fundamental and an aggregate interlock relation is necessary to be defined. To do this, the Gambarova (1983) formulation is extended to cyclic loading. The validity of the formulation is

demonstrated by means of the comparison not only with experimental results on simple RC panels but also with the NLFEA results obtained with DIANA software.

Moreover, in order to properly analyze the dynamic behaviour, the Rayleigh damping stiffness-proportional coefficient is developed.

A proper numerical modelling able to consider shrinkage effect is needed in order to avoid inaccurate predictions of structural performances at serviceability conditions. To this aim, in the PARC\_CL 2.1 model, concrete shrinkage is considered by introducing it as a prescribed deformation. Subsequently, by means of an iterative procedure, the tension stiffening effect is also added to the model, with the aim to evaluate tensile stresses due to the bond between the reinforcing bars and the surrounding concrete. Since shrinkage gradually reduces the beneficial effects of tension stiffening, experimental tests are simulated by NLFEA taking into account both the effects.

The tension stiffening formulation will allow to consider phenomena directly associated with existing buildings. Indeed, in case of bad anchorage, for example, splitting failure and sliding of the bars due to debonding could develop.

Currently, in Italy, it is estimated that 60% of the existing buildings were built and designed without reference to seismic criteria imposed by codes. The need for a correct structural prevision of these types of buildings is evident. Indeed, due to the lack of details, often accompanied by poor material characteristics, these structures show different collapse mechanisms compared to those of new structures.

Despite the vulnerability of existing buildings being a very current topic, only limited research that combines deterioration modelling with numerical analyses is available. For this reason, new formulations are added to the PARC\_CL 2.1 crack model in order to properly evaluate the structural behaviour of existing buildings. To this aim, the buckling of longitudinal rebars is firstly detected and two different constitutive laws able to consider its effect are implemented. In particular, the Kashani et al (2015<sup>a</sup>) formulation, together with the basic formulation for RC elements, has been demonstrated to provide good results. The potentialities of the Kashani et al. (2015<sup>a</sup>) model are many, including the possibility of being extended to corrosion and to consider strength degradation due to low-cycle fatigue.

In conclusion, the proposed model has been able to predict with good accuracy the response of structural elements of increasing complexity, constituting a valid starting point for future extensions. The comparisons with the experimental results of different structural typologies show a good agreement, evidencing the reliability of the PARC\_CL 2.1 model in

reproducing the different mechanism of failure. The potentialities of the model lie in its versatility, in having the direct control of the mechanisms as well as the possibility of adding contributions according to the need.

## 6.1 Recommendation for Future Research

The extension of the PARC\_CL 2.1 crack model to the existing building response prevision represents a fundamental development. For now, only the buckling effect is taken into account but future developments are recommended.

- **Implementation of the low-cycle fatigue degradation**

Experimental evidence has shown that failure in RC members is influenced by the number of loading cycles to which the structure is subject in its life. The main observed failure modes are the fracture of longitudinal reinforcing steel bars due to low-cycle fatigue, the fracture of transverse reinforcement and the buckling of longitudinal reinforcing bars.

The cyclic nature of the earthquake loading causes strength and stiffness deterioration of structural members, resulting in a cumulative reduction of their service life. More specifically, long-duration earthquakes increase the total number of loading cycles which the structure might experience during its lifetime. The seismic damage accumulated by structural elements can lead to increase vulnerability to failure.

For this reason, a cumulative damage model for RC structures in seismic application is needed. The Kashani et al. (2015<sup>a</sup>, 2015<sup>b</sup>) model provides formulation able to simulate the combined effect of buckling and fatigue degradation in RC elements. However, the fatigue contribution is not yet implemented in the PARC\_CL 2.1 crack model.

- **Implementation of hysteretic model for corroded reinforcing bars**

A serious durability problem has been observed in the RC structures exposed to corrosive environments like deicing salts and seawater. In these cases, the main cause of deterioration is related to the corrosion of the embedded reinforcement that provokes the reduction of the structural performance, both in terms of strength and ductility. Indeed, the corrosion process mainly determines a reduction of the steel cross-section (uniform or localized on the entire reinforcement length) and a worsening of the reinforcing steel strength and ductility properties (Cairns et al., 2005; Imperatore and Rinaldi, 2008; Apostolopoulos and Matikas, 2016).

Moreover, corrosion causes reduction of the compressive capacity of the cracked cover concrete and reduction of bond strength at the steel and concrete interface. Consequently, a reduction of the bearing and dissipative capacity of the structural element occurs (Castel et al., 2000; Coronelli and Gambarova, 2004; Rinaldi et al., 2008; Imperatore et al., 2012; Imperatore et al., 2016; Di Carlo et al., 2017).

Even if the issue of the degradation in aged reinforced concrete structures attracts a considerable attention, NLFE models able of predicting the non-linear response with degradation effects are still under development.

Kashani et al. (2013<sup>a</sup>, 2013<sup>b</sup>, 2013<sup>c</sup>) conducted an extended experimental campaign to explore the impact of corrosion on the non-linear behaviour of reinforcement. The authors proposed a more advanced uniaxial material models to improve the accuracy of the prediction, combining the effect of inelastic buckling and low-cycle fatigue degradation in presence of corrosion.

The basic formulation of the Kashani et al. (2015<sup>a</sup>) model for not corroded member is already implemented in the PARC\_CL 2.1 crack model and represents the starting point for future extension to corrosion.

- **Implementation of bond-slip law for corroded rebars**

Corrosion of reinforcing bars greatly influences also the bond between concrete and steel.

The volume increase due to corrosion causes splitting and leads to weakening of the bond, which directly affects the serviceability and the ultimate strength of RC members within a structure (Cabrera, 1996; Yoon et al., 2000; Malumbela et al., 2009). When corrosion affects ribbed bars, reduction of the interlocking forces between the ribs of the bars and the surrounding concrete is verified (Wang and Liu, 2006). The reduction of both the strength and ductility behaviour of RC structures due to corrosion has to be considered, in particular when cyclic loading response is to be detected.

In order to consider this effect in the PARC\_CL 2.1 crack model, the bond-slip law, already implemented in the model, could be modified by translating the curve obtained in absence of corrosion, as a function of the confinement and the level of corrosion of the longitudinal bar (Lundgren et al., 2012).

- **Implementation of cyclic constitutive law for smooth bars**

Existing concrete buildings reinforced by smooth bars were very common in Europe, Asia, and Oceania. They were generally built before the 1970s and were characterized by the absence of seismic detailing in the structural members (e.g. beams, columns, joints, etc.).

Cosenza and Prota (2005, 2009) conducted an extensive experimental campaign on smooth steel bars tested both monotonically and cyclically. The authors explored a broad range of slenderness ratio demonstrating that, for high slenderness values, the reloading branch from compression to tension presented an accentuated pinching effect with a change of sign of the curvature.

In RC structures, smooth bars differ from deformed ones for bond properties. In fact, deformed bar bond to concrete is mostly provided by a mechanical interlock between the ribs and concrete, whereas smooth bar bond to concrete is mostly provided by the chemical adherence of steel to concrete cement paste (Abrams 1913; Feldman and Bartlett 2005). It results in lower bond strength. Due to low bond strength, the seismic response of RC members with smooth bars significantly change compared to members with deformed bars (Arani et al., 2014; Verderame et al., 2008; Di Ludovico, 2014). Experimental investigations have been shown that RC columns reinforced with smooth bars and subjected to lateral displacement are characterized by a limited number of cracks along the specimen length. Furthermore, these columns may experience bar slipping and end rotations for a quasi-rocking mode of deflection.

In order to model all different cases involved in real structures by means the PARC\_CL 2.1 crack model, the definition of an accurate theoretical constitutive law for smooth bars is needed.

- **Modelling of beam to column joints**

Another aspect that can highly influence the vulnerability of non-seismically detailed RC frame structures is the non-linear behaviour of beam to column joints.

Typically, beam to column joints of existing RC structures are characterized by insufficient shear reinforcements, or even lack of shear reinforcement in the joint core and poor seismic details (insufficient anchorage length, short lap splices, and discontinuous longitudinal bars). These lack of structural details increases the probability of shear, bond, or buckling failure in the beam to column joints determining the overall behaviour of the structure. For these reasons, the assessment of the seismic response of RC joints in terms of failure mode, strength, and ductility deserves more attention.

Many investigations have been conducted to evaluate the inelastic response of RC joints but few numerical procedures are able to take into account the beam-to-column joint failure during the overall assessment of the non-linear behavior of an entire building. Multi-layered shell elements could be used to assess the non-linear response of beam to column joints instead of post-analyses checks usually carried out in case of beam element modelling.

- **Application of the PARC\_CL 2.1 to the robustness assessment of RC structures**

Structural robustness is actually one of the major issues faced by the international scientific community. Extreme events (i.e. terrorist attacks, vehicle impacts, explosions, etc.) often cause local damage to building structures as failure of one or more vertical load-bearing components, leading to the progressive collapse of the structure or part of it. The resistant mechanisms, that are activated due to progressive collapses, produce a non-linear behaviour often associated with dynamic effects. Thus, the NLFEA must be capable to provide accurate information about the structural behaviour (Izzudin et al., 2008; Qian et al., 2015; Petrone et al., 2016).

The progressive collapse resistance of one-way reinforced concrete beam–slab substructures under a middle-column-removal scenario has been investigated by Ren et al., 2016. The experimental campaign has shown large areas of concrete spalling and rebar buckling in the severely damaged beam.

The possibility to apply the PARC\_CL 2.1 model to the structural robustness theme could be interesting in order to evaluate the influence of the buckling effect on the NLFEA results.

## 6.2 References

*Abrams D. A.* (1913). Tests of Bond Between Concrete and Steel. University of Illinois Bulletin No. 71, University of Illinois, Champaign, IL, 240 pp.

*Apostolopoulos A., Matikas T.E.* (2016). Corrosion of bare and embedded in concrete steel bar–impact on mechanical behavior. *International Journal of Structural Integrity*, 7(2), 240-259.

*Arani K.K., Di Ludovico M., Marefat M.S., Prota A., Manfredi G.* (2014). Lateral Response Evaluation of Old Type Reinforced Concrete Columns with Smooth Bars. *ACI Structural Journal*, 111(4):827-838.



- Belletti B., Cerioni R., Iori I.* (2001). Physical approach for reinforced-concrete (PARC)membrane elements. *ASCE J Struct Eng*;127(12):1412–26.
- Cabrera J.G.* (1996). Deterioration of concrete due to reinforcement steel corrosion, *Cem. Concr. Compos.* 18:47–59.
- Cairns J, Plizzari GA, Du Y, Law DW, Franzoni C.* (2005). Mechanical properties of corrosion-damaged reinforcement. *ACI Mater J.*;102(4):256–64.
- Castel A, Francois R, Arligue G.* (2000) Mechanical behaviour of corroded reinforced concrete beams – Part 1: experimental study of corroded beams. *Mater Struct/ Mater et Constr* 2000:33. November.
- Coronelli D, Gambarova PG.,* (2004) Structural assessment of corroded reinforced concrete beams: modeling guidelines. *ASCE – J Struct Eng* 2004;130(8):1214–24.
- Cosenza E., Prota A.* (2006). Experimental Behaviour and Numerical Modelling of Smooth Steel Bars Under Compression. *Journal of Earthquake Engineering*, 10(3):313-329.
- Cosenza E., Prota A.* (2009). Cyclic Behavior of Smooth Steel Reinforcing Bars: Experimental Analysis and Modeling Issues. *Journal of Earthquake Engineering*, 13(4):500-519.
- De Risi M.T. and Verderame G.M.* (2017). Experimental assessment and numerical modelling of exterior non-conforming beam-column joints with plain bars. *Engineering Structures* 150(2017):115-134.
- Di Carlo, F., Meda, A., Rinaldi, Z.,* (2017). Numerical evaluation of the corrosion influence on the cyclic behavior of RC Columns. *Engineering Structures* (156), pp. 219-230.
- Di Ludovico M., Verderame G.M., Prota A., Manfredi G., Cosenza E.* (2014). Cyclic Behavior of Nonconforming Full-Scale RC Columns. *J. Struct. Eng.*, 2014, 140(5): 04013107
- Feldman L. R., and Bartlett F. M.* (2005). Bond Strength Variability in Pullout Specimens with Plain Reinforcement. *ACI Structural Journal*, 102(6): 860-867.
- Gambarova PG.* (1983). Sulla trasmissione del taglio in elementi bidimensionali piani di c.a. fessurati. In: *Proceedings of Giornate AICAP*; p. 141–56 [in Italian].

- Imperatore S. and Rinaldi Z.* (2008). Mechanical behaviour of corroded rebars and influence on the structural response of R/C elements. Concrete Repair, Rehabilitation and Retrofitting II: 2nd International Conference on Concrete Repair, Rehabilitation and Retrofitting, ICCRRR-2, 24-26 November 2008, Cape Town, South Africa (p. 203). CRC Press.
- Imperatore, S., Leonardi, A., Rinaldi, Z.,* (2012). Mechanical behaviour of corroded rebars in reinforced concrete elements. Mechanics, Models and Methods in Civil Engineering, 207-220.
- Imperatore, S., Leonardi, A., Rinaldi, Z.,* (2016). Strength decay of RC sections for chloride attack. International Journal of Structural Integrity, 7(2), 194-212.
- Izzudin B., Vlassis A.G., Elghazouli A.Y., Nethercot D.A.* (2008). Progressive collapse of multi-storey buildings due to sudden column loss - Part I: Simplified assessment framework. Engineering Structures, 30(5): 1308-1318
- Kashani M.M., Crewe A.J., Alexander N.A* (2013<sup>a</sup>). Nonlinear stress–strain behaviour of corrosion-damaged reinforcing bars including inelastic buckling. Engineering Structures, 48, 417-429.
- Kashani M.M., Crewe A.J., Alexander N.A* (2013<sup>b</sup>). Nonlinear cyclic response of corrosion-damaged reinforcing bars with the effect of buckling. Construction and Building Materials, 41, 388-400.
- Kashani M.M., Crewe A.J., Alexander N.A.* (2013<sup>c</sup>). Use of a 3D optical measurement technique for stochastic corrosion pattern analysis of reinforcing bars subjected to accelerated corrosion. Corrosion Science, 73, 208-221.
- Kashani MM., Lowes L.N., Crewe A.J., Alexander N.A.* (2015<sup>a</sup>). Phenomenological hysteretic model for corroded reinforcing bars including inelastic buckling and low-cycle fatigue degradation. Computers and Structures, 156:58–71.
- Kashani M.M., Barmi A.K., Malinova V.S.* (2015<sup>b</sup>). Influence of inelastic buckling on low-cycle fatigue degradation of reinforcing bars. Construction and Building Materials 94:644-655.

- 
- Lundgren K.* (2007). Effect of corrosion on the bond between steel and concrete: an overview. Magazine of Concrete Research, Vol 59(6): 447-461.
- Malumbela G., Moyo P., Alexander M.,* (2009). Behaviour of RC beams corroded under sustained service loads. Construction and Building Materials, 23(11):3346-3351.
- Qian K., Bing L., Zhang Z.W.* (2015). Testing and simulation of 3D effects on progressive collapse resistance of RC buildings. Magazine of Concrete Research, ICE Publishing 67(4):163-178.
- Petrone F., Shan L., Kunnath S.K.* (2016). Modeling of RC Frame Buildings for progressive collapse analysis. International Journal of Concrete Structures and Materials, 10(1):1-13.
- Rinaldi Z, Valente C, Pardi L.* (2008). A simplified methodology for the evaluation of the residual life of corroded elements. Structure and Infrastructure Engineering, 4 (2):139 – 152, Taylor & Francis Eds.
- Verderame G.M., Fabbrocino G., Manfredi G.* (2008). Seismic response of r.c. columns with smooth reinforcement. Part II: Cyclic tests. Engineering Structures, 30(2008):2289-2300.
- Wang X., Liu X.* (2006). Bond strength modeling for corroded reinforcements. Construction and Building Materials, 20:177–86.
- Yoon S., Wang K., Weiss J., Shah S.* (2000). Interaction between loading, corrosion, and serviceability of reinforced concrete. ACI Mater J, 97 (6):637-644.



# Curriculum Vitae

---

## Personal information

Name **Francesca Vecchi**  
Email francesca.vecchi1@studenti.unipr.it  
vecchi.francesca89@gmail.com  
Date of Birth 21 November 1989  
Nationality Italian



## Work experience and education

Nov 2015 - Nov 2018 Ph.D. student in Civil Engineering  
Department of Engineering and Architecture (DIA)  
University of Parma, Italy

Apr 2015 - Sep 2015 Research fellowship  
Department of Engineering and Architecture (DIA)  
University of Parma, Italy

Feb 2012 - Jul 2014 Master's degree in Civil Engineering  
Department of Engineering and Architecture (DIA)  
University of Parma, Italy

Sep 2008- Feb 2012 Bachelor's degree in Civil Engineering  
Department of Engineering and Architecture (DIA)  
University of Parma, Italy

Sep 2003 - June 2008 Scientific High School  
Istituto di Istruzione Superiore 'Giovanni Falcone', Asola  
(MN), Italy



# List of Publications

---

## Journal publications

6. **Vecchi F.**, Belletti B. (2018). Prediction of multi-storey RC walls by static and dynamic NLFEA by means PARC\_CL 2.0 crack model, Engineering Structures, submitted.
5. Scolari M., Belletti B., **Vecchi F.** (2017). In-plane and out-of-plane cyclic response prediction of RC structural walls by means of multi-layered shell elements and PARC\_CL 2.0 crack model. Structural Concrete, under submission.
4. Strauss A, Cosma M.P., Belletti B., **Vecchi F.** (2018). Fractile based sampling procedure for the effective analysis of engineering structures, Probabilistic Engineering Mechanics, under submission.
3. Belletti B., Muttoni A., **Vecchi F.**, Ravasini S. (2018). Parametric analysis on punching shear resistance of reinforced concrete continuous slabs, Magazine of Concrete Research, DOI: 10.1680/jmacr.18.00123
2. Belletti B., Stocchi A., Scolari M., **Vecchi F.** (2017). Validation of the PARC\_CL 2.0 crack model for the assessment of the nonlinear behaviour of RC structures subjected to seismic action: SMART 2013 shaking table test simulation. Engineering Structures, Vol. 150, pp. 759-773, <http://dx.doi.org/10.1016/j.engstruct.2017.07.058>
1. Belletti B., Scolari M., **Vecchi F.** (2017). PARC\_CL 2.0 crack model for NLFEA of reinforced concrete structures under cyclic loadings. Computers and Structures, Vol. 191, pp. 165-179, <https://doi.org/10.1016/j.compstruc.2017.06.008>.

---

**Conference publications**

14. Belletti B., Ravasini, S., **Vecchi F.** (2018) Dependency of punching shear resistance and membrane action on boundary conditions of reinforced concrete continuous slabs. IALCEE conference, 28-31 October 2018, Ghent (Belgium).
13. Belletti B., Strauss, A., **Vecchi F.**, Cosma, M.P. (2018) Non linear structural analyses of prestressed concrete girders: tools and safety formats, IALCEE conference, 28-31 October 2018, Ghent (Belgium).
12. Belletti B., **Vecchi F.** (2018) Implementation of steel constitutive model including buckling in PARC\_CL 2.1 crack model, fib Congress 2018, 7-11th October 2018, Melbourne, Australia.
11. Belletti B., Cagnolati E., Cantone R., Muttoni A., **Vecchi F.** (2018) Interaction between longitudinal bending moment and transverse shear strength in RC deck slabs of hollow box bridges, fib Congress 2018, 7-11th October 2018, Melbourne, Australia.
10. Belletti B., **Vecchi F.** (2018) Buckling phenomenon implemented in the PARC\_CL 2.1 crack model, ITALIAN CONCRETE DAYS 2018, 13-16th June 2018, Milano-Lecco, Italy.
9. Lima C., Angiolilli M., Barbagallo F., Belletti B., Bergami A.V., Camata G., Cantagallo C., Di Domenico M., Fiorentino G., Ghersi A., Gregori A., Lavorato D., Luciano R., Marino E.M., Martinelli E., Nuti C., Ricci P., Rosati L., Ruggeieri S., Sessa S., Spacone E., Terrenzi M., Uva G., **Vecchi F.**, Verderame G.M. (2018) Nonlinear modeling approaches for existing reinforced concrete buildings: the case study of De Gasperi-Battaglia school building in Norcia, ITALIAN CONCRETE DAYS 2018, 13-16th June 2018, Milano-Lecco, Italy.
8. Belletti B., Dellapina C., Diemmi N., Halimi M., **Vecchi F.** (2018) Studies on the non-linear behavior of diaphragms of existing RC frames, ITALIAN CONCRETE DAYS 2018, 13-16th June 2018, Milano-Lecco, Italy.
7. Belletti B., **Vecchi F.**, Donninotti A. (2017). Implementazione del fenomeno del buckling delle armature soggette a carichi ciclici nel modello fessurativo PARC\_CL 2.1. Anidis 2017, 17-21 September, Pistoia, Italy (in Italian).
6. Belletti B., **Vecchi F.** (2017). Previsione della risposta di pareti in CA multipiano tramite analisi ad elementi finiti non lineari statiche e dinamiche condotte con il modello fessurativo PARC\_CL2.0. Anidis 2017, 17-21 September, Pistoia, Italy (in Italian).



- 
5. Belletti B., Scolari M., **Vecchi F.** (2017). Simulation of monotonic, static and dynamic response of RC squat walls by means of PARC\_CL 2.0 crack model. Proceedings of the COMPDYN 2017, 15-17 June, Rhodes Island, Greece.
  4. Belletti B., Scolari M., **Vecchi F.** (2016). NLFEA of reinforced concrete shear walls under cyclic loading by means of PARC\_CL 2.0 crack model. Proceedings of the fib Symposium 2016, 21-23 November, Cape Town.
  3. Belletti B., Scolari M., **Vecchi F.** (2016). Pushover, Cyclic and Dynamic Analyses Of RC Shear Walls By Means Of ParC\_CL1.1 Crack Model. Proceedings of the 9th International Conference on Fracture Mechanics of Concrete and Concrete Structures – FraMCoS-9.
  2. Belletti B., Scolari M., Stocchi A., **Vecchi F.** (2015), PARC\_CL and PARC\_CL2.0 for FEM analyses of RC structures subjected to cyclic loads, Proceedings of OpenSees Day, June 10-11, 2015, Salerno, Italy.
  1. Belletti B., Scolari M., Stocchi A., **Vecchi F.** (2014), PARC\_CL model for FEM analyses of RC structures subjected to cyclic loads, Proceedings of the International CAE Conference 2014, October 27-28, Pacengo del Garda Italy, Italy.